IPPT
PAN

Institute of Fundamental Technological Research

Polish Academy of Sciences

A thesis presented for the degree of
Doctor of Philosophy

Sequential Logic and Iterative Systems in Droplet Microfluidics

By

Damian Zaremba

Doctoral thesis supervisor
Piotr M. Korczyk

Warsaw 2023

Acknowledgements

I would like to thank my supervisor Piotr M. Korczyk for introducing me to the fascinating research field of droplet microfluidics, his constant support and involvement in preparation of this thesis.

I would also like to thank Slawomir Blonski for his support in the laboratory and sharing with me his knowledge and experience of experimental work.

Contents

Abstract

Droplet microfluidics is a new tool that is becoming increasingly used in medical, biological, and chemical sciences. Its essential feature is the use of two immiscible liquids in miniaturized devices. One of the liquids forms water-based droplets while the other, usually oil with a surfactant, transports them through a complex network of microchannels. The principal activity is the creation and manipulation of droplets in these devices. The extensive possibilities of droplet manipulation have allowed the implementation of complex algorithms and have enabled novel experiments in these fields. The realization of these functions is still performed using valves, electrodes, pumps, and other components. Using these components requires the proper design of microchannels to allow a microfluidic chip to be combined with external elements in a single device. The complexity and cost of such a device usually increase with the complexity of the laboratory task. The goal of the present work was to reduce the use of external components to the minimum amount necessary while increasing the ability to manipulate droplets by using geometries built directly into a microfluidic system.

This Ph.D. thesis addresses the development of sequential logic inside microfluidic systems for droplet manipulation and the coupling of digital algorithms with the developed microfluidic architecture to condition the contents of droplets. These concepts make microfluidics even more similar to digital circuits and bring the power of computer science, specifically digital signal processing, into the realm of microfluidic droplets. The resulting solutions show that these concepts can increase the complexity and capabilities of a microfluidic system while reducing the required external actuators.

The work is presented as a series of publications consisting of four publications in which the author is the first author and two other publications in which the author appears in another order. The additional publications play a supporting role, especially in describing the initial stages of the research. The published articles can be divided into two groups. The first group, consisting of two primary and additional publications, focuses on the study of single microfluidic geometries, the properties of laminar flow inside these geometries, and the interaction of droplets with them. The second group of articles, consisting of another two primary publications, builds on the previously developed geometries and presents findings regarding the primary research objectives.

This Ph.D. research began with a study of existing microfluidic geometries, such as bifurcations, which provided insight into the limitations of microfluidic modeling using electrical circuit analogies. Next, the author studied the formation of droplets in a T-junction and mechanisms of cutting and immobilization of droplets inside metering traps. These studies assisted the author in discovering that a droplet could effectively activate and deactivate a microfluidic bypass

slit. As a result, a new microfluidic Y-shape junction that forces the direction of the droplet flow to one of the two outputs was developed. Research regarding this junction showed that adding a bypass slit to the channel bifurcation could enable control of droplet flow in loops or more complex networks.

Research related to sequential logic has shown that microfluidic systems can be built as systems exhibiting the so-called internal state. Obstacles add the ability to stop droplets in microfluidic systems at a designated location if there is a bypass for oil flow. Other droplets can then trigger the stopped droplets if the triggering droplet blocks this oil bypass. This simple mechanism, combined with the developed junction, can yield a range of sequential logic geometries, from simple flip-flops and bimodal loops to one-hot counters. Their straightforward integration to larger assemblies in a cascade can result in binary or decimal counters. The research presented here demonstrates the possibility of synchronizing, permuting, and self-counting or decimating droplets. From this study, a designer of a microfluidic device can achieve these operations based on skillfully exploited bypass slits and obstacles.

In studying the metering trap, the author has determined that it is possible to form droplets directly in the feed channel of the droplet phase if the metering trap is placed inside this channel. The metering trap has improved the method of forming droplets inside the microfluidic device and has opened the possibility of creating a microfluidic architecture to condition droplet contents efficiently. Serial combination of a metering and a merging trap has demonstrated that repeated simple droplet operations such as merging, mixing, and splitting droplets can effectively change droplet content while maintaining a uniform droplet size. The author has achieved the ability to generate droplets of arbitrary concentrations using a suitable algorithm, similar to the binary search known in computer science.

This research was experimental and mainly consisted of observing the kinetics of droplets and their interactions with manufactured geometries of microfluidic devices under controlled conditions using known fluids in terms of their physicochemical properties. Obtaining the results required creating an automated experimental configuration, designing and fabricating prototypes, and analyzing the data after conducting a series of experiments. A technique of micromilling on polycarbonate plates was used to construct the prototypes. The final results show that with the proper combination of microfluidic geometries to perform specific functions and the skillful control of pumps, it is possible to perform complex manipulations of droplets within microfluidic systems while reducing the number of components.

Streszczenie (abstract in Polish)

Mikrofluidyka kropelkowa to nowe narzędzie coraz częściej wykorzystywane w naukach medycznych, biologicznych i chemicznych. Jej zasadniczą cechą jest wykorzystanie dwóch nie-mieszających się cieczy w zminiaturyzowanych urządzeniach mikroprzepływowych. Jedna z cie-czy tworzy kropelki na bazie wody, a druga, zazwyczaj olej z dodatkiem surfaktantu, transpor-tuje je przez skomplikowaną sieć mikrokanałów. Podstawową czynnością jest tworzenie i mani-pulowanie kroplami w tych urządzeniach. Szerokie możliwości manipulacji kroplami pozwalają na implementację złożonych algorytmów i umożliwiają przeprowadzenie nowatorskich ekspe-rymentów w wymienionych dziedzinach. Obecnie wciąż odbywa się to za pomocą zaworów, elektrod, pomp oraz innych komponentów. Zastosowanie tych elementów wymaga odpowied-niego zaprojektowania mikrokanałów w sposób umożliwiający ich połączenie z elementami ze-wnętrznymi w jednym urządzeniu. Skomplikowanie i koszt takiego urządzenia zwykle wzrasta wraz ze złożonością zadania laboratoryjnego. Motywacją niniejszej pracy jest ograniczenie sto-sowanych zewnętrznych elementów do niezbędnego minimum przy jednoczesnym zwiększeniu możliwości manipulowania kropelkami poprzez umiejętne wykorzystanie geometrii wbudowa-nych bezpośrednio w układ mikroprzepływowy.

Celem niniejszej pracy jest rozwój logiki sekwencyjnej wewnątrz układów mikroprzepływo-wych do manipulowania kroplami oraz sprzężenie algorytmów cyfrowych z opracowaną archi-tekturą mikroprzepływową do modyfikowania zawartości kropel. Rozwój tych kwestii jeszcze bardziej upodabnia mikroprzepływy do układów cyfrowych lub wprowadzają w świat mikro-przepływów kropelkowych potęgę informatyki, a dokładniej cyfrowego przetwarzania sygna-łów. Uzyskane rozwiązania pokazują, że mogą zwiększyć złożoność i możliwości systemu mikro-przepływowego przy jednoczesnej redukcji wymaganych zewnętrznych elementów wykonaw-czych.

Praca przedstawiona jest jako cykl publikacji składający się z czterech publikacji głównych, w których autor jest pierwszym autorem oraz dwóch publikacji dodatkowych, w których au-tor występuje w dalszej kolejności. Publikacje dodatkowe odgrywają rolę pomocniczą, zwłasz-cza w początkowych etapach badań. Opublikowane artykuły można podzielić na dwie grupy. Pierwsza grupa, zawierająca dwie publikacje główne i dodatkowe, skupia się na badaniach po-jedynczych geometrii mikrofluidycznych, właściwości przepływu laminarnego wewnątrz tych geometrii lub interakcji kropel z nimi. Druga grupa artykułów, składająca się z kolejnych dwóch publikacji głównych, bazuje na wcześniej zbadanych i opracowanych geometriach oraz przed-stawiają badania dotyczące podjętych głównych celów badawczych.

Praca rozpoczęła się od badań istniejących geometrii mikroprzepływowych, takich jak bi-furkacje, dzięki którym poznano ograniczenia modelowania mikroprzepływów przy zastosowa-

niu analogii do obwodów elektrycznych. Następnie badano formowanie się kropel w złączu T czy mechanizmów ucinania i unieruchamiania kropli wewnątrz pułapek tnących. Na podstawie tych badań zaobserwowano, że kropla może efektywnie aktywować i dezaktywować przepływ fazy ciągłej przez boczną szczelinę. Wskutek tego opracowano nowe złącze mikroprzepływowe wymuszające kierunek przepływu kropel do jednego z obu wyjść. Badania nad tym złączem pokazały, że dodanie szczeliny do rozwidlenia kanałów umożliwia kontrolę przepływu kropel w pętlach lub bardziej złożonych sieciach.

Badania związane z logiką sekwencyjną pokazują, że w układach mikroprzepływowych można budować w szerokim zakresie układy wykazujące tzw. stan wewnętrzny. Przeszkody dodają do układów mikroprzepływowych zdolność blokowania kropel w wyznaczonym miejscu, jeśli istnieje ujście dla przepływu oleju. Następnie, inne krople mogą wyzwalać te krople, jeśli kropla wyzwalająca przyblokuje obejście oleju. Ten prosty mechanizm, w połączeniu z wynalezionym złączem, daje szereg geometrii logiki sekwencyjnej: od prostych przerzutników, pętli bimodalnych do liczników pierścieniowych. Ich łatwa integracja w kaskadzie do większych zespołów w wyniku daje liczniki binarne lub dziesiętne. Przedstawione badania pokazują możliwość synchronizacji, permutacji i samo zliczania lub decymacji kropel. Dzięki badaniom te operacje można osiągnąć na podstawie umiejętnie wykorzystanych szczelin i przeszkód.

Podczas badań nad pułapką tnącą autor zaobserwował, że możliwe jest tworzenie kropel bezpośrednio w kanale doprowadzającym fazę kroplową, jeśli pułapka dozująca zostanie umieszczona wewnątrz tego kanału. Usprawniło to metodę formowania kropel wewnątrz urządzenia mikroprzepływowego i otworzyło możliwość stworzenia architektury mikroprzepływowej do efektywnego kondycjonowania zawartości kropel. Szeregowe połączenie pułapki tnącej i pułapki łączącej pokazało, że proste operacje na kropelkach wykonywane wielokrotnie, jak łączenie, mieszanie i rozdzielanie kropel, mogą skutecznie zmieniać zawartość kropel przy zachowaniu ich znormalizowanego rozmiaru. Możliwość generowania kropel o dowolnych stężeniach uzyskano poprzez wykorzystanie odpowiedniego algorytmu, podobnego do znanego w informatyce wyszukiwania binarnego.

Badania mają charakter eksperymentalny i polegają głównie na obserwacji kinetyki kropel i ich interakcji z wytworzonymi geometriami urządzeń mikroprzepływowych w kontrolowanych warunkach z wykorzystaniem znanych cieczy pod względem ich właściwości fizykochemicznych. Uzyskanie wyników wymagało zbudowania zautomatyzowanego stanowiska eksperymentalnego, zaprojektowania i wykonania prototypów oraz dokonaniu analizy danych po przeprowadzeniu szeregu eksperymentów. Do wykonania prototypów wykorzystano technikę mikrofrezowania na płytach poliwęglanowych. Końcowe wyniki badań pokazują, że dzięki odpowiedniej kombinacji geometrii mikroprzepływowych realizujących określone funkcje oraz umiejętnemu sterowaniu pompami możliwe jest wykonywanie złożonych manipulacji kropelkami wewnątrz układów mikroprzepływowych przy jednoczesnym zmniejszeniu liczby komponentów.

Cycle of publications

This Ph.D. thesis is presented as a series of research publications. It includes the following cycle of published research articles:

A Zaremba D., Błoński S., Jachimek M., Marijnissen M.J., Jakieła S., Korczyk P.M.,

Investigations of modular microfluidic geometries for passive manipulations on droplets

Bulletin of the Polish Academy of Sciences: Technical Sciences, Vol.66, No.2, pp.139-149, 2018

impact factor (2018): 1.361

B Zaremba D., Błoński S., Marijnissen M.J., Korczyk P.M.

Fixing the direction of droplets in a bifurcating microfluidic junction

Microfluidics and Nanofluidics, Vol.23, pp.55-1-18, 2019

impact factor (2019): 2.489

C Zaremba D., Błoński S., Korczyk P.M.

Integration of capillary–hydrodynamic logic circuitries for built-in control over multiple droplets in microfluidic networks

LAB ON A CHIP, Vol.21, No.9, pp.1771-1778, 2021

impact factor (2021): 7.517

D Zaremba D., Błoński S., Korczyk P.M.

Concentration on demand – a microfluidic system for precise adjustment of the content of single droplets

Chemical Engineering Journal, Vol.430, No.3, pp.132935-1-16, 2022

impact factor (2022): 13.273

Two additional studies played a supporting role in the research:

E Korczyk P.M., van Steijn V., Błoński S., <u>Zaremba D.</u>, Beattie D.A., Garstecki P.

Accounting for corner flow unifies the understanding of droplet formation in microfluidic channels

Nature Communications, Vol.10, No.1, pp.2528-1-9, 2019

impact factor (2019): 12.121

F Błoński S., <u>Zaremba D.</u>, Jachimek M., Jakiela S., Wacławczyk T., Korczyk P.M.

Impact of inertia and channel angles on flow distribution in microfluidic junctions

Microfluidics and Nanofluidics, Vol.24, No.2, pp.14-1-15, 2020

impact factor (2020): 2.529

Other publications of note are as follows:

- Błoński S., Aureille J., Badawi S., <u>Zaremba D.</u>, Pernet L., Grichine A., Fraboulet S., Korczyk P.M., Recho P., Guilluy Ch., Dolega M.E.

  Direction of epithelial folding defines impact of mechanical forces on epithelial state

  Developmental Cell, Vol.56, pp.3222-3234, 2021

  impact factor (2021): 13.417

- Rabcuka J., Błoński S., Meli A., Sowemimo-Coker S., <u>Zaremba D.</u>, Stephenson D., Dzieciatkowska M., Nerguizian D., Cardigan R. A., Korczyk P. M., Smethurst P. A., D'Alessandro A., Świętach P.

  Metabolic reprogramming under hypoxic storage preserves faster oxygen unloading from stored red blood cells

  Blood Advances, Vol.6, No.18, pp.5415-5428, 2022

  impact factor (2021): 7.637

1   Motivation

The main focus of droplet microfluidics is the design and manufacturing of microfluidic chips for specific applications. Regardless of the application or technology utilized, the most common operations performed on droplets within these devices can be categorized into three groups: droplet formation, manipulation and processing of formed droplets, and sensing of these droplets. This Ph.D. thesis focuses primarily on manipulating droplets, with some consideration given to their formation. Both formation and manipulation of droplets are crucial components of microfluidic devices and are fascinating areas of study in their own right. These operations significantly determine the size and cost of microfluidic chips and the range of possibilities for conducting assays or experiments. Therefore, considering these two operations as research objects can positively impact the potential of the entire field and its applications.

A microfluidic chip itself can be small. However, many additional components such as pumps, valves, and electrodes make the entire device complex and of a considerable size. One solution is to add micropumps [1, 2], microvalves [1, 3], and other miniaturized components directly into the chip itself [4]. Integrating many parts increases the complexity of manufacturing such a chip, which can lead to cost inefficiency. The second solution is to consider designs in which complex droplet manipulation is possible in microfluidic systems using a hard-wired, complex network with functional geometries such as traps, obstacles, bypasses, slits, and bifurcations. Manufacturing microfluidic devices constructed mostly with these elements is easier and cheaper than integrating extra parts into one system. In addition, the skillful use of the hydrodynamic properties of microfluidic geometries to construct microfluidic networks allows complex droplet handling. This idea is presented in [5–7]; however, a lack of knowledge remains regarding mechanisms and opportunities.

The primary motivation of this work was to develop a technique for designing microfluidic systems that enable complex droplet operations while minimizing the use of external elements that can increase system complexity, cost, and size. One promising approach is combining ideas or well-established computer algorithms with an architecture similar to electronics, creating logic-based systems and programmable processors within microfluidic devices. This approach differs from so-called digital microfluidics [8], in which complex droplet manipulation is achieved by using many electrodes controlled by electronic devices. In our case, droplet handling involves the creation of complex microfluidic structures using different geometries that perform the necessary functions. However, the available passive components still require improvement and expansion. The research presented in this work, such as permutations on droplets or arbitrary modification of droplet contents, can positively influence the field and open the way for further development of programmable and logic-based microfluidic devices.

2   Background

2.1   Introduction to microfluidic devices

Miniaturization has played a crucial role in technology development and science for over 50 years [9]. Since the advent of integrated circuits, scientific discovery and technological progress have accelerated. Miniaturization allows the creation of devices that are smaller, faster, and cheaper than their predecessors [10]; at the same time, it has been associated with a spread of the functionality of these devices. This multifaceted process has included the areas of biological, chemical, and medical science, in which complex research apparatuses are essential to conducting experiments and diagnoses.

Research conducted in the above fields requires sophisticated laboratories, is often hazardous to humans, and requires an isolated environment in which to conduct experiments or assays. Lengthy procedures to perform these activities require skilled personnel who may be prone to making errors when performing long, manual steps. Robotization can help constrain these problems, if only through liquid-handling robots [11]. Nevertheless, this solution still operates on large sample sizes, and the associated machines have large dimensions. A different solution that would both assist in procedures and offer miniaturization simultaneously is the lab-on-a-chip, a subset of MEMS technology [12]. The general idea behind lab-on-a-chip is to integrate microfluidic chips and miniaturized non-fluidic systems such as sensors [13]. The strategy involves creating a device that realizes one or several laboratory functions and can process samples in small volumes using at least partially automatized operations [14]. The development of this technology has been directly related to the emergence of microfabrication in electronics [15]. Using lab-on-a-chip not only shortens the waiting time for a result but also increases the availability of diagnostics in areas in which access to specialized laboratories is limited by utilizing point-of-care devices [16].

Microfluidics, one of the essential components of lab-on-a-chip devices, remains a new and rapidly growing field of science and has the potential to affect many areas in chemistry, biology, and medicine and may even have an impact on optics or information technology [17]. Microfluidics typically pertains to devices and techniques that can regulate and direct the flow of fluids at the micron scale [18]; it is associated with creating various microfluidic devices with sometimes complex microchannel geometries and networks [19] in which fluids can circulate in a controlled manner, performing many tasks [20, 21]. The ability to efficiently automate microfluidic systems [22] allows for construction of devices that execute complex algorithms quickly, consuming small amounts of samples and reagents. These aspects describe what is currently expected from lab-on-a-chip devices, but they also open the possibility of conducting novel experiments.

This thesis focuses on experimental fluid mechanics inside droplet microfluidic systems – a subset of microfluidics in which two immiscible liquids are used [23]. Its development began in the 1990s [15]. One of the liquids, called the droplet phase, forms droplets, while the other, as the continuous phase, fills the device and transports formed droplets through microchannels. Three significant phenomena characterize droplet microfluidics [24, 25]: high mass transfer, dominance of viscous over inertial forces, and considerable surface effects. These phenomena mainly affect formation of droplets and their behavior in microfluidic structures. The micron-scale dimension allows the creation of single droplets with very high-precision volumes in the range of picoliters and of uniform size [26]. Each droplet can be treated as a separate environment for biochemical reactions [27] or biological samples [28]. In addition, droplets can be stored side by side without cross-contamination [29], manipulated automatically [22, 30, 31], and used for high-throughput screening [22, 32, 33]. These features allow droplet microfluidic systems to use even less reagent, exhibit higher sample capacity, and present many more possibilities than single-phase devices.

Droplet microfluidics has found particularly fertile ground in some areas due to the properties of droplets, which can be treated as small beakers, and the possibility of creating thousands of droplets with varied compositions inside a single chip. Key applications of droplet microfluidics include the encapsulation of individual cells for high-throughput analysis of single cells [34–37], digital PCR for detecting and quantifying DNA or RNA [38–40] and detection and identification of pathogens [41–43], antibiotic susceptibility testing [44–48], and microbial physiology studies [49]. Droplet microfluidics can also be used for drug discovery [50], for confining enzymes to study their properties [51, 52], and for microscale synthesis of particles or materials with specific properties and functionalities [53, 54]. New applications are constantly emerging, showing that droplet microfluidics technology has high potential and is a powerful tool. Therefore, this class of microfluidic systems in commercial biomedical applications is expected to increase.

The following subsections provide a brief overview of the principles of droplets within microchannels and a short overview of current state-of-the-art methods for droplet formation and manipulation related to the Ph.D. thesis, which concerns the development of logic within microfluidic systems and the coupling of digital algorithms with microfluidic architectures to manipulate concentration in droplets.

2.2   Fundamental aspects of droplets in a microchannel

Droplet microfluidics takes advantage of the unique property of certain immiscible pairs of liquids. Immiscibility occurs when specific proportions of two liquids fail to form a solution but instead create an interface that separates the two phases [55]. At the macroscopic scale, the interface between two liquids is a smooth geometrical surface delineating the two domains [56],

which is essentially a mathematical concept. However, at the microscopic level, liquid immiscibility emerges from molecular interactions between the molecules of each liquid and Brownian diffusion [56, 57]. These molecular interactions mainly involve van der Waals attractions for organic liquids and hydrogen bonds for polar liquids [56].

In the case of immiscible liquids, cohesive forces between molecules of the same substance and repulsions between molecules of different substances result in the formation of separate domains and interfacial tension at their interface [56]. Interfacial tension is the tendency of the surface between liquids to minimize its surface area, leading to a spherical shape for tiny droplets of one liquid surrounded by the second liquid, without any boundary constraints. However, this property enables immiscible liquids to form plug-like volumes separated from each other within microchannels [58, 59].

The small size of microchannels relates to the direct bounding of both liquids by the walls. In our case, the height of the cross-section is less than the capillary length (a scaling factor that relates gravity and the difference in mass density of the liquids to interfacial tension; it governs the behavior of menisci when body forces and surface forces are in equilibrium [56]). Thus, the confined droplet's geometry is primarily influenced by the solid wall constrictions and the Laplace–Young equation (which relates the pressure difference to the curvature of the surface [56]). For technical reasons, the most common microchannel geometry is rectangular in cross-section. An example visualization of a droplet in such a channel is shown in Figure 1. Due to interfacial tension, droplets cannot occupy the entire cross-section, resulting in small areas
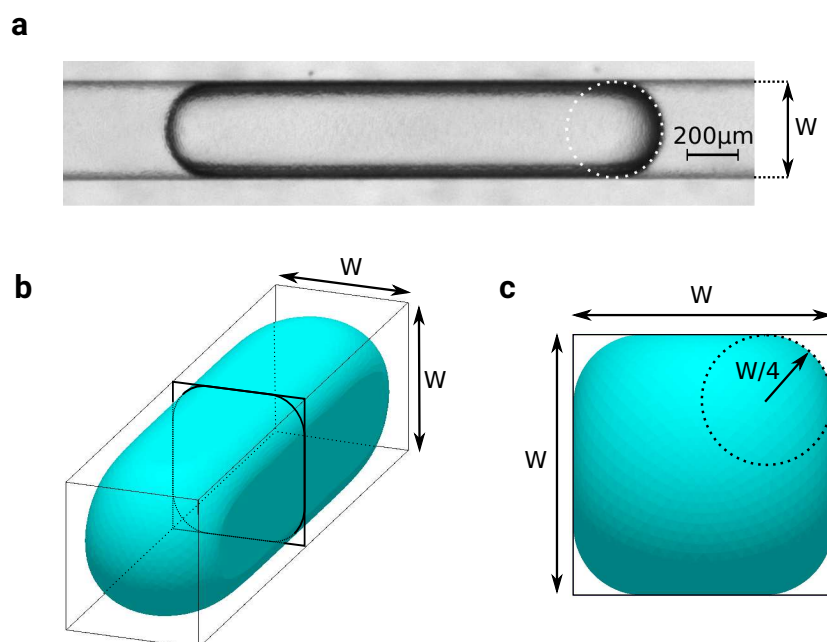

Figure 1: A confined droplet in a rectangular cross-sectional microchannel: a) a snapshot of the droplet in the top view in an experiment, b) and c) the shape of a droplet in this microchannel made using Surface Evolver [60]. (This figure was published in Article **A**.)

of oil at the corners of the microchannels. These corners, known as gutters, create channels where the continuous phase flows, bypassing the droplets [61].

Contact of droplets with the walls creates the issue of adequate wettability of the material being used. In the case of water-based droplets, hydrophobicity of the microchannels is desirable. Wetting the walls of microchannels by droplets prevents proper droplet formation and manipulation; it also disrupts any components that droplets meet and presents the risk of contamination. For this reason, the aim is to use materials that exhibit hydrophobic properties to construct microfluidic devices. Proper wettability mainly depends on the material used, the manufacturing technology [62], and surface modifications that can improve the hydrophobicity of the walls [63, 64].

In droplet microfluidics, surfactants are often added to one of the liquids. Surfactants are molecules with both hydrophilic (water-attracting) and hydrophobic (water-repelling) properties, which allow them to stabilize interfaces between different fluids [29, 65]. They play an essential role in droplet stabilization by affecting the properties of the droplets and their behavior in microfluidic systems. In most cases, the liquid in which the surfactant is most soluble constitutes the continuous phase [66]. Due to the targeted applications, water-based solutions were used in our case as the dispersed phase [35, 67–69]. Thus, suitable surfactants were added to the chosen oil [65]. Adding surfactant to one of the phases reduces interfacial tension value [65, 70] and facilitates droplet deformation [71].

On the other hand, depending on the surfactant used, micelle formation can result in self-induced droplet disintegration [72] if the surfactant concentration is too high (exceeding the critical micelle concentration) [70, 73]. In addition, the presence of the surfactant sometimes introduces complex interface behavior [73], in which local changes in agent concentration affect the stress balance and result in spontaneous interface movements [74, 75]. However, when used properly, surfactants are involved in stabilizing droplet interfaces [65, 76], controlling droplet size [77], preventing the uncontrollable coalescence of droplets [78], helping to create thin films on walls [79, 80], and reducing droplet wettability problems.

Depending on flow conditions and fluid properties, different flow patterns are generated when two immiscible liquid phases encounter a microchannel [81]. However, the flows (with the low capillary number) considered in this study resulted in plug-like droplets moving through a regular channel with speeds proportional to the constant flow of the continuous phase [61, 82]. Nevertheless, the interaction of liquids and microchannels can result in a complex topology inside the droplet and its near vicinity [61, 83, 84]. For example, when a droplet flows through a straight microchannel, it induces recirculation in both phases. This droplet has two symmetric counter-rotating zones that recirculate in each half of the droplet [83].

The composition of the droplets can sometimes be very complex; any additional compo-

nent dissolved in the water can affect viscosity and interfacial tension. Complex fluids exhibiting viscoelastic flows have been used in many applications in materials science or analysis of biological samples [85, 86]. However, in the research presented in this thesis, droplets consisted of water or glycerin solution and color additives, so with the continuous phase were Newtonian fluids, meaning that the incompressible fluid flow was linearly correlated to the local strain rate at every point [87]. The small channel sizes and relatively low flows caused the Reynolds number to have a low value [18]. In general, Navier–Stokes equations to model flows in microchannels could be used. However, under these conditions, the flows of the individual phases were mostly laminar [18], and a designer might consider simplified modeling. In this case, the fluidic resistance in the microchannels is governed by equations with well-known solutions [88]. In microchannels, the Hagen–Poiseuille law can be applied [89] to simplify the design of complex microfluidic networks by analogy to electric circuits [90]. The mere flow of droplets through the channels can be treated as a temporary increase in resistance over some distance [91] and can be represented as equivalent microchannel resistance. The same condition applies to complex geometries such as microfluidic traps with slits and bypasses [5]. The use of such simplifications significantly facilitates the design of complex microfluidic networks.

2.3   Methods of droplet formation

Various methods exist to generate new droplets within microfluidic devices [92, 93]. Research has focused on the mechanisms acting on droplets or classifying droplet behavior when different droplet parameters are used [26, 94–97]; however, many geometries have similar droplet and bubble breakup mechanisms [19]. In microfluidic devices, there can be several significant geometries (shown in Figure 2): T-junction [95], flow-focusing [26, 96], co-flowing [98, 99], and step-emulsification [100]. The mechanisms in these geometries have been well researched, and these methods have been used in many applications.
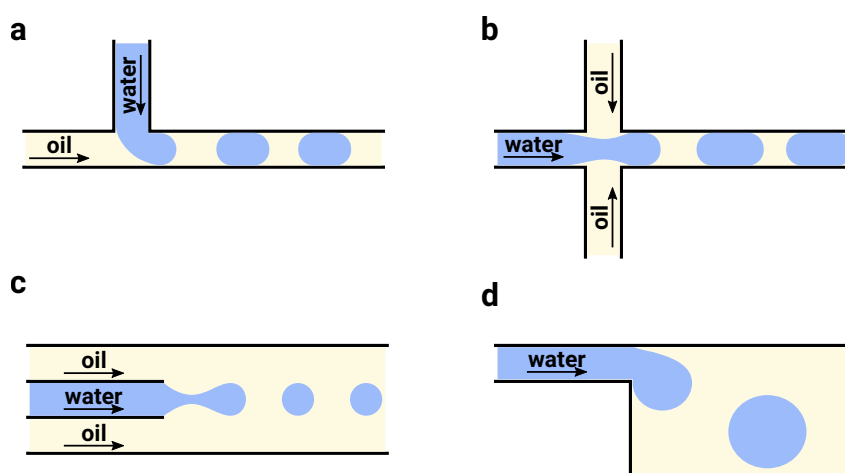

Figure 2: The most significant geometries used to form droplets in droplet microfluidics: a) T-junction, b) flow-focusing, c) co-flowing, d) step-emulsification.

Flow-focusing and co-flowing geometries have found many applications and commercial use [101]. These geometries are useful in high-throughput applications in which droplets are generated at tens of kHz [102]. They lead to better monodispersity with a higher production frequency than T-junctions [103]. They are also superior in areas related to encapsulation [103]. Step-emulsification, on the other hand, has the advantage of controlling the flow of only the droplet phase, in which droplets detach spontaneously due to changes in geometry. Neverthe-less, the most common method of formation involves a T-junction. This geometry connects two channels perpendicularly, supplying droplet and continuous phases. With the simultane-ous flow of both phases, droplet formation occurs through the interaction of the two fluids, in which the droplet phase attempts to block the forced flow of the oil phase to the outlet of the junction and the continuity of the droplet phase is broken, thus generating a new droplet. A user can achieve appropriate droplet lengths depending on flow ratios and the capillary num-ber. Regarding the capillary number, several mechanisms of droplet formation, called regimes, can be distinguished: leaking, squeezing, dripping, and jetting. With leaking and squeezing, it is possible to obtain droplets that are longer than the width of the channel and monodispersed. Monodispersion is also possible with dripping, although the droplet size is smaller than the width of the channel. Jetting applies at very high flow rates, forming tiny droplets with a poly-disperse distribution. In addition, the T-junction can be modified by adding a suitable bypass such as a block-and-brake [6], which stabilizes the length of the droplets formed over a broader range of flow ratios of the two phases. Despite years of research and a strong understanding of some regime operations, the unified T-junction model still requires improvement.

Active droplet generation techniques involve applying external influences such as electric and magnetic fields or centrifugal force [93]. Techniques also include adjusting intrinsic forces by manipulating the fluid's velocity or material characteristics such as viscosity, interfacial ten-sion, or fluid density by temperature control [93]. Active methods improve droplet generation and affect the parameters by modifying their formation frequency, size, and distribution. Of-ten, active methods involve adding external actuators to the previously mentioned geometries. For example, droplets generated in T-junctions with input fluid are controlled with valves [104]. The use of valves allows control of droplet size as well as timing of droplet formation. In this case, maintaining the size of droplets mainly involves an appropriate series of switching fluid flows, and the flow parameters themselves play roles in the background.

In many applications, the creation of uniformly sized droplets is crucial. However, achiev-ing an exact size of droplets can be challenging when designing complex microfluidic networks in which droplets influence flow distribution. Past effective designs have used a droplet gener-ation module at the beginning of a microfluidic system. Precise pressure or syringe pumps that provide stable and accurate flows would be required when using specific geometries.

One notable approach is the formation of droplets using microfluidic traps, in which inter-

action with microfluidic structures, such as obstacles and bypass, and interaction between the two phases occurs. The metering trap was described initially by Korczyk et al. [5] and has appeared in subsequent publications [7, 105]. The studies published thus far have not explained the mechanism and have been limited only to simple demonstrations of droplet operations. The primary function of the trap is to create droplets of the desired size or immobilization if a droplet fits the geometry. The results that have been presented in publications indicate that the formation of droplets in this trap can be exact. However, in a series of experiments [5, 7, 105] in which authors used the metering trap, a longer droplet was first formed with another known method then was cut in this trap to the desired length; excess droplets were generally discarded in a waste container. Using the metering trap in that way has significant drawbacks. First, a very long droplet must be formed using a T-junction or another means. Then, the flow must be controlled to direct the droplet toward the metering trap and cut it to the desired length. This solution complicates the microfluidic system, as pumps or valves must operate additional channels for droplet formation [104, 106]. The second disadvantage is that the excess droplets must be discarded, potentially interfering with further steps using the desired droplet. The lack of redistribution of excess droplets is an unnecessary waste of input fluids.

Despite existing publications documenting the metering trap and complex trap system geometries, a deeper understanding of its primary mechanisms remains necessary. While some essential insights have been gained through intuitive observations, leading to the construction of several microfluidic traps via trial and error, a more comprehensive understanding is necessary to advance the technique. Detailed fundamental investigations regarding the metering trap are required for further use, for example in forming droplets, exploiting the full potential of microfluidic traps, or finding microfluidic geometries with new specific functions.

2.4 Manipulations of droplets

The current state of knowledge and technology regarding the manipulation of droplets offers an enormous range of possibilities: merging several droplets into one [78, 107–109], splitting droplets into two smaller droplets [110–112], transporting through chips [81, 113], sorting based on droplet parameters [114], synchronizing several droplets flowing in parallel [115], guiding droplets through specific paths [116], immobilizing in traps and arrays [5, 116–118], or placing at an exact position [119]. Some manipulation methods employ pure hydrodynamic interactions between the droplet, the continuous phase, and the applied geometry of microfluidic structures. Others require additional actuators such as electric or magnetic fields, laser beams, acoustic waves, and other active components. Thus, these manipulations use both passive and active methods [92]. The manufacturing technology and material of the microfluidic system limit the availability of some droplet manipulation methods. Together with external components, they also define the cost of a microfluidic device.

Complex droplet manipulation in microfluidic devices is still mainly performed by using external actuators. Complex droplet manipulation is understood as implementing an algorithm or protocol to process droplets using at least several of the operations mentioned earlier. To use actuators, it is essential to design microchannels in a way that can connect to the external electromechanical system. Coupling with actuators complicates the manufacturing of a microfluidic device. In addition, the complexity of a device and the use of actuators often grows in tandem with the intricacy of the laboratory task. However, universal droplet manipulation platforms such as digital microfluidics have been to emerge. A digital microfluidics [8, 120] platform based on electrowetting on dielectrics [121] appears to be a superior method for manipulating droplets using complex handling protocols. However, this technology bears some limitations, such as difficulties in integration with application-specific systems and increased costs due to the complicated fabrication of electrowetting on dielectrics chips, which require custom electrical connections and hardware.

Microfluidic systems, in which the manipulation of droplets is performed through embedded structures and microfluidic networks, are less expensive and more accessible than digital microfluidics. Microfluidic networks can sometimes contain complex structures and can be built with multiple bifurcations, in which the flow occurs in parallel in various channels. Bifurcations in microfluidic systems have been intensively investigated, mainly for distributions of short droplets between branches [122–125] or splitting long droplets with higher or lower control of this splitting [111, 126–131]. Controllable flow to one selected output has been achieved for short droplets with some limitations [132]. Flow of droplets through bifurcation can also be supported by using surface acoustic waves [133], electric [134] or magnetic [135] fields, or microvalves [136] such that controlled sorting of droplets could be achieved [114]. However, a solution is still lacking for routing short and long droplets to a single output using only the built-in geometry and hydrodynamic properties over a wide range of flows between branches. An instrument with such capability would allow the design of complex microfluidic networks, enabling the manipulation of droplets would allow new geometries to perform specific functions.

Despite the laminar nature of flows in microchannels [18], notable nonlinear flow behavior can sometimes occur in complex microfluidic networks. Even for single-phase microfluidics, bistability can occur in triangularly shaped networks if the two mixing fluids form a mixture with nonlinear viscosity changes [137]. Experimental findings have also shown that a Braess paradox can occur in microchannel networks, in which the closure of an intermediate channel leads to higher overall flow rather than lower flow [138]. In droplet microfluidics, nonlinearity is due mainly to the complex behavior of the interface between the two phases and interactions with microfluidic structures [139]. In extensive microfluidic networks, short droplets can organize themselves into trains that oscillate between branches and form flow patterns that

depend on the network design and droplet properties [140]. These investigations have shown that microfluidics networks can create complex dynamic systems exhibiting multiple internal states and that flowing droplets can exhibit self-organizing behavior.

Microfluidic systems often resemble electronic devices in functionality and architecture [141]. Electronic circuit theory can be applied to model the intricate microfluidic network [90]. Furthermore, researchers have been exploring the possibility of developing liquid computers [142], a compelling field of study that is not necessarily limited to microfluidics. This idea is notable not only for its computing possibilities but also for achievement of droplet manipulation and self-regulation within microfluidic networks without external actuators. Droplet microfluidics presents specific flow properties that offer the potential for further development in this direction [139]. Droplet microfluidic devices can exploit the nonlinearity of two-phase flows to achieve logical operations such as NOT, OR, AND gates [143–146] and similar digital electronic behavior such as timers [145] or microfluidic shift registers [147]. Researchers have also examined the properties of logic operations in digital microfluidics [144] or other systems in which external forces control the droplets. Katsikis et al. have proposed a logic-based microfluidic system in which a rotating external magnetic field performs automated tasks on ferromagnetic droplets [115].

Previous studies have demonstrated single combinational logic operations in pressure-regulated flows of droplets [143–145]. Integrating them further has proven challenging, hindering the creation of systems with nontrivial functionality. It is sometimes difficult to transfer logic functions at the physical layer known in electronics into the realm of droplet microfluidics. Sequential logic could be more suitable for implementation and integration in droplet-based microfluidic systems based on possible droplet synchronization problems that have been presented in current publications regarding combinatorial logic. In contrast to combinational logic, whose current output depends only on the present input, sequential logic also depends on the past inputs as an internal state. Structures similar to microfluidic traps [5] could be used to support the state. However, sequential logic in droplet microfluidics has remained unexplored, apart from individual publications regarding implementation of flip-flops or single devices that exhibit sequential work [146, 147]. Integration of complex structures with sequential logic that manipulates droplets would make the creation of new microfluidic systems possible. Sequential logic would also make it possible to use complex algorithms for droplet manipulation and to reduce the use of external actuators to a minimum.

A critical goal of complex droplet manipulation is the creation of droplets with a specific composition. Creating droplets of different concentrations in a controlled manner is attractive because of the possibility of using them for further chemical or biological research, for example titration [148, 149], antibiotic testing [48, 150], agglutination [151, 152], or drug development [50]. Obtaining the concentration of a substance in a droplet is necessary for these tasks. Dro-

plet microfluidic systems currently use simple dilution [7, 31] or take advantage of the properties of streams in single-phase flows before droplet formation [153, 154]. However, a solution based on microfluidic structures would still require a microfluidics system that provides arbitrary droplet concentrations. A combination of microfluidic architecture and algorithms well known in computer science may yield a solution that is compact, straightforward to integrate into a more extensive microfluidic system because of simplicity, and capable of generating arbitrary concentrations of one or more substances in the formed droplets. The complexity of the entire system would be more straightforward than existing solutions [7, 155–157], and the system could be readily integrated with a larger one.

3   Aims and Thesis

Research in the selected set of publications undertook three general aims:

I **Investigate fundamental mechanisms inside microfluidic geometries and develop new microfluidic geometries that realize specific functions useful in droplet manipulations.**

II **Develop the idea of sequential logic circuits to control the flow of droplets inside a complex microfluidic network.**

III **Develop a device that combines microfluidic architecture with complex algorithms to manipulate the concentration of single droplets.**

More specifically, the research included the following objectives:

- Studies of the limitations of using simplifications in modeling microfluidic networks using circuit theories that are well known in electronics
- Studies of the mechanism of droplet formation in a T-junction and the factors that affect the length of droplets formed in this junction to create a unifying model
- Explanation of the cutting and immobilization of droplets inside a metering trap
- Development and investigation of new microfluidic geometries that realize specific functions

    - bifurcation, routing droplets into selected outputs in a wide range of flow ratios
    - a droplet-on-demand module to generate droplets in a metering trap
    - single microfluidic geometries to exhibit sequential logic behavior
- Studies of the possibility of integrating sequential logic geometries to construct more complex blocks
- Development of a microfluidic architecture and an algorithm to build a droplet processor that provides arbitrary droplet concentrations

In line with the motivation of the work, I have postulated the following general thesis:

In droplet microfluidic systems, it is possible to create structures that exhibit sequential logic based on three basic geometries: regular channels, bypass slits, and obstacles. We can integrate such geometries into more extensive networks to form microfluidic systems that perform more complex droplet operations.

4 Methodology

4.1 Fabrication of microfluidic devices

The selection of the material and fabrication method for a microfluidic device is the first fundamental step in a chosen application. The system's properties, limitations, costs, and application range depend on the technology [158]. The microfluidic device should be constructed from a material with specific physicochemical properties, especially the surface [24, 159], to make droplet formation and manipulation in microchannels possible. There are also application-related restrictions, for example chemical resistance or biocompatibility. Thus, the range of materials with suitable properties for this purpose is limited. Microfluidic systems have roots in the microelectronics industry and were therefore initially made of silica or glass [15, 158, 160]. Subsequently, polymer-based materials have supplanted them [161]. Most current research has involved microfluidic devices made of these materials, especially PDMS [161, 162].

In the work presented here, polycarbonate was used along with the micro-milling technology method. Micro-milling is a fabrication method that uses cutting tools to remove bulk material and allows microscale features to be created [163]. This method enables 2.5D geometries to be constructed within certain limits, making microfluidic geometries with bypass slits and obstacles possible. Manufacturing using polycarbonate is more accessible, cheaper, and more flexible than that using glass or PDMS [163]. Integration of additional actuators, such as valves or pumps, is possible inside the microfluidic system [4, 161]. However, I chose this technology and this material primarily because of short prototyping and manufacturing times as well as the relatively low cost of the material accessible at the institute. In addition, polycarbonate exhibits effective surface performance for selected liquids [63] and attractive properties for the micro-milling method [164].

Microfluidic devices in this work were generally constructed with two plates: top and bottom. Figure 3 shows a schematic construction of a typical microfluidic device used for experiments. I designed all microfluidic devices using FreeCAD [165] on polycarbonate plates with 2–5 mm thickness. All prototypes were generated using the ErgWind MFG4025P CNC milling machine. In addition, I generated trajectories for the end mills and drill bits in FreeCAD; I then generated G-Code in Delcam ArtCAM Express 2015 from these trajectories. Next, the code was executed using ArtSoft Mach3 CNC software to control the milling machine. All polycarbonate plates were fastened to the perforated vacuum table of the CNC machine by applying low pressure (–0.4 bar) generated by the AGA Labor Basic 20 vacuum pump.

On the bottom plate, I engraved microchannels and other geometries such as bypasses, obstacles, channels for electrodes, and others. The top plate closed the manufactured struc-
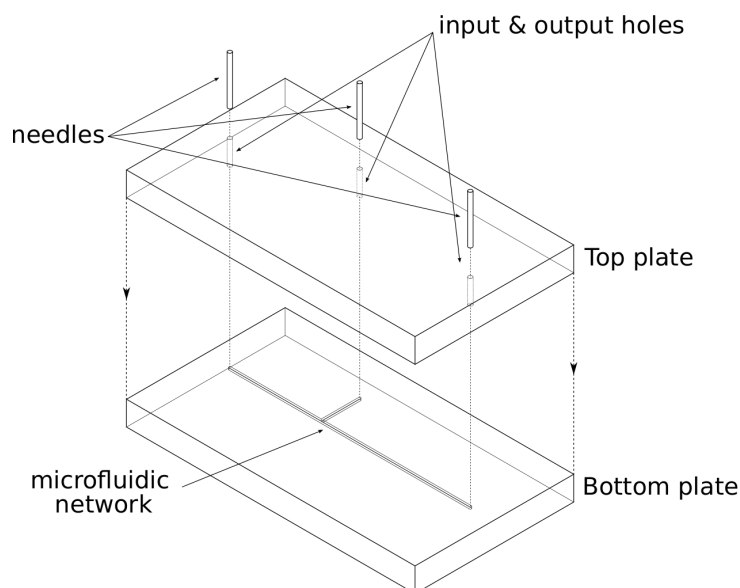
Figure 3: Scheme of microfluidic devices built with two polycarbonate plates. (This figure was first published in the supplementary file of Article **D**.)

tures and provided holes for inlets and outlets. I drilled two additional holes in the corners of both elements to position the two parts precisely by placing cut needles such that the pieces would have the correct positions. Microfluidic structures were milled with a two-flute fishtail milling bit with a diameter of 400 µm. The regular channel cross-section and other geometries were based on this size. At these dimensions, flows still exhibited a laminar character without the influence of inertia, gravitation, or other factors. The microfluidic device was assembled by bonding both plates together at high temperature. The method of bonding is related to [166].

The milled plates underwent a cleaning process before bonding. After engraving, I used a Karcher K7 Premium pressure washer to reduce burrs on the edge of channels. Next, the plates were cleaned in the following order: first with an Alconox solution (approximately 1%) to thoroughly degrease elements, followed by tap water, then isopropanol, and finally a thorough rinse in distilled water. I then placed the cleaned plates, with the positioning needles located in one plate, into an oven heated to 120 degrees C to thoroughly dry the elements and preheat them before putting them into the press. I assembled the heated plates and put them in a press heated to 135 degrees C. The manufacturing device was bonded at a pressure of 0.1 bar/cm^2 for up to 30 minutes (Article **A**), but I later reduced this time to approximately 10 minutes (Articles **B**, **C**, **D**) with the same effective resulting joint. After this time, I turned off the heat in the press, covered the press slots with aluminum foil, and then activated a fan aimed at the bonding press for faster cooling. I removed the systems when the temperature had decreased below 40 degrees C. Before an experiment, trimmed and chamfered needles were pressed into the input and output holes and segments of tubing were placed on them. There were no additional surface modifications to the microfluidic structures. Surface hydrophobicity was sufficient when a specified oil filled the system before the experiment.

4.2   Experimentation and Analysis

The research in the presented articles mainly consisted of observation of droplet kinetics and analysis of their interactions with the geometries of the microfluidic devices that had been produced. The primary approach was to conduct experiments under controlled conditions using liquids with well-known physicochemical properties. I used n-hexadecane with Span-80 surfactant as the continuous phase in all first-author research. The droplet phase was distilled water (Articles **A**–**D**) or glycerin solution (Article **D** only). Various dyes (ink, food coloring, or methylene blue) were added to the droplet phase to facilitate detection and shape analysis and to study the variation in concentration of the droplets obtained.

Major experiments were performed by light microscopy using a Huvitz HSZ-645TR stereoscope with an IDS uEye UI-3274-LE-C-HQ USB camera attached for image acquisition. I used a Cetoni Nemesys low-pressure syringe pump to control flows inside the microfluidic devices. The syringe pumps used were controlled by software on a computer. I wrote libraries in Python to control syringe pumps running on GNU/Linux with SocketCAN and IXXAT drivers for USB-to-CAN interfaces. These libraries were independent of those supplied by the manufacturer, whose libraries were for Windows only; the manufacturer did not offer software to operate the pumps through a USB connection under GNU/Linux at the time the research was performed.

I wrote Python scripts for performing experiments in which the control of the pumps was coupled with image analysis of the investigation being conducted. The experiments described in Articles **A**, **B**, and **C** did not require real-time flow control. In these cases, the experiments were executed by predetermining flows and then starting separate software to perform data acquisition with the camera. I created this software in C/C++ using the OpenCV library [167] to capture videos or image sequences and a low-level library from the camera manufacturer. In the experiments described in Article **D**, I coupled real-time image processing and syringe control in the software. Based on previously written software, I created a library in C/C++ for Python to control and acquire images from the camera, and I used OpenCV for image processing. I used template matching to detect the droplet's front position because of the long-term experimentation and micelle formation that sometimes would prevent the correct operation of more straightforward techniques such as pixel intensity threshold. The use of glycerin solutions reduced the occurrence of micelles, but a small number of micelles were nevertheless present after many hours of experimentation.

In the studies described by Articles **A** and **B**, there was a need to estimate oil phase velocity profiles. I used the particle image velocimetry technique adopted for microchannels [168]. Glass particles (approximately 17 μm in diameter) were added to n-hexadecane with surfactant in the following way: A significant number of particles was added to the oil phase, then the mixture was poured into a measuring cylinder and rested to allow some particles to sink to

the bottom or float to the surface. Using the syringe, I drew off the suspension at the equilibrium from the center of the cylinder. These experiments were performed using a pco.1200 hs high-speed digital camera (PCO Imaging), and a Nikon Eclipse E-50i microscope. I used off-the-shelf software for the PIV, initially vidPIV from ILS GmBh (Article **A**) and then the open-source OpenPIV (Article **B**) [169].

For Article **D**, the experiments required the controlled merging of droplets; droplet electrocoalescence was employed for this purpose [170]. With an alternating electric field of a sufficiently high voltage (on the order of kV) and frequency (hundreds of Hz), the merging of droplets was possible even at high surfactant concentrations [78]. Accordingly, I constructed a simple device that generated HV peaks. To achieve this goal, I used an STM8 system development board that could generate repeating peaks on a transistor (IRF840) that acted as a key and controlled a transformer (BV2020168. 0.35VA, 400VAC – 6V). This solution enabled the generation of peaks ranging up to several kV (depending on input voltage) with a preset frequency of 500 Hz in the embedded software. Such parameters were sufficient to merge the droplets in the merging trap. To keep the electrodes stable in the microfluidic system, I first inserted sanitary silicone into the electrode feed channels and then placed electrodes made of cable.

For the study described in Article **E**, I built an automated system to analyze the formation of droplets in a T-junction made of circular channels. This droplet generator was operated by two syringe pumps pumping two immiscible liquids. Unique to this research, I used FC-40 as the continuous phase and hexadecane as the droplet phase. I used the tools and software developed for the research presented in Articles **A**–**D**. In the study presented in Article **F**, my contribution was limited to manufacturing devices designed by another author, conducting a portion of experiments on the developed experimental setup, and collecting data from a Multiskan GO microplate spectrophotometer (Thermo Scientific).

After conducting the experiments, I performed analyses of the data obtained. Data in the form of videos and image sequences required preprocessing. For simple manipulation of images, I used Fiji [171] to process them by hand. I also wrote Python scripts appropriate for a larger data volume. I performed the analyses mainly using OpenCV, SciPy [172] for image processing, and pandas [173] to manipulate the data for further investigation, primarily using NumPy [174]. In the studies described in Articles **B** and **C**, blob detection [175] implemented in OpenCV was used to detect positions of short droplets whose lengths were close to the width of the channel. The TrackPy library [176] was used to group droplets between frames and to generate trajectories from their positions [177]. For Article **B**, I measured only the interface position on the axis of each channel for the long-droplet kinetics experiments. To create these axes, channel edge detection using the Hough transform [178], implemented in OpenCV, assisted with the measurements.

5   Overview of results

In Articles **A**–**D**, my contribution was predominant with the exception of additional numerical simulations in performed by coauthors of Articles **A** and **B**. Specifically, my contribution included the formation of the concept and the design of microfluidic geometries primarily, developing devices, building and automatizing experimental setups, conducting experiments and measurements, data analyses including image processing and analysis, and finally the preparation of manuscripts with coauthors. In Articles **E** and **F**, my contributions were mainly limited to conducting experiments and analyzing experimental data. Here, I provide an overview of the results obtained and mention my contribution to the work. Nevertheless, the reader should find the details in the articles attached in section **"Original Articles"**.

The research began with investigations of existing microfluidic geometries invented by other researchers. During this research, I learned the principles of how flows occur inside microchannels and how droplets interact with them – in particular, with bypass slits and obstacles. Based on knowledge gained during these studies, I found new opportunities to use the metering trap and became involved in developing new microfluidic geometries. Initially, I focused on single geometries such as guiding junctions or individual flip-flops before creating entire systems containing them. I then investigated the use of the invented geometries to develop more complex systems. I took two separate routes related to the aims. I was concerned with exploring the possibility of integrating sequential logic systems and simultaneously exploring architectures and algorithms for creating droplets of arbitrary content. As a result, I designed various microfluidic devices, including a decimal counter that counts 1,000 droplets or a droplet processor that makes droplets with different contents using only forward and reverse flow of the oil phase.

5.1   Investigations of fundamental mechanisms

5.1.1   Initial studies

In the initial stage of my studies, I contributed to Articles **E** and **F** by participating in experiments and data analysis. Those works focus on fundamental mechanisms in microfluidics, such as droplet formation in a T-junction (Article **E**) and flow distribution in junctions (Article **F**). Although my participation in those works was not primary, the knowledge and expertise gained during the work on those projects were constructive and vital to the subsequent execution of my later projects, described in Articles **A**–**D**.

In Article **E**, the study scope was to elucidate the effect of liquid flow rates on droplet size. For such a purpose, I built an automated experimental configuration to improve data collection and precision efficiency, measuring droplet size in a wide range of flow rates. Using automation

via a PC, it was possible to operate camera and syringe pumps to register and measure hundreds of droplets for multiple fixed flow rates. The massive amount of data stabilized the standard deviation of each measurement point and assisted the theoretical unification of mechanisms in the T-junction.

The most important finding from this work was the consequence of the flow of continuous phases through corners of rectangular channels to form a droplet. Droplet formation regimes such as leaking did not occur in systems with circular channels. At slight flow rates, the gutters in rectangular channels acted as a bypass, resulting in the formation of very long droplets. I then used this phenomenon of bypassing a confined droplet by a continuous phase in constructing microfluidic devices with bypass slits.

For the study described in Article **F**, I was involved in performing flow distribution experiments. The initial assumption was that angles at which channels join in the junction might influence joint flow distribution. For that purpose, a new technique was developed to allow an estimation of the distribution of flows in the simple symmetrical rectangular microfluidic network via spectroscopic measurements of the concentration of a dye. The dye was introduced to one of two inputs of the device. The resultant mixture of the agent and the buffer was collected from the two outputs of the device. Due to the symmetry of the investigated device and the identical flow rates for both inputs, dye concentration on both outlets yielded complete data for accurately estimating flow rates in a rectangular network.

This approach allowed determination of the effect of the geometry of the junction (angles between joined channels) on the split and merging of flows. I improved this technique in Article **A** and adopted it to estimate hydraulic resistances of geometrical elements, for example traps, bypass slits, and obstacles. That research focused on single-phase flows depending on the type of joints of microchannels. Nevertheless, the results were helpful in the design of droplet microfluidic systems and in selecting suitable two-phase flows for experiments.

The essence of the experiments described in Article **F** was the determination of the limits of applicability of simplifying the model for flow distribution, that is, the possibility of using hydraulic resistance to model microchannels and constructing microfluidic networks similar to electrical circuits. The results showed that the applicability of the hydraulic resistance is at relatively low flows of a few mL/h. As a result, the rest of the studies in Articles **A**–**D** were performed within these limits.

5.1.2 Investigations of microfluidic traps

Article **A** presents a comprehensive study of the geometries of components regarding the microfluidic trap. In this paper, I studied the mechanism of trap operation. I designed the experiment, performed it, and analyzed the results. I simultaneously studied the kinetics of droplets in the channels, their interaction with the geometry of the trap, and the velocity

profiles of the continuous phase in the slits using particle image velocimetry. In addition, I performed hydraulic resistance measurements on the entire geometry and its components. For this purpose, I used a novel method of measuring hydraulic resistance, described in the article.

The metering trap combines two essential geometrical elements: the obstacle and the bypass slit. The obstacle locally reduces the lumen of the regular channel. A droplet must change its curvature to pass the obstacle, so the oil flow must apply additional pressure. The bypass slit is a contiguous area along a regular channel that increases the size of this channel in width but not height. The small height of the slit prevents penetration by a droplet, but the continuous phase can freely flow through it, bypassing a droplet in the main channel. Correct positioning of these two elements in a regular channel made it possible to create a trap that could meter and immobilize droplets. Investigation of this novel compound allowed me to study the role of these elements in the flow and then use this knowledge in subsequent studies to design microfluidic modules with new functionalities.

Two droplet types were considered in experiments: a short droplet with a length no greater than the bypass slit and a long droplet with a length significantly longer than this bypass. The short droplet would stop, blocked by the obstacle in the trap. The continuous phase could freely flow through the bypass slits because the droplet could not obstruct this flow. In working conditions, the oil phase flowing through the bypass slit would not create sufficient pressure behind the droplet to push it through the obstacle's gap. The bypass slits served as narrow channels, connected in parallel, whose hydraulic resistance depended on the geometry itself as well as the length of the blocked droplet. Thus, the droplet would be immobilized if the oil flow was not too high. The obstacle breakdown pressure depended on the size of the droplet. In practice, the droplet fitting to the trap was immobilized in oil flows up to several mL/h.

In the case of the long droplet, the bypass slit would remain blocked even if the droplet were touching the obstacle. During flow, the rear part of a droplet would remain in the main channel, pushed by the flow of the continuous phase behind. Therefore, the build-up pressure would force the droplet to change its curvature and flow through the obstacle's gap. The neck connected two pieces of the droplet in the obstacle area. If only the back of the droplet had reopened the inlet to the bypass slit, the continuous phase would begin to flow through the bypasses. Opening the bypass would rapidly decrease the force acting on the part of the droplet occupying the trap while the front of the droplet was forced to move forward. This effect would make the neck linking both parts of the droplet unstable, resulting in its breakup. As a result, a fixed-volume droplet could be metered from the initial long droplet and stopped in the trap. Figure 4 shows this mechanism for metering a long droplet in the metering trap.

A significant finding from the study in Article **A** is that the droplet could effectively block and activate flow in the bypass slits. The experiments performed on the metering trap revealed
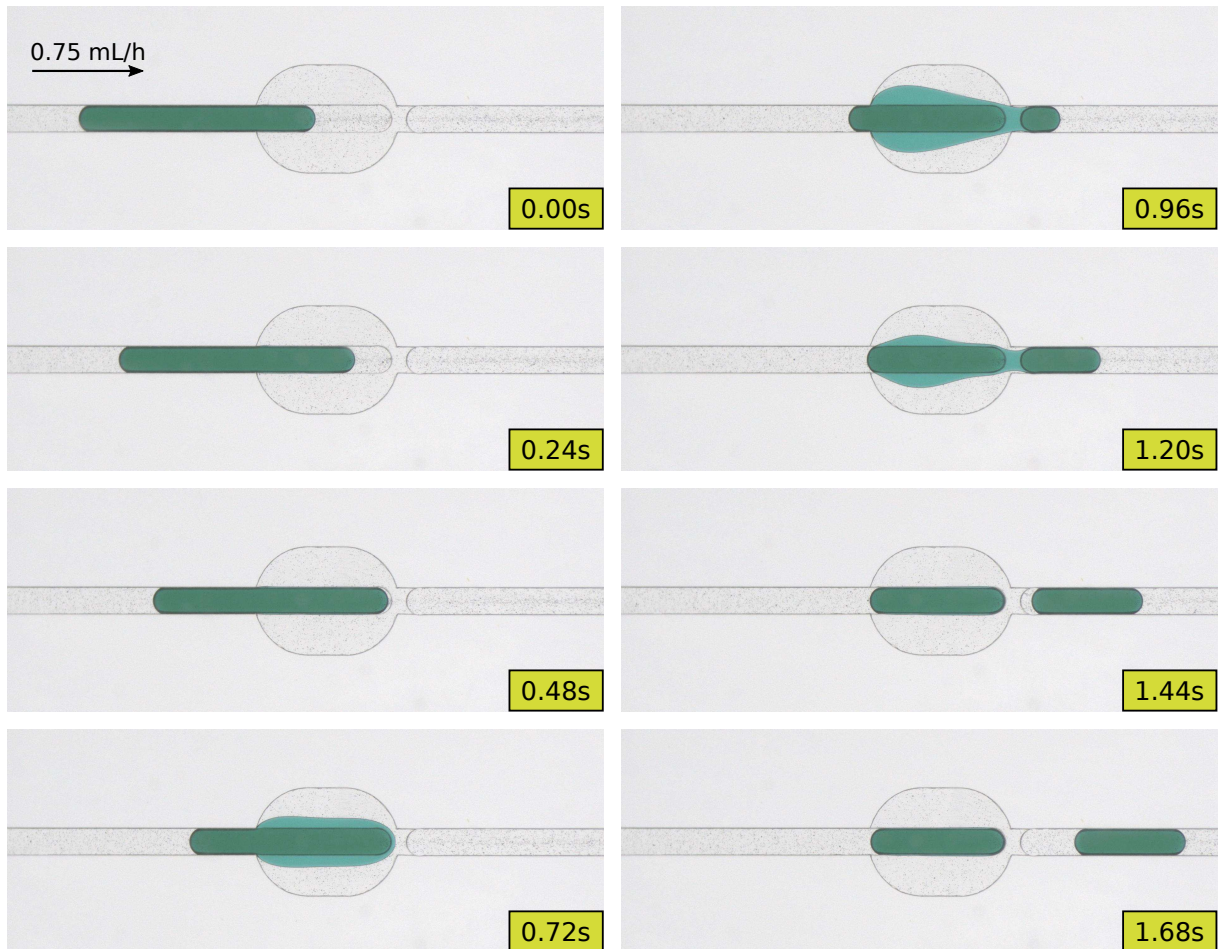
Figure 4: Snapshots of the experiment with a long droplet from Article **A**. The droplet previously formed in the T-junction flows toward the metering trap, pushed by the continuous phase. There, it is cut to a length corresponding to the size of this trap and then immobilized. A redundant droplet is formed and continues to flow. Article **A** presents the experiment in greater detail, and the droplet formation is divided into corresponding stages.

that entrance of the front of the droplet to the trap could effectively block the continuous phase flow in bypass slits until the back of the droplet reopened the bypass. Therefore, the inlet and outlet could be defined as the start and end of the bypass, respectively. Blocking was efficient despite the presence of gutters in channels with rectangular cross-sections. Measurements of the hydraulic resistance of the individual components showed that an obstacle significantly increased the hydraulic resistance of a channel. As expected, the bypass slit decreased the resistance. However, its influence on hydraulic resistance was negligible. In the single-phase flow case, particle image velocimetry measurements revealed that bypass slits weakly affected the distribution of flows. The importance of the slit was only noticed when the droplet flowed in its immediate vicinity. As a result, the metering trap had two static hydraulic resistances, a default lower one when empty and a higher one when it had trapped droplets. These results are relevant to the design of complex microfluidic networks, in which droplet control involves blocking the flow through droplets that encounter obstacles.

5.2 Development and investigations of new microfluidic geometries

5.2.1 Droplet on-demand method in the metering trap

Based on research on the metering trap in Article **A**, I invented a new method to generate single droplets on demand. As I had learned from the previous observations, a metering trap cuts a droplet if a long droplet enters the trap from the obstacle-less side. However, it does not affect the droplet for reversed flow, that is, if a droplet enters the geometry from the side with the obstacle. Knowing this property, I devised a method of generating droplets directly in a metering trap connected to a controllable source (allowing the droplet phases to move forward and backward). The formation of the droplet and its ejection into the rest of the microfluidic system require a sequence of pushing, pulling, and pushing again of the droplet phase. This method is presented in Article **D**, along with conditioning concentration architecture. Generating droplets in this way is much more versatile and could apply to many other applications as a general droplet formation method. The critical issue is the orientation of the metering trap; the side with an obstacle is directed toward the input of the droplet phase. Figure 5 presents the direction of the metering trap in the channel that delivers the droplet phase.
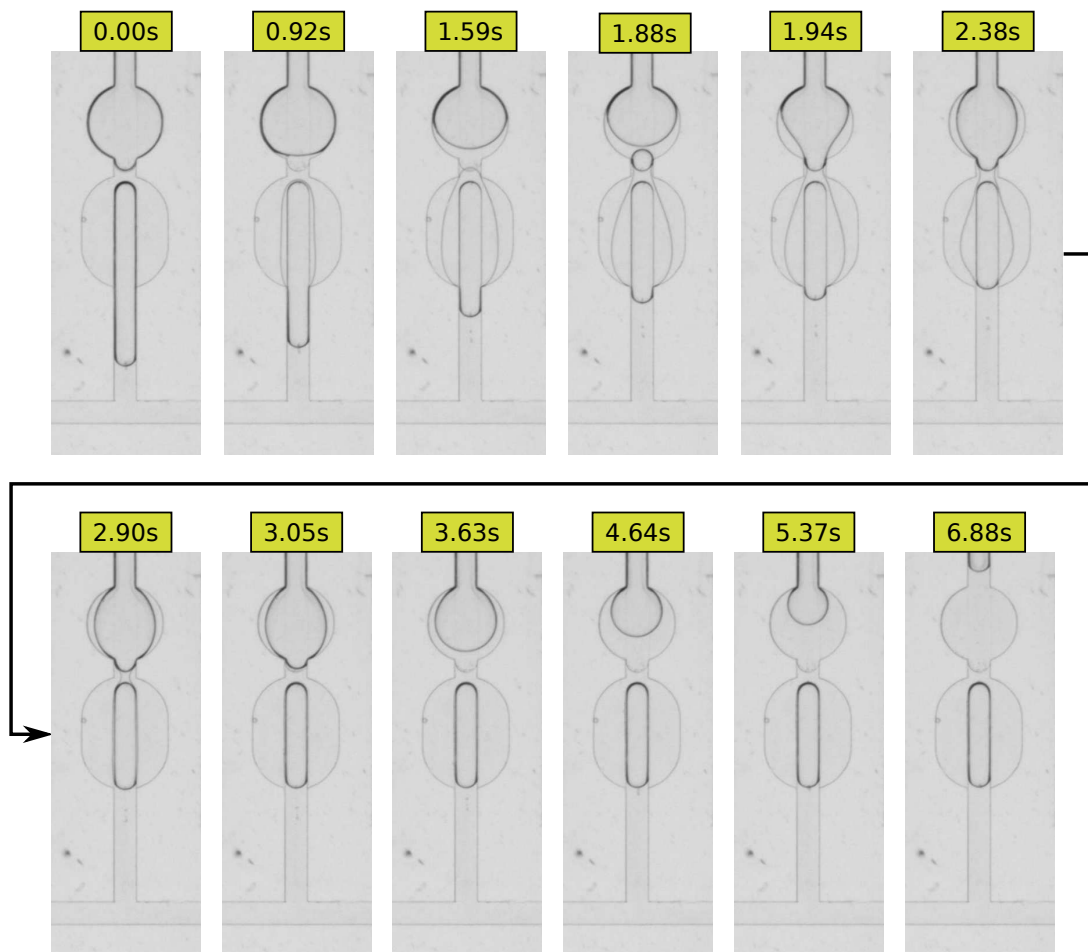

Figure 5: Droplet formation in the metering trap by pulling the droplet phase. The section in which the droplet phase flows forward through the metering trap has been omitted.

Droplet generation begins by switching on the flow of the droplet phase in the direction of the metering trap. When the droplet phase passes through the obstacle, certain conditions must be met if there is a coalescence problem; for example, the droplet phase flow rate should not be too low, or an alternating electric field should be present. Otherwise, the system's behavior can resemble the step-emulsification method, generating a mass of tiny droplets. Once a trap has been loaded (the droplet phase can fill it with excess; the first snapshot in Figure 5 presents this state), the pump is switched to the reversed flow, and the tip of the droplet phase moves back toward the trap. The tip can be seen here as the rear of the very long droplet. The mechanism is analogous to the case of the long droplet studied in Article **A**: Once the tip reaches the position at which it opens the inlets to the bypass slits, the portion of a droplet phase is metered and immobilized in the metering trap.

Thus, the sequence of pump operation described above – first, forward pumping and then reversing the flow – results in detaching the defined volume of the droplet phase to form a new droplet. The continuation of the withdrawal increases the distance between the freshly created droplet and the new tip of the droplet phase. This distance helps displace a new droplet from the generation unit to the rest of the microfluidic network after reapplication of the forward flow in the next droplet formation cycle. In addition, I added a channel widening immediately before the obstacle. This solution prevents generation of excess droplets in the pulling stage. Without modification, the excess droplets could interfere with successive droplet-generating cycles.

The droplet-on-demand module presented here utilized the metering trap, which had been published previously. However, my addition to developing this device was the specific placement in the channel, the development of the flow sequence, and the addition of the widening area to preserve the continuity of the droplet phase. Combining all of these strategies yielded a novel method of generating droplets. This method offers numerous advantages, including the lack of creation of redundant droplets, which has been noted in previous publications using this trap. Only one pump is required to create droplets with a unified length, determined mainly by the trap size. The accuracy and repeatability of the droplets created are very high. I built a microfluidic system to conduct droplet formation experiments depending on parameters such as the trap length, droplet phase pulling speed, or type of liquid. I specifically made the channels narrower to lengthen the droplets and to allow observation of the length spread. The results in the supplementary information for Article **D** show that droplet length was influenced primarily by the trap's design; other parameters had a minor influence.

5.2.2 Bifurcations with the bypass slits

In microfluidics, the junction is generally a T- or Y-shape connection of three regular channels, as shown in Figure 6a. In droplet microfluidics, a bifurcation can distribute droplets in the microfluidic network. In a normal junction, long droplets (whose length significantly exceeds

the width of the channel) usually break and split between two branches. The ratio of the size of the newly formed droplets largely depends on the flow rate. In turn, smaller droplets (of a size comparable to the width of the channel) enter the joint's outlet with a higher flow, resulting in the dynamic distribution of trains of droplets in the networks. Each droplet introduces additional resistance and slows the flow in the occupied channel. In droplet trains entering the loop, droplets tend to distribute in a configuration that ensures that the flows in the branches are approximately equal. In close-to-balance flow distribution, a single droplet can change the faster arm of the loop to the slower one, thus switching the output route preferred by the next droplet.
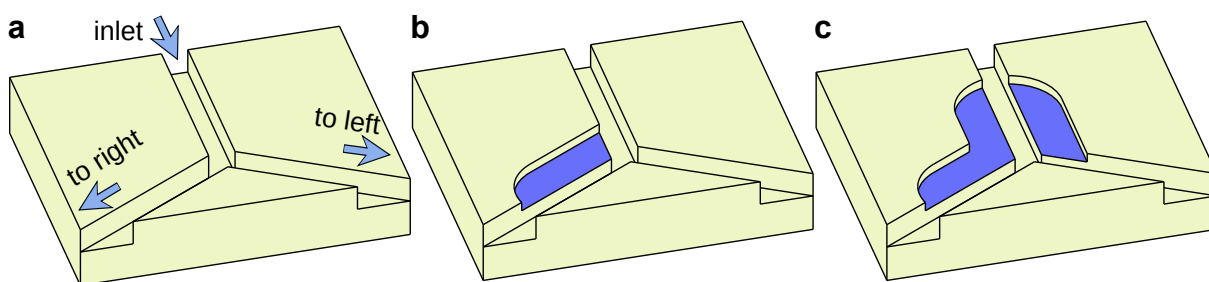
Figure 6: 3D views of different types of bifurcations: a) the regular junction, b) the novel junction with a single bypass slit, and c) the universal junction with both bypass slits. (This graphic is an excerpt from the figure published in Article **B**.)

Aware of the phenomenon of activation and deactivation of bypass slits by flowing droplets investigated in Article **A**, I designed a novel type of microfluidic bifurcating joints that could function differently from the previously mentioned regular junction. Article **B** presents these bifurcations and a series of experimental studies I performed to understand their operational range and properties. The improved bifurcation I discuss in Article **B** introduces three novel features: a) It transfers short droplets to selected output regardless of the ratio of flow rates in outlet channels, b) it transfers long droplets to the selected output without breaking them up in a wide range of flow ratios and capillary numbers, and c) it performs a baker's transformation that helps to mix the droplet's content after the transition.

Examples of the modified junctions are shown in Figure 6b–c. The essence of the modification is the addition of bypass slits to channels at the joint. The bypass slit connects to the channel, increasing its lumen, which the continuous phase can access. The purpose of the bypass slits is to allow the oil to bypass a droplet when it travels through the junction. During dynamic two-phase flow, the output without the bypass slit connection draws in droplets and is the selected output for receiving droplets. I designed and conducted various experiments to study the kinetics of droplets in the channels, their interactions with the geometry of the bifurcation, and the velocity profiles of the continuous phase in the bypass slit (using particle image velocimetry). In addition, I analyzed the breakup of droplets in this type of bifurcation as a function of the capillary number. I proposed and experimentally verified a theoretical model

to obtain operational limitations for transferring long droplets through the junction.

Of note, such a slight and local modification as only adding a bypass slit to the junction can significantly alter the global behavior of droplets flowing in microfluidic networks. The observations presented in Article **B** demonstrated this effect in two devices with simple symmetrical loops, one consisting of a regular joint (presented in Figure 6a) and the other containing novel junction that fixed droplet flow (shown in Figure 6b). As a result, unlike the almost symmetrical droplet distribution in the case of a standard joint, there was vast asymmetry in the distribution of short droplets between the branches in the novel device, even though both channels initially bore the same hydraulic resistances.

As in investigations of the metering trap, the kinetics of long droplets and the flow profiles in the bypass slit showed that a droplet could effectively deactivate and activate the bypass. In this case, the droplet created an additional temporal protrusion branch, initially penetrating the output with the bypass slit, that finally retracted due to the activation of the bypass at the final stage. An example of manipulation of a long droplet is shown in Figure 7. At sufficiently low input flows, interfacial tension keeps the droplet in a single piece, all oil flow dedicated to the opposite branch can flow through the bypass, and the entire droplet is transferred into one selected output. For small capillary numbers, the only restriction on the transfer of an
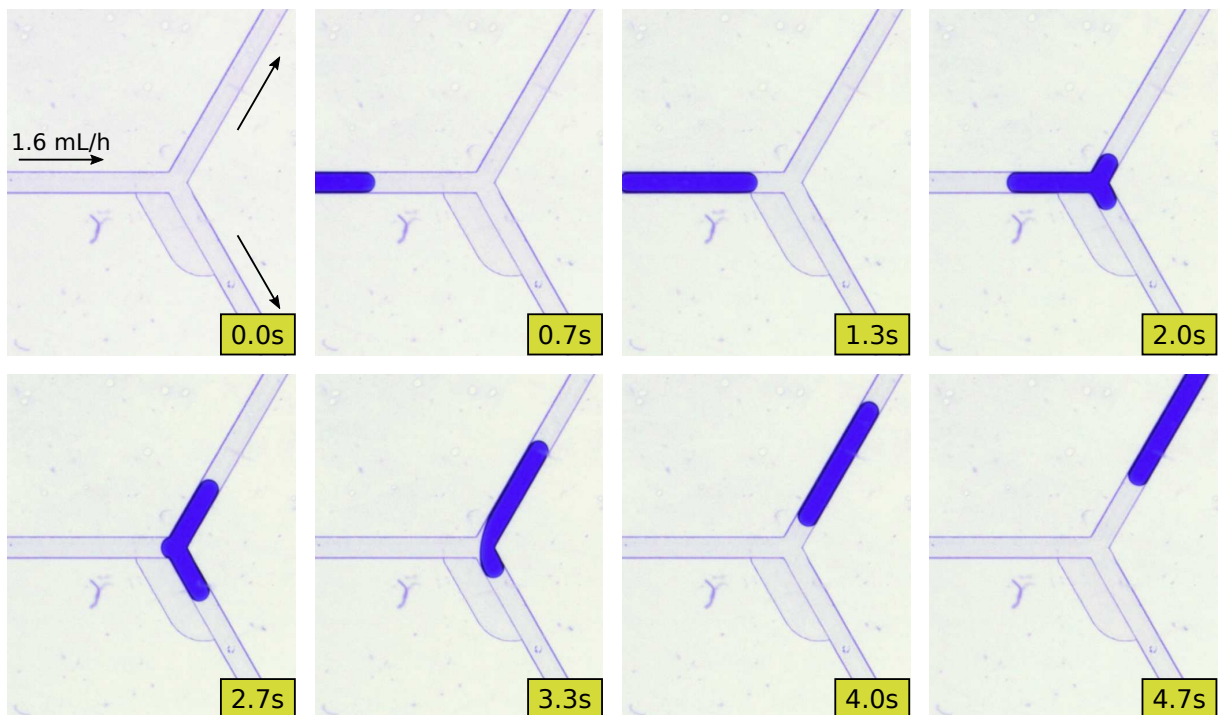

Figure 7: Overview of transferring a long droplet into one output. The junction functions in a configuration with one input and two outputs. The droplets flow into the outlet opposing the bypass slit in this configuration. If the input flow is sufficiently low and the length of the droplet is adequate, the additional branch that is generated does not block the bypass and the droplet is transferred without splitting.

entire long droplet is the length of the bypass slit adjacent to the opposite output. Long droplets whose additional branch exceeds this bypass will break up due to the total flow blockage through this bypass. They initially block the inlet of the bypass but are sufficiently long that the branch then stops the outlet of this bypass. As a result, the bypass is inactive at all times. With sufficiently shorter droplets, the transition between the non-breakup and breakup regimes becomes highly dynamic. The limits of this action are outlined in Article **B**. However, this result shows that a junction with a simple bypass slit can function in a wide range of flows. On the other hand, there are possibilities for optimizing the shape of the bypass slit, for example its length and depth, to achieve the target of the specified application.

By default, the junction contained one input and two output channels, with one dedicated to receiving droplets. If the oil flow were reversed, the joint would have one output and two inputs. In this case, the long droplet flowing into the outlet from one of the two inlets could have a high risk of splitting if the oil flow from the other output were unable to bypass this droplet. Thus, I also improved this junction to become more versatile and also function in the reversed direction without splitting long droplets. Figure 6c shows the novel device modification. I modified the primary bypass slit by elongating the space adjacent to the input channel (terms from Figure 6a). Thus, the droplet from the left channel would not block the oil flow from the right. Next, I added a second bypass slit of a different shape, shorter than the first bypass in the direction of input, to allow the passing of the long droplets from the right; however, in the default case (one input and two outputs), droplet behavior would be similar to the junction with only one bypass slit. A shorter bypass would preserve the transitions of short and long droplets to the selected output, as before. In the case of short droplets, the oil would have a higher resistance through the additional bypass, and short droplets would still tend to flow into the desired outlet even when this bypass was not blocked. Long droplets would block this bypass slit very rapidly when split into two branches. However, modifying the previous junction worsened the operational range of droplet transfer – the junction functioned for higher flow rates in the selected output (compared to the junction in Figure 6b) and had different transitions between non-break and break modes for long droplets. On the other hand, the modified guiding junction may assist in building microfluidic geometries if bidirectional flows are used.

As previously described in Article **A**, bypasses did not significantly affect the flow distribution for the continuous phase flow if a droplet was absent. Thus, a designer could include many guiding junctions without affecting hydraulic resistance. However, the presence of junctions will dramatically alter the flow of droplets in the network. The reason for this effect is that the bypass can operate over an extensive range of flows, making it possible to build complex microfluidic networks in which the hydraulic resistances of the individual branches can vary significantly and change dynamically, for example through the use of droplet traps. The wide working ranges also make the junction a valuable tool for building new microfluidic geometries

in which the direction of droplet flow can be controlled. Depending on the droplet length used – which a designer can standardize – the device can act as a switch if the flow in one outlet is significantly reduced. The junction, working as a switch, passes the droplet, without splitting, into the first or second output depending on the internal state of the receiving microfluidic geometry. I utilized this feature to construct microfluidic systems with sequential logic.

5.2.3 Single microfluidic geometries with features of sequential logic

In droplet microfluidic systems, logic states at a selected location and time can be analyzed as follows: 0 = the absence of droplets; 1 = the presence of droplets. Reading of the logic state can be performed anywhere in the microfluidic network. However, previous results have shown that the obstacle can hold a droplet if the oil flows by another route, such as a bypass slit. Therefore, reading the status adjacent to the barrier may be attractive due to the establishment of steady-state values that only another input droplet can change. The ability to hold and release droplets within structures can be interpreted as the internal state, and the entire system can be interpreted as a finite state machine, as known in automata theory. Using the knowledge gained from previous studies and the microfluidic geometries that had been developed, I began research on sequential logic by examining the feasibility of implementing the simplest sequential logic circuits, flip-flops, in droplet microfluidic systems.

The most straightforward device that realizes sequential logic is an SR flip-flop. In electronics, it is a circuit that has two stable conditions, 0 (low) and 1 (high). It has two inputs: set, setting the internal state to 1, and reset, setting the internal state to 0. I constructed a microfluidic device with behavior analogous to this pattern. This device has not been published directly in articles but has provided the basis for building more complex structures. Figure 8 shows an implementation of the SR flip-flop in a microfluidic circuit with two parallel channels controlled with two independent syringes with the continuous phase. Two narrow slits compound both channels and the oil can only be exchanged between the channels through these slits. One channel has an obstacle that can hold a droplet. However, when the device is empty, the flow through slits is minor, associated with increased resistance through the barrier compared to a regular channel. When a droplet is dropped into the setting channel, it stops on the obstacle. It can be considered that the droplet effectively blocks the flow through the barrier. Even if oil flow through the gutters of a rectangular channel still exists, it is negligible. Thus, the oil flow from the first channel passes through the first slit and returns through the second slit. The device maintains a high state until the flow rate is not too high or until the next droplet flows into the second channel and triggers the first one by blocking one of the slits. The length of the triggering droplet must be sufficient to plug the slit along its entire length; at that point, the pressure increases sufficiently, which on the one hand deforms the flowing droplet but on the other also pushes the first droplet through the obstacle.

The second basic flip-flop is the T flip-flop, which can be constructed from the SR flip-flop
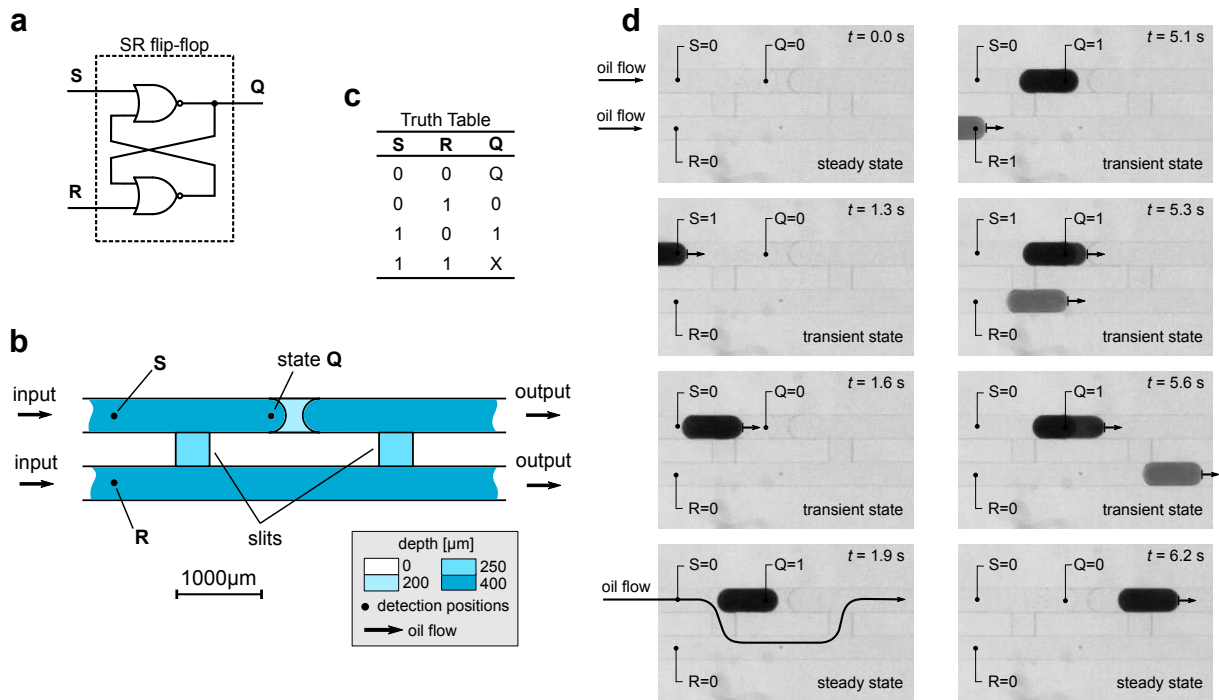
Figure 8: SR flip-flop implemented in droplet microfluidics: a) electrical schematic of the SR flip-flop, b) schematic of the microfluidic circuit realizing the flip-flop, c) truth table of the electronic version of the SR flip-flop, d) snapshots of experiments on the manufactured device. The oil flow in both channels was active throughout the experiment, and the flow rates were equal and constant. The arrows attached to the droplets show they were in a flow and that the system was not yet steady-state. The arrow at the steady state (when Q = 1) shows the flow from the upper channel through the slits. The flow at the bottom channel is intact.

by adding two AND gates, as shown in Figure 9. In this case, there is only one input, the trigger T, which changes the device's internal state each time a high signal is applied. The implementation of this device in droplet microfluidics is based on a loop in which the input channel bifurcates into a state channel and triggering channel. The previously developed junction is optional if droplets are sufficiently short. However, the guiding junction assists in selecting a branch designated to maintain the internal state. Placing an obstacle in this branch in the loop effectively blocks the flow when a droplet is present and redirects all oil flow to the second branch. Due to the small loop size and the redirection of the flow in the junction, instead of compounding two channels by slits, the second obstacle needs to be placed in the second branch. In this case, the next droplet meeting this obstacle will increase pressure and trigger the first droplet, changing the device's internal state to 0. It is worth noting that the specific design of the device swaps the order of droplets in the sequence; that is, the first droplet is released second. This effect is due to placement of the trigger obstacle closer to the inlet than the state obstacle.

Article **C** also demonstrates the T flip-flop as a bimodal loop. In this implementation, the operational behavior was the same as previously presented, but the channels had significantly different lengths. Subsequently, I added more obstacles to the branch in which the internal state could be read. Each barrier introduced an additional internal state to the system. Each
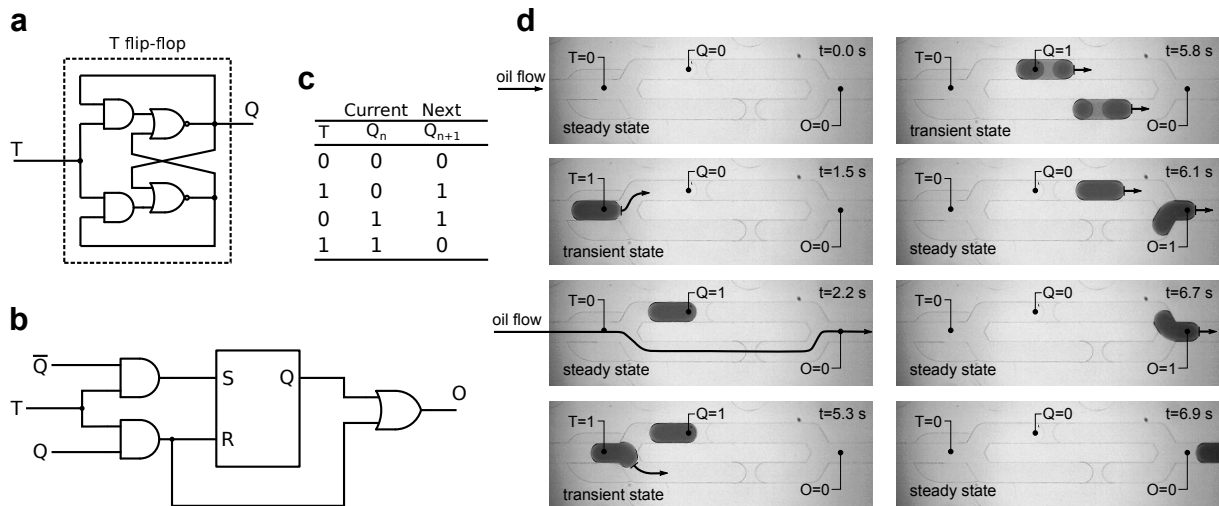
Figure 9: T flip-flop implemented in droplet microfluidics: a) Electrical schematic of a T flip-flop. b) Implementation scheme for a T flip-flop in droplet microfluidics. The guiding junction is interpreted as two additional AND gates. The end joint of the loop collecting droplets from both branches is interpreted as an OR gate. c) A truth table of the electronic version of the T flip-flop. d) Example of microfluidic circuit operation.

triggering droplet shifts a state droplet that flows until it encounters the next obstacle and obtains a new internal state. In the article, we describe experiments using an example device with nine state barriers, which is an analog of the one-hot counter known in electronics and mimics a decimal clock face (counting from 0 to 9). This device is shown in Figure 10. Such a large number of internal states in a single loop is due to the wide operating range of the guiding junction for forcing droplets to flow into a selected output. The length of the channel and the mere presence of obstacles impact the hydraulic resistance of each channel. In turn, the hydraulic resistance affects the maximum possible oil flow that can be used to hold the droplet in the state branch or enforce sufficient pressure to release it by the triggering droplet. Thus, a designer must adjust the height and length of each obstacle to ensure that the system works correctly. The guiding junction is necessary to direct the first droplet to the state branch, allowing correct operation when there is a significant difference in resistance between channels or when more than one obstacle is present.

The devices presented above demonstrate the fundamentals of constructing droplet microfluidic devices exhibiting sequential logic. Obstacles add to microfluidic systems the ability to block droplets at a given location if a bypass exists for oil flow. Next, other droplets can trigger immobilized droplets. The release of a hold droplet can be accomplished in two ways: by deactivating the bypass slit or encountering the triggering obstacle by the next droplet. Both ways increase the pressure in the system and allow the hold droplet to pass through the barrier. This simple mechanism can be used to synchronize droplets inside the microfluidic network and to create entirely new microfluidic geometries that perform particular functions. Moreover, this mechanism can operate within geometrically complex microfluidic networks
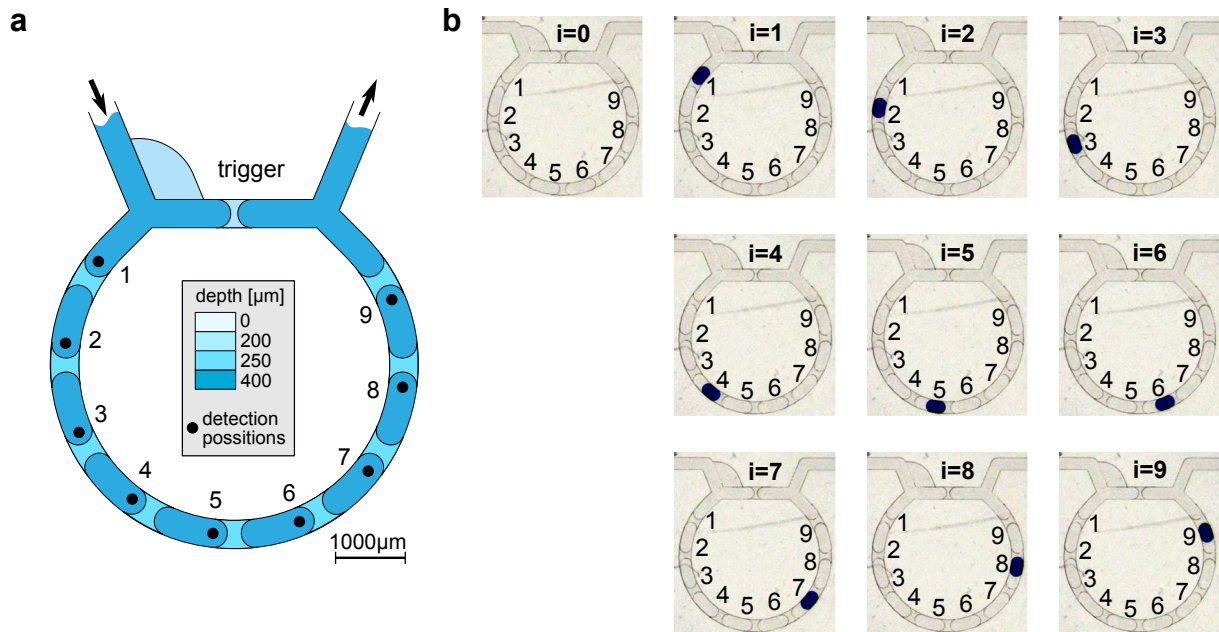
Figure 10: The decimal counter: a) a schematic top view of the counter with nine state obstacles in the more extended branch, b) snapshots with steady-state values in the counter in which the state number i corresponds to the occupied state position. (This graphic is an excerpt of a figure from Article **C**.)

with multiple bifurcations and parallel channels. The novelty of this study was to perform all logic operations based on capillary-hydrodynamic interactions inherent in the two-phase flow in confined embedded microfluidic networks. The limitation of the presented examples of single logic modules for integration is that all droplets entering the system leave it through the shared outlet. Therefore, the output signal, with the state droplets mixed with the trigger droplets, is unsuitable for transferring the information regarding the state of the device to another logic module.

In the next section, I propose a solution for the problem of redundant droplets and present integrated logic circuits.

5.3   Integration of sequential logic systems in microfluidic systems

5.3.1   Three-fold decimal counter

In droplet microfluidic systems, integration of combinational logic systems can be problematic due to the difficulties of droplet synchronization in complex microfluidic networks. For sequential logic, this problem may be less troublesome. However, a second crucial issue is the accommodation of redundant droplets for operations such as AND or OR (when both input droplets are present); this issue also exists for sequential logic. Examples are the T flip-flop and decimal counter implementations presented above in which a state droplet and a triggering droplet move to the shared output to form two nearby signals. These extra droplets should be ejected or intentionally maintained depending on the application. Otherwise, the appearance

of excess droplets or the incorrect position of some droplets in a series would cause confusion in subsequent stages. Therefore, droplet maintenance is crucial in constructing larger microfluidic systems with multiple sequential logic blocks. I have proposed how to separate signal droplets from redundant ones and allow cascade integration of multiple microfluidic geometries implementing sequential logic. Article **C** focuses on this question. The article primarily demonstrates the bimodal loops or one-hot counters presented previously, integrated counters as a direct expansion, and an example of permutation of the sequence of droplets. I developed microfluidic devices for this article, conducted experiments, and analyzed the results.

The proposed solution to the problem of redundant droplets is to use the dual output, separating the trigger droplets from the signal ones. Two output channels are connected by a slit that enables continuous phase flow but is inaccessible for droplets. Thus, pressures in both ducts are equalized, ensuring similar hydraulic conditions for the continuous phase flow. This separation allows the state droplet to be directed to the input of the following sequence block without interference with a redundant droplet. T flip-flops, bimodal loops, one-hot counters, or other devices can be modified to contain loops in this way. Figure 11 shows the modified decimal counter from the previous section.
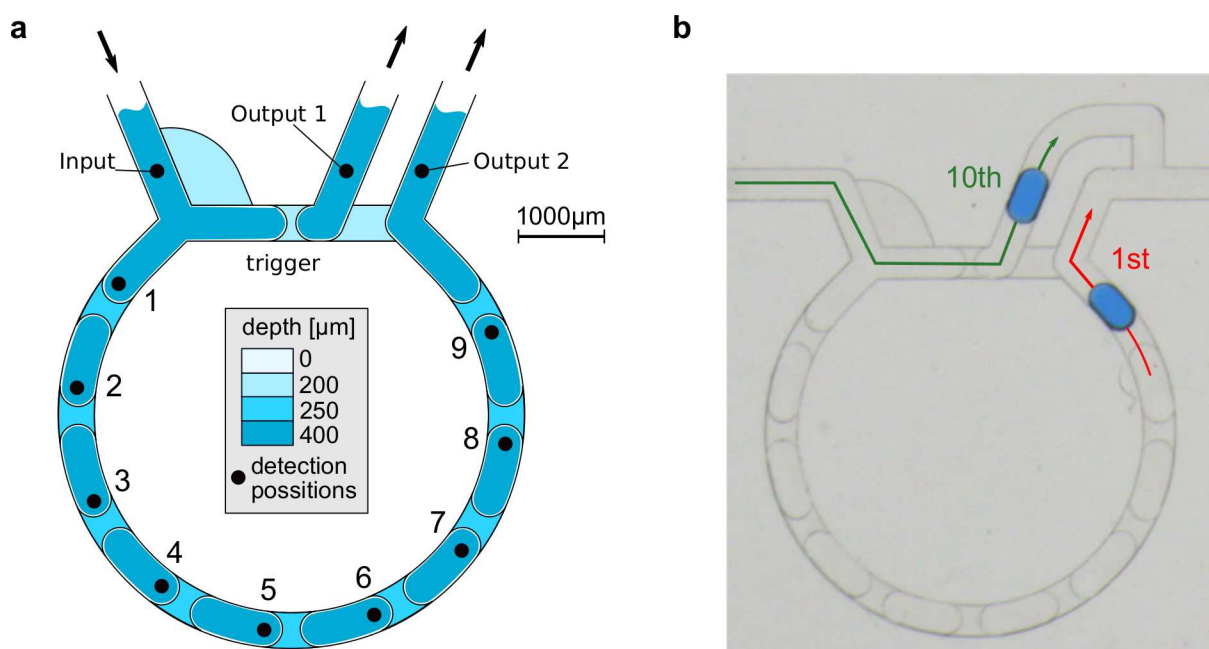

Figure 11: The modified decimal counter: a) a schematic top view of the counter with two outputs – one for triggering droplets, the second for droplets from the state branch; b) a snapshot from the experiment presenting zeroing of the counter. (This graphic is an excerpt from a figure published in the supplementary information for Article **C**.)

With the ability to choose specific droplets to pass through a series of connected sequential blocks, it is possible to build circuits that count values much higher than a single one-hot counter can accommodate. Article **C** presents an integrated counter with up to 1,000 droplets, shown in Figure 12. The device was made with three modified one-hot decimal counters con-

nected in series, in which each block subsequently counted units, decimals, and hundreds, respectively. The construction of the multi-clock counter required an additional channel parallel to the cascade of one-hot counters to collect excess droplets, in which the trigger droplets from each section traveled into this channel. However, we could successfully expand the system with more stages to obtain a higher capacity. Correct operation of a counting device requires a designer to optimize the channel's design to ensure proper hydraulic resistance so that whether it is empty or filled with ejected droplets, the correct operation of individual blocks would not be affected. Reading the counter's status involves determining the droplet's position in each stage. In addition, depending on interpretation and application, the same device can also be used to decimate, that is, to reduce the number of droplets in high-throughput devices with a massive number of droplets.
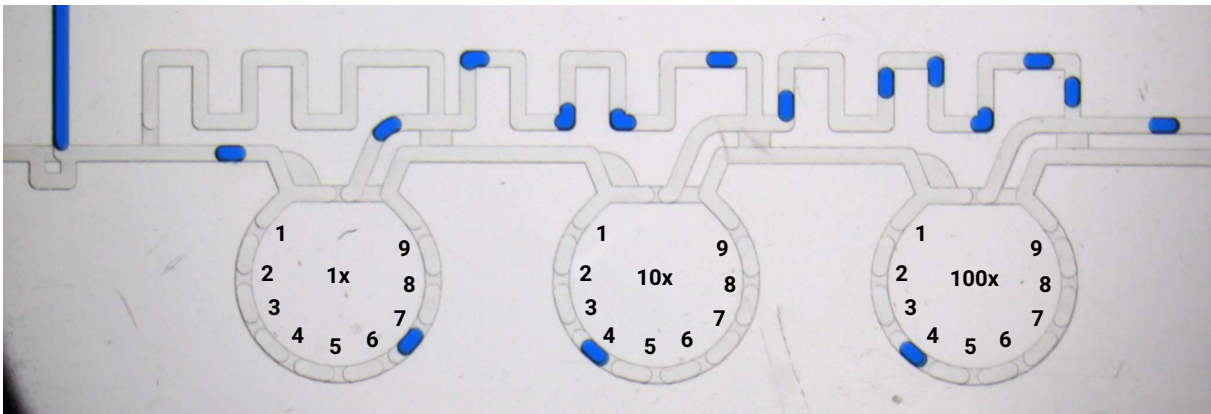

Figure 12: Snapshot of an experiment with the three-fold decimal counter presented in Article **C**. One-shot counters counting units, decimals, and hundreds have been placed from left to right, respectively. The integrated counter indicates the value of 447. The digits were added in graphic processing.

Each sequential block of the counter operated independently. Thus, an intermediate sequential block depended only on the output of the previous sequential block, and the switching of internal states was asynchronous in each stage. However, the switching time between internal states in a single one-hot counter is an important issue. Droplet feeding that is too frequent can cause an extra droplet to flow into the state branch before the unit goes to a steady state. The frequency of droplet delivery is crucial to the first cascade stage because it is decimated in later stages. Thus, switching time of the first stage limits droplet frequency. Switching time also depends on the design of the individual block itself, that is, the droplet's path from obstacle to obstacle or output and the limit of maximum oil flow rate. The constructed decimal counter can still be optimized.

5.3.2 Four-fold binary counter

Another example of the integrated sequential system that I designed is a binary counter that counts up to 16 droplets. It was built with a series connection of modified T flip-flops (pre-

sented in Figure 13) and resembles a ripple counter design, which is well known in electronics. A lower number of internal states in each stage allows for development of more consistent geometry and in fact provides a possibility for increasing the frequency of flowing droplets. On the other hand, generation of a similar capacity requires more sequential blocks to be connected in series compared to the three-fold decimal counter; it also would consume more area. The four-fold binary counter is presented primarily in the supplementary file of Article **C**. Figure 14 shows a snapshot of the working device.
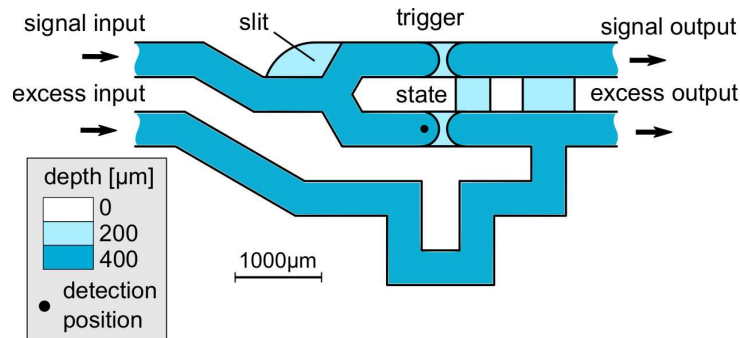

Figure 13: The modified T flip-flop with two outputs and an additional channel for excess droplets. (This is an excerpt of a figure published in the supplementary file of Article **C**.)
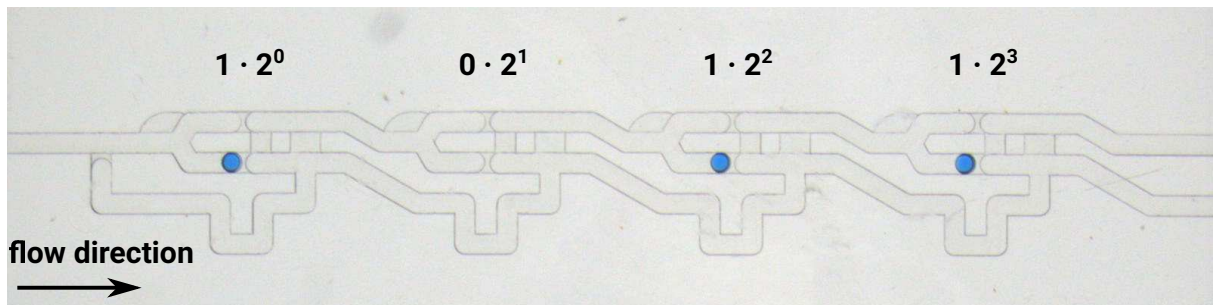

Figure 14: Snapshot of an experiment using the four-fold binary counter presented in the supplementary file of Article **C**. The state of the counter indicates the value 13 (1101 in the binary system).

5.3.3 Permutations of droplet order

Thus far, loops with obstacles have been presented as counters, in which the position of a droplet corresponds to a given numerical value. Another interpretation of this finite state machine could be to make a permutation of the sequence of droplets by distinguishing the order of droplets. The first droplet flows into the state branch due to the guiding junction, and the subsequent droplets flow through the triggering obstacle, leaving a loop before the initially introduced droplet. Finally, the first droplet leaves the block after the series of droplets equals the number of state obstacles. Consequently, it is moved from the beginning to the end of this series. This type of loop is called a rotator in this section. In this case, the issue of redundant droplets does not exist, as all droplets leave the system through the shared output; however, integration into larger systems still requires maintenance of proper flow conditions.

When the system is zeroing out, the key is to ensure that the last triggering droplet flows out first, followed by the droplet in the state branch. It is sufficient for a single sequential stage to properly position the triggering barrier relative to the one in the state branch. When assembling additional blocks in a cascade, it is also essential that there is an adequate gap between these droplets so that the next block has time to stabilize its new value before the last droplet appears. A helpful solution is to use modified loops in integrated counters. Two outputs are combined later into one and feed the next sequential block. However, elongating one output channel adds a delay to the end droplet and provides enough distance between droplets so that the entire system can work correctly. Figure 15 shows an example of two rotators that were used in further experiments.
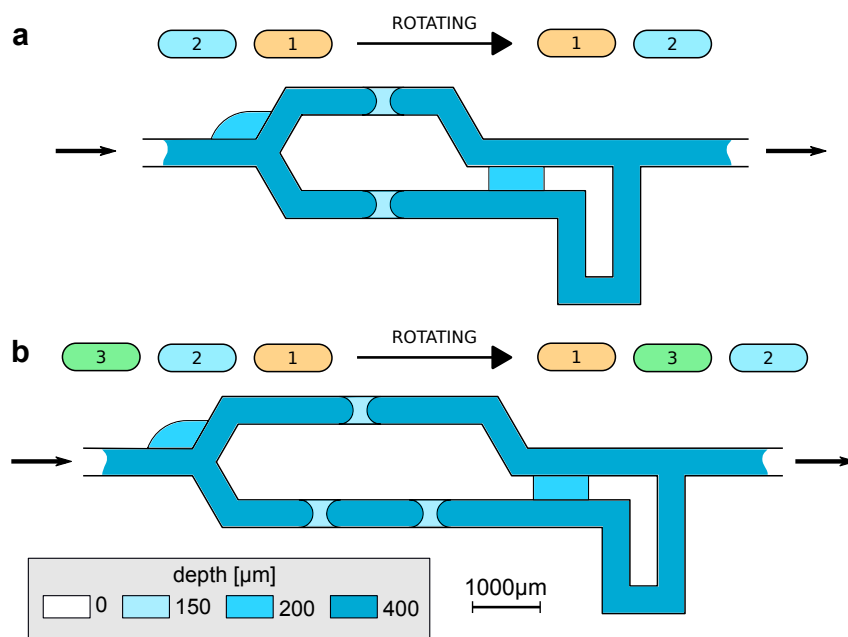

Figure 15: Examples of two rotators: a) swapping a pair of droplets – (1 2) -> (2 1); and b) transferring the first droplet to the end of a sequence of three droplets – (1 2 3) -> (2 3 1). These devices are suitable for integration into larger blocks in a cascade due to use of a channel that delays the transferred droplet.

The substantial power of droplet rotation can be seen when a series of different rotators are cascaded together. The idea studied in Article **C** was to use a series of rotators to permute a sequence of droplets. Such an operation resembles Heap's algorithm, which generates all possible permutations of n elements. The algorithm generates each permutation from the previous one, in which a single step consists of interchanging the positions of only two objects, while the other n – 2 elements remain intact. In the case of droplets, each rotator operates independently on a designated sub-sequence of droplets, flipping the first droplet of that subsequence to the end. Previous studies have shown that nine or even more obstacles can be placed in a single loop. There is also a possibility to create integrated rotators such as integrated counters. However, using a limited range of rotator types still allows for an entire range of per-

mutations. Thus, the target permutation can be achieved by cascading the series of rotators in the proper combination. Using different types of rotators, droplets can be rotated between sub-sequences, even if only by using the droplet pair swapping shown in Figure 15a. The total size of the droplet sequence on which the integrated permutating system operates results from the smallest common multiple of the rotator types used. In the case of an infinite series of droplets, the system would process successive sub-sequences of droplets whose size is associated with the smallest common multiple of all used rotators. The article **C** shows an example of the device inverting a series of droplets (1 2 3 4 5 6) into (6 5 4 3 2 1) using a combination of only two types of rotators (2 and 3), as presented in Figure 15. Figure 16 shows a snapshot of an experiment with rotating droplets.
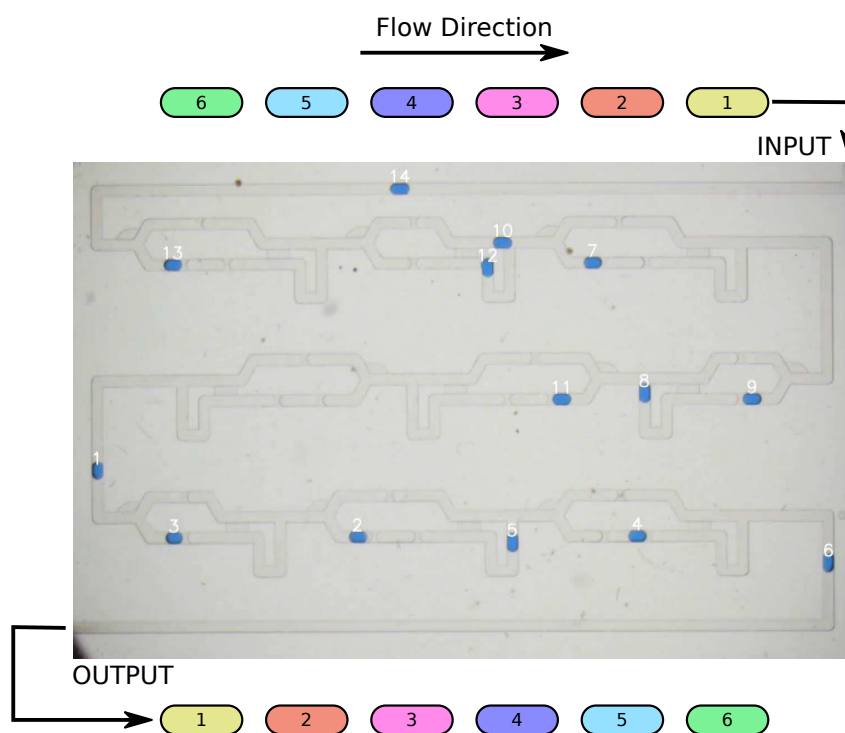

Figure 16: Snapshots of an experiment showing an example of a cascade of rotators to invert the order of every successive group of six droplets.

5.4 Iterative droplet manipulation system – concentration-on-demand device

5.4.1 The idea of conditioning droplets

In computer science, solving problems involves performing multiple, simple operations on quantized data. With algorithms that use these operations as a finite sequence of clearly defined steps, obtaining a wide range of results is possible. In addition, algorithms can be implemented directly in an electronic circuit or realized as a combination of a sequence of micro-instructions with a relatively simple sequential logic device, the so-called micro-programmable system. A feature of micro-programmable systems is their small size and short instruction sets

compared to universal devices such as microprocessors. However, these systems are specially designed and optimized for specific applications. Droplet microfluidic systems can operate similarly to achieve at least some degree of activity and exhibit similar features. In droplet microfluidics, many simple droplet operations, such as merging, mixing, and splitting, can be programmable by flows. Control by flows requires controllable flow sources or other actuators and construction of suitable microfluidic networks whose internal states depend on droplet interactions with microfluidic structures and the flow sequences used. Moreover, an attractive approach is to change a new internal state in the system by changing the direction of the continuous or droplet phase flow. A new internal state generated by switching flow direction is allowed by introducing nonlinearities by microfluidic traps built with bypass slits and obstacles.

In Article **D**, I developed a microfluidic device that realized the above concept of microprogramming to create droplet concentrations. I also developed an algorithm by which arbitrary droplet concentrations could be obtained, performed experiments using it, and validated the generated droplet concentrations. Forming droplets with different concentrations used a set of basic droplet operations. The operations included generating droplets of uniform size, merging two droplets into one double-sized droplet, mixing the contents of the resulting long droplet, and splitting the long droplet into two droplets of uniform size. One of the uniformly sized droplets with a new concentration could be used in the next iteration or could be sent to the system's output, while the other droplet could be sent to the waste collector and ejected from the system. When combined with a suitable algorithm, the given set of fundamental operations could create droplets that comprised a mixture of two base liquids in any desired proportion.

In this system, an input droplet is generated from one of two base liquids: pure solvent or basic reagent solution. The input reagent concentration normalizes the concentration of the input droplets and any droplets in subsequent iterative cycles. The normalization by the input concentration yields a dimensionless concentration of the input droplets equal to 0 (for droplets of pure solvent) or 1 (for droplets of the basic reagent solution). Assuming operation on uniformly sized droplets, each new concentration created is the arithmetic average between the concentration obtained in the previous cycle and the input concentration, that is, 0 or 1. The first step yields a concentration of 0.5 when the two droplets are created from two different input droplet phases. With each successive iteration, an ever-increasing range of possible concentrations can be obtained, creating a so-called binary tree, as shown in Figure 17. Each node directs to the following two possible concentrations depending on which input droplet is used, resulting in one concentration less than and the other greater than 0.5. By operating on the binary tree, a sequence of input droplets for the target droplet concentration of interest can be found. However, it is possible to reverse the problem and search for a series of input droplets when the target concentration is known.
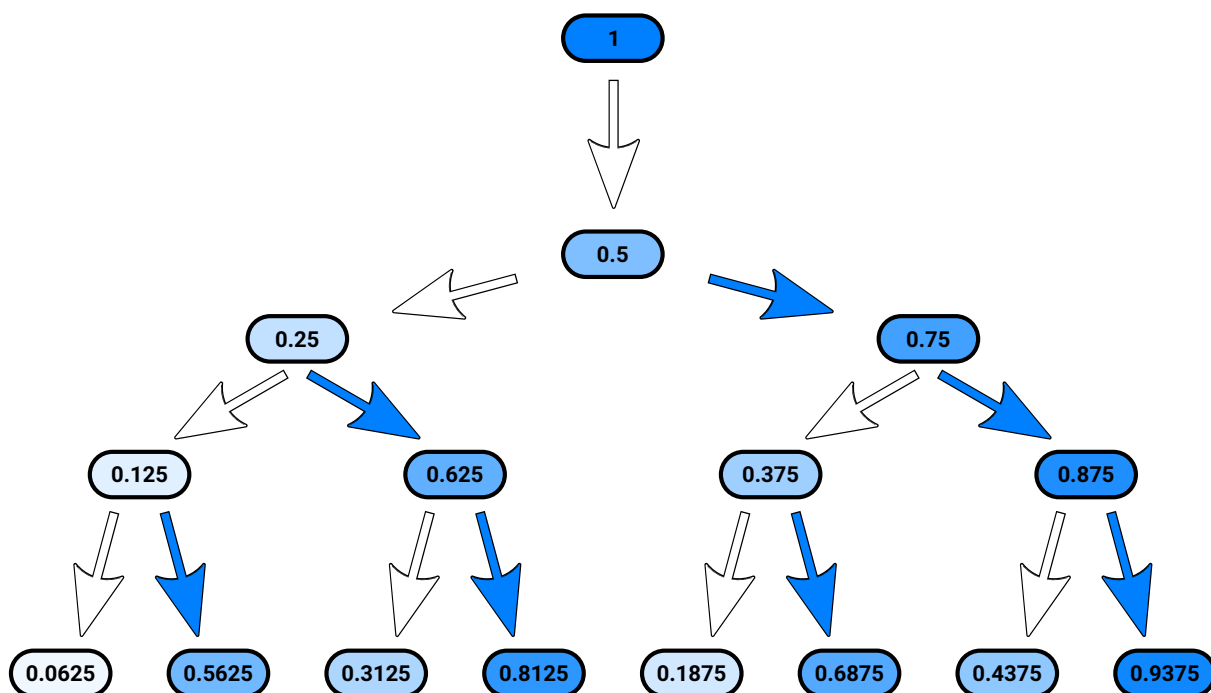
Figure 17: Binary tree for the possible concentrations of droplets. The figure shows only the first four iterations, although the number of iterations can be infinite. The colors of the arrows indicate which input droplet was added to the droplet from the previous iteration: white = 0; blue = 1.

5.4.2 Implementation of the microfluidic device

The microfluidic device was built with two compound microfluidics modules. The scheme of this device is shown in Figure 18. The first module is used to create new droplets and is based on a previously developed method for generating droplets on demand in a metering trap. This method is scalable and allows using two or even more input droplet phases, delivering solvent and different reagents. The second module is used to perform the entire cycle operation, merging and mixing to average the concentration in the double-sized droplet and then splitting that droplet. It consists of a metering trap, a merging trap, and a mixing channel connected in series. The metering trap is shared between both modules, thus ensuring that the trap processes droplets of uniform size. The merging trap acts as a cache for droplets from the previous iteration, allowing it to merge with the next generated droplet. This trap has two obstacles on both sides that are offset appropriately from the bypass slits and have a lower height. As a result, it immobilizes droplets of the size created in the metering trap and merges them with subsequent incoming droplets but freely passes double-sized droplets back and forth without affecting them uncontrollably. However, these two traps should be at an appropriate distance such that the sensor that detects the position of the droplet phase while generating a new droplet can prevent it from accidentally merging with the droplet immobilized in the merging trap.

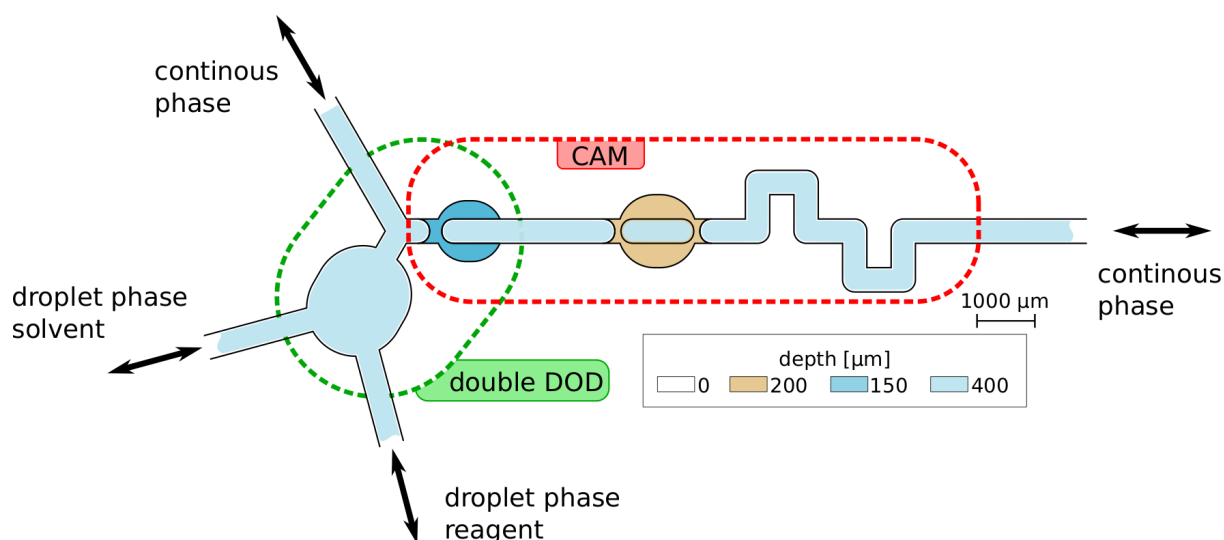The operation of the device begins with generation of a new droplet from the selected

Figure 18: Scheme of a device for creating droplet concentration on demand. It consists of two modules: DOD, droplet-on-demand to create new droplets from droplet phases, and CAM, a concentration averaging module to merge two droplets, mix a double-sized droplet, and split it into uniformly sized droplets. A pump with oil is connected to one channel with a continuous phase, depending on the selected mode of operation. (This graphic is an excerpt from a figure published in Article **D**.)

input droplet phase in the metering trap. The generated input droplet from the metering trap is transferred to the metering trap during oil flow in one direction (enforced by the oil phase pump or one of the droplet phase pumps if they have drawn the proper volume of oil) and then immobilized. Next, a second droplet is generated in the metering trap and flows into the merging trap. Both droplets merge and flow through to the mixing channel. In the mixer, the concentration is averaged across the volume of the double droplet. Depending on further instructions, the oil flow can change flow direction. Thus, the double-sized droplet flows through the merging trap unaffected and is shortened in the metering trap to single-sized droplets. The immobilized droplet is ready for the next cycle, while the excess droplet flushes out of the system. The entire iteration is illustrated in Figure 19.

5.4.3 Modes of operation

The device has two main operating modes that a user can choose to utilize. The selected mode determines where the system's output is located and on which side the continuous phase pump is connected.

The first mode uses double-sized droplets as output droplets when reaching target concentrations. The output is the channel behind the mixer, and the oil syringe pump is connected behind the metering trap. It is necessary to have a waste collector to collect intermediate droplets before achieving the target droplet concentration. In the prototype, the waste collector was a large, deep container placed in the channel connected to the oil syringe pump into which droplets fell; oil flowed freely over ejected droplets in both directions. Creating a droplet with
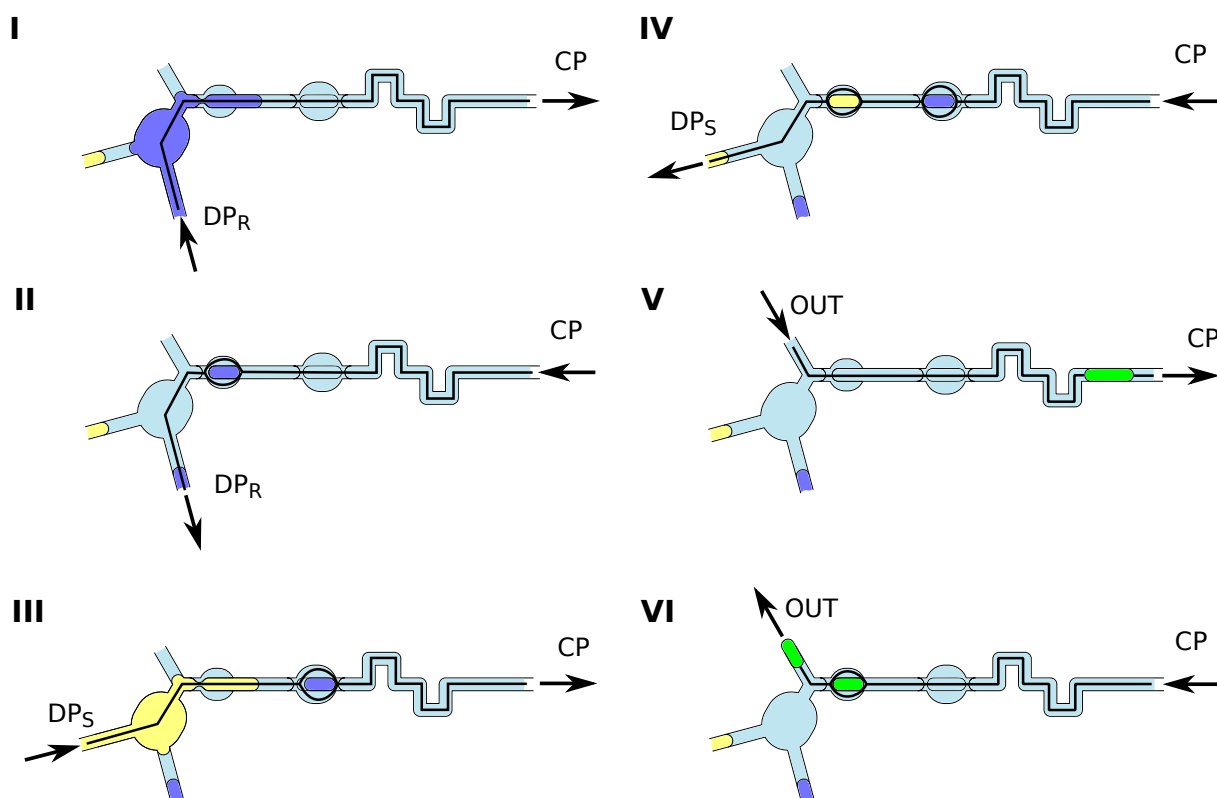
Figure 19: Sequence of one entire iteration proceeding, starting with an empty device: I–II, generating the droplet from the reagent droplet phase; III–IV, generating the droplet from the solvent droplet phase; V, merging both droplets and mixing; VI, splitting a double-sized droplet. (This graphic is an excerpt from a figure published in Article **D**.)

the desired concentration always begins with an empty system in this mode. This configuration delivers the possibility of arbitrary droplet concentration with the appropriate algorithm, as described in Article **D**.

In Article **D**, we describe testing of a prototype based on the scheme in Figure 18. We used dye to readily measure concentration with a camera after calibrating the experimental configuration. The mathematical predictions agreed with the results of the quantitative concentration estimates based on visualization of the color dye. Experiments showed that it was possible to generate droplets of different concentrations with high precision and accuracy.

The second mode of operation uses uniform-sized droplets as output, and the oil syringe pump is connected to the channel behind the mixer. After splitting a double-sized droplet, one travels directly to the system's output while the second droplet, immobilized in the metering trap, is permanently stored. In this case, a waste collector is unnecessary, and there is no discarding of droplet phases. However, the output droplets exhibit concentration sequences that depend on the pattern of the input sequence. This mode mimics the operation of a low-pass, first-order, infinite impulse response filter, which is well known in digital signal processing. In Article **D**, we present several examples of patterns and experimental verification that repeated output concentrations depended on the input droplet pattern that had been used.

5.4.4 Periodic cross-combination

The system presented for generating droplet concentrations can still be improved and expanded. One potential expansion would be to add more droplet phases with different reagents. Using more types of input droplets would make it possible to create droplets with the chosen reagent or a combination of two or more reagents in one droplet. In Article **D**, a prototype for three droplet phases is presented; Figure 20 shows this improved device. Accordingly, the ability to store two double-sized droplets has been added. The bifurcation behind the mixer is used as storage for the two droplets. Selection of the flow of a particular droplet is controlled using a single pump connected to a 3/2 valve. An additional merging trap makes it possible to create concentration maps of two different components in a droplet.
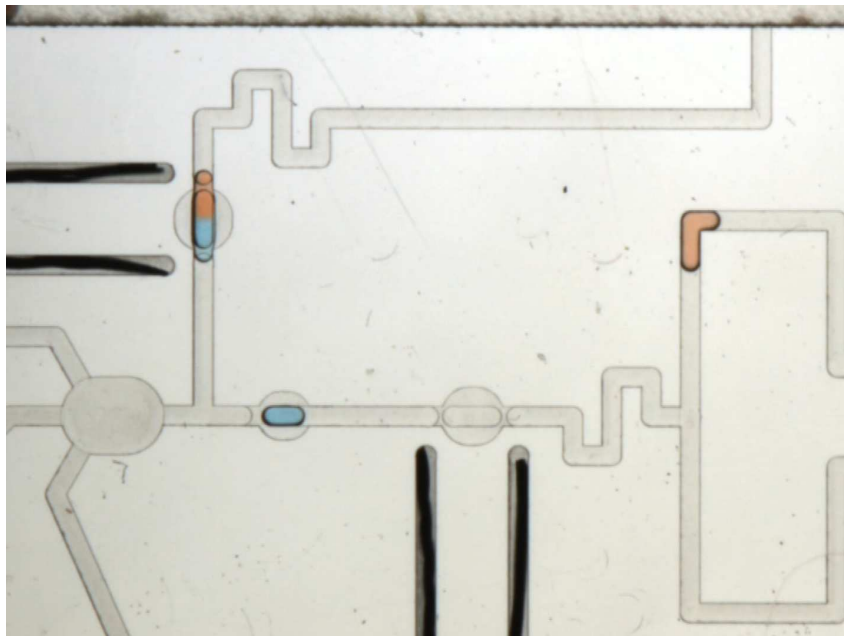

Figure 20: An improved concentration-on-demand device with three droplet phases and an additional merging trap to combine two reagents in one droplet. The snapshot shows the point at which two output droplets have joined in the merging trap placed at the system's output.

6 Conclusions

The research described above validates the thesis posed in this Ph.D. project that the building of sequential logic and integration is available in droplet microfluidic systems. Single sequential blocks allow synchronizing, triggering, counting, decimating, or permuting a series of droplets. Using these simpler blocks according to proper rules for designing microfluidic networks to maintain appropriate flows in branches can create more complex sequential systems. The system's operation directly follows the single elements, and the entire system's functioning is entirely predictable. The flexibility of combining sequential blocks allows a designer to create a device to meet an application's requirements in terms of maximum flow rates, frequency of droplets fed, or whether chip space is occupied. The demonstrations of droplet counting and permutation have shown that within droplet microfluidic systems, droplets can interact and self-organize flows that a designer can fully determine by planning the microfluidic network. The research presented here focuses on the cascade connection of single sequential blocks. However, the idea of sequential logic can still be developed by parallelizing the sequence of droplets, acting on the appropriate sub-sequences in each branch, and then compounding into the target sequence at the output or maintaining parallel processing. This question remains open and unexplored.

Further development of sequential logic will make it possible to create microfluidic devices in which the algorithm performing operations on the droplets is implemented entirely in the network structure of the microfluidic system. For example, the combination of permutating modules with the existing abilities for droplet manipulation, such as merging two consecutive droplets, mixing, and splitting in constant undirected flow, will allow the creation of systems in which appropriate concentrations can be generated in a sequence of droplets with a fixed pattern that has been hard-wired into the structure of the microfluidic system. An analogous electronic solution is a function generator, which produces repeating waveforms with specific shapes and parameters.

The studies presented here show that the bypass slit and obstacle have great potential for construction of structures and networks in microfluidic systems. Activation and deactivation of the bypass slit by droplets and holding and releasing droplets by the obstacle in microfluidic channels both significantly affect the nonlinearity of the system operation, despite the laminar nature of the flow in the microchannels. Thus, it is possible to construct a range of geometries that perform various specific functions on droplets. Previously published studies of microfluidic traps, such as metering and merging traps, have shown that combining these elements can lead to valuable features. This work has significantly highlighted the utility of bypass slits and obstacles inside microchannels.

To manipulate droplets, the possibility of building microfluidic networks using three basic geometries – regular channels, obstacles, and bypass slits – is very promising. Designers can create microfluidic geometries that perform specific functions by modifying the shapes and parameters of these geometries, while preserving the essence of their mechanisms, and can then build complex microfluidic networks based on these geometries. A vital element developed in the present work is the guiding junction that forces the flow of droplets to one of the outputs. The junction's wide range of operation in terms of flow ratios at the output makes it possible to construct single geometries and entire microfluidic networks in which the movement of droplets is fully determined, repeatable, and predictable.

This thesis has discussed two approaches to the construction of microfluidic systems. The first is to create devices in which droplets perform self-organization inside microfluidic structures by interacting with these structures and with each other. Associated with this solution is the presented sequential logic. This approach reduces control, leaving only the need to enforce stable input flows. Droplets are synchronized and positioned by the microfluidic structures themselves, removing the need for detection and droplet tracking.

The second approach involves an application-specific microfluidic structure in which droplet operations are built as an execution block with little control. Its internal state changes not only through the internal interactions of the droplets and the microfluidic geometries being used but also from the flow sequences that are chosen. However, such a solution requires controllable flow sources that should not only be able to change the flow direction but should also maintain standardized flow rates. This approach is related to the concentration-on-demand module that was developed and shows that even a simple microfluidic network design using geometries that perform particular functions combined with algorithms that are well known in computer science can yield a powerful tool that is compact and easy to integrate into a more extensive microfluidic system.

Both approaches ensure that few actuators are required for complex droplet operations while enhancing capabilities for droplet manipulation. The results that have been achieved fully reflect the motivation for the work that was undertaken. The presented solutions are simpler to design and less expensive to manufacture than current platforms, such as digital microfluidics. This research has also shown that digital algorithms operating on droplets can be effective and relatively easily implemented in channel-based microfluidics. Furthermore, microfluidic traps can work similarly to unidirectional diodes in electronics, passing droplets in one order or immobilizing them when the flow is reversed. Combining microfluidics traps, guiding junctions, and sequential logic solutions opens the possibility of constructing devices with subsequent droplet processing using oscillating continuous phase flow. In turn, processing by switch flow direction would allow the use of smaller and simpler flow sources, in which moving only a small volume of liquid would be necessary.

In summary, as a result of the work presented in this Ph.D. thesis, the following scientific achievements can be enumerated:

- **Investigation of the activation and deactivation mechanisms of the bypass slit by a flowing droplet.** In connection with the obstacle, these findings can be leveraged to build microfluidic geometries that perform various functions.

- **Development of a microfluidic junction for redirecting fixed droplets in bifurcation.** This element enables the construction of complex microfluidic networks with fixed droplet routing.

- **Development of basic microfluidic geometries that exhibit sequential logic.** Sequential microfluidic structures use and combine the mechanisms of bypass slits and obstacles.

- **Demonstration of how to integrate single logic geometries into more extensive microfluidic networks.** Decimal and binary fold counters and permutators of droplet sequences were constructed.

- **Improvement of droplet formation in the metering trap.** The droplet phase's push and pull sequence delivers ultra-high precision in generating droplets.

- **Development of a concentration-on-demand device.** This device can form droplets of any concentration on demand and can easily integrate into more complex microfluidic systems.

References

[1] A. K. Au et al. "Microvalves and Micropumps for BioMEMS." In: *Micromachines* 2.2 (June 2011), pp. 179–220. ISSN: 2072-666X. DOI: 10.3390/mi2020179 (cit. on p. 1).

[2] Y.-N. Wang and L.-M. Fu. "Micropumps and biomedical applications - A review." In: *Microelectronic Engineering* 195 (Aug. 5, 2018), pp. 121–138. ISSN: 0167-9317. DOI: 10.1016/j.mee.2018.04.008 (cit. on p. 1).

[3] J.-Y. Qian et al. "Actuation Mechanism of Microvalves: A Review." In: *Micromachines* 11.2 (Feb. 2020), p. 172. DOI: 10.3390/mi11020172 (cit. on p. 1).

[4] M. L. Sin et al. "System Integration - A Major Step toward Lab on a Chip." In: *Journal of Biological Engineering* 5.1 (May 25, 2011), p. 6. ISSN: 1754-1611. DOI: 10.1186/1754-1611-5-6 (cit. on pp. 1, 13).

[5] P. M. Korczyk et al. "Microfluidic traps for hard-wired operations on droplets." In: *Lab on a Chip* 13.20 (Sept. 18, 2013), pp. 4096–4102. ISSN: 1473-0189. DOI: 10.1039/C3LC50347J (cit. on pp. 1, 6, 8, 10).

[6] V. van Steijn et al. "Block-and-break generation of microdroplets with fixed volume." In: *Biomicrofluidics* 7.2 (2013), p. 24108. ISSN: 1932-1058. DOI: 10.1063/1.4801637 (cit. on pp. 1, 7).

[7] W. Postek, T. S. Kaminski, and P. Garstecki. "A precise and accurate microfluidic droplet dilutor." In: *Analyst* 142.16 (Aug. 7, 2017), pp. 2901–2911. ISSN: 1364-5528. DOI: 10.1039/C7AN00679A (cit. on pp. 1, 8, 11).

[8] E. Samiei, M. Tabrizian, and M. Hoorfar. "A review of digital microfluidics as portable platforms for lab-on a-chip applications." In: *Lab on a Chip* 16.13 (2016), pp. 2376–2396. ISSN: 1473-0197, 1473-0189. DOI: 10.1039/C6LC00387G (cit. on pp. 1, 9).

[9] O. J. Dressler, X. Casadevall i Solvas, and A. J. deMello. "Chemical and Biological Dynamics Using Droplet-Based Microfluidics." In: *Annual Review of Analytical Chemistry* 10.1 (June 12, 2017), pp. 1–24. ISSN: 1936-1327. DOI: 10.1146/annurev-anchem-061516-045219 (cit. on p. 2).

[10] K. Sharma. *Nanostructuring Operations in Nanoscale Science and Engineering*. Mcgraw-hill, 2009. ISBN: 978-0-07-162295-0 (cit. on p. 2).

[11] F. Kong et al. "Automatic Liquid Handling for Life Science: A Critical Review of the Current State of the Art." In: *SLAS Technology* 17.3 (June 1, 2012), pp. 169–185. ISSN: 2472-6303, 2472-6311. DOI: 10.1177/2211068211435302 (cit. on p. 2).

[12] J.-Y. Yoon. "Lab-on-a-Chip Biosensors." In: *Introduction to Biosensors: From Electric Circuits to Immunosensors*. Cham: Springer International Publishing, 2016, pp. 257–297. ISBN: 978-3-319-27413-3. DOI: 10.1007/978-3-319-27413-3_14 (cit. on p. 2).

[13] P. S. Dittrich and A. Manz. "Lab-on-a-chip: microfluidics in drug discovery." In: *Nature Reviews Drug Discovery* 5.3 (Mar. 2006), pp. 210–218. ISSN: 1474-1784. DOI: `10.1038/nrd1985` (cit. on p. 2).

[14] L. R. Volpatti and A. K. Yetisen. "Commercialization of microfluidic devices." In: *Trends in Biotechnology* 32.7 (July 1, 2014), pp. 347–350. ISSN: 0167-7799. DOI: `10.1016/j.tibtech.2014.04.010` (cit. on p. 2).

[15] N. Convery and N. Gadegaard. "30 years of microfluidics." In: *Micro and Nano Engineering* 2 (Mar. 1, 2019), pp. 76–91. ISSN: 2590-0072. DOI: `10.1016/j.mne.2019.01.003` (cit. on pp. 2, 3, 13).

[16] S. Sachdeva, R. W. Davis, and A. K. Saha. "Microfluidic Point-of-Care Testing: Commercial Landscape and Future Directions." In: *Frontiers in Bioengineering and Biotechnology* 8 (2021). ISSN: 2296-4185 (cit. on p. 2).

[17] G. M. Whitesides. "The origins and the future of microfluidics." In: *Nature* 442.7101 (July 2006), pp. 368–373. ISSN: 1476-4687. DOI: `10.1038/nature05058` (cit. on p. 2).

[18] H. Stone, A. Stroock, and A. Ajdari. "Engineering Flows in Small Devices: Microfluidics Toward a Lab-on-a-Chip." In: *Annual Review of Fluid Mechanics* 36.1 (Jan. 21, 2004), pp. 381–411. ISSN: 0066-4189, 1545-4479. DOI: `10.1146/annurev.fluid.36.050802.122124` (cit. on pp. 2, 6, 9).

[19] S. L. Anna. "Droplets and Bubbles in Microfluidic Devices." In: *Annual Review of Fluid Mechanics* 48.1 (Jan. 3, 2016), pp. 285–309. ISSN: 0066-4189. DOI: `10.1146/annurev-fluid-122414-034425` (cit. on pp. 2, 6).

[20] P. Tabeling. *Introduction to Microfluidics*. OUP Oxford, May 6, 2010. 312 pp. ISBN: 978-0-19-958816-9 (cit. on p. 2).

[21] M. J. Madou. *Fundamentals of Microfabrication: The Science of Miniaturization, Second Edition*. 2nd ed. Boca Raton: CRC Press, Jan. 31, 2017. 752 pp. ISBN: 978-1-315-27422-5. DOI: `10.1201/9781482274004` (cit. on p. 2).

[22] J. Guzowski et al. "Automated high-throughput generation of droplets." In: *Lab on a Chip* 11.21 (2011), pp. 3593–3595. ISSN: 1473-0197. DOI: `10.1039/C1LC20595A` (cit. on pp. 2, 3).

[23] S.-Y. Teh et al. "Droplet microfluidics." In: *Lab on a Chip* 8.2 (Jan. 29, 2008), pp. 198–220. ISSN: 1473-0189. DOI: `10.1039/B715524G` (cit. on p. 3).

[24] L. Shang, Y. Cheng, and Y. Zhao. "Emerging Droplet Microfluidics." In: *Chemical Reviews* 117.12 (June 28, 2017), pp. 7964–8040. ISSN: 0009-2665. DOI: `10.1021/acs.chemrev.6b00848` (cit. on pp. 3, 13).

[25] J. S. Kuo and D. T. Chiu. "Controlling Mass Transport in Microfluidic Devices." In: *Annual review of analytical chemistry (Palo Alto, Calif.)* 4 (2011), pp. 275–296. ISSN: 1936-1327. DOI: `10.1146/annurev-anchem-061010-113926` (cit. on p. 3).

[26]   P. Garstecki et al. "Formation of monodisperse bubbles in a microfluidic flow-focusing device." In: *Applied Physics Letters* 85.13 (Sept. 27, 2004), pp. 2649–2651. ISSN: 0003-6951. DOI: `10.1063/1.1796526` (cit. on pp. 3, 6).

[27]   H. Song, D. L. Chen, and R. F. Ismagilov. "Reactions in Droplets in Microfluidic Channels." In: *Angewandte Chemie International Edition* 45.44 (2006), pp. 7336–7356. ISSN: 1521-3773. DOI: `10.1002/anie.200601554` (cit. on p. 3).

[28]   T. Schneider, J. Kreutz, and D. T. Chiu. "The potential impact of droplet microfluidics in biology." In: *Analytical Chemistry* 85.7 (Apr. 2, 2013), pp. 3476–3482. ISSN: 1520-6882. DOI: `10.1021/ac400257c` (cit. on p. 3).

[29]   M. S. Chowdhury et al. "Dendronized fluorosurfactant for highly stable water-in-fluorinated oil emulsions with minimal inter-droplet transfer of small molecules." In: *Nature Communications* 10.1 (Oct. 4, 2019), p. 4546. ISSN: 2041-1723. DOI: `10.1038/s41467-019-12462-5` (cit. on pp. 3, 5).

[30]   T. S. Kaminski and P. Garstecki. "Controlled droplet microfluidic systems for multistep chemical and biological assays." In: *Chemical Society Reviews* 46.20 (Oct. 16, 2017), pp. 6210–6226. ISSN: 1460-4744. DOI: `10.1039/C5CS00717H` (cit. on p. 3).

[31]   H. S. Rho et al. "Programmable droplet-based microfluidic serial dilutor." In: *Journal of Industrial and Engineering Chemistry* 91 (Nov. 25, 2020), pp. 231–239. ISSN: 1226-086X. DOI: `10.1016/j.jiec.2020.08.004` (cit. on pp. 3, 11).

[32]   M. T. Guo et al. "Droplet microfluidics for high-throughput biological assays." In: *Lab on a Chip* 12.12 (May 22, 2012), pp. 2146–2155. ISSN: 1473-0189. DOI: `10.1039/C2LC21147E` (cit. on p. 3).

[33]   K. Churski, P. Korczyk, and P. Garstecki. "High-throughput automated droplet microfluidic system for screening of reaction conditions." In: *Lab on a Chip* 10.7 (Apr. 7, 2010), pp. 816–818. ISSN: 1473-0189. DOI: `10.1039/B925500A` (cit. on p. 3).

[34]   L. Mazutis et al. "Single-cell analysis and sorting using droplet-based microfluidics." In: *Nature Protocols* 8.5 (May 2013), pp. 870–891. ISSN: 1750-2799. DOI: `10.1038/nprot.2013.046` (cit. on p. 3).

[35]   D. Liu et al. "Single-cell droplet microfluidics for biomedical applications." In: *Analyst* 147.11 (May 30, 2022), pp. 2294–2316. ISSN: 1364-5528. DOI: `10.1039/D1AN02321G` (cit. on pp. 3, 5).

[36]   J. Zhai et al. "A digital microfluidic system with 3D microstructures for single-cell culture." In: *Microsystems & Nanoengineering* 6.1 (Jan. 27, 2020), pp. 1–10. ISSN: 2055-7434. DOI: `10.1038/s41378-019-0109-7` (cit. on p. 3).

[37]   J. L. Madrigal et al. "Characterizing cell interactions at scale with made-to-order droplet ensembles (MODEs)." In: *Proceedings of the National Academy of Sciences* 119.5 (Feb. 2022). DOI: `10.1073/pnas.2110867119` (cit. on p. 3).

[38] Q. Zhu et al. "Digital PCR on an integrated self-priming compartmentalization chip." In: *Lab. Chip* (Jan. 2014) (cit. on p. 3).

[39] F. Shen et al. "Multiplexed Quantification of Nucleic Acids with Large Dynamic Range Using Multivolume Digital RT-PCR on a Rotational SlipChip Tested with HIV and Hepatitis C Viral Load." In: *Journal of the American Chemical Society* 133.44 (2011), pp. 17705–17712. ISSN: 0002-7863. DOI: 10.1021/ja2060116 (cit. on p. 3).

[40] J. Shen et al. "A rapid nucleic acid concentration measurement system with large field of view for a droplet digital PCR microfluidic chip." In: *Lab on a Chip* 21.19 (Sept. 28, 2021), pp. 3742–3747. ISSN: 1473-0189. DOI: 10.1039/D1LC00532D (cit. on p. 3).

[41] A. Jagannath et al. "Pathogen detection on microfluidic platforms: Recent advances, challenges, and prospects." In: *Biosensors and Bioelectronics: X* 10 (May 1, 2022), p. 100134. ISSN: 2590-1370. DOI: 10.1016/j.biosx.2022.100134 (cit. on p. 3).

[42] D. Zhang et al. "Detection of Pathogenic Microorganisms by Microfluidics Based Analytical Methods." In: *Analytical Chemistry* 90.9 (May 1, 2018), pp. 5512–5520. ISSN: 0003-2700. DOI: 10.1021/acs.analchem.8b00399 (cit. on p. 3).

[43] C. Spatola Rossi et al. "Microfluidics for Rapid Detection of Live Pathogens." In: *Advanced Functional Materials* n/a (n/a), p. 2212081. ISSN: 1616-3028. DOI: 10.1002/adfm.202212081 (cit. on p. 3).

[44] O. Scheler et al. "Droplet-based digital antibiotic susceptibility screen reveals single-cell clonal heteroresistance in an isogenic bacterial population." In: *Scientific Reports* 10.1 (Feb. 24, 2020), p. 3282. ISSN: 2045-2322. DOI: 10.1038/s41598-020-60381-z (cit. on p. 3).

[45] W. Postek and P. Garstecki. "Droplet Microfluidics for High-Throughput Analysis of Antibiotic Susceptibility in Bacterial Cells and Populations." In: *Accounts of Chemical Research* 55.5 (Mar. 1, 2022), pp. 605–615. ISSN: 0001-4842. DOI: 10.1021/acs.accounts.1c00729 (cit. on p. 3).

[46] A. M. Kaushik et al. "Accelerating bacterial growth detection and antimicrobial susceptibility assessment in integrated picoliter droplet platform." In: *Biosensors & Bioelectronics* 97 (Nov. 15, 2017), pp. 260–266. ISSN: 1873-4235. DOI: 10.1016/j.bios.2017.06.006 (cit. on p. 3).

[47] W.-B. Lee et al. "Rapid antimicrobial susceptibility tests on an integrated microfluidic device for precision medicine of antibiotics." In: *Biosensors and Bioelectronics* 176 (Mar. 15, 2021), p. 112890. ISSN: 0956-5663. DOI: 10.1016/j.bios.2020.112890 (cit. on p. 3).

[48] M. Tang et al. "A linear concentration gradient generator based on multi-layered centrifugal microfluidics and its application in antimicrobial susceptibility testing." In: *Lab on a Chip* 18.10 (May 15, 2018), pp. 1452–1460. ISSN: 1473-0189. DOI: 10.1039/C8LC00042E (cit. on pp. 3, 10).

[49] S. L. Pratt et al. "DropSOAC: Stabilizing Microfluidic Drops for Time-Lapse Quantification of Single-Cell Bacterial Physiology." In: *Frontiers in Microbiology* 10 (Sept. 24, 2019), p. 2112. ISSN: 1664-302X. DOI: `10.3389/fmicb.2019.02112` (cit. on p. 3).

[50] O. J. Dressler et al. "Droplet-Based Microfluidics: Enabling Impact on Drug Discovery." In: *Journal of Biomolecular Screening* 19.4 (Apr. 2014), pp. 483–496. ISSN: 1087-0571, 1552-454X. DOI: `10.1177/1087057113510401` (cit. on pp. 3, 10).

[51] F. Gielen et al. "A Fully Unsupervised Compartment-on-Demand Platform for Precise Nanoliter Assays of Time-Dependent Steady-State Enzyme Kinetics and Inhibition." In: *Analytical Chemistry* 85.9 (May 7, 2013), pp. 4761–4769. ISSN: 0003-2700. DOI: `10.1021/ac400480z` (cit. on p. 3).

[52] H. Yuan et al. "Ultrahigh-throughput screening of industrial enzyme-producing strains by droplet-based microfluidic system." In: *Journal of Industrial Microbiology and Biotechnology* 49.3 (May 1, 2022), kuac007. ISSN: 1367-5435. DOI: `10.1093/jimb/kuac007` (cit. on p. 3).

[53] J. H. Kim et al. "Droplet Microfluidics for Producing Functional Microparticles." In: *Langmuir* 30.6 (Feb. 18, 2014), pp. 1473–1488. ISSN: 0743-7463. DOI: `10.1021/la403220p` (cit. on p. 3).

[54] S. Abalde-Cela et al. "Droplet microfluidics for the highly controlled synthesis of branched gold nanoparticles." In: *Scientific Reports* 8.1 (Feb. 5, 2018), p. 2440. ISSN: 2045-2322. DOI: `10.1038/s41598-018-20754-x` (cit. on p. 3).

[55] H. Butt, K. Graf, and M. Kappl. *Physics and Chemistry of Interfaces*. Wiley, 2013. ISBN: 978-3-527-41216-7 (cit. on p. 3).

[56] J. Berthier and K. A. Brakke. *The Physics of Microdroplets*. John Wiley & Sons, Apr. 30, 2012. 556 pp. ISBN: 978-1-118-40133-0 (cit. on pp. 3, 4).

[57] J. Israelachvili. *Intermolecular and Surface Forces*. Intermolecular and Surface Forces. Elsevier Science, 2015. ISBN: 978-0-08-092363-5 (cit. on p. 4).

[58] H. Wong, C. J. Radke, and S. Morris. "The motion of long bubbles in polygonal capillaries. Part 1. Thin films." In: *Journal of Fluid Mechanics* 292 (June 1995), pp. 71–94. ISSN: 1469-7645, 0022-1120. DOI: `10.1017/S0022112095001443` (cit. on p. 4).

[59] H. Wong, C. J. Radke, and S. Morris. "The motion of long bubbles in polygonal capillaries. Part 2. Drag, fluid pressure and fluid flow." In: *Journal of Fluid Mechanics* 292 (June 1995), pp. 95–110. ISSN: 1469-7645, 0022-1120. DOI: `10.1017/S0022112095001455` (cit. on p. 4).

[60] K. A. Brakke. "The Surface Evolver." In: *Experimental Mathematics* 1.2 (Jan. 1992), pp. 141–165. ISSN: 1058-6458. DOI: `10.1080/10586458.1992.10504253` (cit. on p. 4).

[61] S. Jakiela et al. "Discontinuous Transition in a Laminar Fluid Flow: A Change of Flow Topology inside a Droplet Moving in a Micron-Size Channel." In: *Physical Review Letters* 108.13 (Mar. 2012), p. 134501. DOI: `10.1103/PhysRevLett.108.134501` (cit. on p. 5).

[62] K. S. Elvira et al. "Materials and methods for droplet microfluidic device fabrication." In: *Lab on a Chip* 22.5 (Mar. 1, 2022), pp. 859–875. ISSN: 1473-0189. DOI: `10.1039/D1LC00836F` (cit. on p. 5).

[63] M. Jang, C. K. Park, and N. Y. Lee. "Modification of polycarbonate with hydrophilic / hydrophobic coatings for the fabrication of microdevices." In: *Sensors and Actuators B: Chemical* 193 (Mar. 31, 2014), pp. 599–607. ISSN: 0925-4005. DOI: `10.1016/j.snb.2013.11.121` (cit. on pp. 5, 13).

[64] B. Subramanian et al. "Surface Modification of Droplet Polymeric Microfluidic Devices for the Stable and Continuous Generation of Aqueous Droplets." In: *Langmuir : the ACS journal of surfaces and colloids* 27.12 (June 21, 2011), pp. 7949–7957. ISSN: 0743-7463. DOI: `10.1021/la200298n` (cit. on p. 5).

[65] J.-C. Baret. "Surfactants in droplet-based microfluidics." In: *Lab on a Chip* 12.3 (Jan. 10, 2012), pp. 422–433. ISSN: 1473-0189. DOI: `10.1039/C1LC20582J` (cit. on p. 5).

[66] E. Ruckenstein. "Microemulsions, Macroemulsions, and the Bancroft Rule." In: *Langmuir* 12.26 (Jan. 1, 1996), pp. 6351–6353. ISSN: 0743-7463. DOI: `10.1021/la960849m` (cit. on p. 5).

[67] D. J. Beebe, G. A. Mensing, and G. M. Walker. "Physics and applications of microfluidics in biology." In: *Annual Review of Biomedical Engineering* 4 (2002), pp. 261–286. ISSN: 1523-9829. DOI: `10.1146/annurev.bioeng.4.112601.125916` (cit. on p. 5).

[68] W.-L. Chou et al. "Recent Advances in Applications of Droplet Microfluidics." In: *Micromachines* 6.9 (Sept. 2015), pp. 1249–1271. DOI: `10.3390/mi6091249` (cit. on p. 5).

[69] T. S. Kaminski, O. Scheler, and P. Garstecki. "Droplet microfluidics for microbiology: techniques, applications and challenges." In: *Lab on a Chip* 16.12 (June 7, 2016), pp. 2168–2187. ISSN: 1473-0189. DOI: `10.1039/C6LC00367B` (cit. on p. 5).

[70] S. Narayan et al. "Insights into the Microscale Coalescence Behavior of Surfactant-Stabilized Droplets Using a Microfluidic Hydrodynamic Trap." In: *Langmuir* 36.33 (Aug. 25, 2020), pp. 9827–9842. ISSN: 0743-7463. DOI: `10.1021/acs.langmuir.0c01414` (cit. on p. 5).

[71] J.-C. Baret et al. *Kinetic Aspects of Emulsion Stabilization by Surfactants: A Microfluidic Analysis*. Mar. 18, 2009. (Visited on 06/07/2021) (cit. on p. 5).

[72] M. Fukuyama et al. "Controlling water transport between micelles and aqueous microdroplets during sample enrichment." In: *Analytica Chimica Acta* 1149 (Mar. 8, 2021), p. 338212. ISSN: 1873-4324. DOI: `10.1016/j.aca.2021.338212` (cit. on p. 5).

[73] H. Manikantan and T. M. Squires. "Surfactant dynamics: hidden variables controlling fluid flows." In: *Journal of Fluid Mechanics* 892 (June 2020), P1. ISSN: 0022-1120, 1469-7645. DOI: `10.1017/jfm.2020.170` (cit. on p. 5).

[74] L. G. Leal. *Advanced Transport Phenomena: Fluid Mechanics and Convective Transport Processes*. Cambridge Series in Chemical Engineering. Cambridge: Cambridge University Press, 2007. ISBN: 978-0-521-84910-4. DOI: `10.1017/CBO9780511800245` (cit. on p. 5).

[75] Z. Y. Luo, X. L. Shang, and B. F. Bai. "Marangoni effect on the motion of a droplet covered with insoluble surfactant in a square microchannel." In: *Physics of Fluids* 30.7 (July 2018), p. 077101. ISSN: 1070-6631. DOI: `10.1063/1.5026874` (cit. on p. 5).

[76] P. Gruner et al. "Stabilisers for water-in-fluorinated-oil dispersions: Key properties for microfluidic applications." In: *Current Opinion in Colloid & Interface Science* 20.3 (June 1, 2015), pp. 183–191. ISSN: 1359-0294. DOI: `10.1016/j.cocis.2015.07.005` (cit. on p. 5).

[77] Y. Chen and C. S. Dutcher. "Size dependent droplet interfacial tension and surfactant transport in liquid–liquid systems, with applications in shipboard oily bilgewater emulsions." In: *Soft Matter* 16.12 (Mar. 25, 2020), pp. 2994–3004. ISSN: 1744-6848. DOI: `10.1039/C9SM01892A` (cit. on p. 5).

[78] X. B., N. N. -T., and W. T. N. "Droplet Coalescence in Microfluidic Systems." In: *Micro and Nanosystems* 3.2 (June 30, 2011), pp. 131–136 (cit. on pp. 5, 8, 16).

[79] S. Bashir et al. "Dynamic wetting in microfluidic droplet formation." In: *BioChip Journal* 8.2 (June 1, 2014), pp. 122–128. ISSN: 2092-7843. DOI: `10.1007/s13206-014-8207-y` (cit. on p. 5).

[80] N. Shardt et al. "How Surfactants Affect Droplet Wetting on Hydrophobic Microstructures." In: *The Journal of Physical Chemistry Letters* 10.23 (Dec. 5, 2019), pp. 7510–7515. DOI: `10.1021/acs.jpclett.9b02802` (cit. on p. 5).

[81] C. Yao et al. "Two-phase flow and mass transfer in microchannels: A review from local mechanism to global models." In: *Chemical Engineering Science* 229 (Jan. 16, 2021), p. 116017. ISSN: 0009-2509. DOI: `10.1016/j.ces.2020.116017` (cit. on pp. 5, 8).

[82] S. Jakiela et al. "Speed of flow of individual droplets in microfluidic channels as a function of the capillary number, volume of droplets and contrast of viscosities." In: *Lab on a Chip* 11.21 (Sept. 2011), pp. 3603–3608. DOI: `10.1039/C1LC20534J` (cit. on p. 5).

[83] S. Ma et al. "On the flow topology inside droplets moving in rectangular microchannels." In: *Lab on a Chip* 14.18 (Aug. 11, 2014), pp. 3611–3620. ISSN: 1473-0189. DOI: `10.1039/C4LC00671B` (cit. on p. 5).

[84] M. (Li et al. "Flow topology and its transformation inside droplets traveling in rectangular microchannels." In: *Physics of Fluids* 32.5 (May 2020), p. 052009. ISSN: 1070-6631. DOI: `10.1063/5.0004549` (cit. on p. 5).

[85] Y. Jun Kang and S.-J. Lee. "Blood viscoelasticity measurement using steady and transient flow controls of blood in a microfluidic analogue of Wheastone-bridge channel." In: *Biomicrofluidics* 7.5 (Sept. 1, 2013), p. 054122. DOI: 10.1063/1.4827355 (cit. on p. 6).

[86] J. Zhou and I. Papautsky. "Viscoelastic microfluidics: progress and challenges." In: *Microsystems & Nanoengineering* 6.1 (Dec. 14, 2020), pp. 1–24. ISSN: 2055-7434. DOI: 10.1038/s41378-020-00218-x (cit. on p. 6).

[87] G. K. Batchelor. *An Introduction to Fluid Dynamics*. Cambridge University Press, Feb. 28, 2000. 662 pp. ISBN: 978-0-521-66396-0 (cit. on p. 6).

[88] F. M. White and J. Majdalani. *Viscous fluid flow*. Vol. 3. McGraw-Hill New York, 2006 (cit. on p. 6).

[89] S. P. Sutera and R. Skalak. "The History of Poiseuille's Law." In: *Annual Review of Fluid Mechanics* 25.1 (1993), pp. 1–20. DOI: 10.1146/annurev.fl.25.010193.000245 (cit. on p. 6).

[90] K. W. Oh et al. "Design of pressure-driven microfluidic networks using electric circuit analogy." In: *Lab on a Chip* 12.3 (Feb. 7, 2012), pp. 515–545. ISSN: 1473-0189. DOI: 10.1039/c2lc20799k (cit. on pp. 6, 10).

[91] S. Jakiela. "Measurement of the hydrodynamic resistance of microdroplets." In: *Lab on a Chip* 16.19 (2016), pp. 3695–3699. DOI: 10.1039/C6LC00854B (cit. on p. 6).

[92] A. M. Pit, M. H. G. Duits, and F. Mugele. "Droplet Manipulations in Two Phase Flow Microfluidics." In: *Micromachines* 6.11 (Nov. 2015), pp. 1768–1793. DOI: 10.3390/mi6111455 (cit. on pp. 6, 8).

[93] P. Zhu and L. Wang. "Passive and active droplet generation with microfluidics: a review." In: *Lab on a Chip* 17.1 (Dec. 20, 2016), pp. 34–75. ISSN: 1473-0189. DOI: 10.1039/C6LC01018K (cit. on pp. 6, 7).

[94] P. Garstecki, H. Stone, and G. Whitesides. "Mechanism for flow-rate controlled breakup in confined geometries: A route to monodisperse emulsions." In: 94.16 (Apr. 2005), p. 164501 (cit. on p. 6).

[95] P. Garstecki et al. "Formation of droplets and bubbles in a microfluidic T-junction-scaling and mechanism of break-up." In: *Lab. Chip* 6.3 (2006), pp. 437–446 (cit. on p. 6).

[96] S. L. Anna, N. Bontoux, and H. A. Stone. "Formation of dispersions using "flow focusing" in microchannels." In: *Applied Physics Letters* 82.3 (Jan. 20, 2003), pp. 364–366. ISSN: 0003-6951. DOI: 10.1063/1.1537519 (cit. on p. 6).

[97] X. Sun et al. "Dynamics of droplet breakup and formation of satellite droplets in a microfluidic T-junction." In: *Chemical Engineering Science* 188 (Oct. 12, 2018), pp. 158–169. ISSN: 0009-2509. DOI: 10.1016/j.ces.2018.05.027 (cit. on p. 6).

[98]   C. Cramer, P. Fischer, and E. J. Windhab. "Drop formation in a co-flowing ambient fluid." In: *Chemical Engineering Science* 59.15 (Aug. 1, 2004), pp. 3045–3058. ISSN: 0009-2509. DOI: `10.1016/j.ces.2004.04.006` (cit. on p. 6).

[99]   E. Castro-Hernández et al. "Scaling the drop size in coflow experiments." In: *New Journal of Physics* 11.7 (July 2009), p. 075021. ISSN: 1367-2630. DOI: `10.1088/1367-2630/11/7/075021` (cit. on p. 6).

[100]   W. Postek, T. S. Kaminski, and P. Garstecki. "A passive microfluidic system based on step emulsification allows the generation of libraries of nanoliter-sized droplets from microliter droplets of varying and known concentrations of a sample." In: *Lab on a Chip* 17.7 (Apr. 7, 2017), pp. 1323–1331. ISSN: 1473-0197. DOI: `10.1039/c7lc00014f` (cit. on p. 6).

[101]   A. Dewandre et al. "Microfluidic droplet generation based on non-embedded co-flow-focusing using 3D printed nozzle." In: *Scientific Reports* 10.1 (Dec. 10, 2020), p. 21616. ISSN: 2045-2322. DOI: `10.1038/s41598-020-77836-y` (cit. on p. 7).

[102]   R. Shih et al. "Flow-focusing regimes for accelerated production of monodisperse drug-loadable microbubbles toward clinical-scale applications." In: *Lab on a Chip* 13.24 (Nov. 12, 2013), pp. 4816–4826. ISSN: 1473-0189. DOI: `10.1039/C3LC51016F` (cit. on p. 7).

[103]   M. Duran et al. "Microcapsule production by droplet microfluidics: A review from the material science approach." In: *Materials & Design* 223 (Nov. 1, 2022), p. 111230. ISSN: 0264-1275. DOI: `10.1016/j.matdes.2022.111230` (cit. on p. 7).

[104]   K. Churski, J. Michalski, and P. Garstecki. "Droplet on demand system utilizing a computer controlled microvalve integrated into a stiff polymeric microfluidic device." In: *Lab. Chip* 10.4 (2010), pp. 512–518 (cit. on pp. 7, 8).

[105]   L. Derzsi, T. S. Kaminski, and P. Garstecki. "Antibiograms in five pipetting steps: precise dilution assays in sub-microliter volumes with a conventional pipette." In: *Lab on a Chip* 16.5 (Feb. 23, 2016), pp. 893–901. ISSN: 1473-0189. DOI: `10.1039/C5LC01151E` (cit. on p. 8).

[106]   H. Zhou and S. Yao. "A facile on-demand droplet microfluidic system for lab-on-a-chip applications." In: *Microfluidics and Nanofluidics* 16.4 (Apr. 1, 2014), pp. 667–675. ISSN: 1613-4990. DOI: `10.1007/s10404-013-1268-8` (cit. on p. 8).

[107]   V. B. Varma et al. "Droplet Merging on a Lab-on-a-Chip Platform by Uniform Magnetic Fields." In: *Scientific Reports* 6.1 (Nov. 28, 2016), p. 37671. ISSN: 2045-2322. DOI: `10.1038/srep37671` (cit. on p. 8).

[108]   X. Niu et al. "Pillar-induced droplet merging in microfluidic circuits." In: *Lab on a Chip* 8 (2008), p. 1837. ISSN: 1473-0197, 1473-0189. DOI: `10.1039/b813325e` (cit. on p. 8).

[109] N. Bremond, A. R. Thiam, and J. Bibette. "Decompressing Emulsion Droplets Favors Coalescence." In: *Physical Review Letters* 100.2 (Jan. 15, 2008), p. 024501. ISSN: 0031-9007, 1079-7114. DOI: `10.1103/PhysRevLett.100.024501` (cit. on p. 8).

[110] J. Park et al. "On-demand acoustic droplet splitting and steering in a disposable microfluidic chip." In: *Lab on a Chip* 18.3 (Jan. 30, 2018), pp. 422–432. ISSN: 1473-0189. DOI: `10.1039/C7LC01083D` (cit. on p. 8).

[111] X. Wang, Z. Liu, and Y. Pang. "Droplet breakup in an asymmetric bifurcation with two angled branches." In: *Chemical Engineering Science* 188 (Oct. 12, 2018), pp. 11–17. ISSN: 0009-2509. DOI: `10.1016/j.ces.2018.05.003` (cit. on pp. 8, 9).

[112] D. Wong and C. L. Ren. "Microfluidic droplet trapping, splitting and merging with feedback controls and state space modelling." In: *Lab on a Chip* 16.17 (Aug. 16, 2016), pp. 3317–3329. ISSN: 1473-0189. DOI: `10.1039/C6LC00626D` (cit. on p. 8).

[113] I. U. Chowdhury, P. Sinha Mahapatra, and A. K. Sen. "Self-driven droplet transport: Effect of wettability gradient and confinement." In: *Physics of Fluids* 31.4 (Apr. 1, 2019), p. 042111. ISSN: 1070-6631. DOI: `10.1063/1.5088562` (cit. on p. 8).

[114] H.-D. Xi et al. "Active droplet sorting in microfluidics: a review." In: *Lab on a Chip* 17.5 (Feb. 28, 2017), pp. 751–771. ISSN: 1473-0189. DOI: `10.1039/C6LC01435F` (cit. on pp. 8, 9).

[115] G. Katsikis, J. S. Cybulski, and M. Prakash. "Synchronous universal droplet logic and control." In: *Nature Physics* 11.7 (July 2015), pp. 588–596. ISSN: 1745-2481. DOI: `10.1038/nphys3341` (cit. on pp. 8, 10).

[116] P. Abbyad et al. "Rails and anchors: guiding and trapping droplet microreactors in two dimensions." In: *Lab on a Chip* 11.5 (2011), pp. 813–821. DOI: `10.1039/C0LC00104J` (cit. on p. 8).

[117] M. G. Simon et al. "A Laplace pressure based microfluidic trap for passive droplet trapping and controlled release." In: *Biomicrofluidics* 6.1 (Feb. 2012), p. 014110. DOI: `10.1063/1.3687400` (cit. on p. 8).

[118] R. Dangla, S. Lee, and C. N. Baroud. "Trapping Microfluidic Drops in Wells of Surface Energy." In: *Physical Review Letters* 107.12 (Sept. 15, 2011), p. 124501. DOI: `10.1103/PhysRevLett.107.124501` (cit. on p. 8).

[119] M. A. Murran and H. Najjaran. "Capacitance-based droplet position estimator for digital microfluidic devices." In: *Lab on a Chip* 12.11 (May 8, 2012), pp. 2053–2059. ISSN: 1473-0189. DOI: `10.1039/C2LC21241B` (cit. on p. 8).

[120] A. Agarwal. "Digital Microfluidics: Techniques, Their Applications and Advantages." In: *Journal of Bioengineering & Biomedical Science* 03.3 (2013). ISSN: 21559538. DOI: `10.4172/2155-9538.S8-001` (cit. on p. 9).

[121] J. Lee et al. "Electrowetting and electrowetting-on-dielectric for microscale liquid handling." In: *Sensors and Actuators A: Physical*. Papers from the Proceedings of the 14th

IEEE Internat. Conf. on MicroElectroMechanical Systems 95.2 (Jan. 1, 2002), pp. 259–268. ISSN: 0924-4247. DOI: 10.1016/S0924-4247(01)00734-8 (cit. on p. 9).

[122] W. Engl et al. "Droplet Traffic at a Simple Junction at Low Capillary Numbers." In: *Physical Review Letters* 95.20 (Nov. 11, 2005), p. 208304. DOI: 10.1103/PhysRevLett.95.208304 (cit. on p. 9).

[123] F. Jousse et al. "Bifurcation of droplet flows within capillaries." In: *Physical Review E* 74.3 (Sept. 29, 2006), p. 036311. DOI: 10.1103/PhysRevE.74.036311 (cit. on p. 9).

[124] M. Schindler and A. Ajdari. "Droplet traffic in microfluidic networks: A simple model for understanding and designing." In: *Physical Review Letters* 100.4 (Jan. 2008), p. 044501. DOI: 10.1103/PhysRevLett.100.044501 (cit. on p. 9).

[125] O. Cybulski and P. Garstecki. "Dynamic memory in a microfluidic system of droplets traveling through a simple network of microchannels." In: *Lab on a Chip* 10.4 (2010), pp. 484–493. DOI: 10.1039/B912988J (cit. on p. 9).

[126] D. R. Link et al. "Geometrically Mediated Breakup of Drops in Microfluidic Devices." In: *Physical Review Letters* 92.5 (Feb. 2004), p. 054503. DOI: 10.1103/PhysRevLett.92.054503 (cit. on p. 9).

[127] L. Ménétrier-Deremble and P. Tabeling. "Droplet breakup in microfluidic junctions of arbitrary angles." In: *Physical Review E* 74.3 (Sept. 14, 2006), p. 035303. ISSN: 1539-3755, 1550-2376. DOI: 10.1103/PhysRevE.74.035303 (cit. on p. 9).

[128] L. Salkin et al. "Passive breakups of isolated drops and one-dimensional assemblies of drops in microfluidic geometries: experiments and models." In: *Lab on a Chip* 13.15 (2013), pp. 3022–3032. DOI: 10.1039/C3LC00040K (cit. on p. 9).

[129] D. A. Hoang et al. "Dynamics of droplet breakup in a T-junction." In: *Journal of Fluid Mechanics* 717 (Feb. 2013). ISSN: 0022-1120, 1469-7645. DOI: 10.1017/jfm.2013.18 (cit. on p. 9).

[130] Y. Chen and Z. Deng. "Hydrodynamics of a droplet passing through a microfluidic T-junction." In: *Journal of Fluid Mechanics* 819 (2017), pp. 401–434. DOI: 10.1017/jfm.2017.181 (cit. on p. 9).

[131] X. Wang, Z. Liu, and Y. Pang. "Breakup dynamics of droplets in an asymmetric bifurcation by muPIV and theoretical investigations." In: *Chemical Engineering Science* 197 (2019), pp. 258–268. ISSN: 0009-2509. DOI: 10.1016/j.ces.2018.12.030 (cit. on p. 9).

[132] M. Baig et al. "Engineering droplet navigation through tertiary-junction microchannels." In: *Microfluidics and Nanofluidics* 20.12 (Dec. 1, 2016), p. 165. ISSN: 1613-4982, 1613-4990. DOI: 10.1007/s10404-016-1828-9 (cit. on p. 9).

[133] T. Franke et al. "Surface acoustic wave (SAW) directed droplet flow in microfluidics for PDMS devices." In: *Lab on a Chip* 9.18 (2009), pp. 2625–2627. DOI: 10.1039/B906819H (cit. on p. 9).

[134] J.-C. Baret et al. "Fluorescence-activated droplet sorting (FADS): efficient microfluidic cell sorting based on enzymatic activity." In: *Lab on a Chip* 9.13 (2009), pp. 1850–1858. DOI: 10.1039/B902504A (cit. on p. 9).

[135] K. Zhang et al. "On-chip manipulation of continuous picoliter-volume superparamagnetic droplets using a magnetic force." In: *Lab on a Chip* 9.20 (2009), pp. 2992–2999. DOI: 10.1039/B906229G (cit. on p. 9).

[136] A. R. Abate, J. J. Agresti, and D. A. Weitz. "Microfluidic sorting with high-speed single-layer membrane valves." In: *Applied Physics Letters* 96.20 (2010), p. 203509. DOI: 10.1063/1.3431281 (cit. on p. 9).

[137] J. B. Geddes et al. "Bistability in a simple fluid network due to viscosity contrast." In: *Physical Review E* 81.4 (Apr. 2010), p. 046316 (cit. on p. 9).

[138] D. J. Case et al. "Braess's paradox and programmable behaviour in microfluidic networks." In: *Nature* 574.7780 (2019), pp. 647–652. ISSN: 1476-4687. DOI: 10.1038/s41586-019-1701-6 (cit. on p. 9).

[139] S. Battat, D. A. Weitz, and G. M. Whitesides. "Nonlinear Phenomena in Microfluidics." In: *Chemical Reviews* 122.7 (Apr. 13, 2022), pp. 6921–6937. ISSN: 0009-2665, 1520-6890. DOI: 10.1021/acs.chemrev.1c00985 (cit. on pp. 9, 10).

[140] O. Cybulski, P. Garstecki, and B. A. Grzybowski. "Oscillating droplet trains in microfluidic networks and their suppression in blood flow." In: *Nature Physics* 15.7 (July 2019), pp. 706–713. ISSN: 1745-2481. DOI: 10.1038/s41567-019-0486-8 (cit. on p. 10).

[141] S.-S. Li and C.-M. Cheng. "Analogy among microfluidics, micromechanics, and microelectronics." In: *Lab on a Chip* 13.19 (Aug. 28, 2013), pp. 3782–3788. ISSN: 1473-0189. DOI: 10.1039/C3LC50732G (cit. on p. 10).

[142] A. Adamatzky. "A brief history of liquid computers." In: *Philosophical Transactions of the Royal Society of London. Series B, Biological Sciences* 374.1774 (2019), p. 20180372. ISSN: 1471-2970. DOI: 10.1098/rstb.2018.0372 (cit. on p. 10).

[143] M. Prakash and N. Gershenfeld. "Microfluidic bubble logic." In: *Science* 315.5813 (2007), pp. 832–835. ISSN: 0036-8075. DOI: 10.1126/science.1136907 (cit. on p. 10).

[144] L. F. Cheow, L. Yobas, and D.-L. Kwong. "Digital microfluidics: Droplet based logic gates." In: *Applied Physics Letters* 90.5 (Jan. 29, 2007), p. 054107. ISSN: 0003-6951. DOI: 10.1063/1.2435607 (cit. on p. 10).

[145] M. W. Toepke, V. V. Abhyankar, and D. J. Beebe. "Microfluidic logic gates and timers." In: *Lab on a Chip* 7.11 (Oct. 25, 2007), pp. 1449–1453. ISSN: 1473-0189. DOI: 10.1039/B708764K (cit. on p. 10).

[146] K. Azizbeigi, M. Zamani Pedram, and A. Sanati-Nezhad. "Microfluidic-based processors and circuits design." In: *Scientific Reports* 11.1 (May 26, 2021), p. 10985. ISSN: 2045-2322. DOI: 10.1038/s41598-021-90485-z (cit. on p. 10).

[147] M. Zagnoni and J. M. Cooper. "A microdroplet-based shift register." In: *Lab on a Chip* 10.22 (Oct. 27, 2010), pp. 3069–3073. ISSN: 1473-0189. DOI: `10.1039/C0LC00219D` (cit. on p. 10).

[148] A. Baccouche et al. "Massively parallel and multiparameter titration of biochemical assays with droplet microfluidics." In: *Nature Protocols* 12.9 (Sept. 2017), pp. 1912–1932. ISSN: 1750-2799. DOI: `10.1038/nprot.2017.092` (cit. on p. 10).

[149] P. Jarujamrus et al. "Acid–base titration using a microfluidic thread-based analytical device (µTAD)." In: *Analyst* 145.13 (June 29, 2020), pp. 4457–4466. ISSN: 1364-5528. DOI: `10.1039/D0AN00522C` (cit. on p. 10).

[150] K. Churski et al. "Rapid screening of antibiotic toxicity in an automated microdroplet system." In: *Lab on a Chip* 12.9 (Apr. 2012), pp. 1629–1637. ISSN: 1473-0189. DOI: `10.1039/C2LC21284F` (cit. on p. 10).

[151] D.-P. Chen et al. "Micro-Droplet Platform for Exploring the Mechanism of Mixed Field Agglutination in B3 Subtype." In: *Biosensors* 11.8 (Aug. 16, 2021), p. 276. ISSN: 2079-6374. DOI: `10.3390/bios11080276` (cit. on p. 10).

[152] S. Makulska, S. Jakiela, and P. Garstecki. "A micro-rheological method for determination of blood type." In: *Lab on a Chip* 13.14 (2013), pp. 2796–2801. DOI: `10.1039/C3LC40790J` (cit. on p. 10).

[153] J. D. Tice et al. "Formation of Droplets and Mixing in Multiphase Microfluidics at Low Values of the Reynolds and the Capillary Numbers." In: *Langmuir* 19.22 (Oct. 1, 2003), pp. 9127–9133. ISSN: 0743-7463. DOI: `10.1021/la030090w` (cit. on p. 11).

[154] J. Wegrzyn et al. "Microfluidic architectures for efficient generation of chemistry gradations in droplets." In: *Microfluid. Nanofluidics* 14.1 (Aug. 2012), pp. 235–245 (cit. on p. 11).

[155] B. Bhattacharjee and S. A. Vanapalli. "Electrocoalescence based serial dilution of microfluidic droplets." In: *Biomicrofluidics* 8.4 (July 1, 2014), p. 044111. DOI: `10.1063/1.4891775` (cit. on p. 11).

[156] S. Bhattacharjee et al. "Efficient Generation of Dilution Gradients With Digital Microfluidic Biochips." In: *IEEE Transactions on Computer-Aided Design of Integrated Circuits and Systems* 38.5 (May 2019), pp. 874–887. ISSN: 1937-4151. DOI: `10.1109/TCAD.2018.2834413` (cit. on p. 11).

[157] K. Totlani et al. "Scalable microfluidic droplet on-demand generator for non-steady operation of droplet-based assays." In: *Lab on a Chip* 20.8 (Apr. 14, 2020), pp. 1398–1409. ISSN: 1473-0189. DOI: `10.1039/C9LC01103J` (cit. on p. 11).

[158] P. N. Nge, C. I. Rogers, and A. T. Woolley. "Advances in Microfluidic Materials, Functions, Integration and Applications." In: *Chemical reviews* 113.4 (Apr. 10, 2013), pp. 2550–2583. ISSN: 0009-2665. DOI: `10.1021/cr300337x` (cit. on p. 13).

[159]   K. Ren, J. Zhou, and H. Wu. "Materials for Microfluidic Chip Fabrication." In: *Accounts of Chemical Research* 46.11 (Nov. 19, 2013), pp. 2396–2406. ISSN: 0001-4842. DOI: `10.1021/ar300314s` (cit. on p. 13).

[160]   X. Hou et al. "Interplay between materials and microfluidics." In: *Nature Reviews Materials* 2.5 (Apr. 20, 2017), pp. 1–15. ISSN: 2058-8437. DOI: `10.1038/natrevmats.2017.16` (cit. on p. 13).

[161]   C.-W. Tsao. "Polymer Microfluidics: Simple, Low-Cost Fabrication Process Bridging Academic Lab Research to Commercialized Production." In: *Micromachines* 7.12 (Dec. 2016), p. 225. ISSN: 2072-666X. DOI: `10.3390/mi7120225` (cit. on p. 13).

[162]   E. Berthier, E. W. K. Young, and D. Beebe. "Engineers are from PDMS-land, Biologists are from Polystyrenia." In: *Lab on a Chip* 12.7 (Mar. 7, 2012), pp. 1224–1237. ISSN: 1473-0189. DOI: `10.1039/C2LC20982A` (cit. on p. 13).

[163]   A.-G. Niculescu et al. "Fabrication and Applications of Microfluidic Devices: A Review." In: *International Journal of Molecular Sciences* 22.4 (Feb. 18, 2021), p. 2011. ISSN: 1422-0067. DOI: `10.3390/ijms22042011` (cit. on p. 13).

[164]   V. Mishra et al. "Experimental investigations on ultra-precision machining of polycarbonate and related issues." In: *Journal of Micromanufacturing* 4.1 (May 1, 2021), pp. 61–73. ISSN: 2516-5984. DOI: `10.1177/2516598420938495` (cit. on p. 13).

[165]   Jurgen Riegel, Werner Mayer, Yorik van Havre, et al. *FreeCAD*. Version 0.19 (cit. on p. 13).

[166]   D. Ogończyk et al. "Bonding of microfluidic devices fabricated in polycarbonate." In: *Lab on a Chip* 10.10 (May 5, 2010), pp. 1324–1327. ISSN: 1473-0189. DOI: `10.1039/B924439E` (cit. on p. 14).

[167]   G. Bradski. "The OpenCV Library." In: *Dr. Dobb's Journal of Software Tools* (2000) (cit. on p. 15).

[168]   M. Raffel, C. E. Willert, and J. Kompenhans. *Particle image velocimetry: a practical guide*. Springer, 1998. ISBN: 3-540-63683-8 (cit. on p. 15).

[169]   A. Liberzon et al. *OpenPIV/openpiv-python: OpenPIV - Python (v0.22.2) with a new extended search PIV grid option*. July 4, 2020 (cit. on p. 16).

[170]   C. Priest, S. Herminghaus, and R. Seemann. "Controlled electrocoalescence in microfluidics: Targeting a single lamella." In: *Applied Physics Letters* 89.13 (Sept. 25, 2006), p. 134101. ISSN: 0003-6951. DOI: `10.1063/1.2357039` (cit. on p. 16).

[171]   J. Schindelin et al. "Fiji: an open-source platform for biological-image analysis." In: *Nature Methods* 9.7 (July 2012), pp. 676–682. ISSN: 1548-7105. DOI: `10.1038/nmeth.2019` (cit. on p. 16).

[172]   P. Virtanen et al. "SciPy 1.0: Fundamental Algorithms for Scientific Computing in Python." In: *Nature Methods* 17 (2020), pp. 261–272. DOI: `10.1038/s41592-019-0686-2` (cit. on p. 16).

[173] J. Reback et al. *pandas-dev/pandas: Pandas 1.0.3*. Mar. 18, 2020. DOI: `10.5281/zenodo.3715232` (cit. on p. 16).

[174] C. R. Harris et al. "Array programming with NumPy." In: *Nature* 585.7825 (Sept. 2020), pp. 357–362. DOI: `10.1038/s41586-020-2649-2` (cit. on p. 16).

[175] K. T. M. Han and B. Uyyanonvara. "A Survey of Blob Detection Algorithms for Biomedical Images." In: *2016 7th International Conference of Information and Communication Technology for Embedded Systems (IC-ICTES)*. 2016 7th International Conference of Information and Communication Technology for Embedded Systems (IC-ICTES). Mar. 2016, pp. 57–60. DOI: `10.1109/ICTEmSys.2016.7467122` (cit. on p. 16).

[176] D. B. Allan et al. *soft-matter/trackpy: Trackpy v0.5.0*. Apr. 13, 2021 (cit. on p. 16).

[177] J. C. Crocker and D. G. Grier. "Methods of Digital Video Microscopy for Colloidal Studies." In: *Journal of Colloid and Interface Science* 179.1 (Apr. 15, 1996), pp. 298–310. ISSN: 0021-9797. DOI: `10.1006/jcis.1996.0217` (cit. on p. 16).

[178] J. Illingworth and J. Kittler. "A survey of the hough transform." In: *Computer Vision, Graphics, and Image Processing* 44.1 (Oct. 1, 1988), pp. 87–116. ISSN: 0734-189X. DOI: `10.1016/S0734-189X(88)80033-1` (cit. on p. 16).

Original articles

Investigations of modular microfluidic geometries for passive manipulations on droplets

D. ZAREMBA[1], S. BLONSKI[1], M. JACHIMEK[1], M.J. MARIJNISSEN[1],
S. JAKIELA[2], and P.M. KORCZYK[1]*

[1]Institute of Fundamental Technological Research, Polish Academy of Sciences, Pawińskiego 5B St., 02-106 Warsaw, Poland
[2]Department of Biophysics, Warsaw University of Life Sciences, 159 Nowoursynowska St., Building 34, 02-776 Warsaw, Poland

Abstract. Multiple pipetting is a standard laboratory procedure resulting in the compartmentalisation of a liquid sample. Microfluidics offers techniques which can replace this process by the use of tiny droplets. Passive manipulation on droplets is an interesting and promising approach for the design of microfluidic devices which on one hand are easy-to-use and on the other, execute complex laboratory procedures. We present a comprehensive study of the geometry of microfluidic components which encode different operations on droplets into the structure of the device. The understanding of hydrodynamic interactions between the continuous flow and a droplet travelling through confined space of nontrivial microfluidic geometries is crucial for a rational and efficient design of new generation of modular microfluidic processors with embedded instructions.

Key words: microfluidics, two-phase flows, droplets.

1. Introduction

Modern analytical methods (like e.g. digital PCR) often require execution of complex algorithms on numerous compartments of a sample [1]. In this context, the microfluidic technology is highly desirable, as it offers precise handling of small amounts of liquids, allows for parallelisation, integration and automation of multiple processes in a single device [2, 3]. In particular, the use of immiscible liquids allows for generation [4] and manipulation [5] on small droplets. Droplets in microfluidic channels may be considered as isolated biochemical reactors, where each single droplet has a specific composition of reagents or biological content [6, 7]. That provides incredible opportunities for performing a large number of chemical reactions or biological experiments at the same time with very small consumption of reagents and samples [8, 9].

The ability to manipulate droplets in microfluidic devices is crucial for precise control over the composition of such micro-reactors. The current state of microfluidic technology enables to perform such operations as: droplet generation, merging, splitting, moving, positioning by the use of active controllers e.g. electromagnetic valves [9–14].

The potential of the active techniques in automation of droplet traffic control is impressive [9]. However, they require the use of multiple connections and active components such as precise valves and electronics. That increases technical complexity and the cost of the whole setup, which inhibits the application of those solutions in simple in use and inexpensive

Point of Care devices. Hence the development of such systems with a wide range of liquid handling protocols remains one of the important motivations of microfluidics. Some interesting solutions exist, e.g. paper-based microfluidics [15], slip chips [16], or geometric modules for desired operations on microdroplets [17–21]. However, the simplicity of the usage is always achieved by sacrificing accuracy, the throughput and internal complexity. In order to overcome these obstacles, the next generation of lab-on-a-chip devices may contain embedded controls on the chip instead of electronics [22, 23].

In the previous publication, Korczyk et al. [24] showed examples of passive microfluidic modules called microfluidic traps. These traps were built based on two kinds of basic geometries: obstacles and slit-bypasses. Modifications of these elements and their different combinations allowed to construct traps with such functions as i) metering prescribed volume of a droplet; ii) immobilization of a droplet; iii) combining consecutive drops. The other publication by van Steijn et al. [25] demonstrated the use of slit bypasses in a construction of so-called block-and-break droplet generator. These publications presented the potential of the new approach to the construction of functional microfluidic modules. However, there is a lack of comprehensive analysis of principal mechanisms. So far rather only intuitive remarks about the operation of selected modules have been discussed. Our recent observations showed that the behaviour of droplets in some microfluidic geometries may be counter-intuitive. Hence, the intuitive approach to the design of passive elements may cost numerous failed trials and resources. Therefore, effective applications of this technology require detailed investigations on mechanisms ruling movement of droplets in nontrivial geometries [26].

The crucial role in the understanding of those mechanisms plays the confinement of flows of two liquid phases and the

---

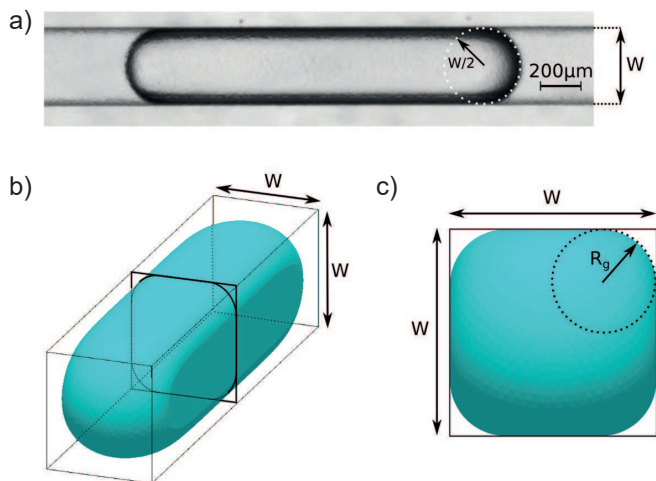*e-mail: piotr.korczyk@ippt.pan.pl

a)

b)

c)

Fig. 1. The shape of a droplet confined in the channel of a rectangular cross-section: a) a micrograph of the real droplet in the channel of the width 385 µm, b) and c) the simulation of the shape of a droplet in the square cross-section channel made by the use of Surface Evolver [27]. The empty corners (gutters) are visible with the radius of curvature of the interface $R_g = W/4$

confinement of the interface between them. This is the fascinating aspect of two phase flows in microfluidic channels. Microfluidics offers the unique situation when the height of the channel is lower than the capillary length, making gravity negligible. Droplets larger than the cross-section of the channel are squeezed between walls of the channel and form elongated plugs. If the vertical dimension of that cross-section is lower than the capillary length, the shape of a confined droplet is determined only by geometrical constrictions of the solid walls and by the Laplace-Young equation which describes the difference in the pressure sustained across the curved interface between two immiscible liquid phases:

$$\Delta p_L = \gamma \left(\frac{1}{R_1} + \frac{1}{R_2} \right) \qquad (1)$$

where γ is the coefficient of surface tension and R_1 and R_2 are principal radii of curvature. In a static droplet both pressures, inside and outside of a droplet are constant and homogeneous. Thus the Laplace pressure drop is constant over the whole interface.

In this paper we consider droplets, which do not wet the walls of the channel (contact angle equals 180°). This condition is commonly obtained by the use of surface modifications and additions of surfactants. For the simplicity of calculations we can assume that the tips of the non-wetting droplet form hemispherical caps of both principal radii equal $W/2$. Hence the Laplace pressure drop at the tips is given by: $\Delta p_{LT} = \gamma(2/W + 2/W)$ (see Fig. 1a). Further, we assume that in the internal part of a droplet, between its cups, radius of the curvature of the interface in the direction along the axis of the channel goes to infinity. Thus, the Laplace pressure in the internal part can be described as: $\Delta p_{LI} = \gamma/R_g$, where R_g is a radius of curvature for the cross-section of a droplet in the internal part. Equating above

formulas for $\Delta p_{LT} = \Delta p_{LI}$, one can obtain $R_g = W/4$. This implies that a droplet in the channel leaves the corners filled by the continuous phase. These corners, so-called gutters, form channels parallel to the droplet, through which the continuous phase can flow around a droplet [28]. This approximated shape of a droplet is confirmed by the observations and numerical simulations of a droplet squeezed in a square-shaped channel (see Fig. 1). It is worth noticing that the equilibrium shape depends only on the dimensions of the channel and is not affected by the value of γ.

In the presence of a constant flow of continuous phase in a regular channel a plug-like droplet moves with constant speed [13, 28]. In the previous paper [24], we showed that some additional geometrical components modifying the geometry of a channel can be effectively used to disturb this movement in a controlled manner.

Let us consider two kinds of geometrical components: a bypass slit and an obstacle, which put together forms the so-called metering trap. A bypass slit is a niche of the height equal to $R_g = W/4$ placed at the top of the main channel (see Fig. 2)
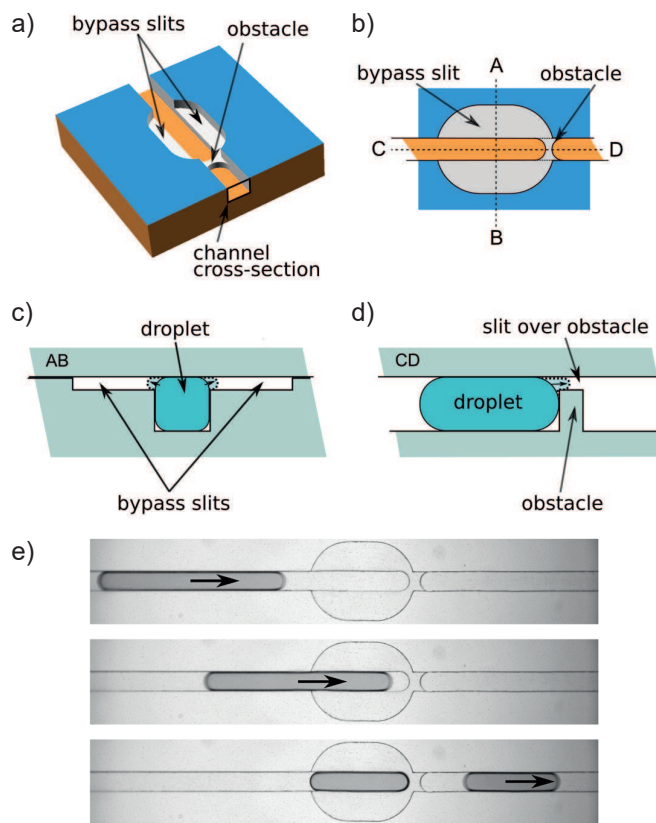

Fig. 2. The metering trap: a) 3-D visualisation of the trap with the construction elements like slit bypasses and an obstacle highlighted, b) top-view of the trap, c) and d) cross-sections through planes AB and CD as described in b). The schematic shapes of droplets in the cross-sectional picture show that the droplet needs to generate finger of the curvature much higher than the mean curvature of the static droplet to penetrate the slits of bypasses or to pass through the obstacle. e) Consecutive snapshots illustrating the main functionality of the trap. The long droplet enters a trap and is divided into two parts. One of them is immobilised in the trap, while the other one goes further

which increases the area of the cross-section of the channel. The height of the bypass equal to the radius of curvature for the interface in gutters, ensures that the shape of a static droplet is not affected by the presence of this slit. Indeed, the bypass slit is an additional narrow channel, which enlarges the gutter. Similarly, like in the regular square channel, the corners cannot be occupied by the static droplet. The role of these additional slits is to enhance the bypass flow of continuous phase.

The other geometrical element we used for the construction of our traps is an obstacle in the main channel, which locally decreases the lumen of the channel. To go across the obstacle, a droplet needs to create a tip with a higher curvature than the curvature in the rest of the channel. This means that additional pressure must be applied to let the droplet pass the barrier. As we have shown before, the combinations of traps allowed for encoding of a digital sequence of operations on droplets. This allowed for a controlled exchange of mass between droplets generating desired distributions of compound concentrations [24]. Despite the previous publication describing traps and whole complex systems of traps, there is still a lack of knowledge about their principal mechanisms. At this point, there are only some, rather intuitive remarks about the operation of traps, which allowed to design a few types of traps through trial and error. The further development of this very promising method requires detailed fundamental investigations.

Here we propose a comprehensive approach that gives insight into mechanisms which are responsible for the specific features of traps. We conducted our analysis on the example of the metering trap. We present the results of both experimental and numerical investigations and show the complex interactions between the droplet and the flow of the continuous phase altered by the confined geometry of the metering trap. The gathered knowledge is vital for the understanding of the principle of passive structures.

2. Materials and methods

The microfluidic devices were fabricated of a transparent polycarbonate plate (Bayer, Makrolon® GP, Germany) of 5 mm thickness via direct milling using a CNC milling-engraving machine (Ergwind, MFG4025P, Poland). During the milling process a polycarbonate plate was fastened to the perforated vacuum table of the CNC machine by applying underpressure (0.4 bar), generated by a vacuum pump (AGA Labor, Basic 20, Poland), which ensured the high precision of mounting of milled material in the Z axis. A 2-flute fishtail milling bit FR208 of diameter 385 μm was used for engraving the channels. For the optimization of the fabrication process, the diameter of the milling tool was set to the width of the main channel W. The half of that diameter sets the minimal radius of the curvature which can be engraved in the plane of the device. In consequence of that geometrical constraint, both faces of the obstacle must be round (with radius equal $W/2$) and concave (see Fig. 2). This shape is compatible with the round and convex shape of the tip of a droplet, which is as well determined by the width of the channel. Engraved structures were cleaned out with

a high-pressure water washer (Karcher, K7 Premium, Germany) and further washed by hand with isopropanol. In the next step, channels were closed by bonding the milled chip with another polycarbonate plate with the use of a heating press (Argenta, AW03, Poland) at a temperature of 135°C and a pressure of 0.1 bar cm^{-2}. The chip was kept in the press at high temperature for about 30 minutes, then allowed to cool down all the time under pressure. Before the bonding procedure the holes of diameter 800 μm were drilled through one of the plates to form inlets and outlet to the channels of the milled device. Pieces of cut needles of the outer diameter 800 μm (Braun, Sterican, Germany) were fixed into the inlet and outlet holes and used to enable tight connection with elastic tubing.

The n-Hexadecane 95% (Alfa Aesar, Germany) was used as the continuous phase (CP) and distilled water coloured with ink (Pelikan 4001, Germany) was used as a droplet phase (DP). The surfactant (Span-80, Fluke Analytical, Germany) was added to the n-Hexadecane with concentration of about 0.2% to avoid the wetting of the walls of channels by the droplets. The n-Hexadecane density is 0.773 g ml^{-1} and dynamic viscosity is 3.0041 mPa s at 25°C. Interfacial tension between n-Hexadecane and water is 0.0048 N m^{-1} ±0.0002 measured by the pendant drop method.

Experiments consisted mainly of visual observations of flows in fabricated transparent microfluidic devices. Liquids were pumped by precise and pulsation-free syringe pumps (neMESYS, Cetoni GmbH) equipped with 1.0 ml syringes made of borosilicate glass with a PTFE plunger (ILS Innovative Labor Systeme GmbH). Syringes were connected with the microfluidic device using polyethylene tubing with inner and outer diameter equal to 0.76 mm and 1.22 mm, respectively (Intramedic®, Becton Dickinson Co.). Droplets are created with the use of a T-junction geometry. The flow rate of the CP was 0.75 ml h^{-1} both for droplet creation and its displacement.

Flows investigated in the microfluidic device were visualised using a Huvitz HSZ-645TR stereoscope equipped with 0.5× objective and IDS UI-3274-LE-C-HQ digital camera. Recorded images were stored on a PC computer for further analysis.

Velocity field of the flow of the CP through the trap was determined using particle image velocimetry technique (PIV) [29, 30]. The analysed flow was seeded by glass spheres (tracer particles) with a diameter of 12 μm and density similar to the liquids, to minimise buoyancy effects. Images were registered using the pco.1200hs high speed digital camera (PCO Imaging) and Nikon Eclipse E-50i microscope equipped with an 10×/0.3 objective (Nikon LU Plan Fluor). Characteristics of the recording system provided 519.5 pixel/mm resolution of the captured images. The recording framerate was set to 100–200 fps (depending on the flow velocity) to ensure the displacement of the tracer particles in the range of 10–15 pixels between sequential frames. The appropriately short exposure time (100 μs) prevented blurring of the images of tracer particles due to their motion. The evaluation of images was performed using the commercial software VidPIV (ILA GmbH). To obtain instantaneous velocity fields, cross-correlation was applied with the interrogation window 128×128 pixels and spatial window separation equal to 32 pixels in both directions, X and Y. After

this preliminary evaluation, a local median velocity filter was applied to compare each vector with a median of the nearest neighbours (i±2) and errors were removed. Filtered out wrong vectors were replaced with vectors determined as an interpolated value of neighbours (i±2). In the second, final step of evaluation, adaptive cross-correlation (interrogation window equal to 128×128 pixels and spatial window separation equal to 16 pixels in both directions) and a local median filter were applied. As a result we obtain more than 1000 instantaneous velocity fields for the whole process of droplet flow through the trap.

We used the Multiskan Go Microplate Spectrophotometer (Thermo Scientific) to measure the absorbance of the mixture collected in the PMMA UV cuvettes (BRAND, Germany) with a minimum filling volume of 1.5 ml. The quantity was measured directly with the use of the spectrophotometer was absorbance, which according to the Beer–Lambert law is proportional to concentration. So the ratio of flows was estimated directly as the ratio of absorbance measurements. This makes the estimation independent from possible fluctuations of starting concentration. In all presented experiments we used as an indicator sodium pyruvate (Sigma-Aldrich, Germany) in aqueous solution with starting concentration $C_0 = 100$ mmol l^{-1}. As the buffer liquid we used distilled water.

For the numerical analysis of the motion of droplets, the volume-of-fluid (VOF) model [31] implemented in ANSYS Fluent was used to simulate the interactions between two liquid phases. This technique uses the finite volume method to solve the Navier-Stokes equations with an additional volume fraction function α, which takes 0 for one of the phases, and 1 for the other. Th evolution of the interface is introduced by the transport equation:

$$\frac{\partial \alpha}{\partial t} + \nabla \cdot (\mathbf{u}\alpha) = 0, \tag{2}$$

where $\mathbf{u}$ – fluid velocity vector. The density and viscosity of the fluid are obtained as:

$$\rho = \alpha\rho_1 + (1 - \alpha)\rho_2, \tag{3}$$

$$\mu = \alpha\mu_1 + (1 - \alpha)\mu_2. \tag{4}$$

The remaining equations are the incompressible Navier-Stokes equations:

$$\nabla \cdot \mathbf{u} = 0, \tag{5}$$

$$\frac{\partial \rho\mathbf{u}}{\partial t} + \nabla \cdot (\rho\mathbf{u}\mathbf{u}) = -\nabla p + \nabla \cdot \left[\mu\left(\nabla\mathbf{u} + \nabla\mathbf{u}^{\mathbf{T}}\right)\right] + \\ + \gamma \frac{pk\mathbf{n}}{\frac{1}{2}(\rho_1 + \rho_2)}, \tag{6}$$

where p – pressure and t – time. The last term in the momentum equation refers to the surface tension. In it γ, k and $\mathbf{n}$ represent the surface tension coefficient, the curvature and the surface

normal, respectively. A variable time stepping method was used allowing the time step to be changed between 1×10^{-7} s and 1×10^{-4} s, predominantly the time step oscillated around 1.5×10^{-5} s. To ensure correct representation of the droplet shape and its movement, the computational mesh should have at least 20×20 regular elements in the cross-section of the central channel, in the plane perpendicular to the droplet movement. This leads to the entire domain, showed in Fig. 3, consisting of 275,302 finite volumes. The use of a rarer mesh would cause interface dispersion.
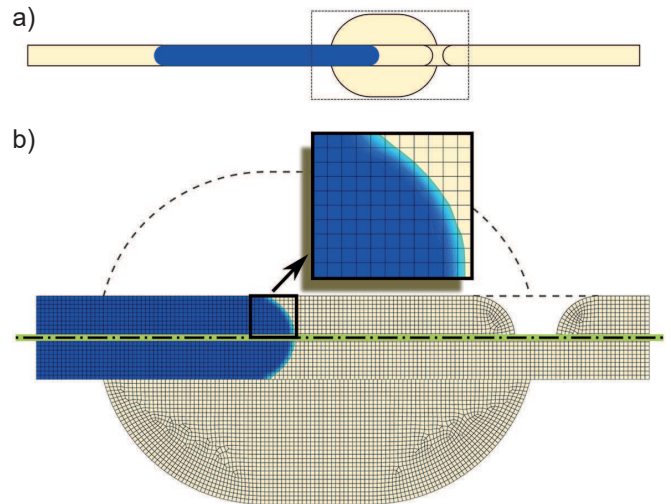

Fig. 3. The mesh used in the simulations. a) an overview of the whole domain with a droplet inside. b) close-up on the trap itself. The composition of two horizontal cross-sections of the simulation mesh taken at two different heights. The top part – at half of the height of the domain (below the bypasses, the obstacle visible), the bottom part – at half of the height of the bypasses (the obstacle invisible). The colours represent the volume fraction of the droplet (blue = droplet). The inset – magnification of the interface of the droplet

3. Results

3.1. Experimental observations of kinetics. Herein we present the experimental analysis of two distinguished examples of flow of droplets through the metering trap. In the first one, we considered a short droplet (of the length not longer than the length of a trap L_T, see Fig. 4). In the other case, we investigated the flow of a long droplet (of the length longer than L_T, see Fig. 5). In both cases, we used the same metering trap. The flow of a droplet was driven by the flow of CP pumped into the microfluidic device with a constant flow rate $Q_C = 0.75$ ml h^{-1}. It is worth noting that the use of syringe pumps ensured the constant flow rate regardless of fluctuations of pressure generated by the droplet travelling through the trap. Before the experiments, droplets had been formed in the T-junction by the injection of the desired volume of droplet phase followed by the switching on of the continuous phase's flow.
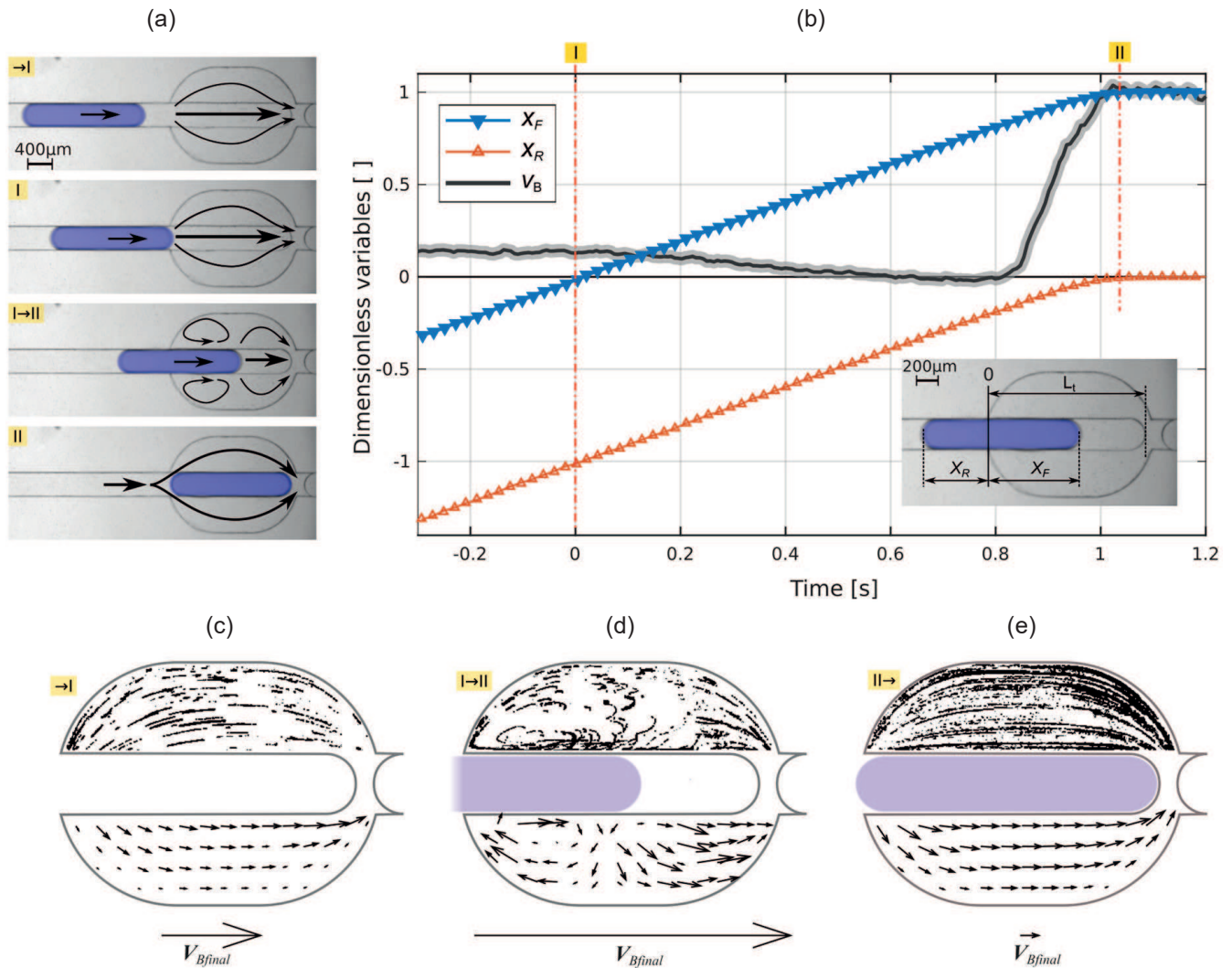
Fig. 4. The kinetics of the flow in the case of a short droplet entering the metering trap. a) Consecutive snapshots showing the moving droplet in different stages and the schematic reconstruction of the flow pattern of continuous phase. b) The measurement of the main kinetic quantities: x_F – position of the front of the droplet, x_R – position of the back of the droplet, v_B – average velocity of the CP in the bypass slit. The estimated errors of measurements of v_B displayed as the accompanying wide grey line. The errors of other quantities were of the order of widths of the displayed lines. c) – e) Experimental visualization of flow patterns in the bypasses in different stages: c) – period →I and stage I, d) period I→II, e) stage II and period II→. The top bypasses – traces of particles, the bottom bypasses – velocity fields measured by PIV. Note different scaling of vectors in the visualisation of different stages. For comparison, the same vector of the constant length V_{Bfinal} is displayed below in the scale of the corresponding velocity field

3.1.1. A short droplet case. The previous observations showed that a droplet which the length is not longer than the internal length of the trap L_T becomes immobilised in the metering trap [24]. This process is illustrated in the snapshots (Fig. 4a). We can see that first the droplet approaches the trap from the left side driven by the constant flow of the CP and finally stops in the trap regardless the fact that the flow of the CP is still the same.

For a better understanding of the spontaneous transition from the initially unsteady flow to finally steady flow, we conducted a series of observations of the kinetics. The quantitative description of the process is provided by the conducted measurements. By the use of high-speed cameras and image processing, we measured the position of the front of a droplet X_F and the positions of its back X_R in time. Simultaneously we measured the velocity field in the bypasses with the use of the PIV technique. In the plot we present the normalised variables: $x_F = X_F/L_T$, $x_R = X_R/L_T$. The value V_B was obtained by spatial averaging of the component of the velocity field parallel to the main channel in the bypasses. Then the normalised value v_B was calculated dividing V_B by V_{Bfinal} – the time average of V_B for a stationary flow after the droplet finally stops in the trap. In this final configuration the V_B reaches its maximum value, hence the maximum level of $v_B = V_B/V_{Bfinal}$ is approximately equal to unity.

On the base of measurements the process can be disassembled into three particular periods with two critical stages between them: stage I, when the front of the droplet reaches the entrance of the trap ($x_F = 0$) and stage II, when the front of the droplet reaches the obstacle ($x_F = 1$). At stage II the front of the droplet stops at the obstacle. In this moment, due to the short length of the droplet equal (or shorter) to the length of the trap L_T, the whole droplet is inside the trap: the front of the droplet touches the obstacle ($x_F = 1$) and its back ($x_R <= 0$) opens the entrance to the bypasses for the flow of the CP. After that, the flow of the CP around the immobilised droplet becomes stationary.

Our observations showed that before a droplet enters the trap (stage → I) it moves with a constant speed and the observed flow in the bypasses is as well constant. Between stage I and stage II the droplet enters into the trap. The flow in the bypasses decreases. This means that the droplet efficiently blocks the inflow of the CP into the bypasses. Once the front of the droplet reaches the barrier ($x_F = 1$) the droplet stops and v_B reaches its maximum value. After stage II the flow becomes stationary, where the droplet is immobilised in the trap and the entire flow of the CP flows around the droplet through the bypasses.

These observations show the interactions between the flows of the two phases in the confined geometry of the trap. Until stage I the flow of the CP in the trap is stationary with the main flow through the central channel and a minor flow passing through the bypasses. In the period between stage I and stage II the droplet effectively switches off the CP flow through the bypasses. It is worth noting, that the flow topology of this period differs from that of other periods. The significant distinction is the presence of additional single circulation zones in each of the bypasses appearing behind the line marking the front of the droplet (see Fig. 4a and d). While the droplet continuously moves forward, the circulation zone (with zero average velocity) enlarges. The consequence of that is the gradual fall of the average velocity in the bypass v_B (see Fig. 4b). After stage II the back of the droplet stops in such a position, that opens a way for the CP into the bypasses and the flow of the CP around the droplet becomes mainly unidirectional and much larger than before stage I. This trap construction utilizes the barrier to hold the droplet in place. It is possible because the viscous pressure drop (due to the flow of the CP around the droplet) is smaller than the capillary breakthrough pressure (required to move the droplet across the barrier).

3.1.2. A long droplet case. In this case we consider the movement of a droplet of the length $2L_T$ – a double length of the trap. We analyzed the kinetics of the process, likewise as in the previous example, measuring such variables as: x_F, x_R and v_B (see the inset in Fig. 5a). Unlike as for a short droplet, in the case of the long one, we observed that the droplet temporarily expands penetrating the slits of the device (Fig. 5b). To take that into account we introduced two additional measured variables W_N and W_I. W_N is the width of the so-called neck (see the inset in Fig. 5a). The neck forms when a droplet is passing across the barrier. It is a liquid bridge connecting two parts of

the droplet on two sides of the barrier. The plotted value of the width of the neck was normalized by the width of the channel: $w_N = W_N/W$. W_I is the width of the side intrusions of a droplet penetrating into the bypasses. The value plotted in Fig. 5a was calculated by averaging the width of intrusions from both sides of a droplet and normalised by W_B – the width of the bypass: $w_I = W_I/W_B$.

On the base of observations and the evolution of measured variables we distinguished 7 critical stages of the process, that we describe below. In stage I the front of the droplet reaches the entrance to the trap ($x_F = 0$). In stage II the tip of the droplet reaches the obstacle ($x_F = 1$). Within the period (I–II) the droplet blocks the flow of the continuous phase to the bypasses, what can be observed in the measurements of v_B. Until stage II the case of the long droplet is similar to the case of the shorter droplet. Just after stage II the front of the droplet is held by the obstacle ($x_F = const = 1$), while the back (in the inlet channel) is still effectively pushed by the flow of the CP. The squeezed droplet is forced to penetrate the bypasses, which is marked by the rise of w_I. In stage III we observe the critical point, where the continuously pushed droplet starts to penetrate the slit over the obstacle (rise of x_F). During the period III → IV, the front of a droplet ($x_F > 1$) starts to move passing across the obstacle and developing the neck ($w_N > 0$). In stage IV both the width of the neck w_N and the intrusions to the bypasses w_I reach their maximum values. The front of the droplet has passed the obstacle and starts to move with a constant speed in the outlet channel (linear growth of x_F).

Stage V – the back of the droplet reaches the entrance to the trap ($x_R = 0$) and allows the CP access to the bypasses. The force pushing the back of the droplet drops rapidly and the back of the droplet stops ($x_R = const = 0$). After stage V the intrusions of the droplet in the bypasses (w_I) recede and are being replaced by an incoming flow of the CP. This generates the flow of the DP through the obstacle inflating the part of the droplet at the front. In stage VI the droplet neck starts shrinking (w_N decreases) and finally breaks in stage VII ($w_N = 0$). This results in the division of the droplet into two separate parts. One of them is kept immobilised in the trap and the rest of the droplet continues the movement with a constant speed.

These observations of kinetics show that the confined flow of both phases directly depends on the current position of both the front x_F and the back x_R of a droplet. The different stages with the different morphology of flow fields are triggered respectively to the position of a droplet relative to the geometry of a trap. Hence the length of a droplet and the geometry of a trap are crucial for the functionality of a trap and their behaviour can be tailored by the proper use of different elements.

Better insight into the dynamics of this process can be provided by numerical simulations, as presented in the next subsection.

3.2. Volume of fluid simulation. We performed numerical simulations of the partitioning process of the long droplet (double of the length of a trap L_T) in the metering trap. The simulation domain consisted of a complete 3D geometry of the trap identical to the design used in the experiments. The input and
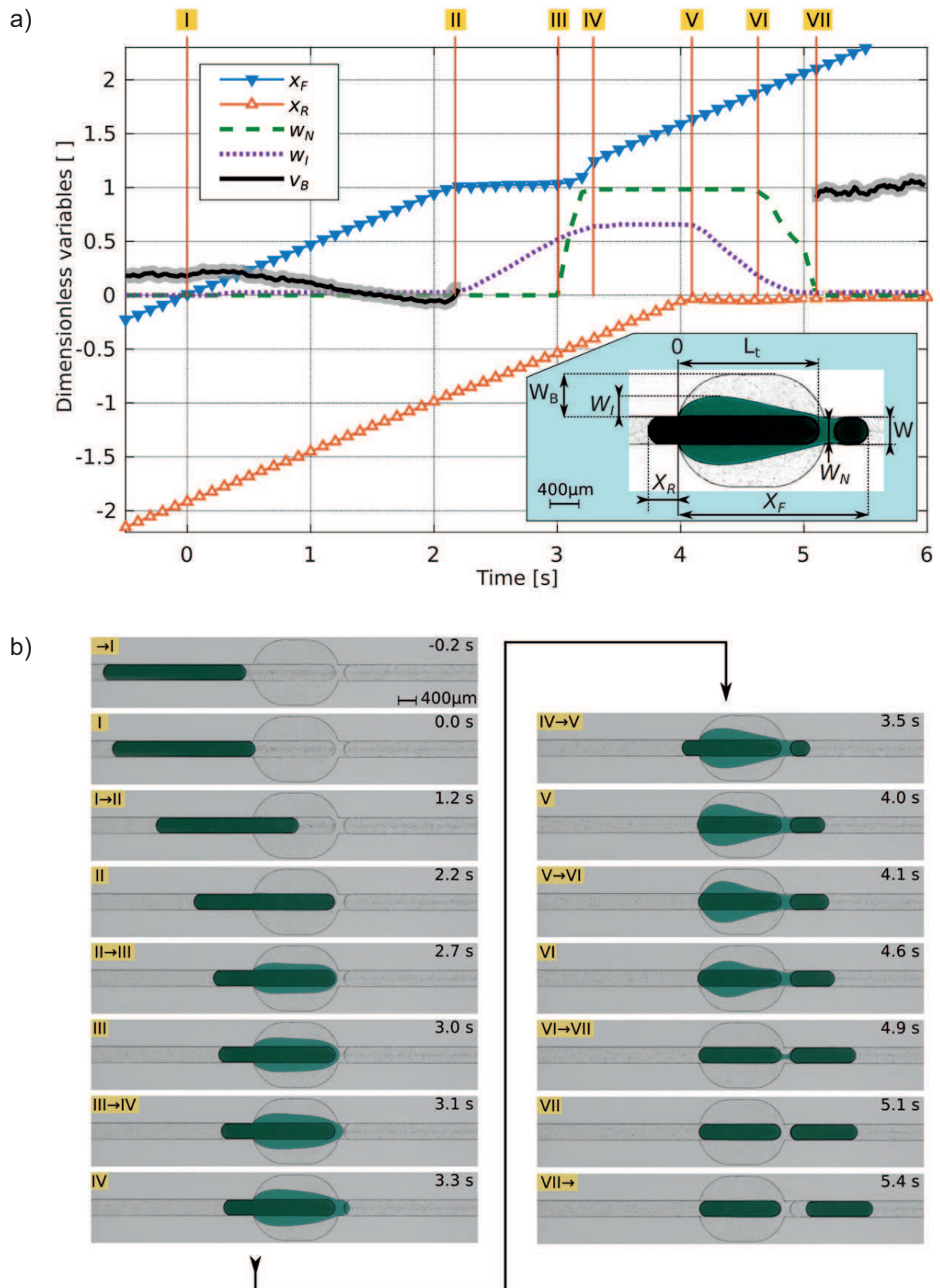
Fig. 5. The analysis of the kinetics in the case of the passage of a long droplet through the metering trap: a) the time plot of measured kinetic characteristics as shown in the inset; v_B – average velocity of the CP in the bypass slit. The estimated errors of measurements of v_B displayed as the accompanying wide grey line. The errors of other quantities were of the order of widths of displayed lines. b) consecutive snapshots recorded during experimental observation

output channels in the simulations, on the one hand, they were shortened to minimize the size of the domain and optimize the computation time, on the other hand, were sufficiently long to enable the observation of the whole investigated process with all the critical stages. The simulation domain is shown in snapshots in Fig. 6b. The constant rate of flow of the CP was fixed at the inlet of the device, what simulate the use of syringe pumps in experiments.

The numerical simulations reveal the same main feature of the metering trap as observed in the experiments. A droplet is partitioned into two parts, where one of them is immobilized in the trap. The comparison of snapshots from simulation and experiments reveals some quantitative differences visible in shapes of the bypass intrusions in stages from III to V (compare snapshots in Fig. 5b and Fig. 6b). They were caused by the imperfections introduced during the fabrication process of the real device. During the bonding, the high temperature and pressure caused the slight collapse of bypasses in the central region of the trap. So the extent of intrusion of the real droplet in the central part of bypasses is lower than in the case of the simulation. Regardless those discrepancies between experiment and simulations, we can distinguish in both situations the same stages of the process. What is more important by the mean of simulations we can analyze the evolution of the pressure in the inlet of the computational domain. In the system driven by a constant flow-rate, the pressure may evolve due to the changes of the hydraulic resistance of the flow. Fig. 6a presents the evolution of the pressure difference Δp between the inlet and the outlet of the device.

The pressure starts to grow very fast after stage II. We can see in Fig. 6a that the period II → III can be divided into two distinct parts with different pressure rise rates. We interpret the first part as the fast build-up of the breakthrough pressure required for the penetration of the slit. In order, to penetrate the narrow slit a droplet needs to develop the interface with the radius of curvature equal to half of the height of the slit (see the inset with the cross-section of the trap in Fig. 6a. In the second part, during the expansion of the droplet into the bypasses the curvature of the interface grows only in the horizontal plane (curvature and its changes are much lower than in the vertical plane), which results in a much lower slope, which is illustrated in the corresponding inset in Fig. 6a.

Between stage III and stage IV, the pressure grows fast and reaches its maximum value. That jump of pressure corresponds to the breakthrough pressure for the obstacle. In the period III → IV the droplet develops the neck and then, in the period V → VI, grows behind the barrier. Once the neck breaks in stage VII the pressure grows again reaching the terminal level. The terminal pressure is higher than before the entrance of the droplet into the trap. This fact can be explained by the change of the geometry of the flow of the CP through the trap. The trapped droplet occupies the central part of the trap forcing the CP to flow entirely through the bypasses. The hydraulic resistance of such restricted flow of the CP is higher than the resistance of the empty trap. It is very interesting and worth noticing that the pressure after the break-up of a droplet is even higher than the pressure during the process of the pumping of a droplet through the obstacle (V → VI).

To understand this fact we should consider the whole process again. During the periods II → IV the pressure is increased and the part of the work exerted on the deformation of a droplet is accumulated in the potential energy of shape deformation. From stage IV to VI this energy is recovered during the process of receding of the droplet from the slits of the bypasses.
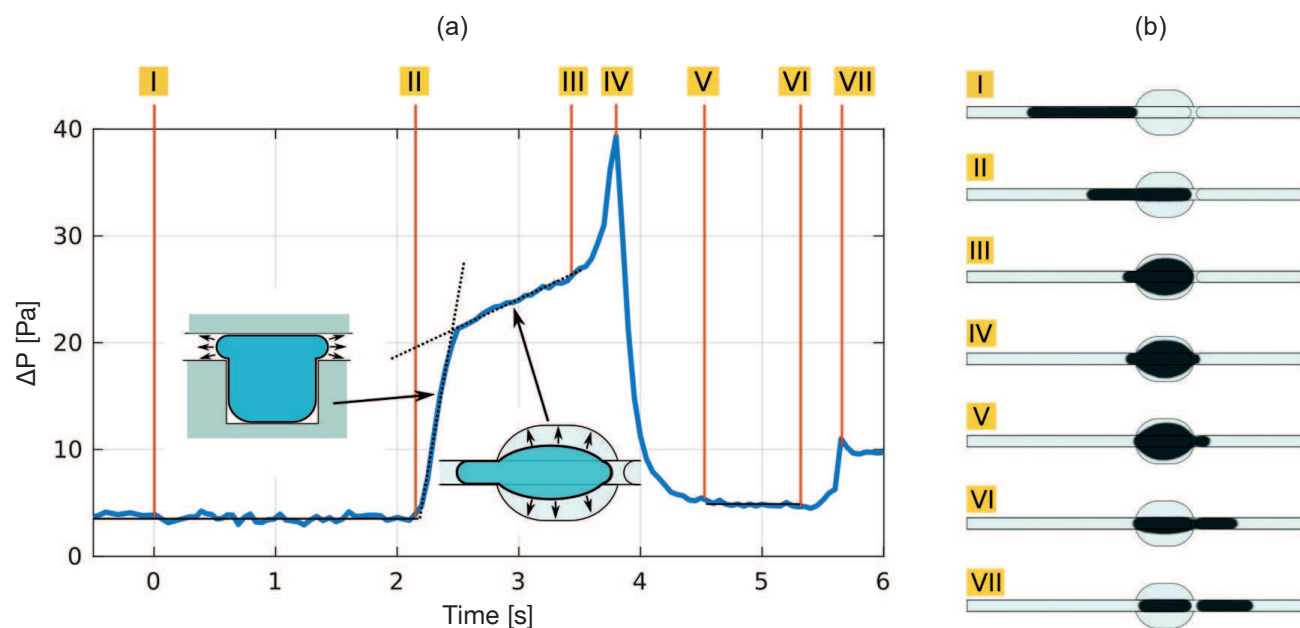

Fig. 6. Results of numerical simulations of the process of a droplet passage through the metering trap: a) time plot of pressure difference Δp along the device, b) top view of the simulation domain with a contour of the droplet in distinguished stages
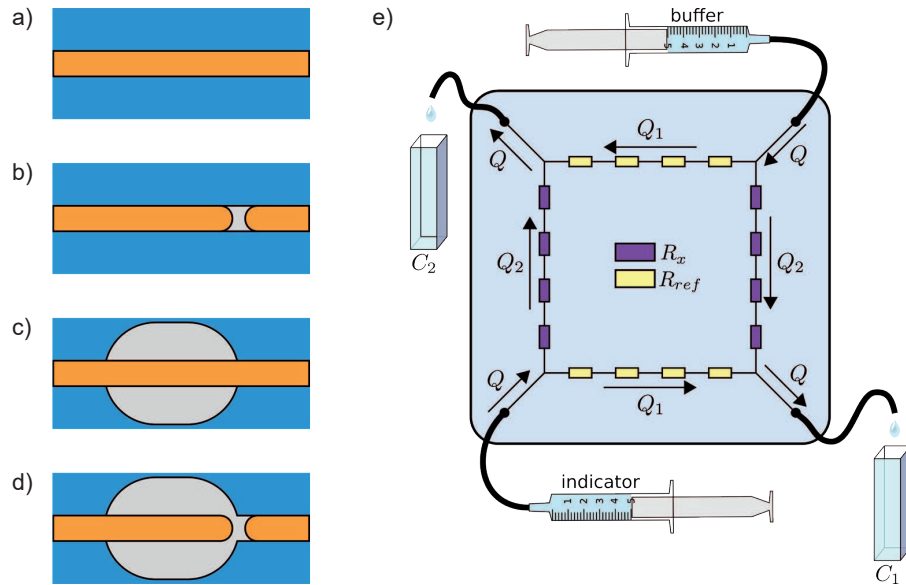
Fig. 7. The measurement method of hydraulic resistance: a) the reference channel, b) the channel only with obstacle, c) the channel only with bypass, d) the channel with full metering trap, e) the device used to measurement of hydraulic resistance

3.3. Measurements of the hydraulic resistance. As we showed in the previous paper [24], the most promising perspective for the application of traps is to use multiple of them in specially designed combinations. Such modular architectures can create integrated circuits with embedded algorithms. The design procedure of such complex microfluidic networks usually utilizes the so-called electric circuit analogy [32]. In this approach, the distribution of flow between junctions of the microfluidic network is predicted by the use of the equivalent electric circuits where each part of the network is characterized by a constant parameter – the hydraulic resistance R.

That resistance describes the relationship between the flow-rate Q and the pressure difference along the fluidic element:

$$R = \Delta p / Q. \tag{7}$$

For a Hagen-Poiseuille flow through a regular channel the resistance is a function of the dynamic viscosity μ, the length of the channel L and its cross-sectional area A:

$$R = \frac{\alpha \mu L}{A^2} \tag{8}$$

where α is a dimensionless geometrical correction factor, which depends on the shape of the cross-section of the channel [33].

The resistance of irregular elements such as the microfluidic traps can be estimated via the numerical simulations [34] or measurements [35, 36]. The numerical simulations seem to be a most convenient tool, however, it is often very difficult to include all imperfections of the fabrication procedure as well as the material properties [34]. Hence the measurements of the hydraulic resistance of irregular elements are of high importance. According to the equation, it can be done by the measurement of

the pressure difference Δp. However, the integration of pressure sensors with the device is technically challenging [35] and the accuracy of this method is limited by a relatively low pressure drop generated by microfluidic elements and the sensitivity of sensors. The alternative method presented by Choi et al. [36] consists of microscopic observations of the interface between parallel flows in a specially designed device.

In this paper, we present our original approach towards the estimation of the resistance. The advantage of the proposed method is the use of the spectrophotometric measurements of the concentration of the indicator dye in a microfluidic device consisting of the investigated resistance and the reference resistance. The main part of the resistance comparator constitutes of a rectangle with replicated resistive elements (Fig. 7e). Each side of the rectangle consists of a number of reproduced and serially connected elements of the same geometry. The opposite sides of the rectangle are identical. One pair of the opposite sides consists of the replicated geometry of unknown resistance R_x, while the other pair consists of the replicated reference geometry of resistance R_{ref}. The reference geometry was just the regular rectangular channel (see Fig. 7a). We investigated the resistances of three different geometries: i) a channel with an obstacle (Fig. 7b), ii) a channel with bypasses (Fig. 7c), and iii) the complete metering trap (Fig. 7d). The first two geometries were the components of the metering trap so that we could analyze resistances of them separately. As showed in Fig. 7a–d each single fluidic module consisted of the channel of the length equal to ten widths of the channel W. Such modules were replicated in the test device.

Two inlets to each device were placed in the opposite corners of the rectangle. Importantly, one of the inputs was fed with the clear buffer, while the other one with the solution of the buffer and the indicator. Two outputs of the device were placed

in the other pair of diagonal corners. Thus the device posses the symmetry concerning the rotation by an angle of 180°.

In order to obtain the same symmetry of flows, we took care to ensure the uniform conditions at both inlets, as well as uniform conditions at both outlets. If all these conditions are satisfied the input streams of equal flow rates Q are divided at the input junctions in the same proportions, each of them into two flows Q_1 and Q_2. Then they meet at the outputs so that the flow Q_2 of the buffer mixes with the flow of the indicator Q_1 in the right bottom corner (relative to the Fig. 7c). In the opposite corner, the flow of buffer Q_1 mixes with the flow of indicator Q_2. The output concentration of the indicator in both outputs C_1 and C_2 are simply given by ratios of flows:

$$C_1 = C_0 \frac{Q_1}{Q}, \tag{9}$$

$$C_2 = C_0 \frac{Q_2}{Q}, \tag{10}$$

where C_0 is the initial concentration of the indicator introduced into the inlet of the device. The equation 7 implies:

$$n_1 R_{ref} = \Delta p_1/Q_1, \tag{11}$$

$$n_2 R_x = \Delta p_2/Q_2, \tag{12}$$

where n_1 and n_2 are the numbers of replicated resistive elements. Δp_1 and Δp_2 are the pressure drops along two types of sides of the internal rectangle of the device. Due to the symmetry of flows, pressures at both inlet corners are equal as well as pressures at both output corners are equal, so: $\Delta p_1 = \Delta p_2$. If $n_1 = n_2$ (in our case $n_1 = n_2 = 4$), solving equations 9–12 we obtain the ratio of resistances given by the following equation:

$$\frac{R_x}{R_{ref}} = \frac{Q_1}{Q_2} = \frac{C_1}{C_2}. \tag{13}$$

Equation 13 implies that the measurements of relative resistance requires only measurements of concentrations of the indicator C_1, and C_2. Due to that fact, the experimental procedure for estimation of the resistance is relatively simple. During the measurements both liquids were pumped with the same flow rates $Q = 5$ ml h^{-1} by the use of syringe pumps. After flushing the channels for 3–5 min and eliminating the bubbles to stabilize the flow, 1.5 ml of the solutions were collected in two UV spectrophotometric cuvettes via tubing of equal lengths. The collecting cuvettes were placed at the same level, which ensured equal pressure at both outlets. In order to reduce evaporation and changes in the concentration of the liquids the cuvettes were closed at the end of every experiments. After that the measurements of concentration from each cuvete were performed by the use of a spectrophotometer. Measurements were repeated at least 3 times and the averaged results with standard deviation calculated for each series are presented in Table 1.

Table 1
Measurements of the relative resistance R_x/R_{ref} for selected microfluidic geometries: the obstacle, the bypass and the metering trap (see Fig. 7b–d)

	obstacle only (b)	bypass only (c)	metering trap (d)
R_x/R_{ref}	2.15	0.939	2.17
standard deviation	0.02	0.003	0.01

The results showed the intriguing fact that the addition of slit-bypasses to the channel does not change significantly the resistance despite of the increase of the cross-section. In the case of the obstacle, on the contrary, even short obstacle, introduces a significant rise of resistance. The advantage of the above proposed method is the simplicity of the whole procedure. As the spectrophotometer is a very common instrumentation, hence this method can be widely available for the researchers working on microfluidics.

We performed additional numerical simulations for the metering trap obtaining a value of 1.74 for the relative resistance of the metering trap. It is significantly lower than the value of 2.17 obtained in the experiments. This discrepancy can be explained by the discussed before deformation of a real device caused mainly by the bonding procedure. The fabricated device is slightly collapsed, what we observed during the investigation of the motion of droplets. In the result the resistance of the fabricated device is higher than the design. This shows that although the numerical simulations are very valuable for the investigations of the principal mechanisms, the more reliable characteristics of real systems can be achieved in the course of experiments.

4. Conclusions

In this paper, we presented the comprehensive analysis of the movement of a droplet through the complex microfluidic geometry – the metering trap. We utilised a set of such tools as image processing based measurements of kinetic properties, PIV measurements of velocity fields, the Volume Of Fluid simulations and measurements of hydraulic resistance. Those tools, coupled together, provide the detailed description of the interactions between two immiscible liquid phases altered by the geometry of the trap. The above analysis was conducted on the example of the metering trap, however, it can be adapted to other geometries. The detailed analysis shows the rich complexity of the flow of a droplet confined by solid walls. As we expected, during the flow of that droplet through traps structures the bypasses are activated or deactivated depending on the actual position of a droplet. That mechanism can be used in triggering specific operation on droplets as merging, splitting or trapping. Combinations of such operations enable the design of microfluidic architectures with embedded algorithms. The understanding of the mechanisms investigated in this paper is crucial for the optimisation of hydrodynamic traps and effective design of new modules with additional desired features.

References

[1] F. Shen, B. Sun, J.E. Kreutz, E.K. Davydova, W. Du, P.L. Reddy, L.J. Joseph, and R.F. Ismagilov, "Multiplexed Quantification of Nucleic Acids with Large Dynamic Range Using Multivolume Digital RT-PCR on a Rotational SlipChip Tested with HIV and Hepatitis C Viral Load", *Journal of the American Chemical Society* 133 (44), 17705–17712 (2011)

[2] G.M. Whitesides, "The origins and the future of microfluidics", Nature 442 (7101), 368–373 (2006)

[3] S.-Y. Teh, R. Lin, L.-H. Hung, and A.P. Lee, "Droplet microfluidics", Lab on a Chip 8 (2), 198 (2008)

[4] P. Garstecki, A. Ganan-Calvo, and G. Whitesides, "Formation of bubbles and droplets in microfluidic systems", *Bull. Pol. Ac.: Tech.* 53 (4), 361 – 372 (2005)

[5] A.M. Pit, M.H.G. Duits, and F. Mugele, "Droplet Manipulations in Two Phase Flow Microfluidics", *Micromachines* 6 (11), 1768–1793 (2015)

[6] H. Song, D.L. Chen, and R.F. Ismagilov, "Reactions in Droplets in Microfluidic Channels", *Angewandte Chemie International Edition* 45 (44), 7336–7356 (2006)

[7] A.B. Theberge, F. Courtois, Y. Schaerli, M. Fischlechner, C. Abell, F. Hollfelder, and W.T.S. Huck, "Microdroplets in Microfluidics: An Evolving Platform for Discoveries in Chemistry and Biology", *Angewandte Chemie International Edition* 49 (34), 5846–5868 (2010)

[8] K. Churski, T.S. Kaminski, S. Jakiela, W. Kamysz, W. Baranska-Rybak, D.B. Weibel, and P. Garstecki, "Rapid screening of antibiotic toxicity in an automated microdroplet system", *Lab on a Chip* 12 (9), 1629–1637 (2012)

[9] S. Jakiela, T.S. Kaminski, O. Cybulski, D.B. Weibel, and P. Garstecki, "Bacterial Growth and Adaptation in Microdroplet Chemostats", *Angewandte Chemie International Edition* 52 (34), 8908–8911 (2013)

[10] S. Zeng, B. Li, X. Su, J. Qin, and B. Lin, "Microvalve-actuated precise control of individual droplets in microfluidic devices", *Lab on a Chip* 9 (10), 1340–1343 (2009)

[11] B.-C. Lin and Y.-C. Su, "On-demand liquid-in-liquid droplet metering and fusion utilizing pneumatically actuated membrane valves", *Journal of Micromechanics and Microengineering* 18 (11), 115005 (2008)

[12] K. Churski, P. Korczyk, and P. Garstecki, "High-throughput automated droplet microfluidic system for screening of reaction conditions", *Lab on a Chip* 10 (7), 816–818 (2010)

[13] S. Jakiela, S. Makulska, P.M. Korczyk, and P. Garstecki, "Speed of flow of individual droplets in microfluidic channels as a function of the capillary number, volume of droplets and contrast of viscosities", *Lab on a Chip* 11 (21), 3603–3608 (2011)

[14] H.-H. Jeong, B. Lee, S.H. Jin, S.-G. Jeong, and C.-S. Lee, "A highly addressable static droplet array enabling digital control of a single droplet at pico-volume resolution", *Lab on a Chip* 16 (9), 1698–1707 (2016)

[15] A.W. Martinez, S.T. Phillips, G.M. Whitesides, and E. Carrilho, "Diagnostics for the Developing World: Microfluidic Paper-Based Analytical Devices", *Analytical Chemistry* 82 (1), 3–10 (2010)

[16] W. Du, L. Li, K.P. Nichols, and R.F. Ismagilov, "SlipChip", *Lab on a Chip* 9 (16), 2286–2292 (2009)

[17] X. Niu, S. Gulati, J. B. Edel, and A.J. deMello, "Pillar-induced droplet merging in microfluidic circuits", *Lab on a Chip* 8, 1837 (2008)

[18] M. Zagnoni and J.M. Cooper, "A microdroplet-based shift register", *Lab on a Chip* 10 (22), 3069–3073 (2010)

[19] X. Niu, F. Gielen, J.B. Edel, and A.J. deMello, "A microdroplet dilutor for high-throughput screening", *Nature Chemistry* 3 (6), 437–442 (2011)

[20] C. Chung, M. Lee, K. Char, K.H. Ahn, and S.J. Lee, "Droplet dynamics passing through obstructions in confined microchannel flow", *Microfluidics and Nanofluidics* 9 (6), 1151–1163 (2010), wOS:000284335800013

[21] M. Sun, S.S. Bithi, and S.A. Vanapalli, "Microfluidic static droplet arrays with tuneable gradients in material composition", *Lab on a Chip* 11 (23), 3949 (2011)

[22] M. Prakash and N. Gershenfeld, "Microfluidic Bubble Logic", *Science* 315 (5813), 832–835 (2007)

[23] B. Mosadegh, T. Bersano-Begey, J.Y. Park, M.A. Burns, and S. Takayama, "Next-generation integrated microfluidic circuits", *Lab on a Chip* 11 (17), 2813 (2011)

[24] P.M. Korczyk, L. Derzsi, S. Jakieła, and P. Garstecki, "Microfluidic traps for hard-wired operations on droplets", *Lab on a Chip* 13 (20), 4096–4102 (2013)

[25] V. van Steijn, P.M. Korczyk, L. Derzsi, A.R. Abate, D.A. Weitz, and P. Garstecki, "Block-and-break generation of microdroplets with fixed volume", *Biomicrofluidics* 7 (2), 024108– 024108–8 (2013)

[26] D. Zaremba, S. Blonski, and P. Korczyk, "Experimental analysis of modular microfluidic geometries for passive manipulations on droplets", *Book of abstracts, 5th Conference on Nanoand Micromechanics, Wrocław 2017* 180–182 (2017)

[27] K.A. Brakke, "The Surface Evolver", *Experimental Mathematics* 1 (2), 141–165 (1992)

[28] S. Jakiela, P.M. Korczyk, S. Makulska, O. Cybulski, and P. Garstecki, "Discontinuous Transition in a Laminar Fluid Flow: A Change of Flow Topology inside a Droplet Moving in a Micron-Size Channel", *Physical Review Letters* 108 (13), 134501 (2012)

[29] M. Raffel, C.E. Willert, and J. Kompenhans, Particle image velocimetry: a practical guide, Springer (1998)

[30] S. Blonski, P. Korczyk, and T. Kowalewski, "Analysis of turbulence in a micro-channel emulsifier", *International Journal of Thermal Sciences* 46, 1126–1141 (2007)

[31] I. Kataoka, "Local instant formulation of two-phase flow", *International Journal of Multiphase Flow* 12 (5), 745–758 (1986)

[32] K.W. Oh, K. Lee, B. Ahn, and E.P. Furlani, "Design of pressure-driven microfluidic networks using electric circuit analogy", *Lab on a Chip* 12 (3), 515–545 (2012)

[33] N.A. Mortensen, F. Okkels, and H. Bruus, "Reexamination of Hagen-Poiseuille flow: Shape dependence of the hydraulic resistance in microchannels", *Physical Review E* 71 (5), 057301 (2005)

[34] K.C. Bhargava, B. Thompson, D. Iqbal, and N. Malmstadt, "Predicting the behavior of microfluidic circuits made from discrete elements", *Scientific Reports* 5 (2015)

[35] D. Kim, N.C. Chesler, and D.J. Beebe, "A method for dynamic system characterization using hydraulic series resistance", *Lab on a Chip* 6 (5), 639–644 (2006)

[36] S. Choi, M.G. Lee, and J.-K. Park, "Microfluidic parallel circuit for measurement of hydraulic resistance", *Biomicrofluidics* 4 (3), 034110 (2010)

RESEARCH PAPER

Fixing the direction of droplets in a bifurcating microfluidic junction

Damian Zaremba[1] · Slawomir Blonski[1] · Michal J. Marijnissen[1] · Piotr M. Korczyk[1]

Abstract

We present a novel type of microfluidic bifurcating junctions which fixes the droplet's route. Unlike in regular junctions, where a droplet chooses one of two outputs depending on the (often instantaneous) flow distribution, our modifications direct droplets only to one preferred outlet. As we show, this solution works properly regardless of the variations of flow distribution in a wide range of its amplitude. Such modified junctions allow for the encoding of the droplet's traffic in the geometry of the device. We compare in a series of experiments different junctions having channels of uniform square cross section. Our observations revealed that a small, local modification of the junction in the form of an additional shallow slit imposes a significant consequence for the flow of droplets at an entire microfluidic network's scale. Another interesting and helpful feature of these new junctions is that they keep the integrity of long droplets, unlike regular junctions, which tend to split long droplets. Our experimental investigations revealed a complex transformation of the long droplet during its transfer through the modified junction. We show that this transformation resembles the Baker's transform and can be used for the enhancement of mixing inside the droplets. Finally, we show two examples of microfluidic devices where the deterministic character of these modified junctions is utilized to obtain new, non-trivial functionalities. This approach can be used for the engineering of microfluidic devices with embedded procedures replacing active elements like valves or magnetic/electric fields.

1 Introduction

Microfluidic networks create very unique environments for droplets. The peculiar character of this micro-world has sparked the curiosity of many researchers, which efforts within the last decades opened the way for the development of various strategies for droplet manipulation such as generation (van Steijn et al. 2013), sorting (Tan et al. 2007), trapping (Huebner et al. 2009), splitting (Park et al. 2018) or merging (Bremond et al. 2008). Moreover, droplets can be considered as tiny biochemical reactors (Debski et al. 2018).

✉ Piotr M. Korczyk
   piotr.korczyk@ippt.pan.pl

   Damian Zaremba
   dzaremba@ippt.pan.pl

[1] Institute of Fundamental Technological Research, Polish Academy of Sciences, Pawinskiego 5B, 02-106 Warsaw, Poland

This opens the way for performing a large number of experiments with slight sample usage.

The specific character of the microfluidic environment consists in the fact that the diameter of microfluidic channels is less than the capillary length. This means that the surface force is the dominant one. Droplets larger than the diameter of the channel are squeezed by the walls and elongated along the channel axis, forming a plug-like shape. Such droplets can be moved by the means of an externally controlled flow of the continuous phase (CP) only in one dimension—along the channel's axis. Thus, the controlling a droplet may resemble operating an electric railway toy. This way of droplet motion prohibits the spontaneous rearrangement of droplets in their sequence. Therefore, the identity of every single droplet can be easily decoded from its position. Additionally, the CP separates droplets from each other and prevents the cross-contamination of droplets.

More complex operations on the population of droplets such as rearrangement of droplets or redistribution of them between multiple branches of microfluidic networks can be done in junctions connecting at least three channels. Hence, junctions are often a crucial part of the microfluidic

networks and, as we will show, the geometry of the junctions can be of critical importance for the flow of the droplets.

As previously shown, the droplets crossing a bifurcating microfluidic junctions can exhibit complex behaviour. Usually, a droplet at a junction either splits into two smaller droplets (Link et al. 2004; Ménétrier-Deremble and Tabeling 2006; Salkin et al. 2013; Hoang et al. 2013; Chen and Deng 2017; Wang et al. 2018, 2019) (for long droplets) or enters one of the two output microchannels (for short droplets) (Engl et al. 2005; Jousse et al. 2006; Schindler and Ajdari 2008; Labrot et al. 2009; Cybulski and Garstecki 2010; Glawdel et al. 2011). In the latter, the choice of the branch into which the droplet enters is determined by the speed and ratio of the outlet flows. Droplets that previously were distributed between different segments of the nontrivial network alter locally the hydrodynamic resistance. In consequence, that leads to a feedback mechanism, where the direction of a single droplet at the junction depends on the state established by previous droplets (Jousse et al. 2006; Cybulski and Garstecki 2010; Glawdel et al. 2011).

Despite the beauty of periodic or chaotic trafficking of droplets in such systems, in some practical applications, it is preferred to make the flow actively controlled or unambiguously determined. The active control on the flow in a junction can be obtained with the use of externally controlled elements as, e.g.: valves (Abate et al. 2010), magnetic (Zhang et al. 2009) and electric (Baret et al. 2009) fields, surface acoustic waves (Franke et al. 2009), electro-wetting (Fair 2007). An overview of different available techniques has been presented by Pit et al. (2015).

Besides the solutions supported by active components, some interesting constructions of junctions have been developed for the passive navigation of droplets. Cristobal et al. (2006) proposed an additional bypass between the output channels to ensure the equal and regular distribution of droplets between the two outlets. Baig at al. proposed a tertiary-junction sensitive to the hydrodynamic properties of the flow of small droplets (Baig et al. 2016). Abbyad et al. proposed the interesting concept of 'rails' and 'anchors' for guiding droplets motion along fine patterns in channels of the width larger than the droplet's width (Abbyad et al. 2011).

Passive elements are of importance for the construction of microfluidic droplet systems, where all processes would be determined at the design stage. In this vision, the encoding of protocols or algorithms would be possible due to the integration of multiple microfluidics modules with different functionalities. However, the set of available passive elements is still not sufficient and it lacks components performing some critical operations. One of them is a guiding junction, which (1) fixes the direction of fully confined long droplets, and (2) keep droplets undivided.

In this work, we propose a simple and robust modification of a junction by the use of a bypass slit. This element is a shallow groove less than half the height of the channel. As we showed in previous publications (van Steijn et al. 2013; Korczyk et al. 2013; Zaremba et al. 2018), the bypass slit can be used for altering the difference between the speed of the droplet and the speed of the CP. Due to the change of dimensions between the main channel and the bypass, the droplet does not penetrate the slit. The penetration would require the formation of a high curvature and an increase of the surface's potential energy, which the droplet tends to minimize. Thus, the bypasses are available exclusively for the flow of the CP.

Intuitively we can expect that the modification of the junction by the addition of a bypass can break the local symmetry of the flow and in consequence can direct a droplet to a preferred output. We show that a junction with an added bypass is a very robust solution working correctly in a wide range of flow parameters. Interestingly, we observed that the kinetic analysis of the droplet's deformation at the junction reveals the complex morphological transformation of its interior. The proposed solution allows for the manipulation on long droplets where the length is several times longer than the width of the channels.

Finally, we present some simple examples of the use of the modified junctions.

2 Materials and methods

2.1 Microfluidic devices fabrication

The microfluidic devices were milled from a transparent polycarbonate plate using a CNC milling-engraving machine. A 2-flute fishtail milling bit of diameter around 400 μm was used to engrave the channels and the slit-bypasses. Microfluidic structures were enclosed by bonding them with another polycarbonate plate from above at high temperature and pressure. The second plate contained the holes that were used for inlets and outlets.

A more detailed description can be found in our previous article where microfluidic devices were fabricated in a similar matter (Zaremba et al. 2018).

2.2 Fluid-specific details

For the CP, we used n-hexadecane 95% (Alfa Aesar, Germany). For the droplet phase, we used distilled water coloured with methylene blue. The surfactant (Span-80, Fluke Analytical, Germany) was added to the n-hexadecane with concentration of about 0.5% to avoid the wetting of the channel walls by the droplets.

The n-hexadecane density is 0.773 g/ml and its dynamic viscosity is 3.0041 mPa s at 25 °C. The surface tension

between the DP and the CP is 5.34 mN/m (after about 45 s since the creation of the droplet) measured with the pendant drop method using DataPhysics OCA15EC instrument and OpenDrop open-source software (Berry et al. 2015). These values were used later in the article to calculate the capillary number.

2.3 Experimental setup and measurements

Experiments consisted only of visual observations of flows in fabricated transparent microfluidic devices. All devices had the same design shown in Fig. 1a and network structure shown in Fig. 1b. Each device had their own type of junction. The used junctions are shown in Fig. 1c–f. The flows investigated in the microfluidic device were visualized using a Huvitz HSZ-645TR stereoscope equipped with a 0.5x objective and an IDS UI-3274-LE-C-HQ digital camera. Recorded images were stored on a PC for further analysis. Software written in Python and using OpenCV and Trackpy were used for the detection of droplets on sequences of images for speed and position estimation.

The velocity field of the CP flow in the bypass was estimated using particle image velocimetry technique (PIV). For this analysis, the pco.1200hs high-speed digital camera (PCO Imaging) and Nikon Eclipse E-50i microscope equipped with a 10 ×/0.3 objective (Nikon LU Plan Fluor) were used. The analysed flow was seeded by glass spheres (tracer particles) with a diameter of 12 μm and a density similar to the liquids, to minimise buoyancy effects. The suspension was obtained by leaving a highly concentrated solution of particles for a few days in a tall cylinder. Afterwards, a syringe was used to extract the solution from the center of this cylinder. In this way, a fairly low concentration of particles in the liquid was obtained. To increase the number of particles in the image, experiments with the same droplet and parameters were repeated many times. Next, sequences were synchronized and merged in one sequence by the minimization of pixel intensity using ImageJ. Only the bypass was analysed using PIV. The binary mask for the analysed part of the velocity field was created based on the detected edges of the image with the use of a raster graphics editor. The recording framerate was set to 100 fps with 100 μs exposure time. To improve the detection of particles in PIV, the background was removed and a median filter and thresholding of images was used. The background was obtained by the maximization of pixel intensity in a sequence of images. The open-source software OpenPIV-C++ (Taylor et al. 2010) was used to calculate the velocity field of the bypass. A window with 64 pixel of horizontal and vertical size and 50% overlap was used for the correlation algorithm.

Liquids were pumped by precise and pulsation-free syringe pumps (neMESYS, Cetoni GmbH) equipped with 1.0 ml syringes made of borosilicate glass with a PTFE plunger

(ILS Innovative Labor Systeme GmbH). Syringes were connected with the microfluidic device using polyethylene tubing with inner and outer diameter equal to 0.76 mm and 1.22 mm, respectively (Intramedic®, Becton Dickinson Co.). The flow rates used in our work are in the 0.4–3.6 ml/h (Ca = $4.243 \times 10^{-4} - 38.263 \times 10^{-4}$) range. Droplets were created with the use of a T-junction geometry (area C in Fig. 1a).

2.4 Numerical approach

For the numerical analysis, we used the volume-of-fluid (VOF) model to simulate the flow of the droplets. Additionally, we used the species transport model to show the Baker's transform. All the computations were done with the use of ANSYS Fluent software based upon the finite volume method. The basic equations to simulate the flow are the incompressible Navier–Stokes equations:

$$\nabla \cdot \mathbf{u} = 0, \tag{1}$$

$$\frac{\partial \rho \mathbf{u}}{\partial t} + \nabla \cdot (\rho \mathbf{u}\mathbf{u}) = -\nabla p + \nabla \cdot [\mu(\nabla \mathbf{u} + \nabla \mathbf{u}^{\mathbf{T}})] + \gamma \frac{p\kappa\mathbf{n}}{\frac{1}{2}(\rho_1 + \rho_2)}, \tag{2}$$

where ρ—density, $\mathbf{u}$—fluid velocity vector, t—time and p—pressure. The last term in the momentum equation refers to the surface tension, wherein γ is the surface tension coefficient and κ is the curvature and $\mathbf{n}$ the surface normal vector. The subscripts in the denominator dictate from which phase's density is used. Additionally, for multiphase flow, a volume fraction function α is added to the set of equations, that takes the value of 0 for one of the phases, and the value of 1 for the other.

$$\frac{\partial \alpha}{\partial t} + \nabla \cdot (\mathbf{u}\alpha) = 0. \tag{3}$$

After obtaining α in the domain, we can compute the density and the viscosity:

$$\rho = \alpha\rho_1 + (1-\alpha)\rho_2, \tag{4}$$

$$\mu = \alpha\mu_1 + (1-\alpha)\mu_2. \tag{5}$$

The species transport model is governed by the following equation:

$$\frac{\partial \rho Y_i}{\partial t} + \nabla \cdot (\rho \mathbf{u} Y_i) = \nabla \cdot (\rho D_i \nabla Y_i), \tag{6}$$

where Y_i is the local mass fraction for each species and D_i is the mass diffusion coefficient. To show the Baker's transform, we limited the mass diffusion by applying a value of order 10^{-15} to its coefficient. We used a variable time stepping method that allowed the simulation to choose a time

(a)

(b)

(c)

type J0

(d)

type J1

(e)

type J2

(f)

type J3
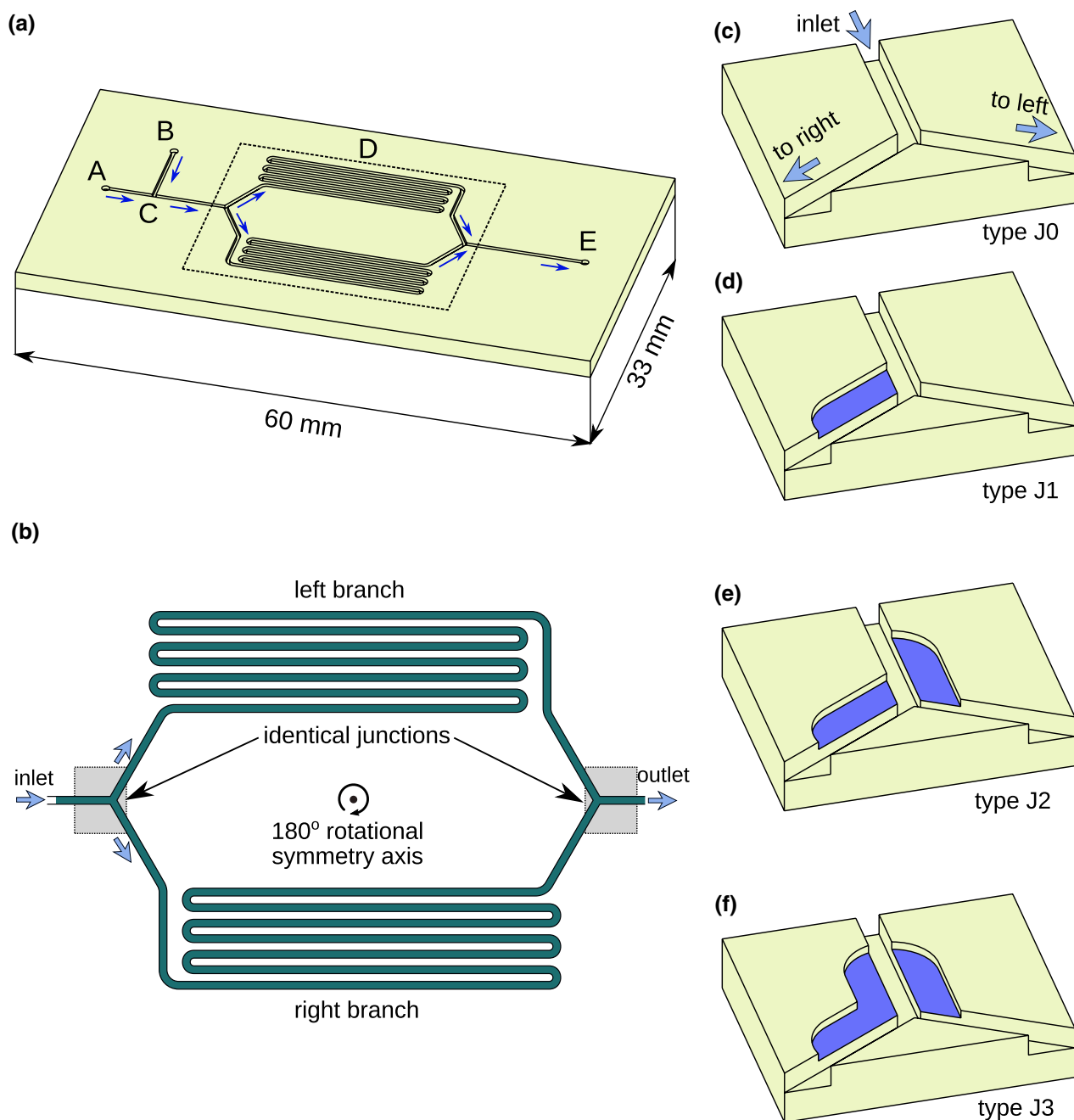
Fig. 1 Scheme of the microfluidic loop-device for the analysis of different constructions of junctions: **a** the general scheme of the device: A—inlet of the continuous phase: B—inlet of the droplet phase, C—junction for the generation of droplets, D—the section with the loop, E—the output; **b** details of the loop consisting of two identical junctions bifurcating the input flow into two branches of the same length. The loop was constructed to obey the rotational symmetry of 180°;

different junctions constructions used in this research: **c** the regular, symmetric junction (type J0); **d** the junction with an additional slit in the right output (type J1); **e** the junction with additional slits in the output channel and in the input channel (type J2); **f** the junction with additional slits in the output and two slits on both sides of the input channel (type J3)

step between 10^{-7} and 10^{-4} s based on the global Courant's number. A computational orthogonal and uniform mesh was

generated upon the constraints of having at least 20×20 elements in the cross section of the channel.

3 Results and discussion

3.1 Observations of the effect of modification J1 on the flow of short droplets

The various observations confirmed that in the bifurcating junction a single short droplet is directed into the channel with the higher flow velocity (Parthiban and Khan 2013; Wang and Vanapalli 2014; Cybulski et al. 2015). As the droplet changes the resistance of the flow in a channel, the distribution of flows between the two outputs will depend on the current number of droplets in each of the branches. This feedback mechanism causes droplets in such systems to exhibit periodical or chaotic behaviour (Engl et al. 2005; Jousse et al. 2006; Schindler and Ajdari 2008; Maddala et al. 2014). Too small distances between droplets entering the junction may result in collisions, which affect the direction of droplets (Belloul et al. 2011). In this work, we made sure that the distances between consecutive droplets were sufficient to avoid collisions.

In this paper, we propose such junction modifications, which fix the direction of droplets regardless of the flow's history. We start by presenting the comparison of a regular junction (type J0—see Fig. 1a) with a simple modified junction (type J1—see Fig. 1b). The only difference between these junctions is an additional slit which disturbs the symmetry of the modified junction in comparison to the regular one.

To investigate the effect of the considered modification, we used two microfluidic loop devices—one with the regular junction type J0, and the other one with the junction J1. Droplets of constant length and with constant frequency were generated in the device at the beginning of the loop and then the chain of droplets entered the loop with a constant speed. The frequency of droplets generation was set low enough to avoid collisions in the junction. Every single droplet getting into the bifurcating junctions can choose between two possible routes: turning left or right. We observed long sequences of short droplets passing through both loops.

Our observations of the regular junction (type J0) confirmed that the symmetry of the device results in the equalization of the distribution of droplets in both arms. The first droplet enters the left branch. The choice of the branch is likely determined by some imperfections during device fabrication resulting in not perfectly equal resistances between both the branches. These imperfections are small in comparison to the increase of resistance introduced by a single droplet so the next droplet enters the opposite branch as the empty branch has smaller resistance. Each next droplet so chooses the route to make the distribution of droplets closer to the equilibrium (see Fig. 2a). The

number of droplets in both branches increases to a maximum value limited by the length of the branches. After that the number of droplets getting into the loop is balanced by the number of droplets coming out. In that case, the system reaches a stationary state with the number of droplets in the loop fluctuating slightly around a constant value (42 droplets in each of the branches—see Fig. 2c).

The situation in the case of the loop with the modified junction type J1 is very different. As shown in Fig. 2b, the first 63 droplets flow only into the left branch. The 64-th droplet is the first one, which turns right. Notice that in the regular junction's case, droplets tend to distribute equally. The intriguing conclusion is that the local asymmetry of the junction—small in comparison to the size of the whole loop—results in a significant asymmetry of droplet flow in the whole device.

More information can be obtained from the quantitative analysis of the processes observed in both devices. Starting from the first droplet entering the loop, each consecutive i-th droplet changes the state of the device. The state established after introducing into the loop the i-th droplet can be characterized by the numbers of droplets $N_L(i)$, $N_R(i)$ and the mean velocities of flows $V_L(i)$, $V_R(i)$ in the left branch (subscript L) and the right one (subscript R), respectively.

Notice that the sum of velocities $V_L(i) + V_R(i) = V_{IN}$ is constant as the velocity in the inlet channel V_{IN} is constant. Hence, we can use only one quantity $v_L(i) = V_L(i)/V_{IN}$ for the description of the flow distribution and we can limit only to the measurement of the speed in the left branch. We estimated $V_L(i)$ assuming that (with the precision sufficient for this simple analysis) it is equal to the measured speed of the droplets in the left branch. V_{IN} was estimated in a similar way by averaging speed measurements of droplets in the input channel. The image analysis of frame sequences was used for the measurements of velocities.

Thus, the quantification of the distribution of flows ($v_L(i)$) can be obtained even in the absence of droplets in the right branch (e.g. for $i < 64$ in the modified junction).

The distribution of droplets between both branches was expressed by the number of droplets in the left branch normalized by the sum of droplets in both branches $n_L(i) = \frac{N_L(i)}{N_L(i)+N_R(i)}$.

The results of the analysis for both junctions are plotted in Fig. 3. Analysing the plots from the beginning of the process one intriguing and not obvious fact can be directly discovered. Here, we assume that the single first droplet does not significantly affect the flow. Thus, the value of v_L ($i = 1$) provides the information about the distribution of the CP flow in the loop device without droplets (for $i = 0$). The fact that the measured values of v_L ($i = 1$) for both types of junctions are almost identical (close to 0.5) reveals that the modification of the junction does not affect the one-phase
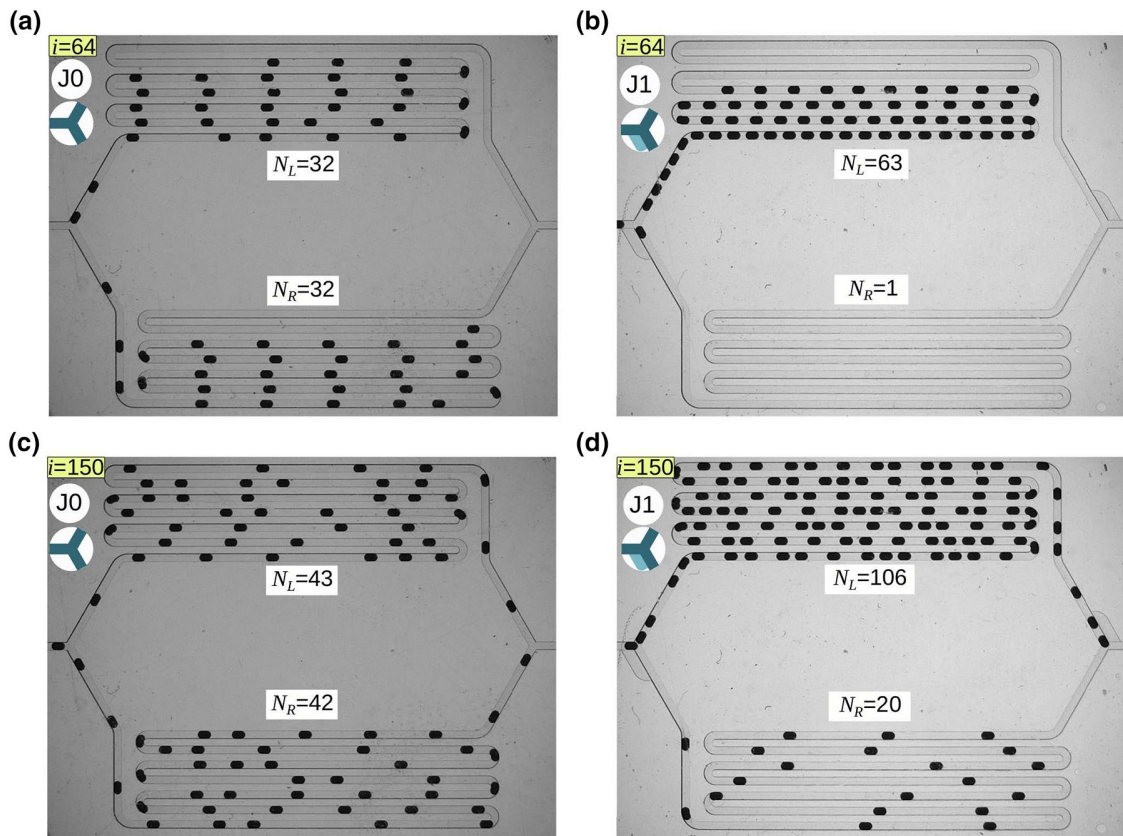
Fig. 2 Observations of droplets in loop devices. Comparison of junctions type J0 and type J1. the snapshots taken after introducing 64 droplets for junctions types J0 (**a**) and J1 (**b**), respectively, and the snapshots taken after introducing 150 droplets for junctions types J0 (**c**) and J1 (**d**), respectively

flow. Before the droplets enter the junctions, the flow of the CP is distributed equally between both branches of the loop due to their equal resistances and regardless of the different geometries of the junctions. These observations indicate the significant difference between one-phase flow and two-phase flow. In the presence of droplets, we observed a substantial flow asymmetry in the modified junction.

Let us analyse the further evolution of the states for both types of junctions exploring the variability with droplet's number i of both $v_L(i)$ and $n_L(i)$ plotted in Fig. 3.

In the case of the regular junction (type J0), the value of v_L is close to 0.5 starting from the first droplet and then fluctuates slightly around it. The value of $n_L(i)$ starts from 1 (the first droplet accidentally chooses the left branch) and quickly converges to the value close to 0.5. This indicates that in the case of the regular, symmetric junction the system tends to restore symmetric state ($n_L = 0.5$, $v_L = 0.5$), reflecting the symmetry of the loop-device.

In the case of the modified junction (type J1), the value of v_L starts from 0.5 and then it decreases with each successive droplet as is shown in the plot. For $i < 64$, droplets enter only into the left branch. Hence, for the first pack of

63 droplets $n_L = \text{const} = 1$. Droplets form a long chain in the left branch with decreasing spaces between consecutive droplets, corresponding to the fall of v_L. For $i > 63$, v_L approaches the value $v_{Lcrit} = 0.26$, where v_{Lcrit} is estimated as an average of v_L for $i > 63$. From this point, some droplets are guided into the right channel, while the majority of them is still guided to the left branch. This is reflected in the decreasing number n_L.

Hence, the proper guiding of the droplets into the left channel is possible for the limited ratio of velocities in both output channels. In this case, droplets are directed into the left channel for $v_L > v_{Lcrit}$ which is equivalent to the critical ratio $V_L/V_R < 0.35$.

The decay of $v_L(i)$ in the modified junction (type J1) can be explained by a simple model. Let us assume that both arms of the loop are characterized by the same value of resistance R. The presence of a single droplet in the channel increases the entire resistance. Let us assume that each next droplet increases the entire resistance of the channel by a constant amount of R_D. Equating instantaneous pressure drops in both branches of the loop, we obtain the equation taking into account the effect of the distribution of droplets:
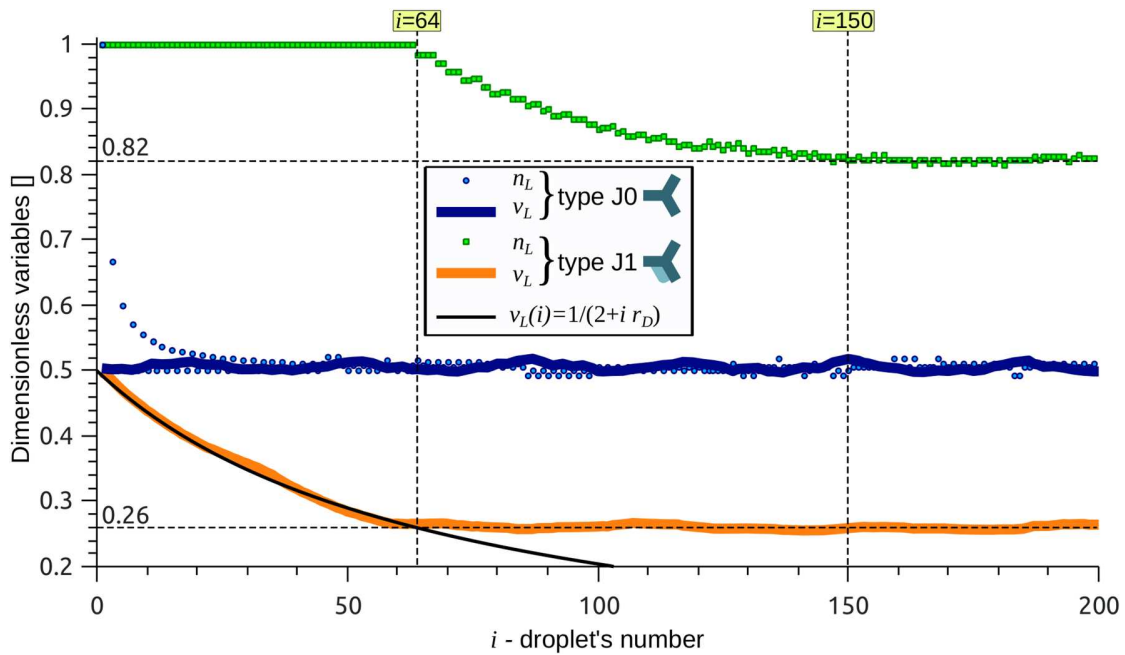
Fig. 3 Quantitative analysis of the effect of junction geometry on the distribution of droplets—comparison of junction types J0 and J1. Measurements of the normalized number of droplets in the left branch of the loop n_L and normalized speed of droplets in the left branch v_L of the loop as functions of the droplet's number i. Experiments were carried out at a constant CP flow equal to 3 ml/h and DP equal to 0.5 ml/h. The length of the droplets was 0.68 mm

$$Q_R \cdot \left(R + N_R R_D \right) = Q_L \cdot (R + N_L R_D), \tag{7}$$

where $Q_R = V_R A_{ch}$, $Q_L = V_L A_{ch}$ are rates of flows in both branches, respectively, with A_{ch} being the area of the cross section of the channel, the same for both branches.

For $i < 64$, there are no droplets in the right branch of the modified junction so $N_R = 0$ and $N_L = i$. The above equation in these conditions yields the equation for the evolution of $v_L(i)$ in the beginning period ($i < 64$), when all droplets go into the left branch and $v_L > v_{Lcrit}$

$$v_L(i) = \frac{1}{2 + i \cdot r_D}, \tag{8}$$

where the coefficient $r_D = R_D/R$ can be found due to the relation:

$$r_D = \frac{1 - 2v_L(i)}{\left(N_R(i) + N_L(i) \right) \cdot v_L(i) - N_R(i)}. \tag{9}$$

This coefficient can be estimated from the values of v_L, N_R, N_L averaged after the system reaches the quasi-steady state (for $i > 150$). In the case of our device, $r_D = 0.038$.

In general, the route of the i-th droplet is determined by the distribution of flows in the junction established due to the flow of previous droplets. Hence, if $v_L(i-1) > v_{Lcrit}$ the i-th droplet goes into the left branch, or contrarily into the right branch if $v_L(i-1) < v_{Lcrit}$. This general rule is valid for

any junction geometry characterized by the specific value of v_{Lcrit}. While the broken symmetry in the modified junction (type J1) establishes $v_{Lcrit} = 0.26$, in the regular junction (type J0), the symmetry of the setup results in $v_{Lcrit} = 0.5$.

This explains the fluctuations of v_L and n_L in the terminal stage after the system reaches the quasi-steady state. Each droplet entering into or getting out of the loop changes the state of the system; hence, the resultant v_L is slightly above or below the value of v_{Lcrit}.

The above analysis shows that the proposed loop device can be used for a comprehensive analysis of the impact of junction modifications on the motion of droplets. Such crucial parameters like v_{Lcrit} and r_D can be estimated with the use of a simple experimental setup and with relatively small effort.

3.2 Observations of long droplets in the modified junction type J1

In the previous examples, we analysed the motion of short confined droplets of comparable length to the width of the channel W. We can expect that the modification of the junction may affect the motion of long droplets (with the length significantly larger than W). As we will show, the proposed modification of the junction significantly extends the possibilities of this simple bifurcation.

Unlike short droplets, long droplets generally break into two parts in regular junctions (Chen and Deng 2017; Sun et al. 2018). We observed that phenomenon in our loop-device with the regular junction J0, but in the case of the modified junctions, a long droplet can go through the junction without splitting.

For the demonstration, we present in Fig. 4 two observations of long droplets series travelling through the loop device with a junction type J1. These two experimental runs were performed for two different values of inlet velocity V_{IN}. They show that for V_{IN} = 1.7 mm/s the long droplet (1) keeps its integrity and (2) enters the left branch of the loop-device (see Fig. 4a). While for V_{IN} = 2.7 mm/s, the droplet is split into uneven parts between both branches (see Fig. 4b).

The sequence of consecutive snapshots of the long droplet during its movement through the junction reveals

(a)

(b)
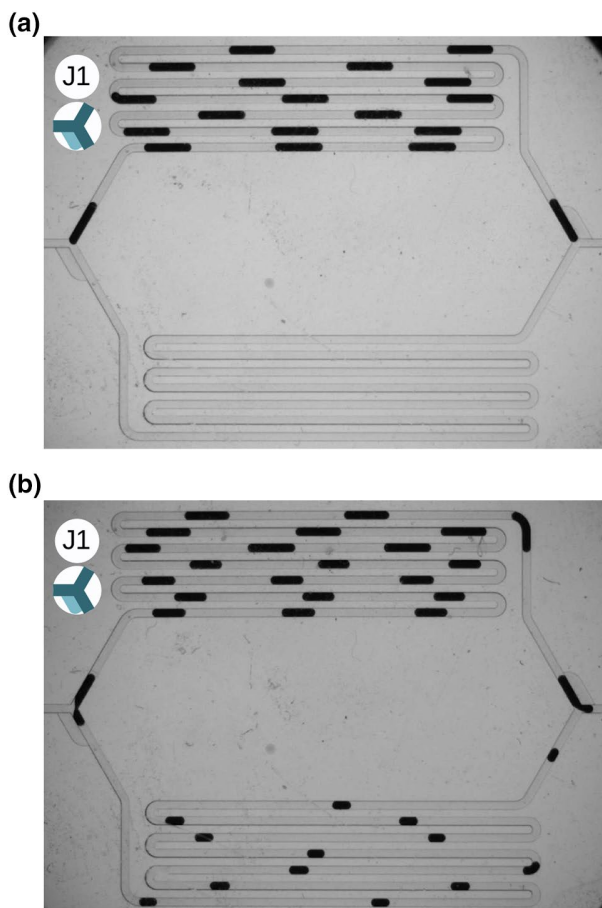
Fig. 4 Images from experiments with long droplets in a microfluidic loop device with a modified junction of type J1. The length of the produced droplets was constant and equal to 5.5 times the width of the channel. Images show the quasi-steady state for two different values of input flow velocity: **a** Q_{IN} = 1.1 ml/h, V_{IN} = 1.7 mm/s. All droplets enter the left branch. **b** Q_{IN} = 1.7 ml/h, V_{IN} = 2.7 mm/s. Droplets partially break in the junction
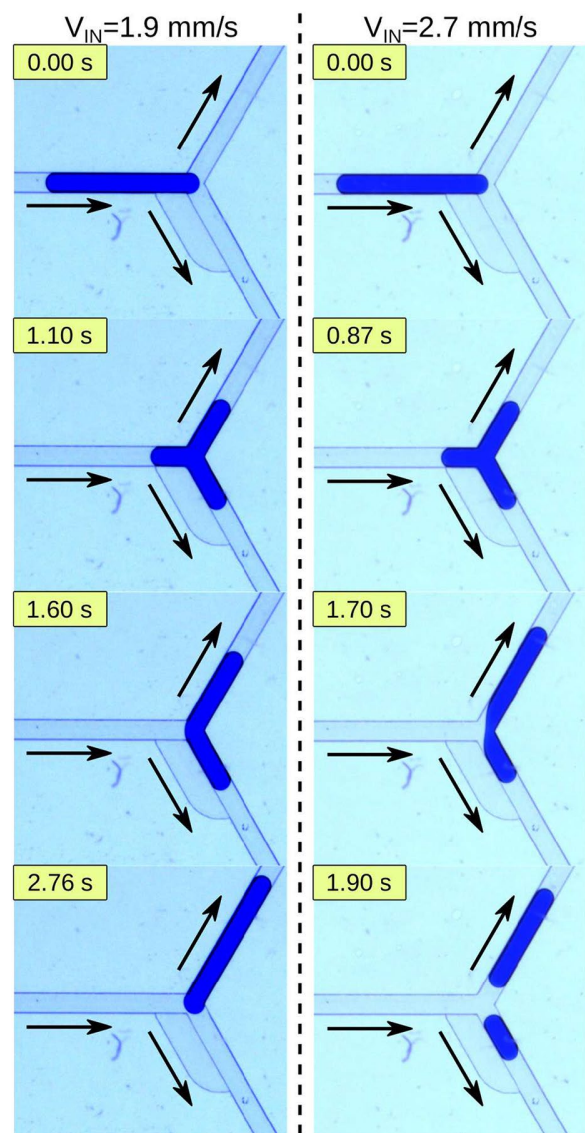
Fig. 5 The long droplet in the modified junction type J1. The sequence of consecutive snapshots for: left column—non-break-up mode for V_{IN} = 1.9 mm/s, and right column—break-up mode for V_{IN} = 2.7 mm/s

the non-trivial transformation of the droplet (see Fig. 5). The droplet produces a temporary 'protrusion' in the right output. Then, depending on the value of V_{IN}, this 'protrusion' can be either pulled by the main part of the droplet into the left output (for small V_{IN}) or can detach from the main part of the droplet and go into the right output (for large V_{IN}).

Thus, we can expect that in general, the behaviour of the droplet in the junction should depend on the set of parameters such as the length of a droplet, the geometry of the modification, capillary number and flow distribution.

3.3 Kinetic analysis of long droplets in the modified junction of type J1

Herein, we present the experimental analysis of the motion of a long droplet travelling through the junction with a single bypass (type J1) without breaking. In the example, we consider an equal flow distribution between both outputs ($V_L = V_R$). Unlike in the previous observations, here only one single long droplet of the length $L_D = 5.5W$ was created and moved at a constant speed ($V_{IN} = 1.6$ mm/s) toward the junction. We observed the process with the use of a microscope and a 100 FPS camera.

These observations allowed us to distinguish between four critical stages of the process as presented in Fig. 6. Besides the observations of the morphological transformation of the droplet, we analysed as well the evolution of the flow through the bypass. The characteristic flow structures were made visible thanks to traces of tiny particles suspended in the CP. The obtained visualizations of streamlines provided insight into the evolution of the morphology and the intensity of the velocity field in the bypass (see Fig. 6b). The flow patterns retrieved from these observations are schematically drafted in the snapshots presenting the droplet at different time points. This shows the interplay between the droplet and the CP flow and reveals the mechanism, which allows the long droplet to keep its integrity. The consecutive stages of the process are labelled in Figs. 6 and 7 by the roman numbers from I to IV. In the following, we will describe the quantitative analysis and then we provide the comprehensive description of these stages.

As we mentioned before, the droplet temporary deforms, expanding into all three channels of the junction (see Fig. 6a, stages from I to III). Hence, in this configuration, the droplet consists of three 'arms' connected in the central part of the
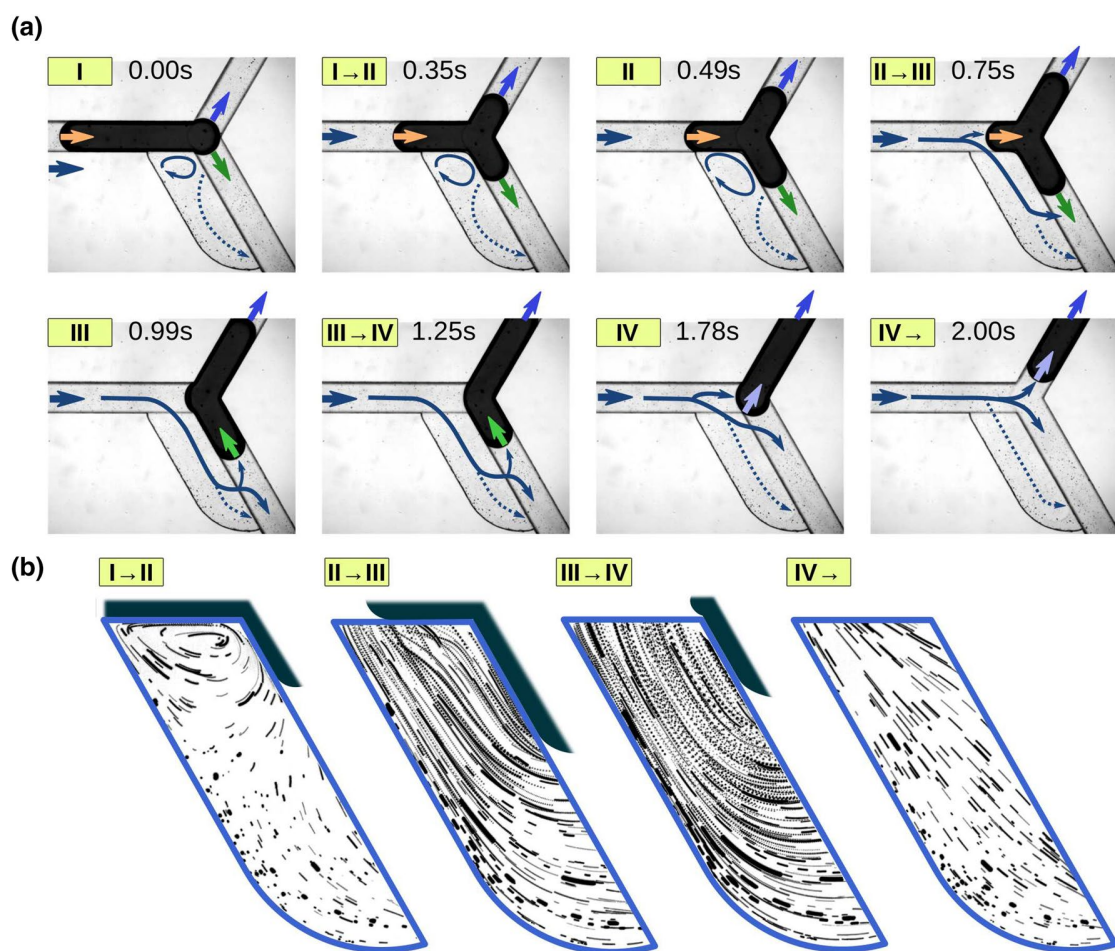
Fig. 6 Kinetics of a long droplet flowing through the junction with a single slit-bypass. **a** The sequence of snapshots of a droplet for four stages labelled by roman numbers from I to IV. The transient periods are labelled by Roman numbers and arrows. The characteristic flow structures (reconstructed on the basis of experiments) are schematically shown as lines with arrows. **b** Direct visualizations of tracer particles trajectories in the bypass. Each image obtained by the imposition of 50 consecutive frames registered at the speed of 100 fps. Thus, the length of the smudges is proportional to the velocity of the tracer particles
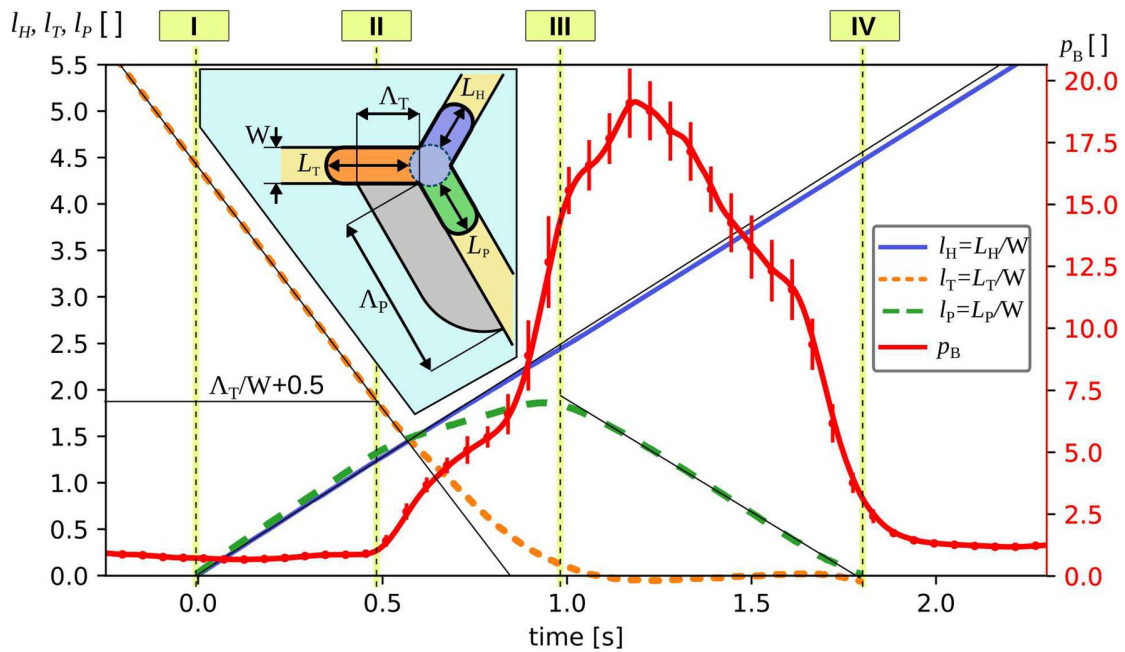
Fig. 7 Kinetics of a long droplet flowing through the junction with a single slit-bypass. Left axis—the time evolution of the length of the 'head' L_H, the length of the 'tail' L_T and the length of the 'protrusion' L_P normalized by the width of the channel W. Right axis—the intensity of the flow through the bypass p_B. In the inset—the scheme illustrating the decomposition of the deformed droplet into 'head'—the purple arm, 'protrusion'—the green arm, the 'tail'—the orange arm of the droplet. The additional part of the droplet connecting all arms is presented as a circle in the centre of the junction. The additional auxiliary thin black lines show the linearity of parts of the droplet's flow occurring at a certain time. (Color figure online)

junction namely: (1) the 'protrusion' in the right-output-channel, (2) the so-called 'tail'—the rear part remaining in the inlet channel and (3) the 'head'—the front of the droplet expanding into the left channel (see the scheme in the inset in Fig. 7).

For a quantitative characterization of the transformation of the droplet's shape, we measured the instantaneous lengths of each of these 'arms', respectively: L_P, L_T, L_H (see inset in Fig. 7). The droplet of the initial length L_D during the deformation in the junction does not change its volume and, hence, the sum of the length of all arms is constant:

$$L_H + L_P + L_T = L_D - L_J, \tag{10}$$

where the constant $L_J = \text{const} = 1.3W$ corresponds to the volume of the droplet in the central part of the junction (see the circle in the graph). The slopes of the length evolution of the arms correspond to the rates of growth of the droplet's arms dL_H/dt, dL_P/dt, dL_T/dt. As the 'head' is pulled into the left branch it expands with the constant rate $dL_H/dt = V_L$. The constant volume of the droplet imposes the speed constraint of the change of L_P and L_T. Indeed, time derivation of Eq. (10) yields:

$$V_L + \frac{d}{dt}L_P + \frac{d}{dt}L_T = 0. \tag{11}$$

The quantification of the CP flow intensity through the bypass was performed due to the analysis of additional data—instantaneous 2D velocity fields obtained by the means of PIV. We estimated the transient intensity of the bypass flow P_B by spatial averaging each velocity field over the whole area of the bypass. The dimensionless equivalent p_B was obtained through the normalization of the averaged value of P_B measured before stage I. This quantity reflects very well the variability of the bypass flow; however, the reader should notice that it is not perfectly equal to the flow rate because of some limitations of the 2D PIV technique. Despite these imperfections, the measurements of the intensity p_B provide important information on the activation and deactivation of the bypass flow by a moving droplet.

Now, we will provide a comprehensive description of all critical stages and intervals between them.

Before the droplet enters the junction (prior to stage I), it travels with a constant speed which is reflected in the constant slope of the plot of L_T/W (the position of the rear of the droplet) in Fig. 7. The magnitude of the flow through the bypass is close to its minimum ($p_B \approx 1$).

In stage I, the droplet's front reaches the junction hence $L_P = 0$ and $L_H = 0$ (see Fig. 6a and snapshot labeled as I). Then, in the interval between stage I and stage II (denoted as I → II), the droplet builds up the 'head' and

the 'protrusion', which is reflected in the increase of L_H and L_P in Fig. 7.

The crucial part in this interval is the position of the 'tail', which completely blocks the access to the bypass slit from the CP flow from the main channel. We can observe the characteristic circulation zone in the 'shade' of the droplet (Fig. 6b). It is related to Lid-driven cavity flow and was observed also in our previous publication (Zaremba et al. 2018). Thus, the activity of the bypass flow measured by p_B is even slightly lower than before stage I.

In consequence, the bypass is effectively switched off and does not affect the droplet. In this situation, the rate of growth of the arms is equal to the flow speed in the branches, so: $dL_H^{I \to II}/dt = V_L$, $dL_P^{I \to II}/dt = V_R$. According to Eq. (11), the expansion of the 'head' and the 'protrusion' must be compensated by the shrinkage of the 'tail' so: $dL_T/dt = -V_{IN}$. During the interval I → II, the length ratio of the different arms is equal to the ratio of velocities in both branches: $\frac{L_H^{I \to II}}{L_P^{I \to II}} = \frac{V_L}{V_R}$.

In stage II, the shrinking length of the 'tail' reaches the value, below which it cannot effectively block the CP flow into the bypass: $L_T^{II} = (\Lambda_T/W + 0.5)W$, where Λ_T is the width of the entrance to the bypass slit from the main channel (see the inset in Fig. 7). The additional term $0.5 \cdot W$ includes the length of the round cap of the droplet. From that point, in the interval II → III the 'tail' opens the entrance to the bypass up until it completely vanishes in stage III. This process gradually raises the bypass flow. The circulation zone observed previously is replaced by the regular flow of the CP bypassing the 'protrusion' in the right output (see Fig. 6b). Due to the activation of the bypass, both the growth of the 'protrusion' and the shrinkage of the tail slow down (see the slope of $L_P(t)/W$ and $L_T(t)/W$).

Stage III marks the point when the 'tail' completely disappears ($L_T^{III} = 0$) and the 'protrusion' reaches its maximum length. What is important, the 'protrusion' immediately transforms from the temporary front of the droplet to its end and reverses its direction from expanding to receding. During the interval III → IV, the entrance of the bypass is completely open for the flow of the CP, while the 'protrusion' still occupies the right channel of the junction. In this configuration, the whole flow of the CP must bypass the protrusion through the slit. In result, the bypass flow is at its highest level, what is visible in the visualization of the flow (Fig. 6b) and indicated by the high value of p_B (Fig. 7).

As the 'head' of the droplet moves with the constant speed $dL_H/dt = V_L$, it pulls the protrusion into the left output. Due to the absence of the tail, the integrity of the droplet requires that both its front and back move with the same velocity, so $dL_P/dt = -dL_H/dt$. The unique and intriguing character of this process consists of the fact that the protrusion moves opposite to the CP flow. The protrusion in the

interval III → IV shrinks after the expansion in the previous interval. This fact is reflected by the change of the slope of $L_P(t)$ in the plot in Fig. 7. In this way, the 'protrusion' is gradually engulfed by the 'head'.

Finally, the last stage IV marks the complete disappearance of the 'protrusion' ($L_P^{IV} = 0$). The whole volume of the droplet has been entirely transferred towards the 'head' in the left output. After that, the whole droplet travels in the left branch of the loop-device with the speed V_L. The transfer process of the droplet from the input channel to the left branch is completed. The bypass flow changes back to its lowest level as before the entrance of the droplet in the junction.

The above analysis shows in details the transfer process of a long droplet into the left branch of the loop. This explains as well the mechanism responsible for the flow of short droplets. Similarly, as in the case of long droplets, the short ones are pulled into the left branch due to the bypass, which redirects the flow of the CP into the right branch. In this case, the flow of two liquid phases can be locally decoupled and become asymmetric. The droplet flows into the channel without the bypass and the CP flows through the bypass into the opposite channel.

3.4 Effect of the Baker's transform

As we showed before, the droplet during its movement through the junction is a subject of a non-trivial transformation which includes the generation of a temporary 'protrusion' and its later shrinkage. In the previous section, we focused on the analysis of the droplet's shape. Now, we discuss the rearrangement of the droplet's internal mass distribution. To visualize the effect of the flow within the droplet, we performed simple observations of Janus droplets, i.e. droplets composed of two different parts.

We generated Janus droplets in a cross junction (Fig. 8a) where two opposite streams of 80% glycerol-in-water solution meet. One of the streams is distinguished by the addition of ink. Due to that, the merged streams form a well-visible two-layered parallel flow in the main channel. The additional cross-flow of the continuous immiscible phase (oil) results in the generation of droplets consisting of two symmetrical halves of different colours. To explain the peculiar character of the droplet's transformation in the modified junction, we firstly present the observations of Janus droplets travelling through a straight channel. It is a well-known fact that the symmetry of the internal flow within the droplet inhibits the exchange of mass across the symmetry plane (Tice et al. 2003). Hence, despite the continuous re-circulating flow inside the droplet, the homogenization of the content of the symmetrical Janus droplet is only thanks to the diffusion across the separation plane.

(a)

(b)

(c)

(d)
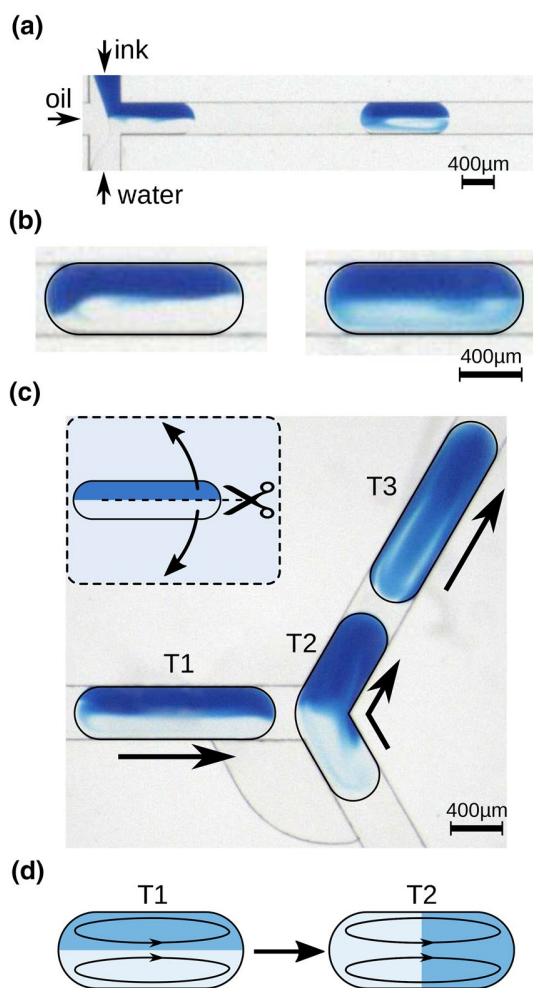
Fig. 8 Visualizations of the mixing process inside the droplet. **a** Microscopic image of the generation of Janus droplets in the cross-flow device. **b** Mixing inside the Janus droplet travelling through a straight channel: the left image—droplet just after its generation; the right image—droplet after travelling the distance of ten droplet's lengths. **c** The Janus droplet flowing through the modified junction—the composition of three images of the same droplet in the consecutive positions from T1 to T3. In the inset—the schematic pictogram of the transformation of the droplet. **d** The schematic view of the separation plane in position T1 and after the transformation in position T2

Figure 8b presents two images of the same droplet, the left one—the droplet just after its generation, the right one—the droplet after travelling the distance of ten droplet's lengths. We can see that the droplet in its initial state is not perfectly symmetrical (with the small dose of ink in the bottom half). Despite that, we observe that the initial stratification is conserved after the droplet moves over the distance of ten its lengths. The ink's concentration is homogenized only within the separated halves. This is the reason why the initially introduced portion of ink in the bottom half, after mixing, results in the fade bright-blue colour of the bottom

half. However, the plane of separation in the middle of the droplet is still well visible and sharp.

Figure 8c presents the results of experiments with the Janus droplet flowing through the modified junction. The image shows the composition of three images of the same droplet in three consecutive positions labelled as T1, T2 and T3. In position T1, the droplet is approaching the junction and we can see the sharp stratification of the ink's concentration in the middle plane of the droplet. The position T2 corresponds to stage III mentioned in the previous section where the 'tail' has completely disappeared and the head starts to pull the 'protrusion' into the left output. What is important is that the whole volume of the blue half of the droplet has been redirected to the 'head' while the bottom, clear half has been redirected to the 'protrusion'.

In other words, the droplet during the transition from T1 to T2 is being precisely cut in the plane of separation. Simultaneously, both halves are being gradually folded out in opposite directions. This process is schematically shown in the inset in Fig. 8c. This transformation resembles one iteration of the Baker's transform applied to the long droplet. In result, the significant rearrangement of the droplet's interior is obtained. Notice that the upper half of the droplet is transferred to its front part, the bottom half to its rear part and the previous rear part is transferred to the central part of the droplet.

Crucial for the homogenization of the droplet's content is the reorientation of the plane of separation of the two aqueous phases (see Fig. 8d). In position T1, the plane of separation is in the plane of symmetry of the droplet and is parallel to the streamlines of the internal flow. In position T2, this plane is reoriented and becomes perpendicular to the streamlines. Afterwards, the plane of separation is carried by the flow and gradually stretched and deformed. This leads to the homogenization of the droplet's content.

The efficiency of this process is clearly seen in the image of the droplet after travelling the distance of about one droplet's length (position T3 in Fig. 8c). Although the droplet is not yet completely homogenized, the blue dye is distributed over the whole droplet without any visible sharp separation of areas with different concentrations of ink, unlike in the case of the straight channel, where the sharp separation between two domains is conserved over a much longer distance. To quantitatively estimate the mixing rate after the reorientation of the separation plane, we conducted numerical simulations (see Fig. 9). The starting point of these simulations was a droplet composed of two parts with different concentrations of the passive indicator with the separation plane perpendicular to the axis of the channel. Initially, the droplet was divided into two halves: (1) the front part with the initial concentration $C_F(t = 0) = C_0$ and (2) the rear part $C_R(t = 0) = 0$ We set a very low diffusion coefficient ($2.88 \times 10^{-15} \mathrm{m^2/s}$ what corresponds to the value for water,
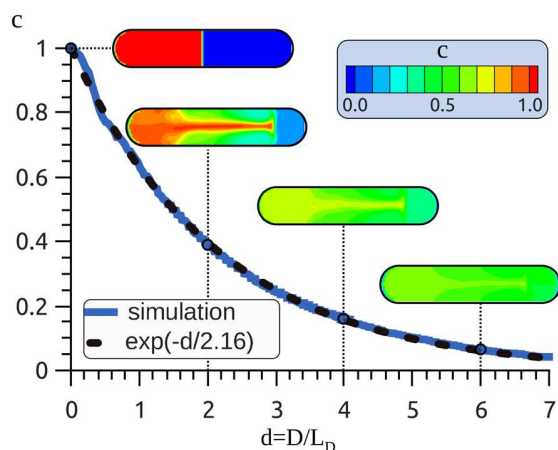
Fig. 9 The mixing process of the reoriented Janus droplet. The contrast of the concentration c as a function of the normalized distance travelled by the droplet $d = D/L_D$. The snapshots from the simulations show the evolution of the instantaneous distribution of the indicator in the middle-plane of the droplet (see the colorbar for reference). (Color figure online)

decreased 10^6 times), so the flow inside the droplet was the only mechanism which would mix the interior of the droplet. During the simulation, the droplet was travelling through a channel of square cross section with a constant speed hence the distance D travelled by the droplet was proportional to time. For each simulation step, we estimated the normalized contrast between the two parts of the droplet defined as $c(d) = (C_F(d) - C_R(d))/C_0$, where $C_F(d)$ and $C_R(d)$ are instantaneous average concentrations in both parts of the droplet, respectively, and $d = D/L_D$ is the distance travelled by the droplet normalized by the length of the droplet. This coefficient starts from the value $c(d = 0) = 1$ and decreases with time. The minimal possible value $c = 0$ corresponds to the equal distribution of the passive indicator in both parts of the droplet. The data obtained from the numerical simulations show the exponential decay of the contrast with the fitted relation in the form: $c(d) = \exp(-d/2.16)$. This implies that after travelling the distance $D = 5L_D$, the contrast c falls to a value of about 0.1.

The modified junction's geometry realizes the Baker's transform on the droplet's interior which radically improves the content's mixing in long droplets. The rearrangement of the spatial distribution of the droplet's content can be used to prevent the sedimentation of particles in the rear part of the droplet (Hein et al. 2015).

3.5 Mechanism of droplet break-up

The splitting of the droplet in the junction may have potential applications; however, here we consider how it can be

avoided. We want to retain the integrity of the droplet. The mechanism of droplet breakup was the subject of numerous investigations (Link et al. 2004; Ménétrier-Deremble and Tabeling 2006; Salkin et al. 2013; Hoang et al. 2013; Chen and Deng 2017; Wang et al. 2018, 2019); however, until now the effect of an additional bypass was not considered. Here, we present the analysis of the transition between break-up and non-break-up modes of a droplet in the junction with the bypass. The comparison of observations of broken droplets and unbroken ones reveals that the transformation of the shape of the droplet in both cases is very similar until stage III, i.e. until the complete disappearance of the 'tail'. This is the critical point, for the further fate of the droplet (compare snapshots in Fig. 5). In the case of the non-break-up mode, after stage III, the 'protrusion' is effectively pulled into the left channel.

In the case of the break-up mode, the split of the droplet occurs in the central part of the junction similarly like in the case of the junction without the bypass. Therefore, we can expect that a similar mechanism of deformation of the 'elbow', connecting the 'protrusion' and the 'head', appears in the modified junction. In the break-up scenario, the incoming flow of the CP causes the deflection of the 'elbow' and the droplet finally breaks.

The bypass in the modified junction lowers the pressure build-up in the junction so the pressure drop along the 'protrusion' ΔP_P can be estimated as:

$$\Delta P_P = \alpha_B \cdot V_{IN} \cdot A_{ch} \cdot (L_P^{III} - L_0) \cdot \mu \cdot A_B^{-2}, \tag{12}$$

where α_B is the geometrical non-dimensional factor of the resistance of the bypass, A_{ch}, A_B are the areas of the cross sections of the input channel and the bypass slit, respectively, μ is the dynamic viscosity of the CP, and L_0 is the additional correction factor.

The mechanism that resists the 'deflection' of the 'elbow' is the Laplace pressure, which can be described as the product of the interfacial tension coefficient and the mean curvature of the 'elbow' H:

$$\Delta P_L = 2\gamma H. \tag{13}$$

Here, we can assume that the shape of the non-deformed 'elbow' is defined single-handedly by the geometry of the device.

Equating ΔP_P and ΔP_L, we obtain the transition between break-up and no-break-up modes:

$$L_P^{III}/W = \beta/Ca + l_0, \tag{14}$$

where $\beta = 2 \cdot A_{ch} \cdot A_B^{-2} \cdot H \cdot W^{-1}$ and $l_0 = L_0/W$ are non-dimensional fitting parameters.

Note that this simplified model does not take into account the velocity of the head and additional shear acting on the protrusion. Despite the assumed simplifications, the model correctly explains the transition from the break-up mode to

the no-break-up mode, what we observed experimentally (see Fig. 10). The values of fitted parameters are $\beta = 0.0041$ and $l_0 = 0.24$. These parameters are specific for the investigated geometry of the junction and may vary for other geometries.

Besides the above-mentioned dynamic constraints for the no-break-up mode, there is an additional geometrical restriction for the maximal length of the 'protrusion'. Indeed, once the 'protrusion' blocks the flow of the CP from the bypass to the right branch, the 'protrusion' is pulled into it with the speed V_R and cannot recede, which results in the break-up of the droplet. This geometrical constriction limits the length of the 'protrusion' to $L_P = \Lambda_P + 0.5W$ and is plotted in the graph as the horizontal line.

The next question is what does the maximal length of the 'protrusion' L^{III} depend on? As we mentioned before, the 'protrusion' develops within the first two intervals $I \rightarrow II$ and $II \rightarrow III$. In the first interval, it grows with the maximal rate $dL_P^{I \rightarrow II}/dt = V_R$. In the interval from $II \rightarrow III$, the activated bypass flow lowers the rate of growth of the protrusion $dL_P^{II \rightarrow III}/dt < V_R$. Taking into account that $dL_H/dt = const = V_L$ we can state:

$$\frac{L_P^{III}}{L_H^{III}} < \frac{V_R}{V_L}. \tag{15}$$

For the given length of the droplet L_D, the maximal available length of the protrusion can be roughly described by the

Fig. 10 Phase diagram of operational modes of the junction type J1 in the space of parameters L_P^{III}/W vs Ca

following form, which includes in addition the geometrical restriction:

$$L_P^{III} \leq (L_D - L_J)v_R < \Lambda_P + 0.5W, \tag{16}$$

where $v_R = V_R/V_{IN} = 1 - v_L$.

Notice that the geometrical restriction for the maximal length of the protrusion in the non-break-up mode sets the limit for the longest droplet, which can go through the junction without being split:

$$L_D \leq (\Lambda_P + 0.5W) \cdot v_R^{-1} + L_J. \tag{17}$$

As the maximal value of v_R is 1, the geometrical restriction does not affect droplets shorter than $L_D <= \Lambda_P + 0.5W + L_J$. Neglecting both latter terms, we can articulate a robust rule for the construction of a microfluidic circuit with a modified junction. The rule states that droplets generated in the microfluidic system must be shorter than the length of the bypass Λ_P. This establishes the design guidelines of both the droplets generator and the junction.

Taking into account the maximal length of the 'protrusion' and the dynamic limitation given by Eq. (14), we obtain the limit of Ca for the non-break-up mode:

$$Ca \leq \frac{\beta}{(L_D/W - L_J/W)v_R - l_0}. \tag{18}$$

This relation sets the maximal limit for the Capillary number at which a droplet of length L_D is not broken at a given v_R. Notice that the value of v_R depends on the number of droplets introduced to the loop device (see Eq. 8 and the discussion there). Thus, depending on the resistance of a single droplet, there is a critical number of droplets in the loop above which the next droplet entering the junction breaks. Hence, appropriate adjustment of both the frequency of droplets and the value of Ca avoids the appearance of droplet's breakage in the microfluidic system (compare Fig. 4a and b).

The above-mentioned experimental analysis of the limits of the non-break-up mode shows that the modified junction can work correctly in a wide range of parameters. However, the knowledge of these limitations is crucial for the proper design of the microfluidic device.

3.6 Improving the junction for multi-directional flows

As for now, we investigated only one type of modified junction (type J1). In Fig. 1, we presented additionally the geometries of other types of junctions. In this section, we discuss additional possible modifications of the junction and their effect on the functionality of the microfluidic architecture.

Let us consider the end of the loop where two branches join forming a joining junction. The configuration of flows in this junction is inverted in relation to the previously
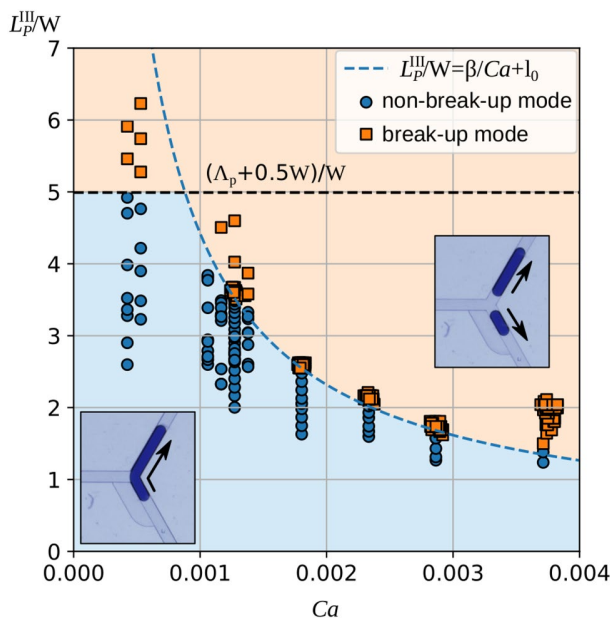
considered dividing junction. The joining junction merges two input flows into one output flow unlike the dividing junction, which splits the one input flow between two outlets. Herein, we consider the additional possible scenario where the droplet from one of the branches of the loop enters the joining junction. Our observations of the regular junction (type J0) and the other one with one bypass (type J1) revealed that once the droplet enters the common channel its front starts to move with a higher speed than the rear part. This usually results in the break-up of the droplet (see Fig. 11, the left column for junction type J1). Indeed, in the case of the joining junction, the speed in the common channel is the sum of speeds in both input channels. This speed difference is responsible for the splitting of the droplet.
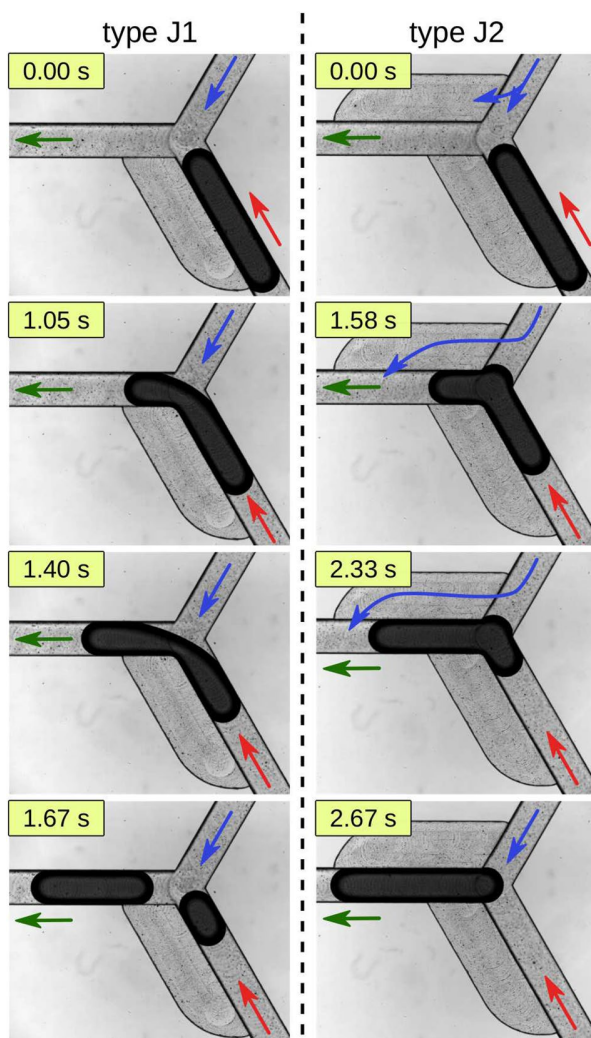
Fig. 11 The behaviour of the long droplet in different junctions with reversed flow—two inputs and one output. The sequence of consecutive snapshots for: left column—type J1 and right column—type J2. For both cases, the output flow is the same and $Q_{\text{OUT}} = 1$ ml/h

Figure 11 shows examples of the different behaviours of a long droplet in the junction type J1 and junction type J2 for the inverted flow configuration. The observations revealed that to keep the integrity of the droplet, an additional bypass must be introduced into the geometry of the junction. For example, to avoid the split of the droplet entering the junction from the right branch, a junction of type J2 should be applied (see Fig. 11 the left column). To increase the functionality and allow as well droplets from the left branch to travel through the branch in one piece, we need to use another additional bypass as in junction type J3.

3.7 Examples

To demonstrate the potential use of the modified junctions in microfluidic devices, we present two examples of small microfluidic geometries with different functionalities.

The first device is presented in Fig. 12. The central part of the device is a small symmetrical loop with two identical junctions of type J2 on both ends of the loop depicted as B1 and B2. The additional traps A1 and A2 are to limit the movement of the droplet. The trap stops the incoming droplet but it releases the droplet after the change of the flow direction. The operation mechanism of these traps was described before (Korczyk et al. 2013; Zaremba et al. 2018). The additional junction C exists only for the generation of a single droplet. After the droplet is in the device, this junction is inactive.

Commencing the description of the functionality of the device from the upper left image. A single droplet has been already generated and moved into trap A1. The flow of the CP is from the right to the left (as indicated by blue arrows). This is the stationary state of the device as the droplet is immobilized. This can be changed by the reversal of the flow direction—see the upper right image (the green arrows indicate the order of the snapshots). The flow of the CP from the left to the right removes the droplet from trap A1, then the droplet travels toward the loop and turns left into the upper branch. This direction is fixed by the geometry of the junction of type J2. Then, the droplet meets the other junction of type J2 at the end of the loop. As we mentioned in the previous section, the special design of the junction keeps the integrity of the droplet either in the inlet to the loop or in the outlet. Finally, the droplet stops in trap A2 (see the bottom right image) and the system reaches its second stationary state. The rotational symmetry of the device implies that after the next flow reversal of the CP (to its initial direction), the droplet will travel a symmetrical route, now through the bottom branch of the loop. In this example, the oscillating flow of the CP is translated to the circulation of the droplet inside the loop. Such a mechanism can be used for the implementation of loop-like laboratory sequences
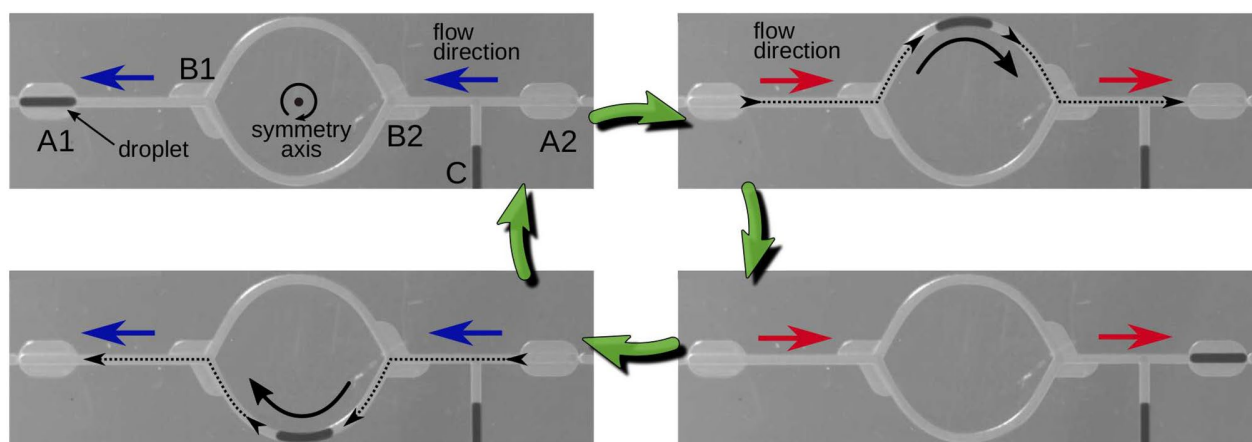
Fig. 12 Circulating loop. Four snapshots representing the complete cycle of circulation of the droplet. Green arrows indicate the order of the sequence. Top left: the stationary state for the flow to the left; the droplet is immobilized in the trap A1. B1 and B2 are two symmetric junctions connecting both branches of the central loop with the main channel. A2—the other trap symmetrical to trap A1. C—the additional channel enabling the generation of the single droplet (not used once the droplet is introduced). Top right: the transitional state after the reversal of the flow direction. The droplet is removed from the trap, moves to the right according to the reversed flow. In junction B1, it turns left and travels through the top branch of the loop to eventually stop in the trap A2. Bottom right: the stationary state for the flow to the right, with the droplet immobilized in trap A2. Bottom left: the transient state after reversing the flow restoring its initial direction. Droplet travels through the bottom branch of the loop to stop in trap A1 (as shown in the top left snapshot) completing a full cycle of the circulation. (Color figure online)

of droplet operations (Debski et al. 2018; Abolhasani and Jensen 2016).

This example teaches as well that the character of the flow of the droplets may be very different than the case of single-phase flow. In the case of single-phase flow at low Reynolds numbers, we can expect the time reversibility of the flow. In the case of the flow of the droplet, we observed that the droplet travels through the upper branch of the loop or through the bottom branch depending on the direction of the input flow of the CP.

In the second example, presented in Fig. 13, we use a constant flow of the CP without changing its direction. In this example, we consider two droplets entering the loop device. The device here is not symmetrical. Each of the branches of the loop consists of an additional element—an obstacle. It is a local constriction of the channel's cross section. The flow is from the left to the right. Without any droplet in the loop, the flow of the CP splits into equal parts between the two branches (Fig. 13a). As we mentioned before, the modification of the junction weakly influences single-phase flow. The obstacles in both branches equally increase the hydraulic resistance.

The flow distribution between both branches can be quantified by the coefficient $v_L = V_L/V_{IN}$, previously introduced in the description of the flow of small droplets in loop devices. In this case, we can state that for the flow of the CP and without any droplet in the device $v_L(0) = 0.5$.

The situation changes after the first droplet enters the device. The junction routes the droplet into the left branch, where it meets the obstacle. To pass through the obstacle, the front of the droplet would require to produce a high curvature to penetrate the constriction of the channel that needs an additional pressure increase—above the specific breakthrough pressure. However, if the flow of the CP through the right branch generates a pressure drop lower than the breakthrough pressure, the droplet will be kept immobilized. A similar mechanism of immobilization is known from microfluidic traps (Korczyk et al. 2013; Zaremba et al. 2018).

In this configuration, the whole CP flows only through the right branch as the left one is closed by the immobilized droplet (see Fig. 13b). This clearly shows that the droplet changes the state of the flow. Now, the coefficient of distribution of the flow can be estimated as $v_L(1) = 0$ (no flow through the left branch). This value is below v_{Lcrit}; hence, we can expect that the next droplet will be directed into the right branch. Indeed, the next droplet entering the loop chooses the right channel; however, something very interesting happens once the second droplet reaches the obstacle. In this situation, the flow of the CP can no longer bypass both droplets; hence, the pressure behind the droplets increases above the breakthrough pressure needed to push the droplets over the obstacles. The pressure acts on both droplets so they are finally released and travel toward the exit of the loop (see Fig. 13c). The important feature of this device is that both obstacles are placed in different positions. Both droplets are triggered simultaneously but have different distances to the exit of the loop. In result, the second droplet leaves the device before the first droplet (see Fig. 13d). This simple
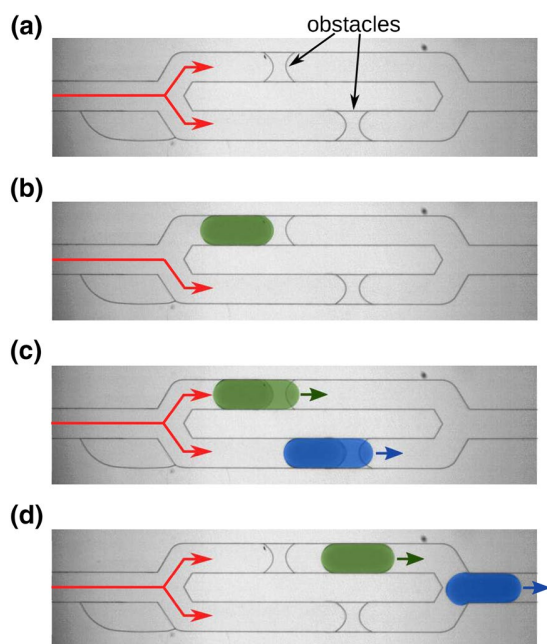
Fig. 13 The microfluidic device rearranging the order of droplets in the sequence. **a** The micrograph of the device without droplets. The flow of the CP is constant—from the left to the right. The junction in the inlet to the loop is of the type J1. The crucial elements are obstacles placed in both branches of the device. In the absence of droplets, the flow of CP is distributed equally between two branches as indicated schematically by bifurcated red arrows. **b** The first droplet (coloured by green) enters the upper branch, stops at the obstacle and blocks the flow of the CP through the upper branch. **c** The second droplet (blue) enters the bottom branch and triggers the release of the first droplet. **d** Both droplets leave the loop with their order changed (the blue droplet goes as the first one). (Color figure online)

device changes the order of the droplets. The mechanism utilized in this example can be used in other devices performing logic operations on the flowing droplets.

4 Conclusions

In this paper, we investigated the behaviours of droplets in junctions modified by additional bypasses. In a series of experiments, we showed the effect of the modifications on both short and long droplets. Our observations revealed that the bypasses in the junctions can be used for guiding droplets to the preferred output and for the preventing of the break-up of long droplets. We provided an experimental analysis of the process of droplet transfer through the junction, which explains the peculiar behaviour of the droplets. This analysis revealed that the droplet is a subject of nontrivial transformation, which resembles the so-called 'Baker transform'. We showed as well that the break-up of droplets can be explained by a simple model.

These modified junctions can be used in microfluidic systems where the motion of droplets is determined by the geometry of the device. This enables the encoding of a sequence of operations on droplets in the architecture of the device. Examples of simple microfluidic modules with non-trivial functions show the potential use of this approach.

References

Abate AR, Agresti JJ, Weitz DA (2010) Microfluidic sorting with high-speed single-layer membrane valves. Appl Phys Lett 96(20):203509. https://doi.org/10.1063/1.3431281

Abbyad P, Dangla R, Alexandrou A, Baroud CN (2011) Rails and anchors: guiding and trapping droplet microreactors in two dimensions. Lab Chip 11(5):813. https://doi.org/10.1039/C0LC00104J

Abolhasani M, Jensen KF (2016) Oscillatory multiphase flow strategy for chemistry and biology. Lab Chip 16(15):2775. https://doi.org/10.1039/C6LC00728G

Baig M, Jain S, Gupta S, Vignesh G, Singh V, Kondaraju S, Gupta S (2016) Engineering droplet navigation through tertiary-junction microchannels. Microfluid Nanofluid 20(12):165. https://doi.org/10.1007/s10404-016-1828-9

Baret JC, Miller OJ, Taly V, Ryckelynck M, El-Harrak A, Frenz L, Rick C, Samuels ML, Hutchison JB, Agresti JJ, Link DR, Weitz DA, Griffiths AD (2009) Fluorescence-activated droplet sorting (FADS): efficient microfluidic cell sorting based on enzymatic activity. Lab Chip 9:1850. https://doi.org/10.1039/B902504A

Belloul M, Courbin L, Panizza P (2011) Droplet traffic regulated by collisions in microfluidic networks. Soft Matter 7:9453. https://doi.org/10.1039/C1SM05559C

Berry J, Neeson M, Dagastine R, Chan D, Tabor R (2015) Measurement of surface and interfacial tension using pendant drop tensiometry. J Colloid Interface Sci 454:226. https://doi.org/10.1016/j.jcis.2015.05.012

Bremond N, Thiam AR, Bibette J (2008) Decompressing emulsion droplets favors coalescence. Phys Rev Lett 100:024501. https://doi.org/10.1103/PhysRevLett.100.024501

Chen Y, Deng Z (2017) Hydrodynamics of a droplet passing through a microfluidic t-junction. J Fluid Mech 819:401–434. https://doi.org/10.1017/jfm.2017.181

Cristobal G, Benoit JP, Joanicot M, Ajdari A (2006) Microfluidic bypass for efficient passive regulation of droplet traffic at a junction. Appl Phys Lett 89(3):034104. https://doi.org/10.1063/1.2221929

Cybulski O, Garstecki P (2010) Dynamic memory in a microfluidic system of droplets traveling through a simple network of microchannels. Lab Chip 10(4):484. https://doi.org/10.1039/B912988J

Cybulski O, Jakiela S, Garstecki P (2015) Between giant oscillations and uniform distribution of droplets: the role of varying lumen of channels in microfluidic networks. Phys Rev E 92(6):063008

Debski P, Sklodowska K, Michalski J, Korczyk P, Dolata M, Jakiela S (2018) Continuous recirculation of microdroplets in a closed loop tailored for screening of bacteria cultures. Micromachines 9:469

Engl W, Roche M, Colin A, Panizza P, Ajdari A (2005) Droplet traffic at a simple junction at low capillary numbers. Phys Rev Lett 95(20):208304

Fair RB (2007) Digital microfluidics: is a true lab-on-a-chip possible? Microfluid Nanofluid 3(3):245. https://doi.org/10.1007/s10404-007-0161-8

Franke T, Abate AR, Weitz DA, Wixforth A (2009) Surface acoustic wave (SAW) directed droplet flow in microfluidics for PDMS devices. Lab Chip 9:2625. https://doi.org/10.1039/B906819H

Glawdel T, Elbuken C, Ren C (2011) Passive droplet trafficking at microfluidic junctions under geometric and flow asymmetries. Lab Chip 11(22):3774. https://doi.org/10.1039/C1LC20628A

Hein M, Moskopp M, Seemann R (2015) Flow field induced particle accumulation inside droplets in rectangular channels. Lab Chip 15(13):2879

Hoang D, Portela L, Kleijn C, Kreutzer M, Van Steijn V (2013) Dynamics of droplet breakup in a t-junction. J Fluid Mech 717:R4

Huebner A, Bratton D, Whyte G, Yang M, deMello AJ, Abell C, Hollfelder F (2009) Static microdroplet arrays: a microfluidic device for droplet trapping, incubation and release for enzymatic and cell-based assays. Lab Chip 9:692. https://doi.org/10.1039/B813709A

Jousse F, Farr R, Link DR, Fuerstman MJ, Garstecki P (2006) Bifurcation of droplet flows within capillaries. Phys Rev E 74(3):036311

Korczyk PM, Derzsi L, Jakieła S, Garstecki P (2013) Microfluidic traps for hard-wired operations on droplets. Lab Chip 13(20):4096. https://doi.org/10.1039/C3LC50347J

Labrot V, Schindler M, Guillot P, Colin A, Joanicot M (2009) Extracting the hydrodynamic resistance of droplets from their behavior in microchannel networks. Biomicrofluidics 3(1):012804. https://doi.org/10.1063/1.3109686

Link DR, Anna SL, Weitz DA, Stone HA (2004) Geometrically mediated breakup of drops in microfluidic devices. Phys Rev Lett 92(5):054503. https://doi.org/10.1103/PhysRevLett.92.054503

Maddala J, Vanapalli SA, Rengaswamy R (2014) Origin of periodic and chaotic dynamics due to drops moving in a microfluidic loop device. Phys. Rev. E 89(2):023015. https://doi.org/10.1103/PhysRevE.89.023015

Ménétrier-Deremble L, Tabeling P (2006) Droplet breakup in microfluidic junctions of arbitrary angles. Phys Rev E 74(3):035303

Park J, Jung JH, Park K, Destgeer G, Ahmed H, Ahmad R, Sung HJ (2018) On-demand acoustic droplet splitting and steering in a disposable microfluidic chip. Lab Chip 18(3):422

Parthiban P, Khan SA (2013) Bistability in droplet traffic at asymmetric microfluidic junctions. Biomicrofluidics 7(4):044123

Pit AM, Duits MHG, Mugele F (2015) Droplet manipulations in two phase flow microfluidics. Micromachines 6(11):1768. https://doi.org/10.3390/mi6111455

Salkin L, Schmit A, Courbin L, Panizza P (2013) Passive breakups of isolated drops and one-dimensional assemblies of drops in microfluidic geometries: experiments and models. Lab Chip 13:3022. https://doi.org/10.1039/C3LC00040K

Schindler M, Ajdari A (2008) Droplet traffic in microfluidic networks: a simple model for understanding and designing. Phys Rev Lett 100:044501. https://doi.org/10.1103/PhysRevLett.100.044501

Sun X, Zhu C, Fu T, Ma Y, Li HZ (2018) Dynamics of droplet breakup and formation of satellite droplets in a microfluidic t-junction. Chem Eng Sci 188:158

Tan YC, Ho YL, Lee AP (2007) Microfluidic sorting of droplets by size. Microfluid Nanofluid 4(4):343. https://doi.org/10.1007/s10404-007-0184-1

Taylor ZJ, Gurka R, Kopp GA, Liberzon A (2010) Long-duration time-resolved PIV to study unsteady aerodynamics. IEEE Trans Instrum Meas 59(12):3262

Tice JD, Song H, Lyon AD, Ismagilov RF (2003) Formation of droplets and mixing in multiphase microfluidics at low values of the reynolds and the capillary numbers. Langmuir 19(22):9127

van Steijn V, Korczyk PM, Derzsi L, Abate AR, Weitz DA, Garstecki P (2013) Block-and-break generation of microdroplets with fixed volume. Biomicrofluidics 7(2):024108

Wang WS, Vanapalli SA (2014) Millifluidics as a simple tool to optimize droplet networks: case study on drop traffic in a bifurcated loop. Biomicrofluidics 8(6):064111

Wang X, Liu Z, Pang Y (2018) Droplet breakup in an asymmetric bifurcation with two angled branches. Chem Eng Sci 188:11. https://doi.org/10.1016/j.ces.2018.05.003

Wang X, Liu Z, Pang Y (2019) Breakup dynamics of droplets in an asymmetric bifurcation by μpiv and theoretical investigations. Chem Eng Sci 197:258. https://doi.org/10.1016/j.ces.2018.12.030

Zaremba D, Blonski S, Jachimek M, Marijnissen M, Jakiela S, Korczyk P (2018) Investigations of modular microfluidic geometries for passive manipulations on droplets. Bull Pol Acad Tech 66:2

Zhang K, Liang Q, Ma S, Mu X, Hu P, Wang Y, Luo G (2009) On-chip manipulation of continuous picoliter-volume superparamagnetic droplets using a magnetic force. Lab Chip 9:2992. https://doi.org/10.1039/B906229G

Lab on a Chip

Check for updates

Integration of capillary–hydrodynamic logic circuitries for built-in control over multiple droplets in microfluidic networks†

Damian Zaremba, [iD] * Sławomir Błoński [iD] and Piotr M. Korczyk [iD] *

Here, we show the successful implementation of advanced sequential logic in droplet microfluidics, whose principles rely on capillary wells establishing stationary states, where droplets can communicate remotely *via* pressure impulses, influencing each other and switching the device states. All logic operations perform spontaneously due to the utilization of nothing more than capillary–hydrodynamic interactions, inherent for the confined biphasic flow. Our approach offers integration feasibility allowing to encode unprecedentedly long algorithms, *e.g.*, 1000-droplet counting. This work has the potential for the advancement of liquid computers and thereby could participate in the development of the next generation of portable microfluidic systems with embedded control, enabling applications from single-cell analysis and biochemical assays to materials science.

Introduction

The implementation of the idea of liquid computer[1] would be revolutionary for microfluidics, not because microfluidics seeks computational capabilities, but because it would enable the encoding of a variety of algorithms (laboratory procedures) into the structure of the device.

In terms of miniaturization and complexity of performed tasks, microfluidics is often compared to microelectronics.[2] The promising vision is that the miniaturization and increase of operational throughput, so fruitful in computer engineering, would be implemented in control over small liquid volumes, thus opening a new era for sample processing and analysis techniques. However, one of the remaining problems in microfluidics is the implementation of the fundamental concept of electronics: the control embedded in integrated circuits. In microelectronics, the most fundamental level is constituted by base modules, where both input and output are of the same nature—they are electric signals. Thus, different elements can be combined directly with each other into hierarchical self-regulated circuitries. Despite their incredible complexity, electronic architectures, *e.g.*, microprocessors, are completely

Institute of Fundamental Technological Research, Polish Academy of Sciences, Pawinskiego 5B, 02-106 Warsaw, Poland. E-mail: dzaremba@ippt.pan.pl, piotr.korczyk@ippt.pan.pl

† Electronic supplementary information (ESI) available: Supplementary notes, supplementary movies and list of supplementary movies. See DOI: 10.1039/d0lc00900h

autonomous; besides the input data and energy supply, they do not require any additional control.

In microfluidics, in contrast, liquids are usually operated by valves, electrodes, pumps, *etc.* that are centrally controlled by a computer.[3–5] This requires the microchannels to be designed to be connectable with the electromechanical regulatory system, the intricacy of which usually increases with the complexity of the laboratory task.[6]

In the article, we focus on two-phase flows in microchannels, where droplets can be formed and used as tiny laboratory beakers. Microfluidics has developed manipulation techniques for droplets enabling such operations such as splitting, merging and positioning.[4,5,7,8] The combinatorial sequences of base operations allow for the implementation of any laboratory procedure. The precision, low consumption of reagents, and automation capabilities render this technology increasingly attractive for biological and chemical experimentations.[8–10]

Droplets are predominantly manipulated by computer-controlled external actuators.[4,5] An intriguing alternative is an idea of a liquid computer[1] with droplets as digital entities self-regulating *via* coupling capillary and hydrodynamic interactions in specially designed geometries.

Thus far, some alternative strategies of the embedded control devices for both single-phase flow[11–14] and droplets[4,15–23] have been proposed. In the case of droplets, the system that is probably the closest to computer technology is the system presented by Katsikis *et al.*,[20] where automated tasks were performed on ferromagnetic droplets activated by a rotating external magnetic field. Actually, droplets in microfluidics do not require any additional force

to be self-regulated, which is important for a variety of applications, where droplets can not be ferromagnetic. The intriguing aspect of confined, biphasic microflows is that the surface tension is relatively large and introduces non-linearity into Stokes flows, opening the perspectives for purely hydrodynamic built-in control. Prior examples exploiting this approach encompass cascades of consecutive dissolution encoded by the use of hydrodynamic traps.[17–19] However, without logic elements, the coding capabilities of such systems are insufficient for the programming of arbitrary algorithms. Although single logic operations were shown in pressure-regulated flows of droplets over a decade ago,[15,16,24] their further integration has proved difficult, inhibiting the creation of systems with nontrivial functionalities. Advanced built-in control remains one of the most important and open problems of microfluidics, hampering the development of autonomous and portable devices in line with the lab-on-a-chip concept.

Here, we address this issue and propose a droplet logic platform enabling the building of sequential logic units with multiple internal states. We use water droplets that do not wet the channel walls, surrounded by oil as the continuous phase (CP) that wets the channel walls. Droplets larger than the channel cross-section are squashed between walls. This peculiar environment limits the height of droplets to dimensions where capillarity dominates over gravity, rendering the latter negligible. Thus, the capillarity, minimizing the surface area, forms elongated plug-shaped droplets with rounded ends.[25] The interface curvature introduces the capillary pressure difference P_L, sustained across the interface and described by the Young–Laplace equation, which for a droplet confined by the rectangular channel of width W and height H and the surface tension γ can be estimated as $P_L = \gamma(2H^{-1} - 2W^{-1})$. Here, we assume the shape of the droplet's end to be prescribed by circles spanned between opposite walls of radii $W/2$ and $H/2$, respectively.

The dependence of P_L on the local dimensions of the duct implies that the transfer of a droplet to the more constricted region increases the pressure inside the droplet. Thus, a change of the channel lumen can be used to establish a capillary well for the droplet.[26]

A convenient way to introduce such a barrier for droplets is to provide obstacles that locally decrease the height of the channel from H to ω (Fig. 1a). In crossing the obstacle, a droplet penetrates the narrow slit, developing there the protrusion with curvature radii $\omega/2$ and $W/2$ (Fig. 1a). Hence, the breakthrough pressure P_B, defined as a difference of P_L between the front and the back of a droplet, is:

$$P_B = \gamma(2\omega^{-1} - 2W^{-1}) - \gamma(2H^{-1} - 2W^{-1}) = 2\gamma(\omega^{-1} - H^{-1})$$

The droplet crossing the obstacle raises the pressure behind it to P_B (Fig. 1b), generating the pressure impulse, which propagates in the network, carrying the information about the droplet travelling through the barrier. However, until the pressure drop acting across the droplet reaches P_B, the
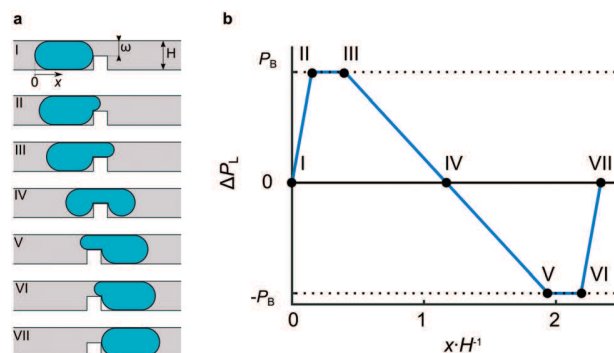
Fig. 1 The evolution of a droplet shape when crossing a barrier in a channel. (a) Schematic side view of the channel with a barrier. H and ω – the height of the channel and the slit above the obstacle, respectively. (I–VII) Consecutive shapes of a droplet during its travel across the barrier from left to right. (b) Difference of Laplace pressure between the front and the back of a droplet (estimated from curvatures) as a function of the position of a droplet x relative to the obstacle and normalized by H. The roman numbers (I–VII) correspond to the pictures in (a).

droplet cannot cross the barrier. Such a situation can occur in microfluidic networks distributing the flow of CP between parallel structures, where a droplet can be effectively immobilized at the capillary barrier while the entire stream of CP flows around through bypasses.[18,23,26]

In this work, we exploit both these advantages of the use of obstacles—the generation of a pressure impulse and droplet trapping. We design microfluidic structures with stationary droplets assigned to logic states, where pressure impulses are used for remote communication and for triggering the device's embedded logic operations for the sequential switching of states. We present this idea starting from the experimental analysis of a simple example of a two-state flip-flop device. Then, we develop the multi-state decimal ring-counter. Finally, we demonstrate the feasibility of the integration of such devices with the example of the three-fold decimal counter counting 1000 droplets.

Results and discussion

Bimodal loop

First, let us consider a simple loop, which bifurcates the incoming flow between two branches and then merges them into one output. Simple laminar hydrodynamics explains that the pressure drop Δp in a channel is proportional to the flow rate Q with the linear relation $\Delta p = RQ$ (ref. 27 and 28) introducing the resistance R proportional to the length of the channel and inversely proportional to the square of the cross-sectional area.[27] Analysis of the loop as two parallel resistors implies that the incoming stream distributes between branches with the ratio of flow rates inversely proportional to the ratio of the resistances of the branches (see methods). Therefore, in the case of an asymmetric loop, the flow through the branch of lower resistance is the faster one. While such a single-phase flow is steady, groups of flowing droplets distribute between

branches of the loop in a highly dynamic way, disclosing complex periodic or chaotic behaviour.[21,29] The reason is that the feedback mechanism was introduced by the droplets, which prefer the channel of the higher flow rate while also lowering the flow through the channel they resided in.[29]

Here, we present the construction of a loop, where the flow of droplets is deterministic, reproducible, and exhibits the functionality of a simple finite state machine. Our design (Fig. 2a) comprises two unequal branches with obstacles (Fig. 2b) in each of them (for practical reasons, the dimensions of these obstacles vary slightly – see methods). As we can expect, the first droplet entering the loop travels to the shorter and faster branch until it reaches the obstacle there (Fig. 2c). In the series of trials, we set the constant input flow rate Q_{in} sufficiently low to keep the first droplet immobilized in such a configuration (see methods). Therefore, even if the short branch is blocked by the droplet ($Q_{short} = 0$), directing the whole flow to the longer branch ($Q_{long} = Q_{in}$), the generated pressure drop does not exceed the breakthrough pressure of the obstacle, $Q_{in}R_{long} < P_B$. Here, Q_{short} and Q_{long} are the flow rates in the short and the long branch of the loop, respectively, and R_{long} is the resistance of the long branch.

Such an altered flow of CP moves the second droplet to the long branch. Hereby, the second droplet 'knows' about the first droplet occupying the short branch and 'decides' adequately (Fig. 2d). When the second droplet reaches the obstacle in the long branch (Fig. 2e), both channels become obstructed, and the incoming flow of the CP builds up the pressure behind droplets, exceeding breakthrough pressure and allowing both droplets to cross the obstacles simultaneously (Fig. 2e). In this way, the first droplet, previously immobilized in the short branch, is now released (Fig. 2f), and then both droplets leave the loop, resetting the state of the device to the initial condition (Fig. 2g). Each consecutive pair of droplets repeats the above sequence.

The presented system exhibits the functionality of the so-called flip-flop sequential logic unit with two internal states defining different functionalities of obstacles: the presence of a droplet at the state-obstacle in the short channel indicates the excited state, while the other trigger-obstacle initiates a reset to the ground state without any droplet in the loop.

We conducted the quantitative investigation of the device operation *via* the analysis of the selected pixels' brightness in consecutive frames of the movie recorded during the experiments (see methods). Thanks to that, we retrieved the time-dependent digital signals, which assume only values of 0 or 1, corresponding to a droplet's absence or presence at a given point, respectively (see methods for more details). The signals from the selected points of the device put together in the form of timing diagrams (Fig. 2h and i) show the device's repetitive operation.

Decimal counter

In the considered above bi-modal loop, the first droplet enters the branch of lower resistance. As we showed in our
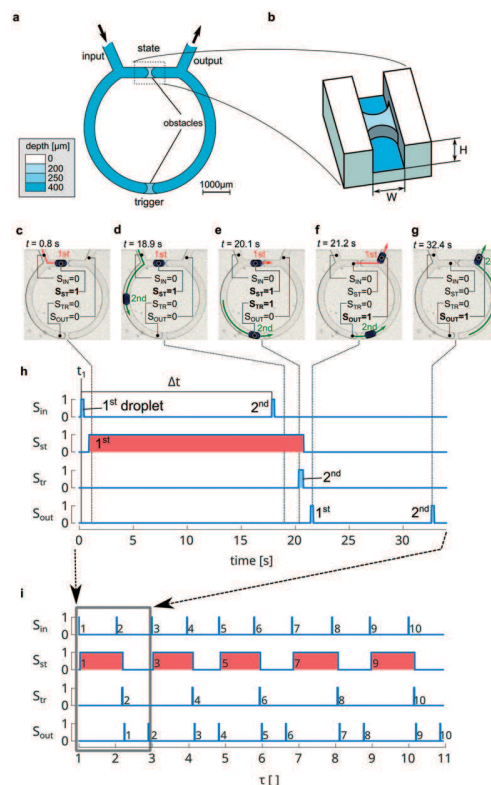
Fig. 2 Bimodal loop. (a) Schematic view of the bimodal loop. (b) 3D view of an obstacle fabricated by milling. (c–g) Experimental micrographs of the flow of two consecutive droplets through the bimodal loop (see Movie S1†). Black dots – positions of the measurements of droplet-presence-signals; S_{in} (in the inlet), S_{st} (at the state), S_{tr} (at the trigger), and S_{out} (in the outlet). The signals were obtained by the analysis of the brightness of pixels (see methods), where two values, 0 and 1, are assigned to the absence and the presence of a droplet, respectively. (h) Timing diagrams presenting all signals together during the flow of the two droplets as a function of time. Droplets in motion occupy a given position for a relatively short time, thus marking narrow peaks in time-diagrams. The spikes in S_{in} indicate consecutive droplets entering the system and can be seen as a digital clock-signal. Soon after the peak of the first droplet in S_{in}, the 'state' signal S_{st} assumes value 1, and the droplet is immobilized at this position. After the next peak of S_{in} indicating the entrance of the second droplet, the peak of S_{tr} appears with the delay proportional to the distance between input and trigger positions. Simultaneously, with the S_{tr}-peak, the S_{st} assumes value 0, and the first droplet leaves the static state position. Then, two peaks of S_{out} appear, indicating the release of both droplets from the device. After that, the device resets to its ground state (without droplets). (i) The repeatability of the process – timing diagrams for the sequence of 10 droplets as functions of dimensionless time τ, where $\tau = $ (time $- t_1 + \Delta t)/\Delta t$: t_1 is the time of the appearance of the first droplet and Δt is the mean delay interval between droplets (see (h)). The rounded down value of dimensionless time τ corresponds to the total number of droplets, which have been introduced to the device so far. For the convenience, we will use the dimensionless time τ in the subsequent analysis in this article. After the first pair of droplets, the next third and fourth droplets entering the system reproduce the identical sequence. Thus, the process is reproduced for each consecutive pair of droplets. For the reference, the rectangle shows the part of the timing diagram for the first two droplets equivalent to the whole time-diagram showed in (h). The mean time interval between two consecutive droplets entering the loop was $\Delta t = 17.2$ s, equivalent to the frequency of operations which is equal to 0.058 Hz.

previous work,[30] a modified junction with a slit can fix the custom direction of a droplet regardless of the resistances of the branches. Such a solution provides a higher degree of control, allowing the direction of the first droplet to the long branch and swapping functionalities between loop-branches. Thus, we can put the trigger-obstacle in the short branch, while the state-obstacle is in the long branch (see Note S1 and Movie S2†).

In the next example (Fig. 3), we use such a modified junction (Fig. 3b) to place 9 subsequent state-obstacles in the long branch (Fig. 3a); hence, accounting for the empty loop as the 0-state, the device exhibits ten states (Fig. 3h). The first droplet entering such a refashioned loop halts at the first

obstacle in the long branch assigned to the first state (Fig. 3c). As in the bi-modal loop, the next droplet chooses the opposite, empty branch—in this case, the shorter one (Fig. 3d)—and after touching the trigger-obstacle, it releases the state-droplet from the first state (Fig. 3e). The state-droplet keeps moving until it meets the next obstacle (Fig. 3f), then sets the second state (Fig. 3g). Each subsequent droplet moves the state-droplet one obstacle forward so that its current position corresponds to the count of all droplets that have been introduced to the loop thus far (Fig. 3h and see Movie S3†). After the 10th droplet, the state-droplet leaves the loop, resetting it to the ground state, and the sequence starts from the beginning (Fig. 3i).

Permutations

In addition to the obvious analogy to the 10-modulo ring-counter, the device performs a transformation by rearranging the initial droplet sequence. Indeed, all droplets from the second to 10th one leave the system before the first droplet. Thus, the device performs the circular shift permutation $\sigma(i) = (i + 1)$ modulo 10, transforming the sequence (1 2 3 4 5 6 7 8 9 10) into (2 3 4 5 6 7 8 9 10 1).

In order to increase the spectrum of permutations available, we can use the serial combinations of the ring-counters utilizing the fact that more complex permutation can be decomposed into a series of base permutations, e.g., in computational science, the Heap's[31] algorithm is used for the efficient generation of all possible permutations. The target permutation is decomposed into the series of operations, wherein the single step, only a single pair of elements interchanges.

The application of modified Heap's algorithm allows the achievement of wide spectrum of permutations by combining different circular shift permutations in a series, e.g., permutation transforming the sequence (1 2 3 4 5 6) into (6 5 4 3 2 1), as presented in Fig. 4 and Movie S4.†

Fig. 3 The decimal counter. (a) The schematic top view of the counter with a trigger-barrier in the short branch and 9 state-barriers in the longer branch. (b) 3D view of the special junction with a slit used to direct the first droplet to the longer branch.[27] (c–g) Experimental micrographs of the flow of two subsequent droplets introduced to the counter (see Movie S3†). (h) The position of the indicator-droplet assigned to the state number i corresponding to the occupied state position. The empty device is assigned to $i = 0$. (i) Signals of the presence of a droplet S_i from all 9 positions measured continuously during the introduction of the series of 13 consecutive droplets. The presence of the state-droplet at each i-th position was analysed by the use of brightness analysis of pixels and assigned to the digital signal S_i (see methods). (j) The readout of the current count. Due to the orthogonality of signals S_i, the instantaneous vector of 9 signal values can be transformed into one value of the readout (see methods). The value of the readout (from 0 to 9) indicates the currently active state and equals the result of the counting. The mean time interval between two consecutive droplets entering the counter was $\Delta t = 2.7$ s, equivalent to counting 0.37 droplets per second.

Fig. 4 Microfluidic system performing permutation of the set (1 2 3 4 5 6) into (6 5 4 3 2 1). (a and b) Schemes of the microfluidic loops performing base permutations. (a) 'SWAP' permutation: (1 2) into (2 1). (b) 'ROTATE' permutation: (1 2 3) into (2 3 1). (c) The scheme of the permutation-device consisting of base permutation-loops, 'SWAP' and 'ROTATE', connected in series. (d) The photo of the fabricated device used in Movie S4.† The single permutation of six droplets was completed within about 100 s.

Three-fold decimal counter

The advanced finite state machines in microelectronics utilize the integration of multiple elements in cascades so that the number of all available states is the multiplication of states of all connected components. For example, n bimodal loops create a binary counter comprising 2^n states (see Note S2 and Movie S5†).

To integrate the decimal counters in a series, we augmented the previous design with two separate outlets: the excess-output and the signal-output channels (Fig. 5a, Note S3 and Movie S6†). Two corresponding inlets ensure the compatibility for connections of subsequent units. Such a

construction separates the trigger droplets from the state droplets. Droplets that have passed through the trigger branch are directed to the excess-output (Fig. 5b). Thus, the excess collector channel receives trigger-droplets from all antecedent counters. The state-droplet leaving a counter enters the signal-inlet of a subsequent counter, thus transmitting the information about each count of 10 to the next counter (Fig. 5c). We integrated three such modules, obtaining a 3-fold decimal counter (Fig. 5b). In such a system, the first so-called 1×-counter counts units, and after the enumeration of each 10 droplets, it sends the signal-droplet to the next 10×-counter, which counts tens. Consequently, the third 100×-counter receives a signal from the 10×-counter and enumerates hundreds of droplets. The running result of the count can be directly read out from the positions of the droplets in the counters (Fig. 5d and e). The experiments showed that the 3-fold counter works without errors, correctly processing every 1000 droplets (Fig. 5f and Movie S7†).

Conclusions

In the article, we aimed to restore, and substantially advance, the original idea of purely hydrodynamic-regulated droplet logic,[15] whose beauty consists in the utilization of nothing more than the interactions inherent for the confined biphasic flow.

The examples of systems that we demonstrated here showed that the large-scale integration of microfluidic logic circuitries is feasible and can facilitate the device's embedded encoding of the arbitrary analytical algorithm executed on multiple beaker-like droplets. The exploration of this field is promising for the development of lab-on-a-chip devices *inter alia* for medical diagnosis and biochemical analysis.

In terms of the speed of operation, the presented devices, performing about 1 operation per second, may look modest, especially when compared with high-throughput automated systems, *e.g.*, for droplet sorting or cells counting. Indeed, the maximal flow-rate and the efficiency are limited in order to satisfy demanding conditions imposed by capillary well's concept. However, the presented technology is attractive for the applications demanding embedded control and high accuracy of the combinatorial algorithms more than the high throughput.

The implementation of advanced assays in portable devices is one of the main motivations stimulating the development of microfluidics. Modern analytical methods like digital PCR or screening rely on the processing of multiple independent compartments of the sample.[9] Thanks to the use of droplets as tiny beakers, microfluidic techniques offer the minimization of the volume of single compartments, capacity for the processing of a large number of aliquots, and precise manipulation techniques, which can be applied to every droplet individually.[32]

The development of microfluidic methods must account for seemingly contradictory market-related demands – the optimization of the compactness, portability, and ease of use
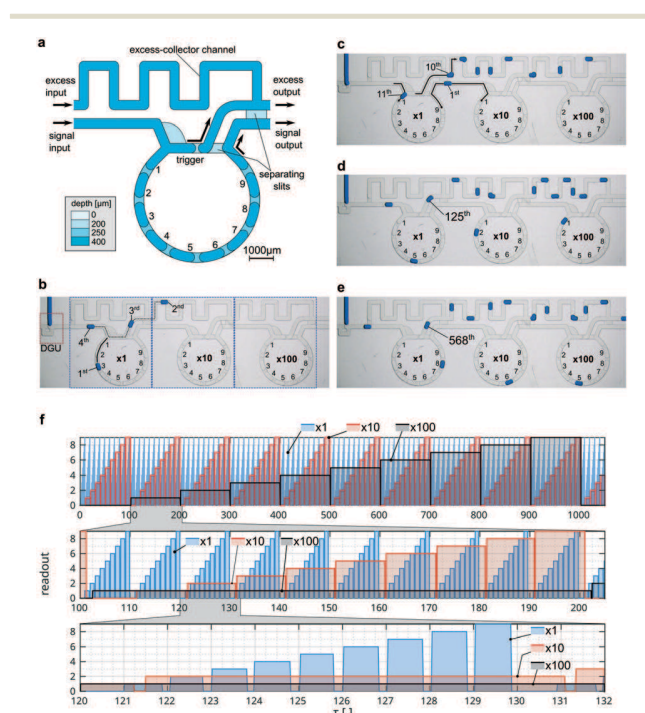
Fig. 5 The 3-fold cascade decimal counter. (a) The schematic top view of the single counting-module. (b) Photo of the whole device (taken after the counting of three droplets) with highlighted droplet generation unit (DGU) and three counting-modules. The black dotted line shows the trajectory of trigger-droplets, which travel *via* the excess output into the excess-collector channel of the subsequent clock-module. (c) The mechanism of the signal transfer between subsequent counting-modules. The 10th droplet triggers the release of the state-droplet from the 1×-counter. The state droplet travels through the signal channel to the 10× counter and stops at the first state position initiating the count of tens. The 11th droplet enters the empty 1×-counter and initiates the next unit's counting sequence. (d and e) Micro-graphs showing examples of the instantaneous positions of droplets for 125 and 568 counted droplets, respectively. (f) The readout from all counters together. We obtained the readout for each counting-module separately, as described in methods. The top – the sequence of 1050 droplets. The middle – magnification for the range from 100 to 205 droplets. The bottom – magnification for droplets from 120 to 132. The visible delay between signals from different counters is caused by the time the signal-droplet needs to travel between subsequent modules. The mean time interval between two consecutive droplets entering the counter was Δt = 0.91 s, equivalent to counting 1.1 droplets per second.

on the one hand, *versus* the increasing complexity of laboratory algorithms on the other hand.

Thus, the integrated fluidic logic in microfluidics appears as an attractive solution, offering both the passive regulation in place of mechanical activators and the encoding of advanced procedures in the architecture of the device.

We showed that our logic platform enables a variety of concepts of microelectronics to be applied to droplet microfluidics. Besides the examples presented in the article, we can mention some other modules that can emerge *via* further modifications and combinations of already known structures, *e.g.*, an adjusted version of the bimodal device can work as a set/reset flip-flop for the synchronization of droplets from two different sources (see Note S4 and Movie S8†). Another solution can distribute droplets from a single channel to several parallel ducts in ordered combination (*e.g.*, see Note S5 and Movie S9†). Such a joint or a split of outputs is well-known in electronics as a multiplexer and demultiplexer, respectively. They allow for the implementation of droplet buses in microfluidic devices similar to the data bus in computer processors.

In this preliminary research, we focused on the presentation of the feasibility of the large scale integration, providing the principles of the design and fabrication of logic circuitries. The advantage of the presented platform is that its elements can be connected (in series or in parallel) with other microfluidic modules.

In the next step, we envision the combination of logic structures with hydrodynamic traps,[18] which can process the content of droplets thanks to the operations like merging and splitting of droplets. This set of functions is enough to mix the content of two droplets and divide it into even parts again. In this way, two droplets align the concentrations of reagents or interchange the populations of bacteria or cells.

As we showed in the previous work,[18] the iterative repetition of this procedure to the series of droplets dissolves the reagent from the first droplet gradually in droplets containing the buffer, finally resulting in the array of droplets with descending concentrations. Such an operation can be seen and described as a numerical low-pass filter processing the initial vector of concentrations represented by a series of input droplets. The logic operations can facilitate both the setting of the custom input vector of droplets and the realization of more complex procedures represented by other numerical filters.

The examples presented in the article allow for the synchronization of droplets from different sources and their permutations. Hence, two kinds of droplets (with and without the reagent) can be independently generated and then arranged in the desired order so that the application of the filter would result in the custom shape of the output signal of concentration distributions, *e.g.*, sinus, saw-tooth, triangular, *etc.* The output stream of droplets can be permutated and processed again by the use of droplet to droplet interchange. Such an iterative approach allows for the realization of more advanced algorithms improving the dynamical range of the concentration control.

The microfluidic hardware with built-in algorithms manipulating the concentration of reagents in droplets and interchanging the microbial populations can advance the application and development of biological assays utilizing statistical analysis of numerous sample divisions. Thus, we envision that integrated logic circuitries are a promising field of exploration as a potential direction of future microfluidics evolution.

Materials and methods

Device fabrication

All the presented devices were fabricated by the milling of channels, obstacles, and slits in a plate of polycarbonate (Macrolon, Bayer, Germany) using a CNC milling machine (Ergwind, Poland) with a reproducibility of the positioning of 5 μm. The chips with channels were bonded to flat slabs of polycarbonate using a hot press at 135 °C for 10 minutes. No further channel modifications were applied.

The height and width of the square cross-section of regular channels were 400 μm. In the course of numerous trials, for the more reliable performance of the logic systems, the dimensions of obstacles in the long and the short branch of the loop were varied. We fabricated the obstacle in the short branch with a width of 100 μm (measured along the central axis of the channel) and a height of 200 μm (depth of the gap above – ω = 200 μm), while the obstacle in the long branch had a width of 150 μm and height of 150 μm (depth of the gap above – ω = 250 μm). Varying dimensions allow for the compensation of the contrast of resistances between branches, thus improving the robustness of the microfluidic logic systems. The height of all other slits in the modified junctions or those connecting channels was 200 μm.

Liquids and flow control

To feed our systems with liquids, we used Nemesis pumps (Cetoni GmbH, Germany) with glass syringes connected to the inlets of the devices *via* PE-60 tubing (Beckton-Dickinson, USA). In all experiments, we used two syringe pumps for independent injection of two immiscible liquids. The outlet channel was connected through the tubing to the waste container.

We used hexadecane (Sigma Aldrich Co.) with the addition of 1.3% Span 80 (Sigma Aldrich Co.) as the CP and Milli-Q water as the droplet phase (DP). The DP was coloured by methylene blue to increase the contrast between liquids for the better visualization of droplets and for image analysis improvement. The viscosity of the CP was estimated *via* the measurement of the time within which the fixed volume of the liquid flows through the calibrated capillary under a known pressure drop. The viscosity of liquids (at 22 °C) was 3.6 mPa s for CP and 0.95 mPa s for DP. The interfacial tension was measured by means of a pending droplet method and for our set of liquids was 4.8 mN m^{-1} (at 22 °C).

Distribution of flows in a loop-like channels

The simple loop bifurcates the incoming flow Q_{in} between two streams, Q_1 and Q_2, in the two branches and then merges them into one output, $Q_{out} = Q_{in}$. Analysing the single-phase flow of CP, we use the linear Ohm-like[28] relation $\Delta p = RQ$, relating pressure drop Δp to flow rate Q. $R = \alpha \mu_C L A^{-2}$ is a hydraulic resistance, where α is a geometrical factor,[27] μ_C is the dynamic viscosity of CP, and L and A are the length and cross-sectional area of the channel, respectively. Considering the loop as a parallel circuit of two resistors, we obtain the splitting ratio $Q_1/Q_2 = R_2/R_1 = L_2/L_1$, implying that the flow through the shorter branch (with lower resistance) is the faster one.

The breakthrough pressure estimation

We estimated the breakthrough pressure experimentally for both dimensions of the obstacles used in this paper. For this purpose, we fabricated two loop devices (for each geometry of the obstacle) with only one obstacle in the short branch. After placing one droplet at the obstacle, we increased the flow rate of CP until the droplet was removed from the loop. In this way, in the series of trials, we estimated the critical flow rate Q_{crit}, which demarcates the transition between immobilization and passing-through modes.

Then, the values of breakthrough pressure were calculated using the relation $P_B = R_{long} \times Q_{crit}$. Here, we assume that the whole flow is through the long branch only and $R_{long} = \alpha \mu_C L A^{-2}$, where $\alpha = 28.4$ is the geometrical coefficient of the square-shape cross-section of the channel, μ_C is the viscosity of CP, $L = 6.9$ mm is the length of the long branch, and $A = H \times W = (400 \ \mu m)^2$ is the cross-sectional area. The values of breakthrough pressure, estimated in the above-described way, are 7.78 ± 0.37 Pa and 12.59 ± 0.37 Pa for the obstacles of the slit depth ω which is equal to 250 μm and 200 μm, respectively.

Droplet generation

Droplets were produced in the block-and-brake type T-junction generator,[33] which produces droplets of similar size regardless of the ratio of rates of flow of both phases[34] (see Note S6†). This solution ensures the appropriate size of droplets required for the correct performance of microfluidic logic units. The other factor that needed to be adjusted was the frequency of droplets, which could not be too high. Stationary flows of both phases yielded a constant frequency of mono-dispersed droplet generation.

Image acquisition

The sequences of droplets flowing through the investigated microfluidic devices were observed by the use of a stereoscope (Huvitz HSZ-645TR) equipped with a CCD camera (IDS UI-3274LE-C-HQ) to record movies during the experiments. The recorded movies were stored for evidence and further analysis.

Measurement of the signal of the presence of droplets

The presence or absence of a droplet at a given point of the microfluidic network can be assigned to the signal, which assumes Boolean values. We obtained time-dependent signals from experiments *via* analysis of the light intensity of selected pixels in the recorded movies. Due to the enhanced contrast between both liquid phases, the value of intensity fluctuates between two well-distinguishable levels. Applying an appropriate threshold (average of extreme values) yields a digital signal assuming only values of 0 or 1, indicating the absence or presence of a droplet, respectively.

The readout of the droplet counting

All signals $S_i(t)$ from the decimal counter (see Fig. 3i) are orthogonal ($\langle S_i(t) | S_j(t) \rangle = \delta_{ij}$), which means that only one state can be active at one time, so the product of signals from different state positions is 0. This feature can be used for the transformation of the vector of the 9 signal values into only one value of the readout: $\text{readout}(t) = \sum_{i=1}^{9} i \times S_i(t)$. Such a transformation yields the number from 0 to 9, indicating the currently active state. The readout equals the modulo-10 counting of droplets.

Conflicts of interest

There are no conflicts to declare.

Acknowledgements

Notes and references

1 A. Adamatzky, *Philos. Trans. R. Soc., B*, 2019, **374**, 20180372.
2 G. M. Whitesides, *Nature*, 2006, **442**, 368–373.
3 D. Mark, S. Haeberle, G. Roth, F. von Stetten and R. Zengerle, *Chem. Soc. Rev.*, 2010, **39**, 1153–1182.
4 A. M. Pit, M. H. G. Duits and F. Mugele, *Micromachines*, 2015, **6**, 1768–1793.
5 P. Zhu and L. Wang, *Lab Chip*, 2016, **17**, 34–75.
6 R. Gómez-Sjöberg, A. A. Leyrat, D. M. Pirone, C. S. Chen and S. R. Quake, *Anal. Chem.*, 2007, **79**, 8557–8563.
7 S.-Y. Teh, R. Lin, L.-H. Hung and A. P. Lee, *Lab Chip*, 2008, **8**, 198–220.
8 L. Shang, Y. Cheng and Y. Zhao, *Chem. Rev.*, 2017, **117**, 7964–8040.
9 T. S. Kaminski and P. Garstecki, *Chem. Soc. Rev.*, 2017, **46**, 6210–6226.

10 O. Scheler, W. Postek and P. Garstecki, *Curr. Opin. Biotechnol.*, 2019, **55**, 60–67.

11 B. Mosadegh, C.-H. Kuo, Y.-C. Tung, Y. Torisawa, T. Bersano-Begey, H. Tavana and S. Takayama, *Nat. Phys.*, 2010, **6**, 433–437.

12 S.-J. Kim, D. Lai, J. Y. Park, R. Yokokawa and S. Takayama, *Small*, 2012, **8**, 2925–2934.

13 P. N. Duncan, S. Ahrar and E. E. Hui, *Lab Chip*, 2015, **15**, 1360–1365.

14 D. J. Case, Y. Liu, I. Z. Kiss, J.-R. Angilella and A. E. Motter, *Nature*, 2019, **574**, 647–652.

15 M. Prakash and N. Gershenfeld, *Science*, 2007, **315**, 832–835.

16 L. F. Cheow, L. Yobas and D.-L. Kwong, *Appl. Phys. Lett.*, 2007, **90**, 054107.

17 X. Niu, F. Gielen, J. B. Edel and A. J. deMello, *Nat. Chem.*, 2011, **3**, 437–442.

18 P. M. Korczyk, L. Derzsi, S. Jakieła and P. Garstecki, *Lab Chip*, 2013, **13**, 4096–4102.

19 S. S. Bithi and S. A. Vanapalli, *Sci. Rep.*, 2017, **7**, 41707.

20 G. Katsikis, J. S. Cybulski and M. Prakash, *Nat. Phys.*, 2015, **11**, 588–596.

21 M. J. Fuerstman, P. Garstecki and G. M. Whitesides, *Science*, 2007, **315**, 828–832.

22 M. Zagnoni and J. M. Cooper, *Lab Chip*, 2010, **10**, 3069–3073.

23 P. Abbyad, R. Dangla, A. Alexandrou and C. N. Baroud, *Lab Chip*, 2011, **11**, 813–821.

24 M. W. Toepke, V. V. Abhyankar and D. J. Beebe, *Lab Chip*, 2007, **7**, 1449–1453.

25 C. N. Baroud, F. Gallaire and R. Dangla, *Lab Chip*, 2010, **10**, 2032–2045.

26 R. Dangla, S. Lee and C. N. Baroud, *Phys. Rev. Lett.*, 2011, **107**, 124501.

27 N. A. Mortensen, F. Okkels and H. Bruus, *Phys. Rev. E: Stat., Nonlinear, Soft Matter Phys.*, 2005, **71**, 057301.

28 K. W. Oh, K. Lee, B. Ahn and E. P. Furlani, *Lab Chip*, 2012, **12**, 515–545.

29 O. Cybulski, P. Garstecki and B. A. Grzybowski, *Nat. Phys.*, 2019, **15**, 706–713.

30 D. Zaremba, S. Blonski, M. J. Marijnissen and P. M. Korczyk, *Microfluid. Nanofluid.*, 2019, **23**, 55.

31 B. R. Heap, *Comput. J.*, 1963, **6**, 293–298.

32 S. Jakiela, T. S. Kaminski, O. Cybulski, D. B. Weibel and P. Garstecki, *Angew. Chem., Int. Ed.*, 2013, **52**, 8908–8911.

33 V. van Steijn, P. M. Korczyk, L. Derzsi, A. R. Abate, D. A. Weitz and P. Garstecki, *Biomicrofluidics*, 2013, **7**, 024108.

34 P. M. Korczyk, V. van Steijn, S. Blonski, D. Zaremba, D. A. Beattie and P. Garstecki, *Nat. Commun.*, 2019, **10**, 2528.

SUPPLEMENTARY INFORMATION

INTEGRATION OF CAPILLARY-HYDRODYNAMIC LOGIC CIRCUITRIES FOR BUILT-IN CONTROL OVER MULTIPLE DROPLETS IN MICROFLUIDIC NETWORKS

DAMIAN ZAREMBA[1]*, SLAWOMIR BLONSKI[1], PIOTR M. KORCZYK[1]*

1   Institute of Fundamental Technological Research, Polish Academy of Sciences, Pawinskiego 5B, 02-106 Warsaw, Poland

* Corresponding authors:

Damian Zaremba: dzaremba@ippt.pan.pl

Piotr M. Korczyk: piotr.korczyk@ippt.pan.pl

Supplementary Note 1
Bimodal loop with the modified junction

Here we present the bimodal loop with the modified junction to show how we can use the modification for the enhanced control on droplets motion.

In the bi-modal loop considered in the main article, the first droplet entered the branch of the smaller resistance (the shorter one). Here we use the modified junction with the slit to fix the custom direction of the first droplet regardless of the resistances of branches. Such a solution provides a higher degree of control, allowing to direct the first droplet to the long branch and swap functionalities between loop-branches.

Supplementary Fig. 1 shows the analysis of the motion of the pair of droplets through the modified junction. Thanks to the modification, unlike the case of the regular bimodal loop, the first droplet enters the long branch (compare Supplementary Fig. 1c and Supplementary Fig. 1d), where it stops at the obstacle setting the excited state. As a result, the functionalities of obstacles have been swapped: trigger-obstacle is placed now in the short branch while the state-obstacle in the long branch.
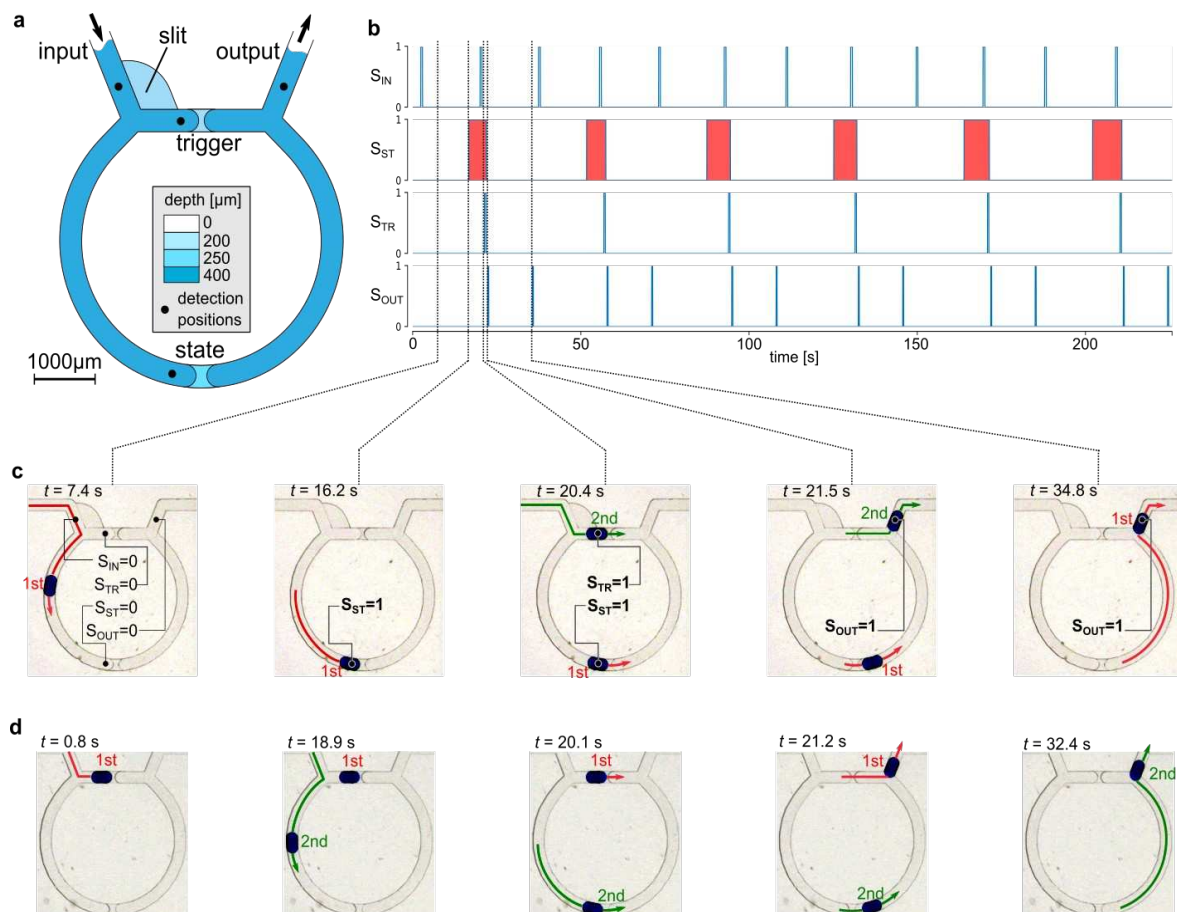
Supplementary Fig. 1 The bimodal loop with a slit in the input junction. **a** schematic view of the loop. Time diagram of the droplet-presence-signals. **c** experimental micrographs - the flow of two consecutive droplets through the bimodal loop with a modified junction, and **d** – micrographs from the regular junction for the reference.

As we showed in this example, a modified junction provides more flexibility for encoding the motion of droplets in a parallel system of channels.

The additional important implication is that in such a modified loop, the first droplet is released after the second one. The change of droplets order occurs because the trigger-obstacle lies closer to the outlet than the state-obstacle and, additionally, the flow-through the shorter branch is faster. Such a mechanism can be used for the realization of permutations, rearranging the order of droplet in the sequence.

Supplementary Note 2
Binary counter

We integrated serially four bimodal loops with a slit (see Supplementary Note 1) to obtain a binary counter. Optimizing the device for the increase of its operational speed, we reduced the lengths of both the trigger- and the state-branch in every single counting-module (see Supplementary Fig. 2a). Additionally, similarly to the design of the 3-fold decimal counter (see the Main Article and Supplementary Note 3), we augmented the bimodal loop with two separate outlets: the excess-output and the signal-output channels, respectively (see Supplementary Fig. 2a). Two corresponding inlets ensure the compatibility for connections of subsequent units. Such a construction ensures that after resetting the state in the bimodal loop, only one of two emitted droplets enters the signal-inlet of the following counter. The other droplet is directed to the excess collector channel. We integrated four such modules obtaining a 4-fold binary counter (see Supplementary Fig. 2b). In such a system, the state positions of 4 counter modules form the four-bits binary display (which assumes values from 0 to 15 – see Fig. 2d), where the result of the droplets counting can be readout. The experiments showed that the binary counter works without errors, correctly processing every 16 droplets (Fig. 2d and Supplementary Movie 5).

Unlike in the other systems presented in the paper, in the case of the binary counter we used standard T-junction droplet generator[1].
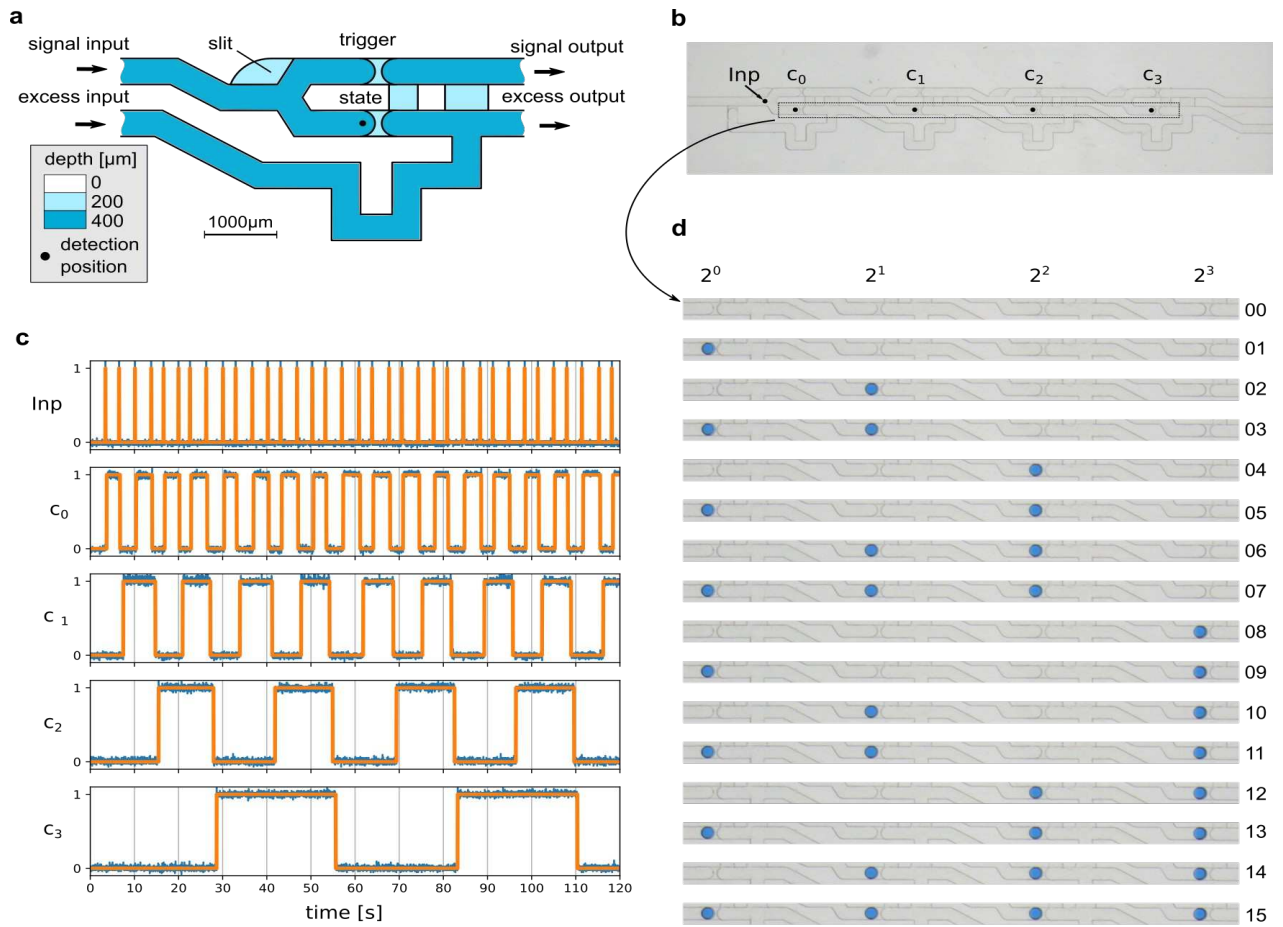
Supplementary Fig. 2 The 4-fold cascade binary counter. **a** schematic top view of the single counting-module. **b** photo of the whole device (taken before the start of droplets generation). Black dots – detection points for the droplet-presence-signals. Inp – the signal from droplets entering the system. C_0, C_1, C_2, C_3 – state-signals from each counting module. The black frame indicates the part of the device comprising of all state positions and can be seen as a binary 'display'. **c** time diagrams for all measured signals. The blue noisy lines – the brightness of pixels at the measurement position as a function of time (normalized and inverted so that the high value corresponds to the presence of a droplet). Orange lines – the digital droplet-presence-signals obtained by thresholding of the brightness signals. We can see that each subsequent module divides the incoming frequency by 2. This frequency division is well known in electronic binary counters. **d** experimental micrographs of the 'display' taken after introducing subsequent droplets. The number of introduced droplets is shown in right column. The readout from the display equals $\sum_{i=0}^{3} c_i \cdot 2^i$ where c_i assumes value 1 for the presence of a droplet at i-th position or 0 for its absence. So the 'display' accurately indicates the result of the droplets counting (see Supplementary Movie 5).

5

Supplementary Note 3
Decimal counter with two outlets

  In order to adapt the decimal counter loop to the cascade-integration, we augmented it with two outputs. This solution enables the separation of trigger-droplets from the droplets leaving the state branch. In such a way, 10th droplet, and generally the last droplet per every ten droplets, is directed to separate output and is used as a signal informing about the counting of 10 droplets (see Fig. 3). The additional slit connecting the outputs allows for the flow of continuous liquid while ensures separation of the routs of droplets outgoing from opposite branches of the loop. That element reduces the pressure difference between outlets ensuring similar hydrodynamic conditions as in the case of the decimal loop with a single output.

  As we showed in the Main Article, the decimal counter with two outlets allows for effective cascade integration of multiple decimal counters.
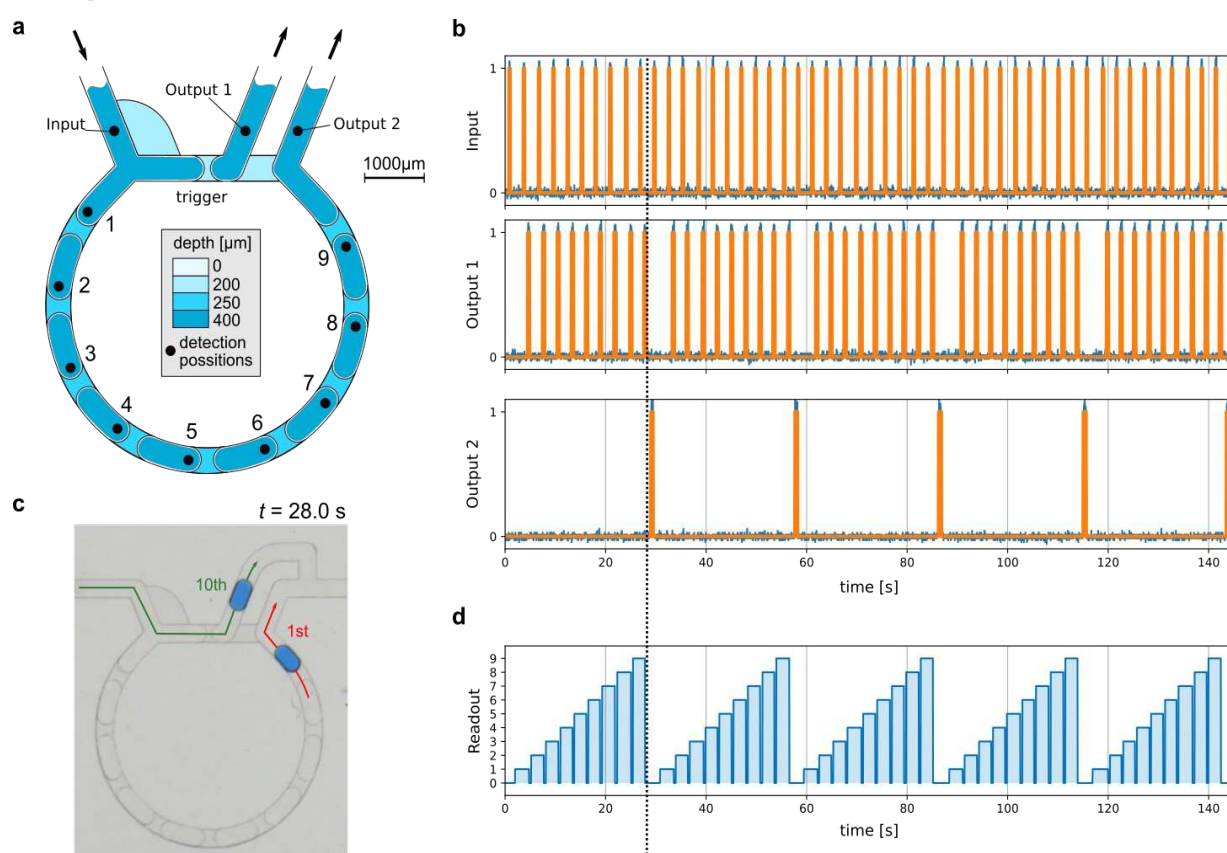
Supplementary Fig. 3 The decimal counter with two outputs. **a** the schematic top view of the counter with a trigger-barrier in the short branch and with 9 state-barriers in the longer branch. Both Output 1 and Output 2 are connected by the slit, which on the one hand allows for the flow of continuous phase and so that reduces the pressures difference, on the other hand, separates the motion of droplets. **b** experimental micrograph taken after the inflow of the 10th droplet. The first droplet is released from the loop and enters the Output 2, while the 10th droplet travels through the Output 1. **c** signals of the presence of a droplet at measurement positions Input, Output 1 and Output 2 as indicated in **a**. The blue noisy lines – the brightness of pixels at the measurement positions as a function of time (normalized and inverted so that the high value corresponds to the presence of a droplet). Orange lines – the digital droplet-presence-signals obtained by thresholding of the brightness signals. **d** the readout obtained by analysis of the presence of droplets in state positions (see the analysis of the decimal counter in the Main Article).

6

Supplementary Note 4
3 – way

Here we present an additional example of the 3-way device to show that further modifications of the base elements can yield new functionalities. The device consists of a 3-way junction dividing the input channel into three parallel channels, each of them equipped with one obstacle (Supplementary Fig. 4 and Supplementary Movie 8). The construction of a 3-way junction ensures, that 3 subsequent droplets are distributed between outlets in a specific way - the first droplet to the middle channel (Supplementary Fig. 4b), the second one to the top channel (Supplementary Fig. 4d), and the third one to the bottom branch (Supplementary Fig. 4e). Two first droplets are immobilized in the structure while the third one blocks the last bypass-channel and triggers the release of all droplets (Supplementary Fig. 4e-h). Hence we obtain 3 states - Besides the ground state (without any droplet trapped in the device), there are two excited states with immobilized droplets. The first excited state with the first droplet in the middle channel (Supplementary Fig. 4b) and the second excited state - with the additional second droplet immobilized in the top channel (Supplementary Fig. 4d).

As all droplets are released from the obstacles simultaneous, the appropriate arrangement of obstacles allows for setting different delays between droplets, thus, the encoding of custom order of droplets leaving the device. In this case, we set the positions of obstacles in such a way, that releases the third droplet as the first one, while the droplet being previously the first one is moved to the third position (Supplementary Fig. 4f-h).

This example shows that modifications of such base geometrical components as slits, obstacles, and junctions allow for achieving novel functionalities, which have the potential for the encoding variety of algorithms on droplets in microfluidic channels.
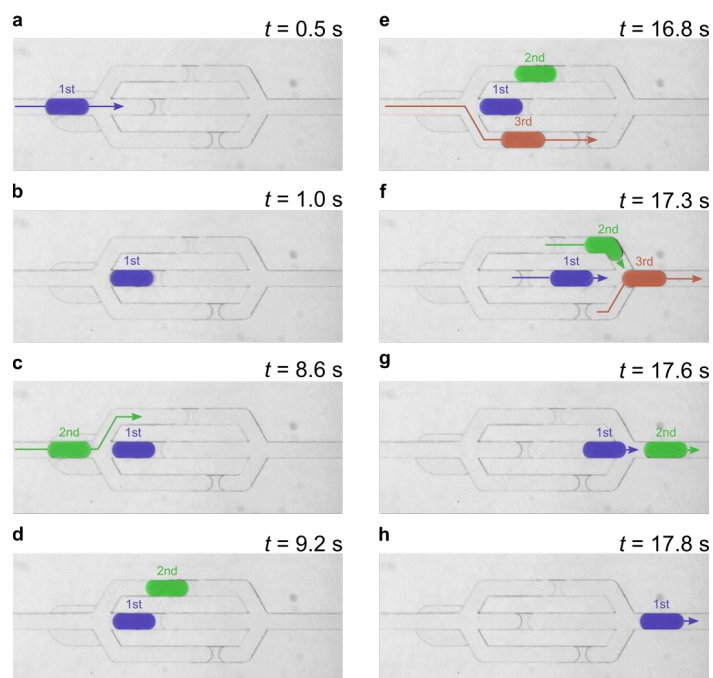
Supplementary Fig. 4 The system of three parallel channels with 3-way junction – experimental observations. We add artificial colors to droplets for the visualization of the transformation of the initial sequence of droplets (see Supplementary Movie 8).

Supplementary Note 5
Droplet Generator Unit

Supplementary Fig. 5 shows the Droplet Generation Unit we used for the fabrication of droplets. It is a modified version of the previous block-and-brake type generator[2]. Such a construction, unlike the regular T-junction generator, produces droplets of similar size regardless of flows of both phases[1].

During the first trials with droplet-logic, we realized that the optimal size of droplets in most cases is about double the channel width. The other crucial parameters were the speed of the flow and frequency of generated droplets. The speed of the flow on the one hand, cannot be too fast (it cannot generate pressure drop exceeding the break-through pressure), but on the other hand, it should not be too slow to ensure a reasonable time of experiments. The frequency of the generation of droplets must be sufficiently low to avoid the interference of numerous droplets at once in the microfluidic units.

As known, both the frequency and the length of droplets generated in the regular T-junction depend on the flows[1]. Hence, those parameters cannot be adjusted independently. In the case of our experiments, droplets would be too small if produced in regular T-junction.

The solution we used provided more flexibility to the control over the crucial parameters, which could be effectively adjusted, thus, ensuring the robust performance of the investigated systems.
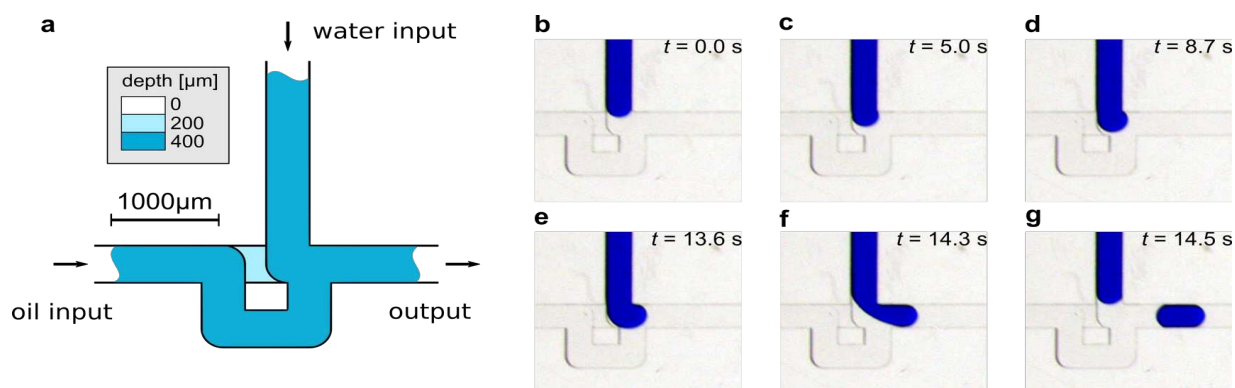
Supplementary Fig. 5 Droplet generation unit used in the work. **a** schematic top view. **b-g** micrographs showing the complete sequence of the generation of a single droplet.

Supplementary references

1. Korczyk, P. M. *et al.* Accounting for corner flow unifies the understanding of droplet formation in microfluidic channels. *Nat. Commun.* **10**, 2528 (2019).

2. van Steijn, V. *et al.* Block-and-break generation of microdroplets with fixed volume. *Biomicrofluidics* **7**, 024108-024108–8 (2013).

Concentration on demand – A microfluidic system for precise adjustment of the content of single droplets

Damian Zaremba, Slawomir Blonski, Piotr M. Korczyk [*]

Institute of Fundamental Technological Research, Polish Academy of Sciences, Pawinskiego 5B, 02-106 Warsaw, Poland

ABSTRACT

We present a novel microfluidic system that produces the required concentration of a reagent in a single droplet or that produces a sequence of droplets with a defined periodic distribution of concentrations. We use digital algorithms that, through a series of simple operations, such as merging and splitting droplets, ensure superior precision, repeatability and flexibility in concentration setting.

Unlike Digital microfluidic (DMF) systems based on electrowetting on dielectric (EWOD) commonly used to implement digital algorithms in the droplet world, our approach is based on much more available channel-based microfluidics operated by programmable syringe pumps. Furthermore, the small footprint of our system makes it easy to integrate with other structures of microfluidic networks. Thus, this technique is a comprehensive component that can be built into the microfluidic networks executing laboratory analytical tasks in chemistry or biology to enrich their performance and offer new functionalities.

1. Introduction

Droplet microfluidic techniques enable the formation and analysis of droplets, each equivalent to a tiny reactor that can include samples, reagents, or biological components for chemical synthesis, analytical assays, biological processes, drug discovery, and more. In these and other applications, obtaining the concentration of a given component in a precise, accurate, and above all, reproducible manner is paramount [1].

This requires a method for the manipulation of the content of droplets. For this purpose, Digital microfluidic (DMF) systems based on electrowetting on dielectrics (EWODs) provide superior control methods for manipulating droplets within multistep and complex handling protocols [2]. Each droplet can be seen as a digital entity, addressed individually and processed with a sequence of merging and splitting selected droplets. EWOD-based DMF systems exploit electrowetting effects that rely on modulation of the interfacial energy of a polar liquid that is deposited on a solid surface by an external electric field. The surface where droplets are processed is coated with individually operated electrodes. A water droplet moves to the electrode in its vicinity that has the highest electric field magnitude. Individual control over the electrodes enables the implementation of liquid handling protocols comprising merging, mixing, and splitting droplets. Although the basic

set of operations is strictly limited, the application of digital algorithms offers freedom of concentration creation by using multiple repetitions of primitive operations [3,4] (like a basic computation performed by an algorithm in computer science such as assigning a value to a variable, comparing two numbers, indexing into an array, calling a function/method and returning from a function/method). Thanks to computer-aided systems controlling the electrodes, complicated and reconfigurable procedures can be automatically conducted. However, this technology also presents some limitations. Droplets are in contact with the substrate, and in sliding on its surface can leave some residue, which can result in cross-contamination. Compared to the soft lithography or micromachining commonly used to fabricate conventional channel microfluidic chips, the fabrication of EWOD chips is much more complicated. Operation of the numerous electrodes requires custom electrical connections and custom hardware that demand specific electronics knowledge and skills of their designer.

This disadvantage renders EWOD technology less available to researchers. Fast and relatively cost-effective prototyping techniques for channel microfluidics, such as micromachining, lithography, and 3D printing, are popular. In addition, channel microfluidics has developed various strategies for manipulating the content of droplets that are alternatives to EWOD-based methods. Channel technologies can utilize single-phase gradient generators to prepare concentration before the

droplet formation or adjust the concentration of a droplet via merging and splitting of droplets with different content.

Droplets with varied concentrations can be achieved by combining the streams of two or more droplet liquids before droplet generation [5]. Mixing takes place after the formation of a droplet due to internal advection [6]. This design allows for the droplet concentration to be varied by adjusting the input liquid ratio while fixing the total flow rate of the droplet phase to ensure monodispersed droplets. Alternatively, droplets of constant size and varying concentrations can be obtained using a fixed-volume droplet generator [7]. More advanced automated systems allow for the choice of the droplet phase from numerous sources [8], or the proportions of composites can be actively tuned by a system of integrated valves [9]. A well-defined spectrum of concentrations can be prepared before droplet generation in a tree-like network that interchangeably splits and combines streams of buffer and reagent within a cascade of junctions. Thus, multiple parallel branches are dedicated to specific output concentrations. Then, each separate output stream is combined with a droplet generator to produce droplets of different concentrations [10,11].

Another category of channel-based microfluidics encompasses systems that rely on the liquid exchange between droplets of different concentrations via series of droplets fusion and fission. Some such systems conduct a series of mass exchanges between a droplet of reagent and a series of input buffer droplets. As a result, the reagent concentration decreases gradually within the stream of resultant droplets. Two different approaches can be applied to serial dilutions - with reagent droplets immobilized [12–14] or moving [13,15,16] while the buffer droplets move or are stopped in the array of traps, respectively. The concentration can be changed gradually in a single droplet by a series of coalescences with small droplets so that the entire volume increases [17]. Dilutions can also be performed in minimalist, iterative systems [18].

While serial dilutions produce series of droplets with gradually distributed concentrations, more control on the individual droplet concentration can ensure merging selected droplets of different liquids. The final concentration is then equal to the proportion of input reagent droplet in the total volume of the resultant droplet. Thus, manipulating the droplet volumes or the number of droplets enables the adjustment of the resultant droplet concentration. This can be done in passive systems [19,20]. Nevertheless, better control over the composition of a single droplet is ensured by active systems supported by the droplet on demand methodology. Individual droplets are made on demand with computer-controlled actuators, so the resultant concentration can be set by adjusting the volumes of constituent droplets [21,22] or their numbers [17]. Similar methods can be adopted to control the number of cells in droplets [23].

Most advanced controlled droplet microfluidic systems allow for iterative operations in oscillatory systems. Here, a train of droplets can be seen as a memory stack. Its controlled motion positions a selected droplet where it can be analyzed by sensors [24–26] or processed, e.g., by an auxiliary junction that removes part of the droplet or adds a portion of a new liquid [27]. Other researchers use addressable static droplet arrays [28].

Such channel-based systems exhibit a level of complexity of operations like that reached in EWOD-based DMF systems. However, the increased complexity of protocols is achieved at the cost of increased complexity of active controller systems. This hampers the wide use of these methods by researchers focused on solving biological or chemical problems who require comprehensive and robust tools without hardware development.

Here, we propose a minimalist channel-based semiautomatic system for precise concentration control whose performance is ensured with digital algorithms. The device's semiautomatic character is due to the use of passive elements such as the metering trap and the merging trap we described above. Therefore, processes such as droplet formation, merging, and splitting do not require any modulation of flows or pressures. Instead, they proceed spontaneously if basic conditions such as the flow direction are met. Thus, the operation is conducted solely by the setting of flows between selected points in the microfluidic setup. The flows are controlled by switching the syringe pumps connected to the channels on or off. The syringes are operated by the time-based controller implemented in software with simple feedback from the camera to track droplets and maintain their position.

Our system exhibits its minimalist character in two aspects. First, the microfluidic structure is relatively small and simple; it consists of only one metering trap and one merging trap, and in the extended dual version, one more merging trap. Second, we use syringe pumps (one per liquid, one additional 3/2 valve in the dual system) as the only actuators in the system that are controlled by the computer software. In this work, we use the auxiliary high voltage electrodes, which are not an intrinsic part of the system but are used only to facilitate droplets' coalescence in the presence of surfactant.

Previously, combinations of microfluidic traps were applied to generate a series of 2-fold dilutions. Here, we propose implementing advanced iterative algorithms, where a so-called beaker droplet can be serially mixed with either a buffer or a reagent droplet, averaging the concentrations of both constituents. This either decreases or increases the initial beaker-droplet concentration in each step of the procedure.

Our procedure exhibits the advantages of both channel-based concentration-control approaches we discussed above without sharing their limitations. First, serial dilution can produce any small concentration, but the resolution of the concentrations in the middle of the range is limited by the fold-number characterizing dilutor. For example, in a 2-fold dilutor, we obtain the first dilution equal to half of the initial concentration, but we cannot obtain any more concentrations greater than half. Similarly, concentrations between a quarter and half of the range are not accessible.

In coalescence-based methods, we have freedom of concentration setting in the middle of the range by tuning the volumes of merged droplets of two liquids. However, in the vicinity of both range limits, this approach requires the precise generation of appropriately small droplets, but the minimum droplet size is determined by the channel dimensions, which introduces a limited concentration adjustment.

We show that our approach is free from those limitations, offering a superior dynamic range within the whole range of concentrations. We analyze the mathematical features of the algorithms used and create the method for generating streams of droplets with concentrations that vary periodically or streams of droplets with the same concentration distribution. We show the practical application of this method for the generation of varying combinations of two reagents in a stream of droplets.

We show that advanced digital algorithms can be effectively implemented in channel systems that are simpler in fabrication and use than EWOD-based DMF systems. Moreover, with its small footprint and minimal set of actuators, the presented solution is suitable as a sub-module that can be easily integrated with other modules on a chip device in a lab.

2. Discussion and results

2.1. Mathematical description of the operations on droplets

2.1.1. Averaging of concentration

The concept of the system for control of the concentration in droplets is based on the utilization of a set of base operations on droplets as i) generating droplets of uniform size, ii) merging two droplets, iii) mixing the content of resulting long droplet, and iv) splitting the long droplet into two uniform-sized droplets.

Such a simple set of basic operations can produce droplets containing a combination of two base liquids in any required proportions [4].

The merging of two uniform-sized droplets and mixing of their content results in an averaging of their concentrations. After splitting a double-sized droplet in two, we obtain two unit-sized droplets of

identical concentration. One of the resultant droplets can be used to repeat the operation to modify its concentration.

The droplet being processed in such a way is the *beaker-droplet*, the droplet used to modify the concentration of the *beaker-droplet* is the *input droplet*, and the excess droplet after splitting is the *output droplet* (see Fig. 1a).

The *input droplet* is made directly with one of two base liquids: i) clear solvent or ii) base solution of the reagent. Normalizing the concentration of input droplets by the base reagent concentration, we obtain the dimensionless concentration of the input droplets m, which equals 0 or 1 for the droplet without and with a reagent, respectively. Consequently, the normalized concentration of the reagent in the beaker droplet c can take a value from 0 to 1. Therefore, the base solution of the reagent sets the maximal reagent concentration that can be obtained via droplet combinations.

Let us consider the series of consecutive concentration modifications. The i-th step of the operation can be described as follows:

$$c_i = \langle c_{i-1}, m_i \rangle = (c_{i-1} + m_i) \cdot 2^{-1} \tag{1}$$

where c_i is the concentration of the beaker droplet after the i-th modification, c_{i-1} is the concentration obtained in the previous step or particularly for $i = 1$, $c_{i-1} = c_0$, where c_0 is the concentration of the initial beaker droplet, m_i is the concentration of the input droplet used in the current step, and $\langle , \rangle$ represents averaging. As m_i can be 0 or 1, a single modification can lead to a decrease or increase in the concentration c_i, respectively.

Note that for $i > 0$, the concentration of the i-th output droplet equals the concentration of the beaker droplet c_i. In the following, we will use c_i to describe both the beaker droplet and the output droplet concentration except c_0, which is reserved for the initial beaker droplet concentration only.

We can express c_i as a sum of a geometric series:

$$c_i = c_0 \cdot 2^{-i} + \sum_{k=1}^{k=i} m_k \cdot 2^{(k-i-1)} \tag{2}$$

In general, the initial beaker-droplet concentration c_0 can be any real value from 0 to 1. For example, it can be the residue of the previous sequence of operations.

However, when starting the operation from scratch, c_0 can be 0 or 1, as the initial droplet can be made of one of the base liquids. Thus, in the first step ($i = 1$), we can produce a concentration of 0.5, averaging droplets of different kinds ($\langle c_0 = 0, m_1 = 1 \rangle = \langle c_0 = 1, m_1 = 0 \rangle = 0.5$). In the second step, we have more possibilities, as we can obtain $c_2 = 2 \cdot 2^{-2}$ or $c_2 = 3 \cdot 2^{-2}$ using $m_2 = 0$ or $m_2 = 1$, respectively. In the third step, the tree of all possibilities has four branches representing an additional four intermediary concentrations ($1 \cdot 2^{-3}$, $3 \cdot 2^{-3}$, $5 \cdot 2^{-3}$, $7 \cdot 2^{-3}$ - see Fig. 1b). Therefore, limiting our exemplary series of operations to three steps of modifications, we can obtain any concentration from the spectrum of nine different concentrations given by $A \cdot 2^{-3}$, where A is an integer from 0 to 2^3.

Generally, starting from scratch and within n steps, we can generate any concentration c given by:

$$c = A \cdot 2^{-n} \tag{3}$$

where A is an integer from 0 to 2^n. Hence, increasing the number of steps increases the resolution of the spectrum of available concentrations.

2.1.2. Concentration on demand

For any concentration given by $c = A \cdot 2^{-n}$ and an arbitrarily chosen c_0 (0 or 1), there is a unique sequence of input droplets that can be described as a series of zeros and ones:
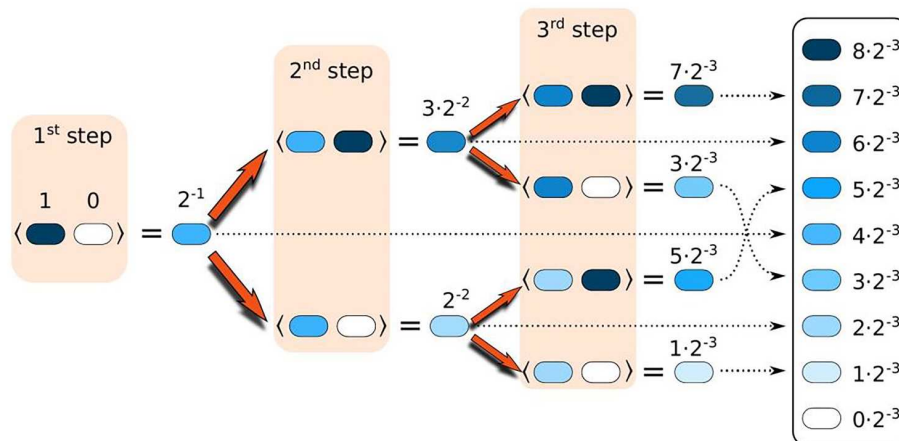
a)
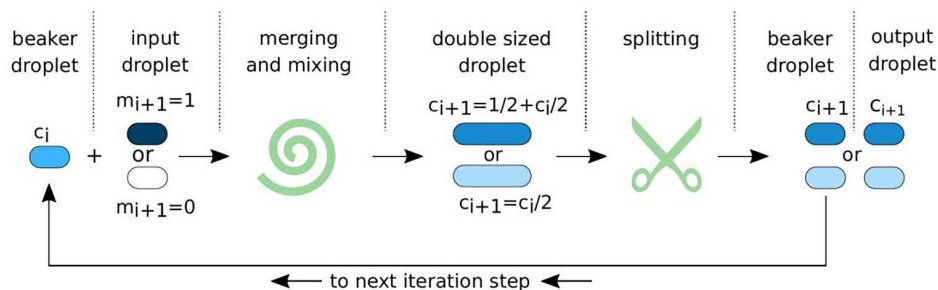
b)

Fig. 1. Concept of the operation on the concentration of droplets. a) Schematic representation of one step of the algorithm for manipulating the concentration by merging and splitting of droplets. The image shows two possibilities – the initial concentration of the beaker droplet c_i is modified through the coalescence with an input droplet of the concentration $m_{i+1} = 1$ or $m_{i+1} = 0$. b) Tree of all possible merge-and-split-operations and resultant concentrations obtained after applying three steps of droplet combinations.

$$m(c_0, c) = [m_1, ... m_\nu] \qquad (4)$$

Such a series is an instruction required for the generation of the desired concentration c. The length of the input sequence ν is equal to n only if A is an odd number. Otherwise, we can express the concentration as:

$$c = \phi \cdot 2^{-\nu} \qquad (5)$$

where $\phi = A \cdot 2^{-(n-\nu)}$ is not divisible by 2. For example, in the case of $c = 6 \cdot 2^{-3}$, $n = 3$ and $\nu = 2$, we can reduce the exponent: $c = 3 \cdot 2^{-2}$. This means that $c = 6 \cdot 2^{-3}$ is obtained in 2 steps (see Fig. 1b).

Having the complete input sequence $m(c_0, c)$ as given in Eq. (4), the final concentration can be calculated from Eq. (2), substituting $i = \nu$:

$$c = c_0 \cdot 2^{-\nu} + \sum_{k=1}^{k=\nu} m_k \cdot 2^{(k-\nu-1)} \qquad (6)$$

2.1.3. Reversal problem

An important task for the application of the procedure is to find the input sequence m for any desired concentration $c_{desired}$ described according Eq. (5) by coefficients ϕ and ν as $c_{desired} = \phi \cdot 2^{-\nu}$. One can use Eq. (6) to calculate the whole tree of resultant concentrations for all possible $m = [m_1, ... m_\nu]$ sequences and finally find the unique m giving $c_{desired}$. However, this method is ineffective, especially for large values of ν. To find the input sequences m for any $c_{desired}$, the simplest way is to use Eq. (1) to find all intermediate steps starting from the target concentration $c_\nu = c_{desired}$ and moving step by step back.

From Eq. (1) we have the following formula for the previous-step concentration:

$$c_{i-1} = 2c_i - m_i \qquad (7)$$

Starting from $i = \nu$ and $c_\nu = c_{desired}$, we can guess value m_ν having in mind that for any i, all intermediate concentrations c_i can only have values from 0 to 1. The value of m_ν that satisfies that condition can be 0 or 1 and depends only on the known value c_ν. According to Eq. (7), we have two possible situations: if $c_\nu < 0.5$, m_ν should be 0; otherwise, $c_{\nu-1}$ would be less than 0; and if $c_\nu > 0.5$, m_ν should equal 1; otherwise, $c_{\nu-1}$ would exceed 1. This applies for any step of the sequence i within the interval from $i = 2$ to $i = \nu$, so we can write:

$$m_i = \begin{cases} 0 & if \quad c_i < 0.5 \\ 1 & if \quad c_i > 0.5 \end{cases} \qquad (8)$$

which is equivalent to the following equation:

$$m_i = 1/2(1 + sgn(c_i - 1/2)) \qquad (9)$$

Starting from the target value c_ν, the value of m_ν comes from Eq. (8) or Eq. (9). Then, putting c_ν and m_ν into Eq. (7) we obtain $c_{\nu-1}$ which is used as the input to Eq. (8) for the estimation of $m_{\nu-1}$. We can repeat that operation until we obtain m_2 and $c_1 = 0.5$. The value of m_1 depends on the arbitrarily chosen c_0.

2.1.4. Approximation of any concentration

In practice, the desired concentration $c_{desired}$ is generally a real number. To use the above algorithm, we first need to use the following approximation:

$$c_{desired} \approx c_{approx} = A \cdot 2^{-n} \qquad (10)$$

where the accuracy of the approximation is set by the number n and equals 2^{-n}.

The first step is to set the arbitrary resolution of the concentration approximation determined by the coefficient 2^{-n}. Then, we estimate A as rounded value of the product $c_{desired} \cdot 2^n$ and estimate c_{approx} using Eq. (10). If A is the even number, we replace it (as described above) by an odd number ϕ (see Eq. (5)) yielding $c_{approx} = \phi \cdot 2^{-\nu}$. Then, we can use the above described algorithm (Eq. (7) and Eq. (8)) to find the input droplet sequence that produces the concentration c_{approx} closest to $c_{desired}$.

2.2. Implementation in a microfluidic device

2.2.1. Concentration averaging module

The concept of the concentration averaging module (CAM) is based on the use of microfluidic traps described previously [13,29]. As shown in the case of the DOMINO device [13] and the precise dilutor [18], a serial combination of two elements, a metering trap (Fig. 2a) and a merging trap (Fig. 2b), can be used for serial dilutions.

Both traps are composed of slit bypasses along both sides of the channel and obstacles in the lumen of the channel (Fig. 2a and 2b). The metering trap consists of one obstacle, which results in diodicity – the behavior of a droplet depends on the direction of its motion through the trap. The metering trap does not affect droplets entering the trap through the obstacle side, but it influences droplets when they are moving in the opposite direction. That effect depends on the droplet size. A long droplet disassembles into two parts: i) a droplet of the size precisely defined by the trap dimensions that is immobilized in the trap, and ii) an excess droplet that continues traveling [13,29]. All droplets of a size not exceeding the trap dimensions stop in the trap when entering from the unobstructed side. Due to their diodicity, droplets immobilized in the metering trap can be easily released by flow reversal.

The metering trap is used for the metering of base size droplets. That size is determined by the geometry of the trap and hardly depends on the flow or liquid properties (see Supplementary Materials for more details on the measurements of droplets size dependence on the rate of flow). For all operations and specified liquids, we establish fixed parameters of flows at the start of the algorithm. Therefore, the metering trap can be used for precise formation of uniform-sized droplets.

Despite the similar construction of both traps, the merging trap exhibits other functionalities. It immobilizes a droplet of the base size (or smaller) regardless of the flow direction. Due to the symmetry of the trap, which possesses two barriers, after a droplet enters the trap interior, it cannot pass the trap barriers again.

However, in this case, the height of the barriers is smaller than those in the metering trap. The effect is that the merging trap cannot either cut or immobilize longer droplets. For example, double-sized droplets can pass through the trap unaffected. This trap configuration is used to merge pairs of droplets. Once the first droplet is immobilized, the next droplet entering the trap collides and coalesces with the initially immobilized droplet. The resultant double-sized droplet leaves the trap.

In previous publications [13,18], a serial composition of the metering trap and the merging trap was used to generate serial 2-fold dilutions, where the sample was gradually diluted in a cascade of repetitive dilution operations. As a result, the available concentrations were limited and could not be customized at will.

Here, we use a similar composition of traps to develop the semi-automatic system – concentration averaging module, which can execute the algorithm described in section 2.1, allowing for the generation of any required concentration in a small droplet. The base operation of the device is averaging two droplets of identical size by merging them, homogenizing their content and splitting them back into two droplets.

The concentration averaging module consists of the metering trap, the merging trap and the bent section of the channel serving as a mixer [30], all serially connected via a channel (see Fig. 2c). The base size of droplets used in the averaging operation is set by the length of the metering trap. Consequently, the size of the merging trap is adjusted to allow for the immobilization of single-sized droplets and prevent the stoppage of double-sized droplets.

It is important that the metering trap is placed with its barrierless side toward the merging trap. In the module's orientation shown in Fig. 2c, the metering trap does not affect droplets moving from the left.

Let us consider a beaker droplet of concentration c_i introduced to the CAM and stored in the merging trap (Fig. 2c). Now, we send the input droplet from the left with concentration $m_{i+1} = 0$ or $m_{i+1} = 1$ (see Fig. 2d). The input droplet carried by the flow of CP passes the metering trap and then merges with the beaker droplet in the merging trap. The
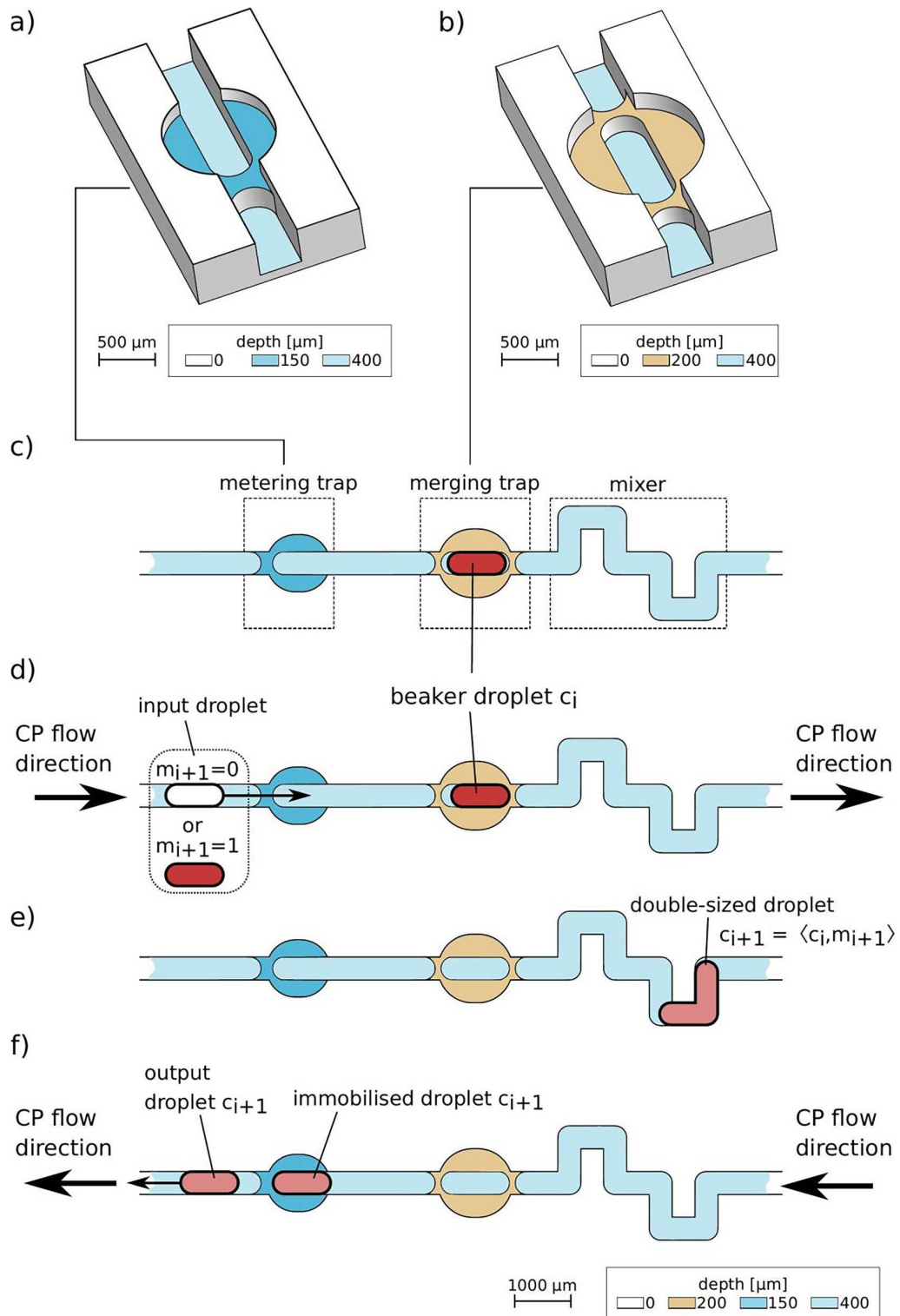
Fig. 2. Concept and operating principles of the microfluidic concentration averaging module. a) and b) 3D schemes of a) metering trap and b) merging trap. c) Concentration averaging module scheme consisting of metering trap, merging trap and bent section of channel serving as a mixer, all serially connected via a channel. In the default configuration, the module contains a single-sized beaker droplet of concentration c_{i-1}. d) In the first step of the operation the direction of the flow is from the left to right and one input droplet of the concentration $m_i = 0$ or $m_i = 1$ is introduced. The input droplet moves toward the trapped beaker droplet. Droplets meet in the merging trap and merge creating a double-sized droplet, which leaves the merging trap and travels through the mixer, homogenizing the content to the concentration $c_i = (c_{i-1} + m_i)/2$ - (e). Then, the flow is reversed. The double sized droplet passes through the merging trap and is divided into two droplets of the same size and concentration c_i - (f) in the metering trap. One of the droplets continues traveling to the left, while the other one is trapped in the metering trap.

resultant double-sized droplet leaves the merging trap and travels through the channel's bends (see Fig. 2e), which facilitates homogenization of the content by enforcing irregular internal convection. As a result, according to Eq. (1), the mixing of the two collided droplets yields a double-sized droplet of concentration $c_{i+1} = (c_i + m_{i+1}) \cdot 2^{-1}$. Then, the flow direction is reversed, and the double-sized droplet passes the merging trap and enters the metering trap, where it divides into two equal droplets of the base size (see Fig. 2e). One droplet (the output droplet) leaves the module, while the second droplet (the beaker droplet) stays inside the module. Thus, the module is ready for the next input droplet to alter the beaker-droplet concentration further.

The above-mentioned operation scheme assumes the perfect mixing and homogenization of the content of the double-sized droplet after merging two droplets of different concentrations. The mixing in the droplet proceeds due to the internal circulation forced by the confined flow conditions. For this purpose, the distance that double-sized droplet travels from its creation to its splitting is ensured sufficiently long – 13.4 of the double-sized droplet lengths. Additionally, the mixing is enhanced by the bendings [30] of the mixer zone what ensures the required homogenization of the droplet content.

2.2.2. Droplet on demand module

The implementation of the algorithm described in section 2.1 requires the delivery in each step of an input droplet of solvent or droplet of reagent, selected according to the demand of the algorithm. Here, we propose a novel and simple Droplet On Demand system (DOD), which utilizes the metering trap (see Fig. 3a).

The main part of the module is a metering trap connected via the channel and tubing directly to a DP syringe that is operated by a bidirectional syringe pump. Importantly, the metering trap is oriented with the barrier side directed toward the DP inlet. Thus, it can meter a droplet when the flow is from right to left (according to the layout in Fig. 3). The additional channel expansion prevents the spontaneous formation of unwanted droplets.

The syringe pump operating such a DOD system must work in both directions – in the injection and withdrawal modes.

In the base position of the DOD, the DP fills the whole tubing, and the tip of the DP is in the channel between the inlet and the metering trap (see Fig. 3b I). In the first stage of DOD module operation, the droplet phase is pumped forward until its tip passes the whole metering trap (see Fig. 3b I-IV). Therefore, the DP fills the whole input channel, the channel expansion and the metering trap (Fig. 3b IV). In the next step, the syringe pump works in withdrawal mode which forces the flow from right to left (see Fig. 3b V-VI), and the tip of the DP moves to the left. As a result, a droplet forms in the metering trap. Further withdrawal of DP increases the gap between the DP and the droplet immobilized in the trap. This gap is filled with CP. Then, the injection of DP moves the droplet from the trap, and the device is ready for the generation of the next droplet.

This procedure does not require any calibration and is simple in operation, requiring only a sequence of flow reversals. Therefore, it resembles the push-and-release procedure in hand pipettes.

The volume of droplets produced in our DOD system is about 114nL. The high reproducibility of the formed droplets is confirmed by the small relative standard deviation of droplet size measurements estimated in the series of repetitions to be about 1.5%.
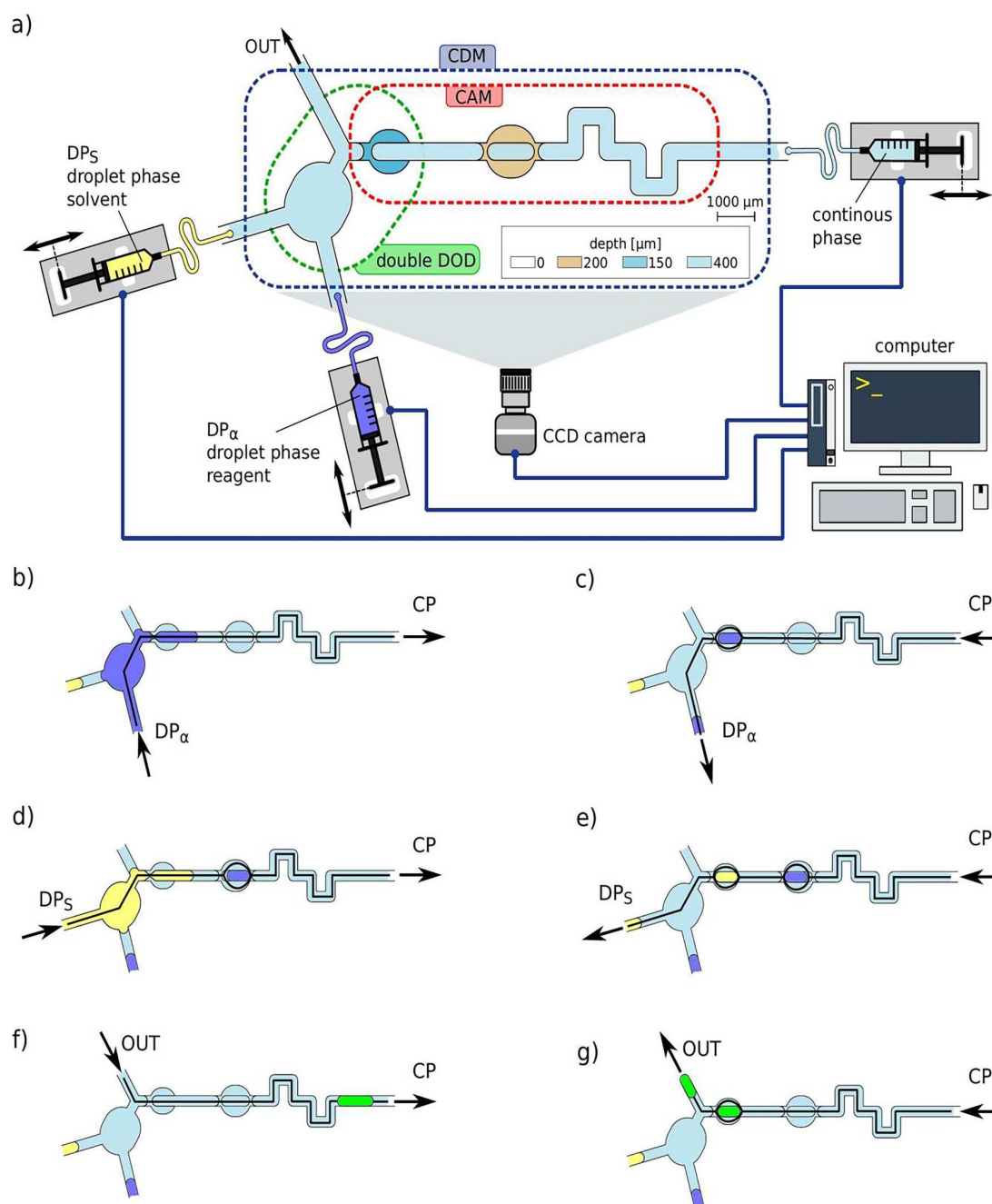
2.2.3. Concentration on demand module

We integrated both CAM and DOD modules shown in sections 2.2.1 and 0, obtaining the functional Concentration on Demand Module (CDM - see Fig. 4). What is important and beneficial is that the device's design includes only one metering trap shared between the modules. Thus, the device consists of one metering trap, one merging trap, and the inlet of the CP connected to the mixer side of the CAM. The output is placed between the channel expansion of the DOD and the metering trap. Two inputs of different droplet phases are connected directly to the expansion of the DOD.

Each liquid is managed by a dedicated bidirectional syringe pump controlled by the computer. The custom-made software drives switching sequences of syringe pumps in different configurations, inducing flows
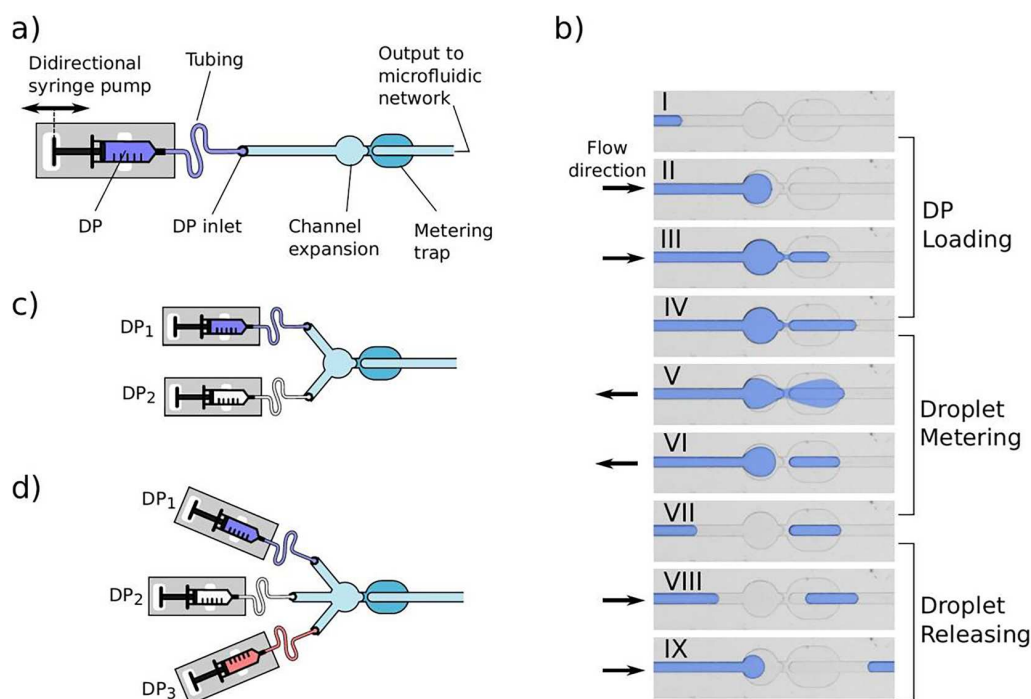
Fig. 3. Droplet on demand module with the metering trap. a) Scheme of the microfluidic module and its connection to the bidirectional syringe pump with DP, b) experimental images showing the working device and subsequent stages of operation of DOD, c), d) examples of extended DOD modules for the generation of droplets of different droplet phases, c) DOD module with two different droplet phases DP_1 and DP_2, and d) configuration of DOD for three different DPs: DP_1, DP_2, DP_3.

Fig. 4. Concept of the automated concentration on demand module and its operating principles. a) Scheme of the microfluidic CDM and diagram showing connections to three bidirectional pumps. Pumps and CCD camera observing the system are connected to a computer and operated by the software which executes the algorithms and b) – g) schematic representation of all base operations of CMD for performing the complete Concentration on Demand algorithm.

between selected points of the microfluidic device (see Fig. 4b–g). In this way, the CDM executes the algorithms described above autonomously and automatically.

Two droplet phases used in the CDM encompass the base reagent solution, here called DP_α, and the solvent DP_S.

Let us analyze the CDM principles in the schemes shown in Fig. 4b–g. In the beginning, DP_α is injected into the system, while the flow of CP is reversed by the withdrawal mode of the CP syringe pump. The induced flow is between the DP_α inlet and the CP inlet (see Fig. 4b). This stage encompasses the loading of DP_α into the DOD as described before in Section 0 (see Fig. 3 II-III). Once the tip of DP_α is detected behind the metering trap, the previous flow pattern is reversed, i.e., the DP_α syringe

pump is switched to withdrawal mode, while the CP is run in the forward mode. As a result, a single droplet of DP_α is created and immobilized in the metering trap, and the tip of DP_α recedes and hides in the DP_α inlet channel (see Fig. 4c).

In this paper, we use a digital camera to detect the DP tip presence behind the metering trap. Then, the feedback signal from the camera is used by the operating software to reverse the DP's flow once the DP fills the metering trap. Importantly, the flow reverse must occur before the DP tip enters the merging trap. We chose the distance between traps arbitrarily long enough to avoid biases due to possible delays in the feedback system.

The analogical process performed using the DP_S syringe pump in

place of the DP$_\alpha$ syringe pump leads to the creation of a DP$_S$ droplet in the metering trap (see Fig. 4d and 4e). The DP$_\alpha$ droplet produced previously in the metering trap moves to the merging trap during DP$_S$ injection into the DOD system.

Finally, two single-sized droplets, the beaker droplet and the input droplet, occupy the merging tap and the metering trap, respectively (see Fig. 4e). Then, the flow of CP switched in reverse mode removes the droplet from the metering trap and merges it with the other droplet in the merging trap. The resultant double-sized droplet's content is homogenized as it travels through the mixer (see Fig. 4e). Then, after switching the CP syringe to forward mode, the double-sized droplet divides in the metering trap into equal parts. The output droplet leaves through the outlet, while the second droplet, the beaker droplet, remains trapped in the metering trap. Finally, the system is ready for the next step of the algorithm, where through the operations described above, a droplet of DP$_\alpha$ or DP$_S$ is created and collides with the beaker droplet.

Thus, the presented system performs all operations required for the execution of the Concentration on Demand algorithm.

2.2.4. Experimental verification

We tested a real microfluidic CDM fabricated in polycarbonate (see SM device 1) that was aimed at the generation of concentrations predicted by Eq. (6). We produced all concentrations that are available in 4 steps of the algorithm, which together with varied concentrations of base liquids yielded 17 different concentrations.

Using the procedure described in section 2.1.3, we estimated the sequences of input droplets for each concentration, shown symbolically in Fig. 5 as rows of dark and white droplets. Then, the computer-aided system performed the appropriate operations. The images of the resultant droplets show a smooth transition of blue dye intensity for droplets put in their concentration order. Movie 1 shows the example of the generation of a droplet with a concentration of 0.4375.

In additional experimental runs, the concentration was measured

(see Methods). The results were plotted in a graph. Both the color dye visualization and quantitative estimation of the concentration show agreement with the mathematical predictions.

2.3. Periodical sequences of droplet

2.3.1. Theoretical description

Previously, we focused on setting the concentration of one beaker droplet. The procedure described included the retraction of output droplets as an excess in each step of the iterative algorithm.

Now we focus on the output droplets. Hence, we can see the device as a numeric filter that processes the sequence of our input droplets and produces a series of excess droplets.

We show that periodicity in the input signal results in periodicity of the output signal, enabling the periodic generation of concentrations in droplets.

Let us assume the periodicity of the input sequence of carrier droplets:

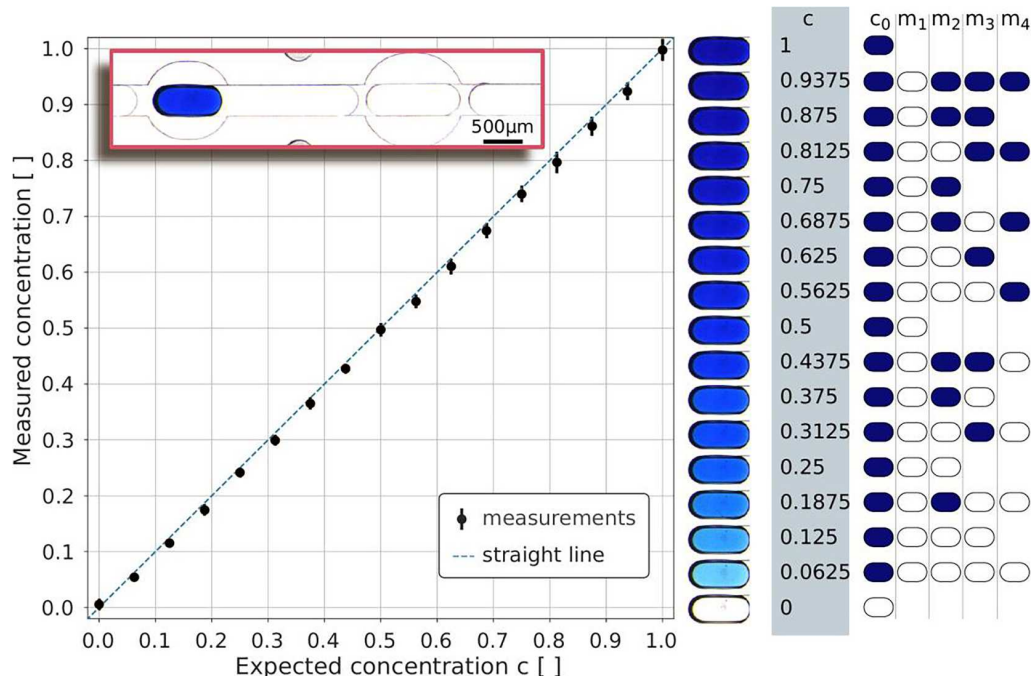$$m_{i=p \cdot \omega + s} = \pi_s \qquad (11)$$

where ω is the length of a single period (number of droplets in a single period). p is the number of complete periods. $s \in [1, \omega]$ is a droplet's position within the period and can be described in terms of the modulo operation:

$$s = [(i - 1) \bmod \omega] + 1 \qquad (12)$$

$\boldsymbol{\pi} = [\pi_1, \pi_2, ..., \pi_\omega]$ is a vector containing ω elements which define the periodic input pattern.

Substituting $i = p \cdot \omega + s$ to Eq. (2) gives:

$$c_{p \cdot \omega + s} = c_0 \cdot 2^{-(p \cdot \omega + s)} + 2^{-(s+1)} \left(\frac{1 - 2^{-p \cdot \omega}}{2^\omega - 1} \sum_{\sigma=1}^\omega 2^\sigma \pi_\sigma + \sum_{\sigma=1}^s 2^\sigma \pi_\sigma \right) \qquad (13)$$

Fig. 5. Experimental verification of the microfluidic module for concentration manipulations. The graph shows the results of experimental runs, where we produced all 17 possible concentrations for 4 steps of the algorithm. For each concentration, at least 10 repetitions were performed. Plotted points indicate the mean value of the measurements (with error-bars indicating standard deviations of measurments) and the corresponding images of droplets show the visualization obtained from the dissolution of blue dye in water. The inset shows a section of a microfluidic device with a beaker droplet inside. Images of droplets in column right show a smooth transition of blue dye according to the expected concentration. Column c lists all expected concentrations in order. The rows of dark and white droplets symbolize the sequences of input droplets used to generate each corresponding concentration.

The terms with $2^{-p \cdot \omega}$ quickly vanish with increasing $p \cdot \omega$ so that the dependency on both c_0 and p disappears, yielding:

$$\lim_{i \to \infty} c_{i=p \cdot \omega+s} = \eta_s = 2^{-(s+1)} \left(\frac{1}{2^\omega - 1} \sum_{\sigma=1}^{\omega} 2^\sigma \pi_\sigma + \sum_{\sigma=1}^{s} 2^\sigma \pi_\sigma \right) \tag{14}$$

Thus, Eq. (14) defines a periodic output pattern $\eta = [\eta_1, ..., \eta_\omega]$ of a length equal to the length of the input pattern π.

In summary, if an input sequence m is the repetition of the base pattern π: $m = [\pi, \pi, \pi, ...]$, the output for large i is periodic and converges to a periodic stream of droplets

$$\zeta = [\eta, \eta, \eta, ...] \tag{15}$$

where $\eta = [\eta_1, ..., \eta_\omega]$ is given by Eq. (14).

Note that the vanishing dependence on the initial concentration implies that the periodic series is stable against perturbations. Indeed, the initial concentration c_0 can be seen as a perturbation if there is any error. We can see that the system quickly restores the defined periodic sequence.

2.3.2. Examples of experimental runs for periodic patterns

To clarify the periodicity of output droplets, we consider two examples of periodic input patterns:

$$\pi = [0, 1] \tag{16}$$

and

$$\pi = [0, 1, 0, 0, 0, 1, 0, 1, 1, 1] \tag{17}$$

The first example uses the simplest nontrivial pattern (Eq. (16)) with length $\omega = 2$. Repeating this pattern, we produce the input sequence m, where the concentration of all odd input droplets is 0 and the concentration of all even input droplets is 1:

$$m_{p \cdot 2+1} = 0, m_{p \cdot 2+2} = 1 \tag{18}$$

Let us analyze the periodicity of the output assuming $c_0 = 1$. Eq. (13) yields:

$$c_{p \cdot 2+s} = 2^{-(p \cdot 2+s)} + 2^{-(s+1)} \left(\frac{1 - 2^{-p \cdot 2}}{3} 4 + \sum_{\sigma=1}^{s} 2^\sigma \pi_\sigma \right) \tag{19}$$

For odd droplets ($s = 1$), the output is:

$$c_{p \cdot 2+1} = \frac{1}{3} + \frac{4^{-p}}{6} \tag{20}$$

For even droplets ($s = 2$), the output is:

$$c_{p \cdot 2+2} = \frac{2}{3} + \frac{4^{-p}}{12} \tag{21}$$

As the number of repetitions of the periodic pattern p increase, the term containing 4^{-p} vanishes in both Eq. (20) and Eq. (21). Thus, the concentration of odd output droplets converges to 1/3, while the concentration of even output droplets converges to 2/3 (see Fig. 6 and Table 1.).

Hence, after an initial transition, the output stabilizes, and the device produces droplets of two well-defined concentrations, resulting in a periodic output stream of droplets with repetition of the pattern:

$$\eta = (1/3, 2/3) \tag{22}$$

The same η as in Eq. (22) we obtain applying Eq. (14) to pattern π given in Eq. (16).

In the next example, we consider a periodic input pattern of length $\omega = 10$ and of the form $\pi = [0, 1, 0, 0, 0, 1, 0, 1, 1, 1]$. Applying Eq. (14) to this pattern, we obtain the following periodic output (see Fig. 7 and Table 2.):
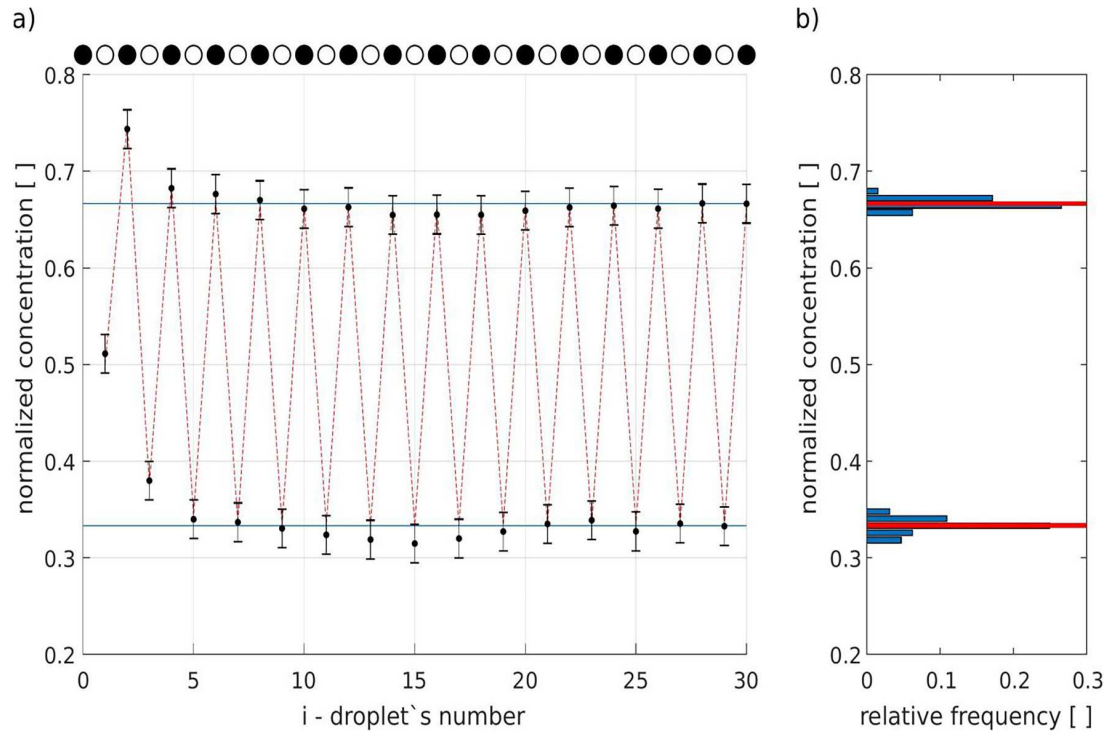

Fig. 6. Measurements of the concentration of output droplets for the input sequence $m = (\pi, \pi, \pi, ...)$ consisting of repetitions of the pattern $\pi = (0, 1)$ with the initial $c_0 = 1$. a) Plotted points are measurements based on pixel values from images of the output droplets. The red line connects points of theoretical prediction (Eq. (2)). White and black spots above the plot indicate the concentration of the i-th input droplet (white-filled $= 0$, black-filled $= 1$) and b) histogram of measured concentration taken for 65 consecutive droplets after arbitrary output stabilization from the 6th to 70th droplets.

Table 1

Values of i, s, p, m, c, ζ and c- ζ for first 5 periods for the input pattern given in Eq. (16) and $c_0 = 1$. Values of c calculated using Eq. (2) and values of ζ calculated using Eq. (14) and Eq. (15).

i	1	2	3	4	5	6	7	8	9	10
s	1	2	1	2	1	2	1	2	1	2
p	0	0	1	1	2	2	3	3	4	4
m	0	1	0	1	0	1	0	1	0	1
c	0.500	0.750	0.375	0.688	0.344	0.672	0.336	0.668	0.334	0.667
ζ	0.333	0.666	0.333	0.666	0.333	0.666	0.333	0.666	0.333	0.666
c-ζ	0.167	0.083	0.042	0.021	0.010	0.005	0.003	0.001	0.001	0.000
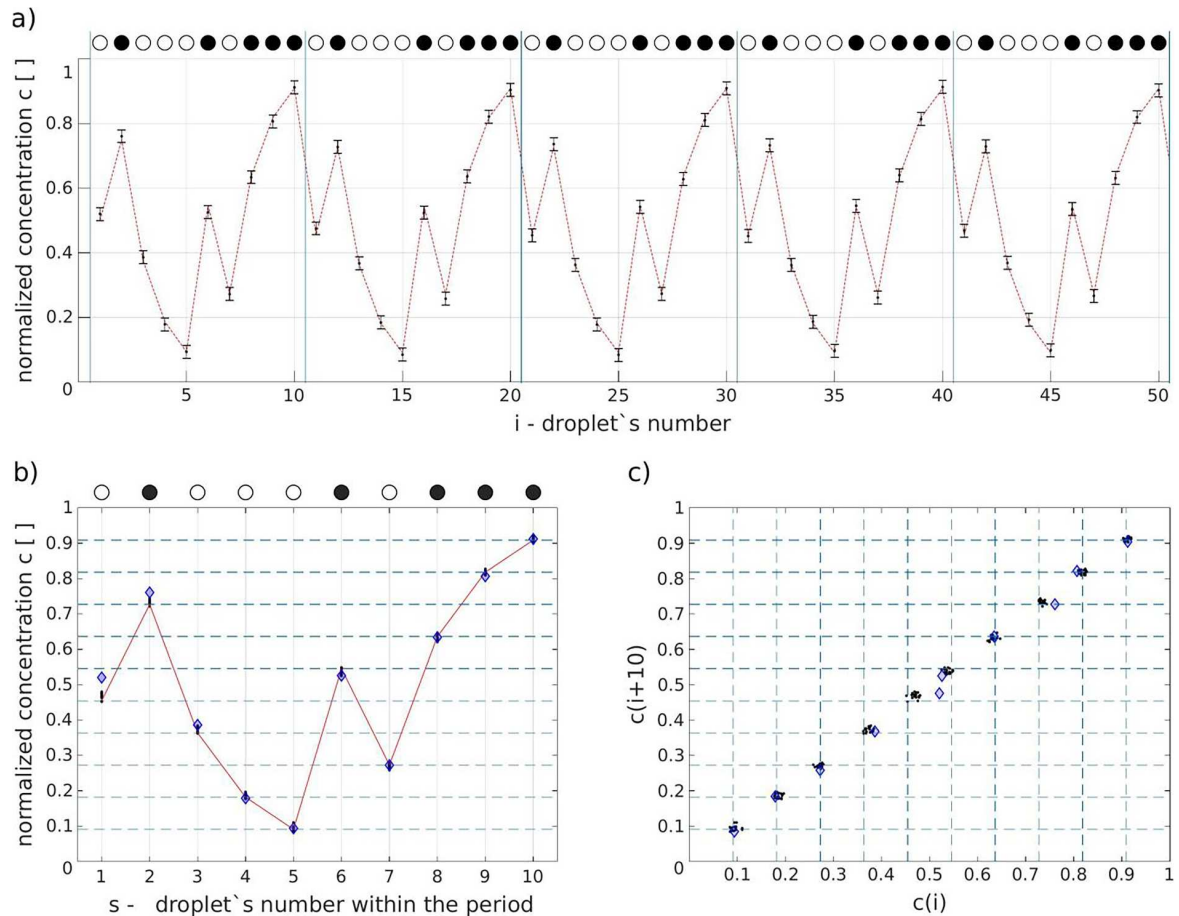
Fig. 7. Experimental analysis of the series of concentrations resulting from the processing of input droplets with the input sequence $\boldsymbol{m} = (\boldsymbol{\pi}, \boldsymbol{\pi}, \boldsymbol{\pi}, ...)$ where the periodic pattern is $\boldsymbol{\pi} = (0, 1, 0, 0, 0, 1, 0, 1, 1, 1)$ and initial concentration is $c_0 = 1$. a) Black dots with error-bars: measurements of the concentration of dye for the first five periods of resultant droplets. The single periods are separated by vertical blue lines. The red line connects theoretical points calculated according to Eq. (2), b) data for the sequence of 197 droplets plotted together as a function of $s = [(i-1)\mathrm{mod}\omega] + 1$: all output periods overlapped by shifting their origins to position 1. The red line connects points calculated according to the periodic solution given in Eq. (14), and c) Poincaré plot: c_{i+10} versus c_i for all 197 droplets showing that each period consists of 10 unique concentrations uniformly distributed. The points from the first period are plotted in b) and c) as blue diamonds. The rest of the measurements are black dots. White and black circles above the plots a) and b) indicate the concentration of the ith input droplet (white = 0, black = 1).

$$\boldsymbol{\eta} = [0.455, 0.727, 0.364, 0.182, 0.091, 0.546, 0.273, 0.636, 0.818, 0.909]$$
(23)

Interestingly, in this case, all resultant concentrations are integers (from 1 to 10) multiplied by the concentration equal to $c_{\text{step}} = 0.0909$, so the output pattern can be expressed as follows:

$$\boldsymbol{\eta} = [5, 8, 4, 2, 1, 6, 3, 7, 9, 10] \cdot c_{\text{step}}$$
(24)

The experimental analysis shows that the results quickly converge to the periodical series of concentrations. This particular pattern can be used for the generation of concentrations that are linearly distributed.

2.3.3. Linear- and logarithmic-scaled series of concentrations

In the previous example (shown in Fig. 7), we showed that an input sequence given in Eq. (17) of length $\omega = 10$ provides a linear-scaled set of concentrations. We observed that linear-scaled concentrations can be obtained from other input sequences. The prerequisites are that the length of the sequence ω is an even number, and one half of the sequence is the Boolean negation of the second half ($\pi_i = \neg\pi_{i+\omega/2}$). We obtained linear-scaled concentrations, for example, for the sequences $\boldsymbol{\pi} = [0, 1]$, $\boldsymbol{\pi} = [1, 1, 0, 0]$ and $\boldsymbol{\pi} = [0, 1, 0, 0, 0, 1, 0, 1, 1, 1]$. However, satisfying the abovementioned prerequisites does not guarantee a linear distribution, and we did not find a general rule.

Table 2

Values of i, s, p, m, c, ζ and $c-\zeta$ for first 2 periods for the input pattern given in Eq. (16) and $c_0 = 1$. Values of c calculated using Eq. (2) and values of ζ calculated using Eq. (14) and Eq. (15).

i	1	2	3	4	5	6	7	8	9	10	11	12	13	14	15	16	17	18	19	20
s	1	2	3	4	5	6	7	8	9	10	1	2	3	4	5	6	7	8	9	10
p	0	0	0	0	0	0	0	0	0	0	1	1	1	1	1	1	1	1	1	1
m	0	1	0	0	0	1	0	1	1	1	0	1	0	0	0	1	0	1	1	1
c	0.500	0.750	0.375	0.188	0.094	0.547	0.273	0.637	0.818	0.909	0.454	0.727	0.364	0.182	0.091	0.545	0.273	0.636	0.818	0.909
ζ	0.455	0.727	0.364	0.182	0.091	0.545	0.273	0.636	0.818	0.909	0.455	0.727	0.364	0.182	0.091	0.545	0.273	0.636	0.818	0.909
$c-\zeta$	0.045	0.023	0.011	0.006	0.003	0.001	0.001	0.000	0.000	0.000	0.000	0.000	0.000	0.000	0.000	0.000	0.000	0.000	0.000	0.000

The repetition of serial 2-fold dilutions is natural for the generation of logarithm-scaled sets of concentrations. Note that for the input period $\boldsymbol{\pi}$ containing only a nonzero value at its first position ($\pi_1 = 1$) while containing zeros at the remaining positions ($\pi_{s \neq 1} = 0$), Eq. (14) simplifies to:

$$\eta_s = 2^{-s}(1 - 2^{-\omega})^{-1} \qquad (25)$$

Thus, we obtain a series of consecutive 2-fold dissolutions that uniformly cover the logarithmic scale:

$$\boldsymbol{\eta} = (1 - 2^{-\omega})^{-1} \cdot [2^{-1}, 2^{-2}, ..., 2^{-\omega}] \qquad (26)$$

Notice that the term $(1 - 2^{-\omega})^{-1}$ in Eq. (25) for $\omega = 2$ equals $4/3$, for $\omega = 3$ equals $8/7$, and for further increasing length of the input pattern ω it converges to a value close to unity. For example, for $\omega = 7$, $(1 - 2^{-\omega})^{-1} = 1.0079$ which less than 1% different than 1.

This means that for $\omega \geq 7$ we can state $(1 - 2^{-\omega})^{-1} \approx 1$. Thus, the output periodic pattern simplifies to the form

$$\boldsymbol{\eta} \approx [2^{-1}, 2^{-2}, ..., 2^{-\omega}] \qquad (27)$$

In such a case, we can neglect the transient character of the beginning of the output sequence.

2.4. Periodic cross-combinations

2.4.1. The concept

As we show here, the periodic properties of a series of concentrations allow for effective generation of a broad number of cross-combinations of the concentrations of two different reagents.

Let us consider two parallel streams of input droplets, each droplet with varying concentrations of two different reagents represented by α and β, respectively. Assume that those streams are periodic with different periodic patterns $\boldsymbol{\pi}_\alpha$ and $\boldsymbol{\pi}_\beta$ of lengths ω_α and ω_β and produce the sequences $\boldsymbol{c}_\alpha$ and $\boldsymbol{c}_\beta$ of output concentrations with periodic patterns $\boldsymbol{\eta}_\alpha$ and $\boldsymbol{\eta}_\beta$. Colliding pairs of droplets from two independent sequences, we obtain combinations of concentrations $c_{\alpha,i}$ and $c_{\beta,i}$ for each $i-th$ resultant αβ-droplet.

To make the idea clearer, let us consider a simple example with $\omega_\alpha = 2$ and $\omega_\beta = 3$. Let $\boldsymbol{\pi}_\alpha = [1, 0]$ and $\boldsymbol{\pi}_\beta = [1, 0, 0]$ be periodic input patterns (see Fig. 8a), which according to Eq. (14) results in periodic output patterns

$$\boldsymbol{\eta}_\alpha = (4/3) \cdot [2^{-1}, 2^{-2}] \qquad (28)$$

and

$$\boldsymbol{\eta}_\beta = (8/7) \cdot [2^{-1}, 2^{-2}, 2^{-3}] \qquad (29)$$

respectively (see Fig. 8c). For the simplicity, let's assume that the initial concentrations equal the last elements of periodic output patterns ($c_{\alpha,0} = \eta_{\alpha,\omega_\alpha} = (4/3) \cdot 2^{-2}$ and $c_{\beta,0} = \eta_{\beta,\omega_\beta} = (8/7) \cdot 2^{-3}$) what ensures the periodicity of the output concentrations starting from the first droplet, without any initial transition ($\boldsymbol{c}_\alpha = \boldsymbol{\zeta}_\alpha$ and $\boldsymbol{c}_\beta = \boldsymbol{\zeta}_\beta$).

Repeating α pattern ω_β times and β pattern ω_α times, we obtain two periodic sequences, each of the same length $\omega_\alpha \cdot \omega_\beta = 6$ (see Fig. 8d):

$$\boldsymbol{c}_\alpha = \boldsymbol{\zeta}_\alpha = [\boldsymbol{\eta}_\alpha, \boldsymbol{\eta}_\alpha, \boldsymbol{\eta}_\alpha] = (4/3) \cdot [2^{-1}, 2^{-2}, 2^{-1}, 2^{-2}, 2^{-1}, 2^{-2}] \qquad (30)$$

and

$$\boldsymbol{c}_\beta = \boldsymbol{\zeta}_\beta = [\boldsymbol{\eta}_\beta, \boldsymbol{\eta}_\beta] = (8/7) \cdot [2^{-1}, 2^{-2}, 2^{-3}, 2^{-1}, 2^{-2}, 2^{-3}] \qquad (31)$$

Pairing droplets at the same position i from both sequences creates double-sized αβ-droplets of unique combinations of both reagent concentrations. Thus, we obtain $n_\alpha \cdot n_\beta = 6$ combinations covering the complete spectrum of all possible pairs for 2- and 3-element sets (see Fig. 8e). Note that the final merging of droplets results in an additional single-fold dilution of reagents; thus, the final concentrations in an
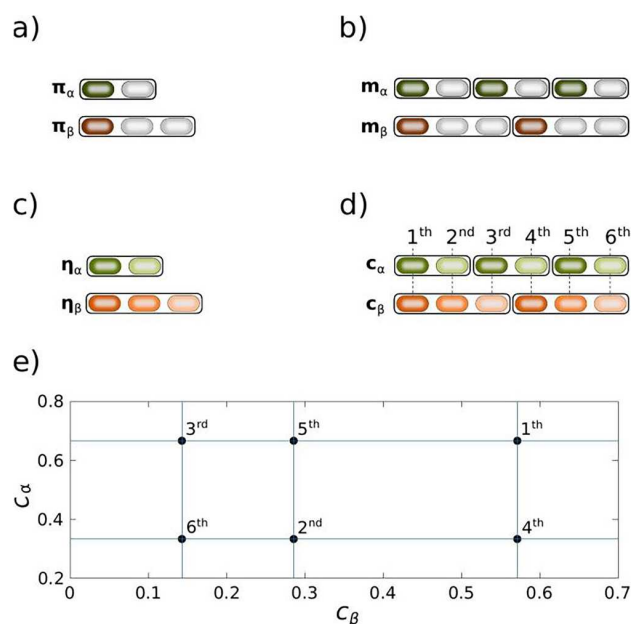
Fig. 8. The concept of cross-combination of concentrations from two periodic sequences. a) Schematic presentation of input periodic patterns $\boldsymbol{\pi}_\alpha = [1,0]$ and $\boldsymbol{\pi}_\beta = [1,0,0]$ of lengths $\omega_\alpha = 2$ and $\omega_\beta = 3$ for two different reagents α and β, respectively. Dark colored droplets contain reagents while the bright colorless ones are of pure solvent, b) two periodic input sequences $\boldsymbol{m}_\alpha$ and $\boldsymbol{m}_\beta$ of $\omega_\alpha \cdot \omega_\beta$ elements each, constructed by the repetition of the $\boldsymbol{\pi}_\alpha$ pattern ω_β times and the $\boldsymbol{\pi}_\beta$ pattern ω_α times, c) output period patterns $\boldsymbol{\eta}_\alpha$ and $\boldsymbol{\eta}_\beta$, and d) output sequences $\boldsymbol{c}_\alpha$, $\boldsymbol{c}_\beta$ – repetitions of output period patterns, and e) plot showing all obtained combinations of concentrations c_α, c_β.

$\alpha\beta$-droplet are halves of the concentrations of single-sized droplets: $c_{\alpha,i} = 0.5c_{\alpha,i}$, $c_{\beta,i} = 0.5c_{\beta,i}$. Thus, the maximum concentration that we can reach is half of the maximum concentrations of the input liquids. This should be considered at the design stage of the experiment and preparation of the base concentrations to ensure the desired range of the concentrations in the combined droplets.

This procedure can be used for longer sequences, resulting in a larger number of pairs and denser coverage of the plane of cross-combinations. The prerequisite is that the least common multiple of ω_α and ω_β be equal to their product $\omega_\alpha \cdot \omega_\beta$.

2.4.2. Microfluidic implementation of periodic cross-combinations

To execute the abovementioned cross-combinations of sequences, we built a system (see Fig. 9a and SM device 2) that is an extension of the CDM described in Section 2.2.3. The first obvious extension is adding the DP_β input droplet supplying phase with reagent β. Thus, in the Dual-CDM, a triple DOD module replaces the double DOD module previously used in the single CDM version.

The next key difference is the bifurcation of the CP inlet channel into two channels called α-storage and β-storage. These bifurcated ducts extend behind the microfluidic chip in tubing, come together at an external 3/2 solenoid valve, and then connect to the CP syringe pump via common tubing.

The 3/2 valve allows for the active switch of CP flow between the bifurcations. Therefore, the entire CP flow is directed through the currently selected storage channel, while the opposite flow is inactive (with zero flow). These two flow configurations are the two modes of the device.

Fig. 9b and Fig. 9c show the flow patterns and active syringes in both device modes. We can see that those modes functionally represent two single CDMs that are partially overlapped and divergent at the channel's bifurcation.

Each mode, together with its assigned storage channel, is dedicated to processing a single reagent: α or β. The dual-CDM operates similarly to the single device in each of its modes, performing all operations (as described in Section 2.2.3) for each reagent independently.

Reagents cannot be processed simultaneously using the same device, so interchangeable switching of modes is required to perform collision-free sequences by suspending one reagent's processing while the other is being processed.

The algorithm assumes that mode swapping is performed once the double-sized droplet (created after merging the beaker droplet with the input droplet) passes the mixer channel (see Fig. 4f for a reference) and enters the dedicated storage channel. The switching proceeds automatically. The control software detects the appearance of a droplet in the storage channel (thanks to the use of the camera) and changes the setting of the 3/2 valve. Thus, the storage channel receiving the incoming droplet now becomes deactivated, halting the droplet there and suspending its processing until the next mode swap. Simultaneously, that event activates the opposite storage channel, resuming the other reagent's processing starting from when the previous mode swap suspended it. Thus, the double-sized droplet of the other reagent is released from its activated storage channel and continues in the CDM sequence.

Thanks to such a device's configuration, instead of using two independent CDMs, we use only one shared module to generate both sequences of α and β reagents independently. This ensures that a minimal set of traps is used to proceed with the whole algorithm. As a benefit, we use only one metering trap, so all droplets are generated based on its geometry, which avoids any size differences among multiple traps due to fabrication tolerances.

The last modification of the device is an additional merging trap placed in the output channel. The role of this trap is the pairing of droplets from both sequences containing dilutions of different reagents.

The empty trap catches the output droplet of one of the reagents. Due to alternate switching of processed reagents, the next output droplet is made of the other reagent. Thus, a pair of droplets of different reagents meet at the merging trap, forming $\alpha\beta$-droplets of double size that leave the system, emptying the trap for the next pair. As a result, this mechanism pairs and merges every i-th α-droplet with the i-th β-droplet of concentrations $c_{\alpha,i}$ and $c_{\beta,i}$, respectively, creating double $\alpha\beta$-droplets of concentrations $c_{\alpha,i} = 0.5c_{\alpha,i}$ $c_{\beta,i} = 0.5c_{\beta,i}$. Thanks to this design, the pairing of droplets is performed passively simply by taking advantage of the merging trap.

The $\alpha\beta$-droplet can be directed from its output to another section of a microfluidic device for further processing and analysis (e.g., the addition of a bacterial culture). Fig. 9d shows an experimental image from the dual-CDM after the creation of a cross-combined $\alpha\beta$-droplet. That double-sized droplet of color, resulting from the mixing of base colors (red and blue in appropriate proportions), is moving to finally leave the device.

We tested the device and the above-described algorithms on the sequences defined by the following periodic patterns:

$$\boldsymbol{\pi}_\alpha = [0,1,0,0,0,1,0,1,1,1] \tag{32}$$

and

$$\boldsymbol{\pi}_\beta = [0,1,0,0,0,1,0,1,1,1,1] \tag{33}$$

of lengths $\omega_\alpha = 10$ and $\omega_\beta = 11$, respectively. The least common multiple of ω_α and ω_β equals their product $\omega_\alpha \cdot \omega_\beta = 110$. Hence, for a fully periodic series, we can obtain 110 unique cross-combinations of concentrations.

Starting the sequence from the scratch (in this case with initial $c_0 = 0$), we should be aware that the initial concentrations of droplets may substantially diverge from the theoretical periodic series; however, by expanding the whole sequence with additional (e.g., 9) droplets, we can recover the periodic values of the first droplets. Starting from the 111th droplet, we initiate the next period, e.g., the 111th droplet is equivalent
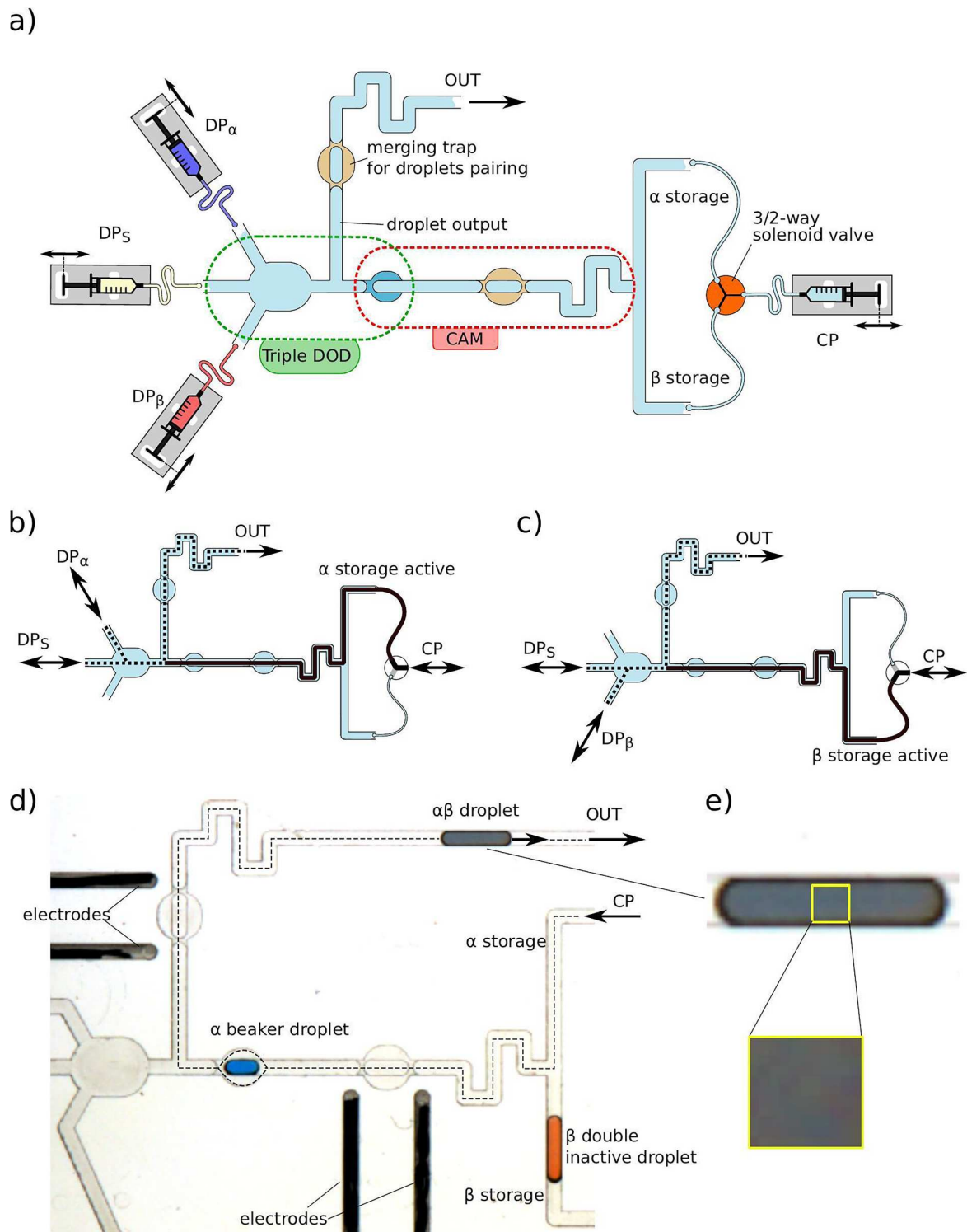
Fig. 9. Dual concentration on demand module. a) Scheme of the microfluidic dual-CDM and diagram showing connections to four bidirectional pumps operating the setup. Pumps are connected to a computer (not shown here) and operated by the software which executes the algorithms, b), c) flow patterns for two settings of the 3/2 valve, b) flow patterns for α-storage active. c) flow patterns for β-storage active, d) experimental image from the running dual-CDM, and e) magnified image of the αβ-droplet with an 11 pixels × 11 pixel square from its interior used to create the collage in Fig. 10b.

to the first droplet of a fully periodic series. The transient initial stage results provide some additional points scattered between the points for a fully periodic solution (see Fig. 10b).

In experimental tests, we used input sequences $m_\alpha = [0, \pi_\alpha, \pi_\alpha, ...]$ and $m_\beta = [0, \pi_\beta, \pi_\beta, ...]$ with initial concentrations $c_{\alpha,0} = c_{\beta,0} = 0$. The additional input droplets with zero concentration at the beginning of the m_α and m_β sequences ensure that the first output droplet is made of the solvent only ($c_{\alpha,1} = c_{\beta,1} = 0$), adding the auxiliary reference point in the
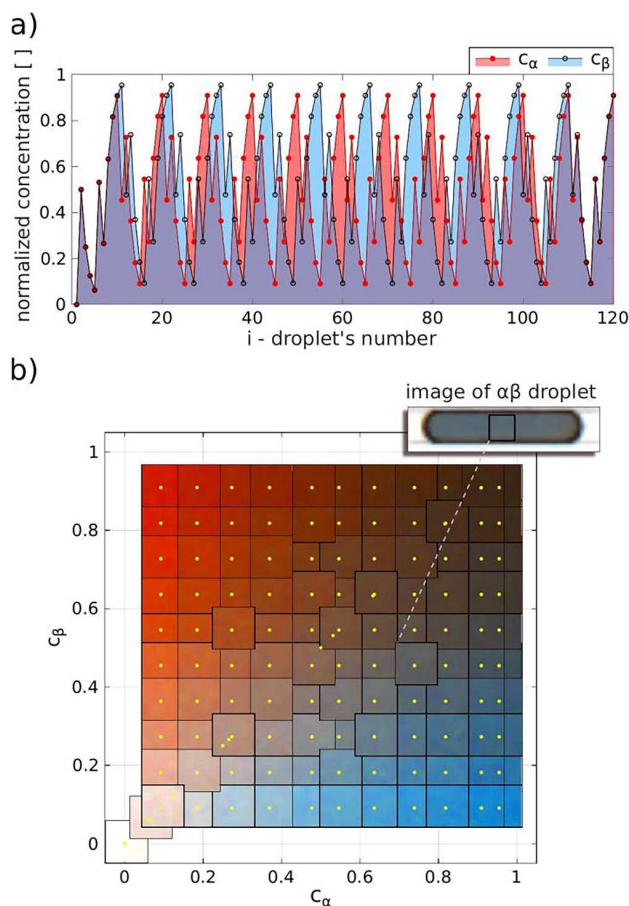
Fig. 10. Experimental examination of the dual-CDM. a) Plots of predicted concentrations c_α and c_β resulting from processing the input sequences $\boldsymbol{m}_\alpha = [0, \boldsymbol{\pi}_\alpha, \boldsymbol{\pi}_\alpha, ...]$ and $\boldsymbol{m}_\beta = [0, \boldsymbol{\pi}_\beta, \boldsymbol{\pi}_\beta, ...]$, where $\boldsymbol{\pi}_\alpha = [0, 1, 0, 0, 0, 1, 0, 1, 1, 1]$ and $\boldsymbol{\pi}_\beta = [0, 1, 0, 0, 0, 1, 0, 1, 1, 1]$, calculations made using Eq. (1) and b) diagram showing all possible combinations of c_a versus c_b obtained by combining droplets from two periodic series. The color collage was created by putting 120 squares (11 pixels × 11 pixels), each taken from the interior of experimental images of αβ-droplets (see the inset in the right top corner and Fig. 9e). Images are distributed according to coordinates given by assigned expected output concentrations c_α and c_β (i.e., i-th image occupies the position $c_{\alpha,i}$, $c_{\beta,i}$).

measurement series. Furthermore, as pointed out above, we extended the number of processed droplets with an additional 9 droplets for a total of 120 to recover the periodical results for the first droplets. Movie 2 shows the beginning of the conducted experiment.

We calculated the expected sequences of concentrations c_α and c_β by applying Eq. (1) to input sequences $\boldsymbol{m}_\alpha$ and $\boldsymbol{m}_\beta$. The plots of both c_α and c_β sequences are presented in Fig. 10a.

Fig. 10b shows the results of the experiments with the Dual-CDM which processed input sequences defined by $\boldsymbol{m}_\alpha$ and $\boldsymbol{m}_\beta$. The base liquids α and β were aqueous solutions of color indicators – blue and red, respectively – while the solvent was clear water. Therefore, every combination of concentrations of both dyes is assigned to the unique color of a droplet.

Fig. 10b shows 120 squares (11 pixels × 11 pixels), each taken from the interior of experimental images of subsequent αβ-droplets (see Fig. 9e and the inset in Fig. 10b). Those images are distributed according to coordinates given by assigned expected output concentrations, creating a collage on the $c_\alpha c_\beta$-plane (i.e., i-th image occupies the position $c_{\alpha,i}$, $c_{\beta,i}$). The smooth color transition in all directions visualizes the correct operation of the device and the validity of the proposed algorithm.

3. Conclusions

In this paper, we designed and built devices that use complex digital procedures to adjust the concentration of reagents within droplets in microfluidic channels. The small device's footprint and minimal sets of actuators (only syringe pumps for the basic variant) render this architecture a comprehensive module that can be built into a larger device for processing a series of further operations on droplets. Moreover, the system shown can work in a variety of configurations. For example, the syringe pump with CP can be connected from the other side and collect excess droplets, as shown in Fig. 4. Each double-sized droplet would potentially be an output droplet, as well. Due to its reconfigurability, a CDM built into a microfluidic network can be adjusted to avoid any disturbance of flows in the rest of the channel systems.

In the presented device, we used the microfluidic traps reported previously as components of microfluidic systems for the production of serial dilutions in droplets [13,18]. Here we show the module composed of the minimal set of traps integrated with the novel DOD system. Unlike previous traps systems, the new device avoids the waste of samples while offering programmable execution of a much more comprehensive range of different laboratory procedures beyond the consecutive dilutions.

As shown, the only mechanical parts are pumps, and the operation of the systems relies on the sequence of their switching actions to forward or backward directions or stopping. Due to passive elements, the system does not require any calibration to achieve satisfactory precision and accuracy. Syringe pumps are quite common, so the proposed technology can be adapted in most laboratories without additional purchases. Most commercial and open-source syringe pumps are available with drivers and libraries, allowing for their control by custom software written in popular environments.

The presented system and algorithms are envisioned to be developed toward better usage of resources. For example, implementing temporal storage for the output droplets would decrease the time and minimize waste in the precise adjustment of the concentration of a single droplet [3]. The simplest way to implement storage is to use a long channel connected to the CDM on one side and to add a pump on a second side. This would realize a stack memory, adding two principal operations to the system: store, which would add a droplet to the collection, and load, which would remove the most recently added droplet. One or more stacks added to the device would convert the device into a stack machine that could execute many other algorithms and be a more general-purpose processor.

Another perspective may emerge from implementations of sequential logic microfluidic circuits, which, with a series of permutations [31], could prepare a required sequence of input droplets. Such systems would produce the encoded distribution of concentrations with passive self-organization of the flow, requiring fewer external manipulations by programmed sequences of flow reversals. This would open the possibility of creating compact microfluidic devices, such as the function generators used in electronics to generate different types of waveforms.

The other interesting aspect of the presented system is that it can be seen as a linear time-invariant system and described as digital signal processing, where the input sequence of droplets can be described as a digital signal. In linear time-invariant systems, convolution of the input signal with the impulse response results in the output signal. The algorithm presented in the paper describes the ideal system. It implements a first-order infinite impulse response filter with constrained coefficients equal to 0.5, which makes it a low-pass filter. The impulse response of the filter is well-known. Unfortunately, in real systems, some imperfections exist, for example, due to fabrication or the constraints of pumps. This can result in systematic differences in generated droplets. Therefore, the impulse response can also be measured in the device to obtain improvements in achieving the demanded concentrations by adding corrections to the described algorithm.

The article presents examples close to linear distributed

concentrations, while logarithmic dilutions are more common in analytical practice. As we mentioned, our system is capable of the preparation of serial dilutions and their cross-combinations for two-reagent systems. Moreover, the logarithmic dilutions are simpler for the implementations in our systems than nonlogarithmic dilutions. We wanted to show less obvious linear-like distributions to emphasize that the presented system is much more flexible in setting different concentrations than simple dilution-based microfluidic systems.

Finally, we show that digital algorithms operating on droplets are not only the domain of EWOD-based DMF systems but can be effective and relatively easily implemented in channel-based microfluidics.

Besides the above-mentioned advantages and novelty, the main shortcoming of our system is the relatively low throughput. Indeed, the hydrodynamic traps require flows with sufficiently low Capillary numbers [29], which is achieved by keeping the flow rate below some critical level, limiting the efficiency.

In the case of the experiments presented in this article, the single step of the algorithm, including sequence of i) generation of a droplet, ii) merging droplets, iii) mixing, and iv) splitting, takes about 19 s. This time can be lowered a few-fold by the further optimization of the device. Still, because of the limit for Capillary number, the efficiency cannot approach the level offered by the high-throughput microfluidic systems [32]. However, this paper aimed rather at the microfluidic system's precision, controllability, automation-ability, and simplicity than at high throughput. Still, the low-throughput offering by our system is not problematic in the potential applications, where the investigated reaction time is relatively long, e.g., amplification of DNA or biological assays involving cell cultures.

As we mentioned before, the proposed system can be developed to implement more advanced algorithms, including memory-like storage of droplets. Additionally, it can be enriched with feedback from the measurements of the reaction in droplets. Thus, searching for the optimal reaction condition can be adjusted in each step and focused on the more narrow range of parameters. Thus, this approach differs from the other titration-like methods requiring high throughput, where the reaction results are scanned through a series of numerous dilutions covering the whole range densely. Our system's ability to implement algorithms based on numerical methods such as, e.g., the bisection method, can increase the efficiency at a minimal number of steps, compensating the operations' low throughput.

4. Materials and methods

4.1. Liquids

We used hexadecane (Sigma Aldrich Co.) with the addition of approximately 0.2% Span 80 (Sigma Aldrich Co.) as CP and 6% or 24% glycerine (Sigma Aldrich Co.) water solution as DP. In all experiments, one syringe was filled with colorless DP, and the others were filled with the same DP with added dye. We used methylene blue (Sigma Aldrich Co.) for experiments presenting single droplet diluters. Food dyes (Allura Red AC (E129) and Brilliant Blue FCF (E133), Sigma Aldrich Co.) were used for the dual-droplet dilution experiment.

4.2. Microfluidic devices

All the presented devices were fabricated by milling geometries in 4- or 5-mm plates of polycarbonate (Makrolon, Bayer AG, Germany) using a CNC milling machine (Ergwind, Poland) with 0.4-mm end mills (FR208, inGraph, Poland). In the case of milled surfaced, the value of the profile roughness parameter is Ra = 0.742 ± 0.072 μm (measured using the Keyence VK-X100 profilometer). The fabricated devices were additionally inspected using a profilometer toward the agreement of the fabricated geometrical details to the design (see Supplementary Information). The contact angle for the milled surface was 104.3° ±2.5° measured using Data Physics OCA 15 goniometer.

After engraving the microfluidic geometries in one plate of PC, the other plate was bonded to close channels. Finally, the device was sealed and had only holes for inlets and outlets. To align both plates in the correct position, we used steel pins inserted into auxiliary holes. An exploded view of a fabricated microfluidic device is shown in Supplementary Material.

The plates were bonded using a hot press at 135° C for 10 min. We applied no further channel modifications. Before the first use, the devices were kept filled with CP for several minutes.

We used additional electrodes to facilitate the coalescence of merging droplets. Electrodes were made from wire (UL3239 28AWG with insulation XLPE, rated voltage 6 kV-DC). We inserted electrodes into dedicated channels to place their ends close to the merging trap where droplets coalescence.

To simplify our experiments, we added a large container at the output (channel with depth and width of at least 3 mm) which collected output droplets. This container's far larger depth than the output channel of the diluter prevented the return of irrelevant droplets to the system when the flow reversed. The container also had two outlets connected to a waste container outside of the microfluidic device. The volume of the tank allowed several hundred superfluous drops to be collected. It allowed each presented experiment to be conducted without a break. The filled container was flushed out manually using one of the outputs connected to the waste container.

4.3. Experimental setup

To control the system, we used syringe pumps (Low Pressure Syringe Pump neMESYS 290 N, Cetoni GmbH, Germany) with 1 ml glass syringes (1001TTL, Hamilton, USA) connected to the inlets of devices via PTFE tubing (S1810-10, Bola GmbH, Germany) with an 0.8 mm inner diameter and a 1.6 mm outer diameter. Tubing was connected to the system with cut needles that were pressed into the input and output holes of the microfluidic system. We used up to four syringe pumps and one 3/2-way solenoid valve (ASCO 067 Rocker, Emerson, USA) controlled through one of the syringe pump modules. Each liquid used in the experiments was acted on by only one dedicated pump. Hence, the number of pumps equaled the number of liquid types. The valve was connected to the syringe with CP and used to change channels that store droplets in the two-droplet mixing experiments.

The use of a surfactant prevented wetting of the channel walls by the DP, disrupting droplets.

Droplets flowing in the investigated microfluidic devices were observed using a stereoscope (HSZ-645TR, Huvitz, South Korea) equipped with a CCD camera (UI-3274LE-C-HQ, IDS, Germany). The camera was used to synchronize transitions and to record images of transitional and final concentrations of droplets. To increase the accuracy of the measurement of methylene blue, we added a bandpass filter of 550 nm – 570 nm in the c-mount of the stereoscope.

4.4. Calibration of the concentration measurements

A calibration curve was measured for experiments where methylene blue was used, and measurements of the concentrations of droplets formed were presented. For this purpose, intermediate concentrations between colorless and colored DP were made manually using a pipetting device. The following concentrations were used: 0, 0.125, 0.250, 0.375, 0.5, 0.625, 0.750, 0.875, and 1. The system was manually filled with each concentration using a syringe. For each concentration, the image brightness was measured at the same location where the image brightness was measured for the measured droplets and the background. As a result, a calibration curve was obtained by fitting a polynomial to the experimental data.

Declaration of Competing Interest

The authors declare that they have no known competing financial interests or personal relationships that could have appeared to influence the work reported in this paper.

Acknowledgements

Appendix A. Supplementary data

Supplementary data to this article can be found online at https://doi.org/10.1016/j.cej.2021.132935.

References

[1] X. Wang, Z. Liu, Y. Pang, Concentration gradient generation methods based on microfluidic systems, RSC Adv. 7 (2017) 29966–29984, https://doi.org/10.1039/C7RA04494A.

[2] E. Samiei, M. Tabrizian, M. Hoorfar, A review of digital microfluidics as portable platforms for lab-on a-chip applications, Lab. Chip. 16 (2016) 2376–2396, https://doi.org/10.1039/C6LC00387G.

[3] S. Roy, B.B. Bhattacharya, K. Chakrabarty, Optimization of dilution and mixing of biochemical samples using digital microfluidic biochips, IEEE Trans. Comput.-Aided Des. Integr. Circuits Syst. 29 (2010) 1696–1708, https://doi.org/10.1109/TCAD.2010.2061790.

[4] S. Bhattacharjee, A. Banerjee, T.-Y. Ho, K. Chakrabarty, B.B. Bhattacharya, Efficient generation of dilution gradients with digital microfluidic biochips, IEEE Trans. Comput.-Aided Des. Integr. Circuits Syst. 38 (2019) 874–887, https://doi.org/10.1109/TCAD.2018.2834413.

[5] J.D. Tice, H. Song, A.D. Lyon, R.F. Ismagilov, Formation of droplets and mixing in multiphase microfluidics at low values of the reynolds and the capillary numbers, Langmuir. 19 (2003) 9127–9133, https://doi.org/10.1021/la030090w.

[6] H. Song, M.R. Bringer, J.D. Tice, C.J. Gerdts, R.F. Ismagilov, Experimental test of scaling of mixing by chaotic advection in droplets moving through microfluidic channels, Appl. Phys. Lett. 83 (2003) 4664–4666, https://doi.org/10.1063/1.1630378.

[7] V. van Steijn, P.M. Korczyk, L. Derzsi, A.R. Abate, D.A. Weitz, P. Garstecki, Block-and-break generation of microdroplets with fixed volume, Biomicrofluidics. 7 (2013), 024108, https://doi.org/10.1063/1.4801637.

[8] F. Gielen, L. van Vliet, B.T. Koprowski, S.R.A. Devenish, M. Fischlechner, J.B. Edel, X. Niu, A.J. deMello, F. Hollfelder, A fully unsupervised compartment-on-demand platform for precise nanoliter assays of time-dependent steady-state enzyme kinetics and inhibition, Anal. Chem. 85 (2013) 4761–4769, https://doi.org/10.1021/ac400480z.

[9] H.S. Rho, Y. Yang, L.W.M.M. Terstappen, H. Gardeniers, S. Le Gac, P. Habibović, Programmable droplet-based microfluidic serial dilutor, J. Ind. Eng. Chem. 91 (2020) 231–239, https://doi.org/10.1016/j.jiec.2020.08.004.

[10] J. Wegrzyn, A. Samborski, L. Reissig, P.M. Korczyk, S. Blonski, P. Garstecki, Microfluidic architectures for efficient generation of chemistry gradations in droplets, Microfluid. Nanofluidics. 14 (2013) 235–245, https://doi.org/10.1007/s10404-012-1042-3.

[11] C.-G. Yang, Z.-R. Xu, A.P. Lee, J.-H. Wang, A microfluidic concentration-gradient droplet array generator for the production of multi-color nanoparticles, Lab. Chip. 13 (2013) 2815–2820, https://doi.org/10.1039/C3LC50254F.

[12] X. Niu, F. Gielen, J.B. Edel, A.J. deMello, A microdroplet dilutor for high-throughput screening, Nat. Chem. 3 (2011) 437–442, https://doi.org/10.1038/nchem.1046.

[13] P.M. Korczyk, L. Derzsi, S. Jakieła, P. Garstecki, Microfluidic traps for hard-wired operations on droplets, Lab. Chip. 13 (2013) 4096–4102, https://doi.org/10.1039/C3LC50347J.

[14] B. Bhattacharjee, S.A. Vanapalli, Electrocoalescence based serial dilution of microfluidic droplets, Biomicrofluidics. 8 (2014), 044111, https://doi.org/10.1063/1.4891775.

[15] J. Shemesh, T.B. Arye, J. Avesar, J.H. Kang, A. Fine, M. Super, A. Meller, D. E. Ingber, S. Levenberg, Stationary nanoliter droplet array with a substrate of choice for single adherent/nonadherent cell incubation and analysis, Proc. Natl. Acad. Sci. 111 (2014) 11293–11298, https://doi.org/10.1073/pnas.1404472111.

[16] M. Sun, S.S. Bithi, S.A. Vanapalli, Microfluidic static droplet arrays with tuneable gradients in material composition, Lab. Chip. 11 (2011) 3949, https://doi.org/10.1039/c1lc20709a.

[17] K. Totlani, J.-W. Hurkmans, W.M. van Gulik, M.T. Kreutzer, V. van Steijn, Scalable microfluidic droplet on-demand generator for non-steady operation of droplet-based assays, Lab. Chip. 20 (2020) 1398–1409, https://doi.org/10.1039/C9LC01103J.

[18] W. Postek, T.S. Kaminski, P. Garstecki, A precise and accurate microfluidic droplet dilutor, Analyst. 142 (2017) 2901–2911, https://doi.org/10.1039/C7AN00679A.

[19] E. Um, M.E. Rogers, H.A. Stone, Combinatorial generation of droplets by controlled assembly and coalescence, Lab. Chip. 13 (2013) 4674–4680, https://doi.org/10.1039/C3LC50957E.

[20] X. Niu, S. Gulati, J.B. Edel, A.J. deMello, Pillar-induced droplet merging in microfluidic circuits, Lab. Chip. 8 (2008) 1837, https://doi.org/10.1039/b813325e.

[21] K. Churski, T.S. Kaminski, S. Jakiela, W. Kamysz, W. Baranska-Rybak, D.B. Weibel, P. Garstecki, Rapid screening of antibiotic toxicity in an automated microdroplet system, Lab. Chip. 12 (2012) 1629–1637, https://doi.org/10.1039/C2LC21284F.

[22] K. Churski, P. Korczyk, P. Garstecki, High-throughput automated droplet microfluidic system for screening of reaction conditions, Lab. Chip. 10 (2010) 816–818.

[23] H. Babahosseini, T. Misteli, D.L. DeVoe, Microfluidic on-demand droplet generation, storage, retrieval, and merging for single-cell pairing, Lab. Chip. 19 (2019) 493–502, https://doi.org/10.1039/C8LC01178H.

[24] D. Cottinet, F. Condamine, N. Bremond, A.D. Griffiths, P.B. Rainey, J.A.G.M. de Visser, J. Baudry, J. Bibette, Lineage tracking for probing heritable phenotypes at single-cell resolution, PLOS ONE. 11 (2016), e0152395, https://doi.org/10.1371/journal.pone.0152395.

[25] P. Debski, K. Sklodowska, J. Michalski, P. Korczyk, M. Dolata, S. Jakiela, Continuous recirculation of microdroplets in a closed loop tailored for screening of bacteria cultures, Micromachines. 9 (2018) 469.

[26] K. Sklodowska, P. Debski, J. Michalski, P. Korczyk, M. Dolata, M. Zajac, S. Jakiela, Simultaneous measurement of viscosity and optical density of bacterial growth and death in a microdroplet, Micromachines. 9 (2018) 251, https://doi.org/10.3390/mi9050251.

[27] S. Jakiela, T.S. Kaminski, O. Cybulski, D.B. Weibel, P. Garstecki, Bacterial growth and adaptation in microdroplet chemostats, Angew. Chem. Int. Ed. 52 (2013) 8908–8911, https://doi.org/10.1002/anie.201301524.

[28] H.-H. Jeong, B. Lee, S.H. Jin, S.-G. Jeong, C.-S. Lee, A highly addressable static droplet array enabling digital control of a single droplet at pico-volume resolution, Lab. Chip. 16 (2016) 1698–1707, https://doi.org/10.1039/C6LC00212A.

[29] D. Zaremba, S. Blonski, M. Jachimek, M.J. Marijnissen, S. Jakiela, P.M. Korczyk, Investigations of modular microfluidic geometries for passive manipulations on droplets, Bull. Pol. Acad. Sci.-Tech. Sci. 66 (2018) 139–149, https://doi.org/10.24425/119068.

[30] J. Wang, J. Wang, L. Feng, T. Lin, Fluid mixing in droplet-based microfluidics with a serpentine microchannel, RSC Adv. 5 (2015) 104138–104144, https://doi.org/10.1039/C5RA21181F.

[31] D. Zaremba, S. Błoński, P.M. Korczyk, Integration of capillary–hydrodynamic logic circuitries for built-in control over multiple droplets in microfluidic networks, Lab. Chip. 21 (2021) 1771–1778, https://doi.org/10.1039/D0LC00900H.

[32] T.S. Kaminski, P. Garstecki, Controlled droplet microfluidic systems for multistep chemical and biological assays, Chem. Soc. Rev. 46 (2017) 6210–6226, https://doi.org/10.1039/C5CS00717H.

Supplementary Material

# Concentration on-demand – the microfluidic system for precise adjustment of the content of single droplets

Damian Zaremba, Slawomir Blonski, Piotr M. Korczyk

Construction of Microfluidic Devices

Here we provide additional details on the design and construction of the microfluidic devices. The general construction of the device is shown in Figure 1 on the example of the simple T-junction. The concept of the device, which consists of:

i) the bottom polycarbonate plate with engraved channels,

ii) the top plates with holes for connection ports and

iii) part of needles inserted in holes to connect with tubings

is common for all devices used in the article except the particular designs of channels.
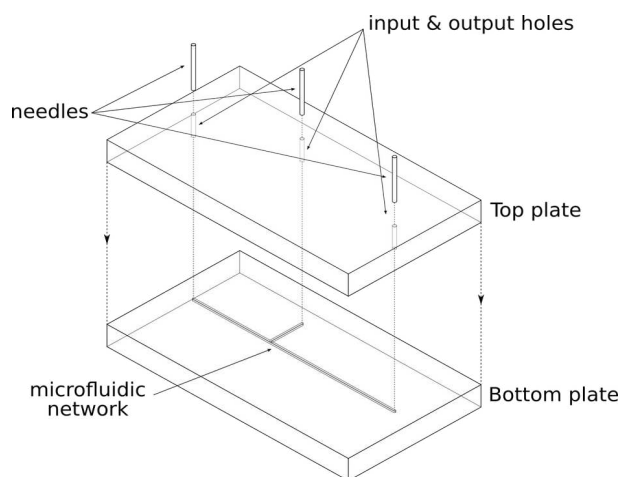
Figure 1 The composition of a microfluidic chip on the example of a simple T-junction design. Exploded view of a fabricated microfluidic device. The bottom plate of polycarbonate compromises the engraved channels. The top plate consists of the holes-through overlapping the ends of channels. The steel tubings made of needles serve as an interface enabling the tight device's connection to elastic tubing and then to flow sources or output containers.

Figures 2 and 3 show the CDM and Dual-CDM devices designed and fabricated for the presented work.

Additionally, we provide supplementary files the CAD designs of CDM and Dual-CDM devices in DXF format.
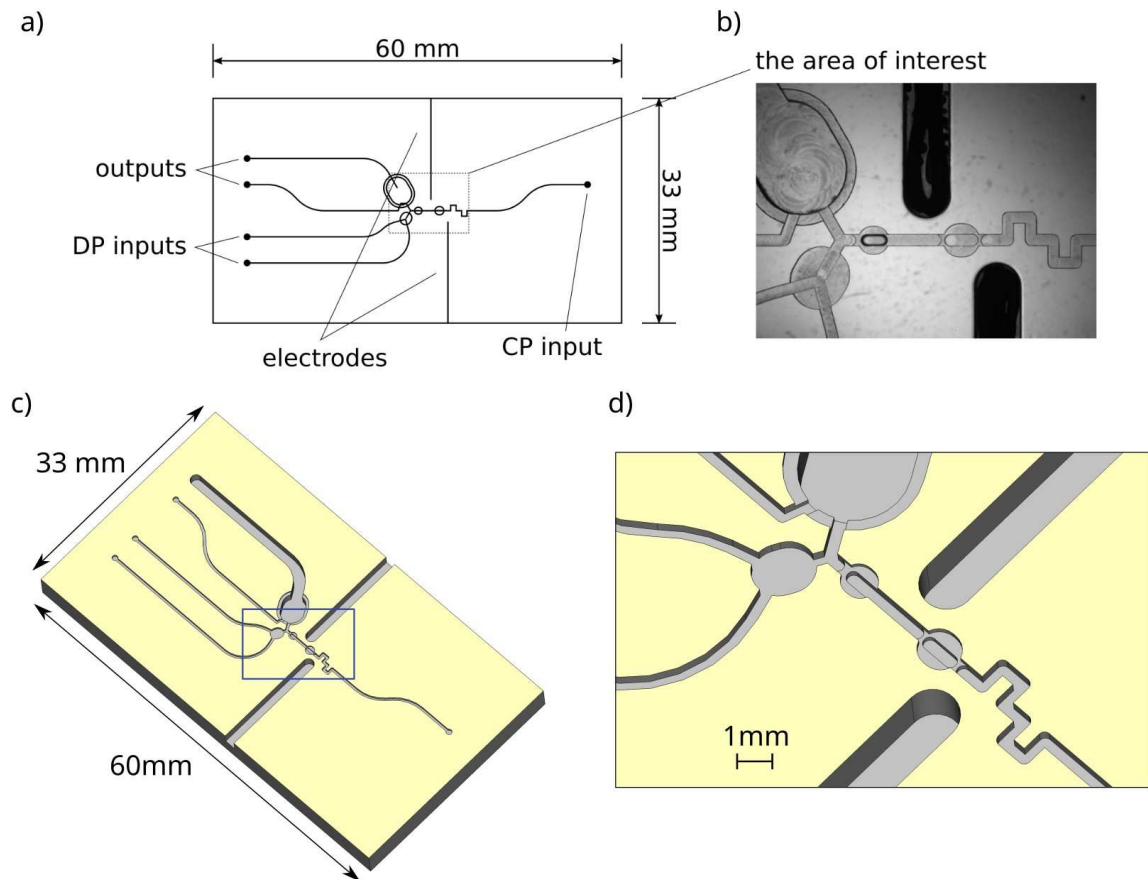
Figure 2 Complete scheme of the single CDM microfluidic device used in the presented research. a) the top-view of the scheme. b) top-view image of the details of the fabricated device. c) 3D render of the design with a close-up of details – d).
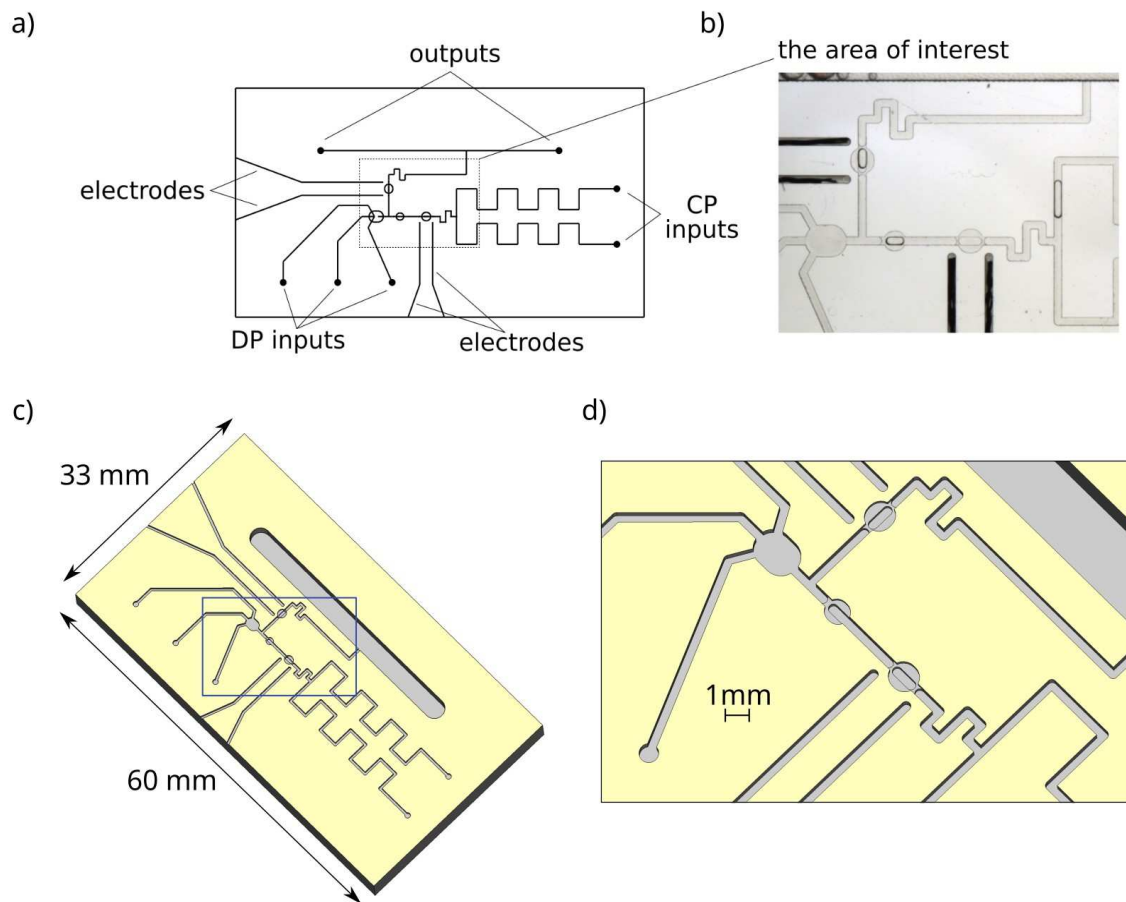
Figure 3 Complete scheme of the Dual-CDM microfluidic device used in the presented research. a) the top-view of the scheme. b) top-view image of the details of the fabricated device. c) 3D render of the design with a close-up of details – d).

Cross-sectional view of microfluidic traps

We inspected the geometry of the fabricated traps before bonding using the Keyence VK-X100 profilometer. Figure 4 shows the results, which agree well with the geometry of the design of traps described in the main article and shows the good precision of the fabrication method.

We estimated the value of the profile roughness parameter Ra to be equal to 0.742±0.072 µm.
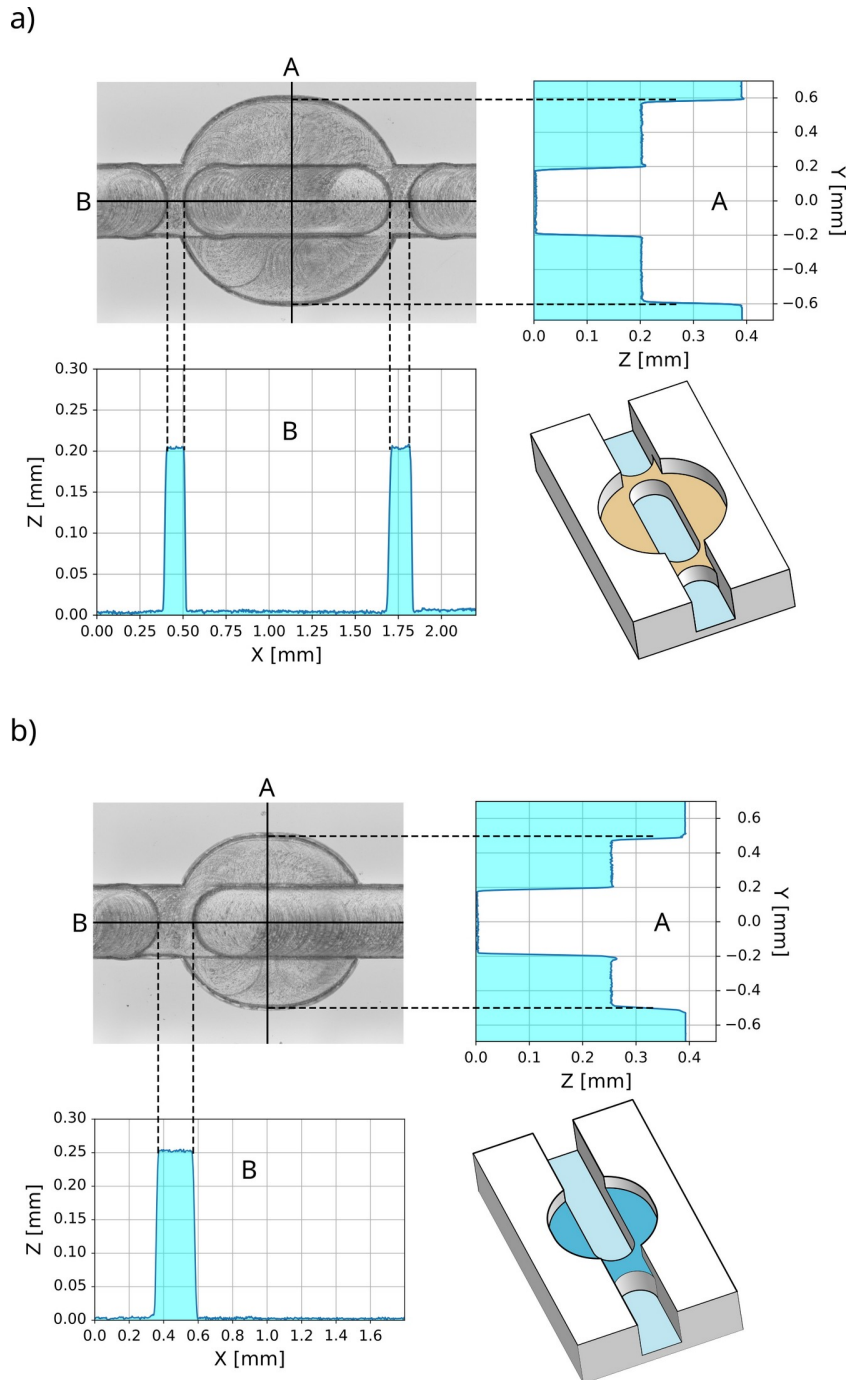
Figure 4 Details of the microfluidic traps obtained from profilometer measurements. a) the merging trap. b) the metering trap. The experimental images show the top-view projections of the fabricated traps used for the measurements. Lines A and B show the positions of the measurements of profiles. The additional 3-D images are added for reference.

Examination of the droplet on-demand generator accuracy and precision

We carried out investigations to check the repeatability of droplet formation in the DOD system presented in this research. First, an additional microfluidic system was constructed, as shown in figure 5. Then, a metering trap of the same dimensions as in the other devices was connected by a T-junction to a straight channel, which then connects to a measuring channel of the smaller dimension (200 µm x 200 µm). Finally, we applied a step transition of the cross-section dimensions from an initial channel 400 µm x 400 µm to a 200 µm x 200 µm channel to avoid droplet split.

The reduction of the channel's cross-section area elongates droplets, improving the droplet's length measurement. The volume of droplets formed can be estimated using the formulas published by Musterd et al.[1] Nevertheless, measurement of droplet length alone under constant conditions is sufficient for comparative analysis and determination of repeatability. The length was measured using a CCD camera between the outermost points of the droplet in the channel section.
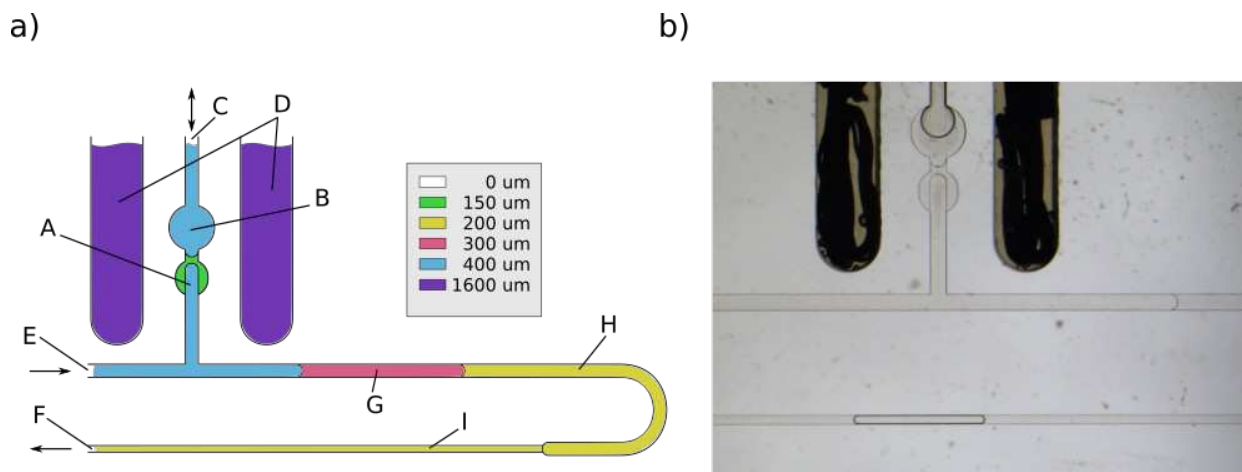
Figure 5 Microfluidic system for measuring the length of a formed droplet in a metering trap: a) Schematic diagram. Elements: A - metering trap. B - Channel expansion to merge redundant droplets with the input liquid. C - Input to the liquid forming the droplet phase. D - channels for electrodes. E - input channel for the oil phase. F - output channel of the system. G - channel section 400µm x 300µm. H - channel section 400µm x 200µm. I - section of the channel with cross-section 200µm x 200µm, in which the drop length is measured.

Three types of liquids were tested: clear water, water with methylene blue, and glycerine solution 24% V/V. We used the same continuous phase as in the article (hexadecane + span-80). Droplet length measurements were carried out for different flow rates of the droplet phase during the pulling step. The experiment consisted of creating a new droplet, pushing it out of the channel with the metering trap, transferring it to the measuring place, and then, with all syringe pumps stopped, measuring the length normalized to the width of the measuring channel. The push flow rate of the droplet phase was constant at 1ml/h for each droplet and all types of fluids. The flow rate of the oil phase during transferring each droplet to the measuring place was 0.5 ml/h. The detection of a droplet in the measuring channel was in the same way as in the article.

The only kinetic parameter relevant in the droplet formation process in our DOD system is the magnitude of the DP reversed flow. Therefore, we investigated the effect of variation of this

---

1   Musterd et al., "Calculating the Volume of Elongated Bubbles and Droplets in Microchannels from a Top View Image."

parameter on the length of droplets. Thanks to numerous repetitions of measurements for the fixed value of pulling flow rate of DP, we examined the repeatability of the droplet size, presenting the standard deviations of measurements as error bars in Figure 6.

The results shown in Figure 6 reveal the plateau of resultant droplet length for a pulling flow rate of DP between 0.6 ml/h and 1.2 ml/h, where the variations of droplet size are small. The droplet length within this range hardly depends on either the set pull-up flow rate, interfacial tension, or viscosity of the droplet phase. The small error bars in this range show excellent repeatability of the size of formed droplets.
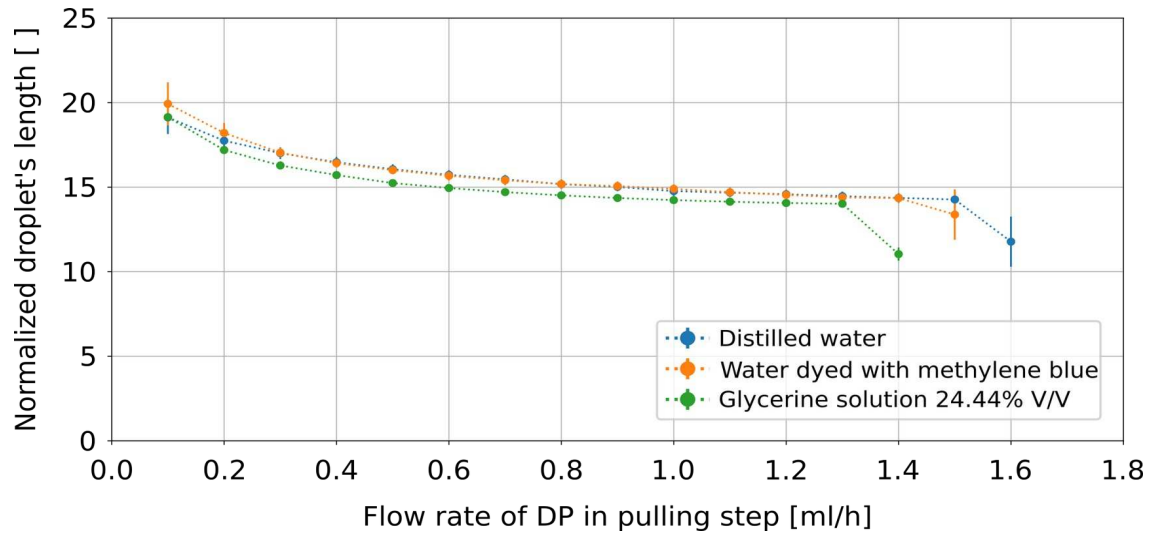
Figure 6 Measurement results for droplet formation in the metering trap as a function of the magnitude of the reversed flow of the droplet phase.

Accounting for corner flow unifies the understanding of droplet formation in microfluidic channels

Piotr M. Korczyk [1,5], Volkert van Steijn [2,5], Slawomir Blonski [1], Damian Zaremba [1], David A. Beattie [3] & Piotr Garstecki [4]

While shear emulsification is a well understood industrial process, geometrical confinement in microfluidic systems introduces fascinating complexity, so far prohibiting complete understanding of droplet formation. The size of confined droplets is controlled by the ratio between shear and capillary forces when both are of the same order, in a regime known as jetting, while being surprisingly insensitive to this ratio when shear is orders of magnitude smaller than capillary forces, in a regime known as squeezing. Here, we reveal that further reduction of—already negligibly small—shear unexpectedly re-introduces the dependence of droplet size on shear/capillary-force ratio. For the first time we formally account for the flow around forming droplets, to predict and discover experimentally an additional regime—leaking. Our model predicts droplet size and characterizes the transitions from leaking into squeezing and from squeezing into jetting, unifying the description for confined droplet generation, and offering a practical guide for applications.

In spite of the beautiful regularity in flows of droplets in microfluidic networks at low Reynolds and capillary numbers, their dynamics offers rich phenomenological complexity[1–4] that prohibits predictive understanding. A striking example is the flow of a single droplet through a microchannel[5–8] for which the most basic question how the speed of the droplet depends on flow conditions, fluid properties, and the level of confinement still lacks a full answer. The generation of droplets in microchannels[9,10] using T-junctions[11–19], flow-focusing[20–22], co-flow[23], step emulsification[24–29] and parallel devices[30–32], opened the new discipline of droplet microfluidics[33,34] that revolutionized analytical methods in biology[35] and medicine with digital assays[36], single cell sequencing[37], or systems for research on biological evolution[38]. Droplet microfluidic systems are also used to create new materials for pharmaceutical[39–41], cosmetics[42] and food[43] industries. In a stark contrast to the bulk process of shear emulsification that is one of the more illustrative and simple textbook examples of dimensional analysis, generation of droplets in confinement is still not completely understood.

The first microfluidic device used for the generation of droplets, a T-junction, was proposed by Thorsen et al.[11], who demonstrated that the dynamics of droplet formation is generally governed by surface tension and viscous shear, while body forces such as inertia or gravity play little role[9,13]. Depending on the relative magnitude of surface tension and shear, as captured by the capillary number (Ca), and on the contrast of viscosities between the two phases, distinct "visco-capillary" regimes have been identified[10]: dripping[13,14,16,22,44,45], jetting[44–46] and parallel co-flow[47]. Soon after, it was discovered that "capillary-dominated" formation of droplets in microconfinement results in droplet sizes that only depend of the ratio of the flow rates of the two immiscible liquids, completely independent of Ca, as described by the squeezing model[12,48]. This simple relation between droplet size and flow rates as well as the low polydispersity of the generated droplets makes the squeezing regime attractive for applications, where high precision and reproducibility are required in combination with independence on material parameters such as, e.g., the viscosity of the sample liquid. Efficient use of this technique thus requires a good understanding of the limits of the squeezing regime. However, the squeezing model, while commonly accepted, does not account for the flow of continuous liquid past the droplet while it is formed.

We show in this paper that the neglect of this corner flow entails spectacular failure of the squeezing model for vanishing values of capillary numbers. By formally accounting for this leaking flow we predict and verify experimentally a number of new features of generation of droplets in microconfinement, including an additional leaking regime at the lowest values of capillary number, the existence of a previously unknown lower bound of the squeezing regime, and scaling of the upper bound—the transition from squeezing to jetting. The model that we here demonstrate offers the unique attempt to a unified mechanistic description of the dynamics of droplet formation in microfluidic confinement.

Results

Experimental evidence for the leaking regime. We studied the formation of droplets in the commonly used geometry of the-so-called T-junction[11] (Fig. 1a). Our device comprises a perpendicular intersection of two inlet channels that deliver two immiscible liquids, the droplet phase (DP) and the continuous phase (CP), and a common output from the junction. The CP preferentially wets the walls of the channels and the droplets never contact the walls, always being separated from them by at least a thin film of the CP. This prevents pinning of a contact line, which
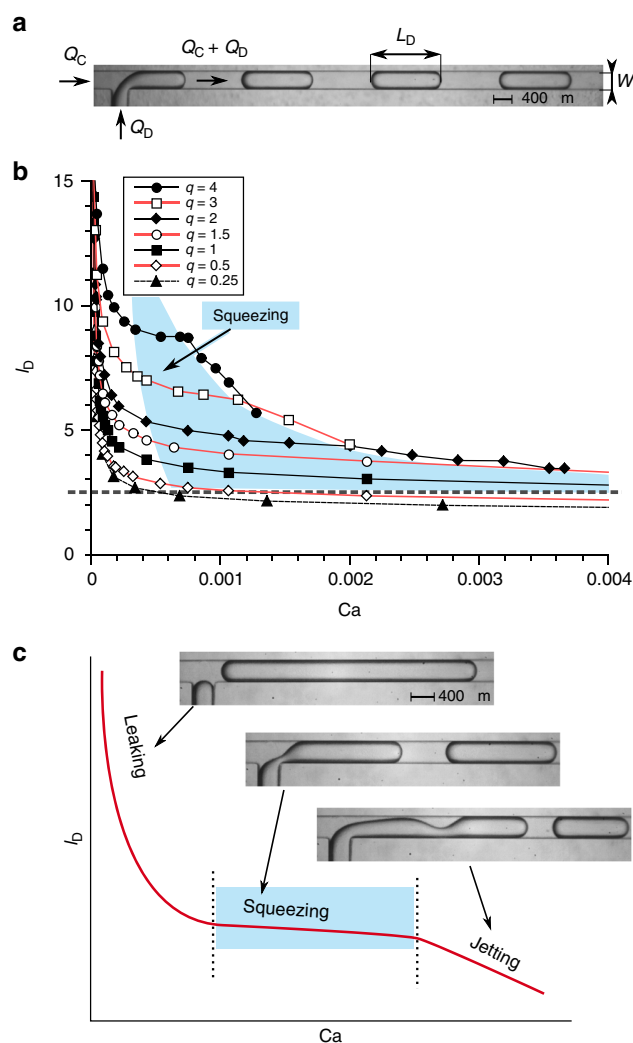
Fig. 1 Droplet formation at a microfluidic T-junction and experimental data for the length of droplets versus the capillary number. **a** Snapshot illustrating the geometry of the T-junction with channels of a square cross section, i.e. $W = H = 360\,\mu m$. Q_C and Q_D are the flow rates of the CP (hexadecane) and DP (fluorinated oil FC-40), respectively. L_D is the length of a droplet. **b** Experimental data—normalized length of a droplet $l_D = L_D/W$ as a function of the capillary number Ca for different $q = Q_D/Q_C$. The blue area highlights the region, where all curves have a plateau, interpreted as the squeezing regime. The boundary at the bottom of this area is taken as the minimum length for which squeezing is operative ($l_D \approx 2.5$, dashed line). **c** Schematic picture of the scaling of the normalized length of a droplet, l_D, with the capillary number Ca, as extracted from the full experimental data set in **b**, illustrating the leaking, squeezing, and jetting regimes

would render the dynamics irreproducible and hard to control. Stationary inflow of both phases into the junction causes a periodic breakup of the DP into droplets.

We measured the length of droplets as a function of Ca, for various ratios $q = Q_D/Q_C$ of flow rates of the DP and CP (see Fig. 1b). We normalized the length of the droplets, L_D, using the width of the channel, W, as $l_D = L_D/W$, and defined the capillary number as $Ca = \mu_C U/\gamma$, with μ_C the dynamic viscosity of the CP, $U = Q_C/HW$ the mean speed of the CP, H the channel height, and γ the liquid–liquid interfacial tension. The qualitative behaviour obtained from these measurements is illustrated in Fig. 1c. The plateau in which droplet length is virtually independent of Ca,
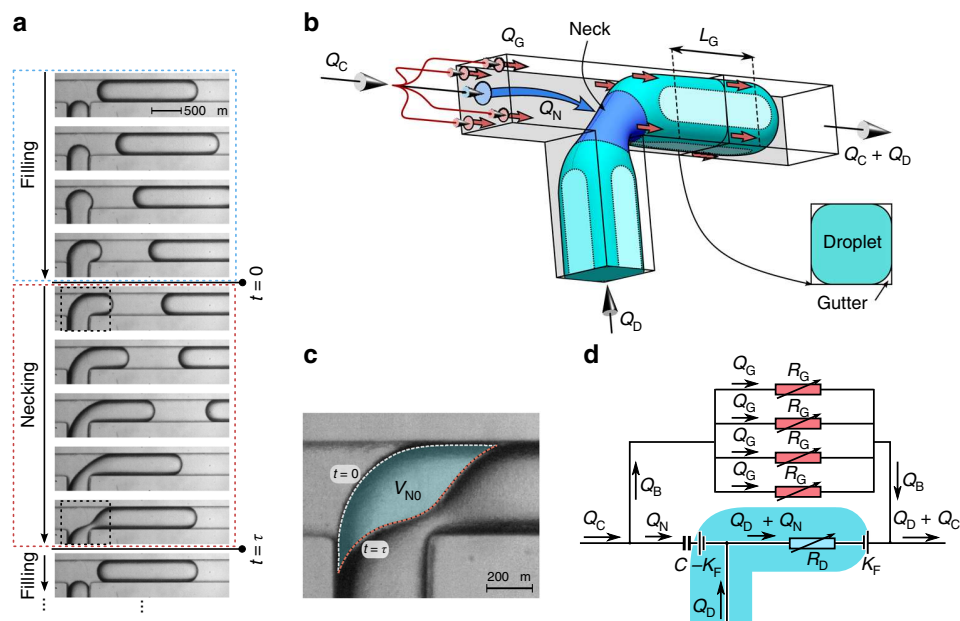
Fig. 2 The process of droplet formation and concepts behind the theoretical model. **a** Consecutive snapshots showing a complete droplet formation cycle comprising a filling and a necking stage. **b** 3D schematic view of the geometry of a forming droplet in the necking stage showing the decomposition of the incoming CP flow (Q_C) in a flow towards the neck (Q_N) and four flows through the gutters (Q_G). **c** Comparison of shapes of the neck at the start of the necking stage ($t = 0$) and just before the neck breaks ($t = \tau$), (both images were extracted from the highlighted rectangles in the snapshots in **a**). The difference of these shapes defines the volume of the neck V_{N0}, which must be filled by the continuous phase to induce pinch-off. **d** Circuit diagram illustrating how flows towards and around the forming droplet depend on the time-dependent resistances (R_G for viscous resistance in a gutter and R_D for viscous resistance inside the forming droplet). Laplace pressure jump at the front of a droplet is shown schematically as an 'electromotive force' established by the curvature of the interface K_F. The change of the Laplace pressure jump due to the accumulation of the CP behind the forming droplet is modelled as the combination of a capacitance C and the electromotive force with reversed direction in respect to the front of a droplet $-K_F$

confirms the well-accepted squeezing regime[12]. The Ca-dependent region at higher Ca indicates the—also known—jetting regime. The most intriguing aspect of the data in Fig. 1b, c is in the range of vanishing Ca, where the length of droplets explodes with Ca → 0. The squeezing regime not only spans a narrower range of Ca than previously expected[13] due to the existence of the lower boundary, but also due to the dependence of the upper boundary on q. Generally, the higher q, the narrower the range of Ca for the squeezing regime, as clearly illustrated by the highlighted area in Fig. 1b. Given the strong Ca-dependence in the here identified leaking regime, a good understanding of the mechanism that introduces this dependency is crucial for practical applications and presented next.

Mathematical model of the leaking regime. The starting point for our theoretical framework is the original squeezing model[12,48], which considers droplet formation as a two-step process (Fig. 2a). During the first 'filling' stage, that starts when the previous droplet has detached, the tip of the DP expands into the main channel and fills most of the junction. In the second, 'necking' stage, the droplet grows, extending downstream from the junction, while the CP squeezes the 'neck' (Fig. 2b). Defining the volume occupied by the neck, $V_N(t)$, with respect to the shape of the neck at pinch-off, this volume gradually decreases from V_{N0} at the start of the necking stage ($t = 0$) to zero at pinch-off ($t = \tau$) (see Fig. 2c). The space left behind the moving interface is filled by the incoming volume of CP: $V_N^*(t) = V_{N0} - V_N(t)$. The final volume of a droplet, V_D, can be decomposed as the volume at the end of the filling stage, V_{fill}, and the volume added at a rate Q_D during the time τ of the necking stage. Hence, $V_D = V_{fill} + Q_D\tau$. The original squeezing model assumes complete blockage of the channel by the forming droplet during the necking stage and calculates the necking time

as—simply—the time required for the continuous phase to displace the volume initially occupied by the neck V_{N0}, i.e. $\tau = V_{N0}/Q_C$ (see Fig. 2c). This assumption overlooks that a non-wetting droplet does not fill the corners of a channel that has a rectangular cross section[49,50], allowing the CP to flow (leak) by the droplet through these corners, the so-called 'gutters'[15] (see Fig. 2b). For an elongated droplet steadily pushed through a straight rectangular channel, Wong et al.[5] pointed out that such a droplet acts as a leaky piston with the fraction of the incoming CP flowing around the droplet (through the gutters) increasing as Ca → 0. At low Ca, it is hence expected that the fraction of incoming liquid that passes by a forming droplet, and thus does not contribute to the squeezing, is no longer negligible. This introduces a Ca-dependence in the duration of the necking stage and hence qualitatively explains the here observed Ca-dependence of the volume of the droplets at Ca → 0. In channels without gutters, this Ca-dependence hence should be absent. Indeed, additional experiments using a T-junction with 'gutter-free' circular channels reveal that the length of the droplets varies weakly with Ca in comparison to T-junctions with square channels (see Supplementary Note 1 and Supplementary Fig. 1). An interesting complication in the description of corner (or gutter) flow around a forming droplet—as compared with a droplet moving steadily through a straight channel—is that the gutter flow is dynamic due to the simultaneous change in its driving force (interface curvature) and in its resistance to flow (length of gutters). Although earlier work did assume a fixed, non-zero, fraction of the CP stream to flow around a forming droplet[15], here we introduce the functional dependence of the leaky flow through the gutters on fluid properties and flow conditions to establish a unifying description.

Specifically, we define the instantaneous flow rate of the CP through a single gutter as $Q_G(t)$ and through all four

gutters combined as $Q_B(t) = 4Q_G(t)$ (see Fig. 2b, d). Then, the flow contributing to squeezing of the neck is $Q_N(t) = Q_C - Q_B(t) = dV_N^*/dt = -dV_N/dt$. The necking time thus equals $\tau = V_{N0}/\bar{Q}_N$, with $\bar{Q}_N$ being the time-averaged squeezing rate. Introducing $\eta = Q_B/Q_N$ as the relative leaking strength and $\bar{\eta}$ as its time average, we obtain $\tau = \frac{V_{N0}}{Q_C}(1 + \bar{\eta})$. The droplet volume hence becomes $V_D = V_{fill} + qV_{N0}(1 + \bar{\eta})$. Rewritten in terms of the non-dimensional length $l_D = L_D/W$, using $L_D \approx V_D/HW$, as is valid for long droplets[51], we obtain:

$$l_D = l_0 + qv_{N0}(1 + \bar{\eta}) \qquad (1)$$

with $l_0 = V_{fill}/HW^2$ and $v_{N0} = V_{N0}/HW^2$. This analysis generalizes the original squeezing model, recovered for $\bar{\eta} = 0$. In order to quantitatively predict the size of the droplets in the leaking regime, we next derive the functional dependence of $\bar{\eta}$, on q and on Ca.

We start from the flow scheme depicted in Fig. 2d and note that the pressure difference associated with viscous flow of the CP through the gutters balances the pressure difference arising from the sum of viscous flow inside the DP and the difference in curvature of the interface at the front and at the back of the forming droplet. For the leaking and squeezing regimes (i.e. for low Ca), viscous shear is unable to deform the interfaces such that the Laplace law is used to calculate the pressure difference due to a difference in curvature (K_F versus K_B) of the quasi-static interfaces as $\gamma(K_F - K_B)$. The viscous pressure head over the droplet and over the gutters equals $R_D(Q_D + Q_N)$ and $R_G Q_B/4$, respectively, with R_D and R_G the hydrodynamic resistances of the droplet and the gutter. The balance hence equals $\gamma(K_F - K_B) + R_D(Q_D + Q_N) = R_G Q_B/4$. For systems with a moderate viscosity contrast, μ_D/μ_C, the viscous pressure difference inside the droplet can be neglected with respect to that in the gutters, because the cross-sectional area of the gutters A_G is much smaller compared with that of the droplet A_D. We hence continue with the simplified balance:

$$\gamma(K_F - K_B) = R_G Q_B/4. \qquad (2)$$

Considering the right-hand side of Eq. (2), the hydrodynamic resistance of a gutter (R_G) increases proportionally to the length L_G of the gutter: $R_G = \frac{\alpha_G \mu_C}{A_G^2}L_G$, with A_G the cross-sectional area of a gutter (in good approximation constant along the gutter and independent of time) and α_G a dimensionless geometrical factor[52]. Referring to Fig. 2d, we estimate the velocity of the front of the droplet as $(Q_D + Q_N)/A_D$ and that of the back of the droplet as Q_N/A_D, such that the length of the gutter increases at a rate equal to the velocity difference, i.e. $\frac{dL_G}{dt} = Q_D/WH$, where we approximate the cross-sectional area of the droplet (A_D) with the area of the lumen of the channel WH. Considering the left-hand side of Eq. (2), we note that the curvature at the front of the droplet, $K_F = \frac{2}{W} + \frac{2}{H}$, is approximately constant in time. The curvature at the rear (i.e., at the neck) depends on the neck shape, which is determined by the amount of the CP collected behind it, i.e. by the value of the volume V_N^*. Adopting the electric–hydraulic analogy that can be applied to single phase low Reynolds number flows, we describe the accumulation of the CP behind the droplet akin to a charging capacitor: the further the rear interface is pushed into the junction, the larger the difference in curvatures at the rear and front, and hence the more charge is stored. If one were able to instantaneously release the driving pressures in the system during the formation of a droplet (akin to switching off the main voltage supply in an electric circuit), the capacitor would discharge, i.e., the forming droplet would relax its shape inside the T-junction to an equilibrium shape with similar curvatures at its front and rear.

Similar to electric RC circuits, the product of the capacitance and resistance can be seen as the characteristic relaxation time. A quantitative analysis of this time scale is provided in Supplementary Note 2. Using this analogy, we model the curvature difference as: $K_F - K_B = \frac{V_N^*}{C} = \frac{1}{W^3 H}\frac{V_N^*}{c} = \frac{1}{W}\frac{v_N^*}{c}$, with C a constant (analogous to capacitance) characterising the rate of change of the curvature with V_N^*. Here $c = \frac{C}{W^3 H}$ and $v_N^* = \frac{V_N^*}{W^2 H}$ are dimensionless equivalents of C and V_N^*, respectively. Before using the thus obtained relation, we provide an intuitive physical interpretation of the capacitance by connecting it to the classical derivation of the Young–Laplace law. Considering a droplet of volume, V, and surface area A, the Helmholtz free energy, dF, equals $dF = -pdV + \gamma dA$. Near equilibrium ($dF = 0$), the pressure difference across the droplet interface equals $\Delta p = \gamma\frac{dA}{dV} = \gamma K$. The curvature difference for a forming droplet, $K_F - K_B$, being equal to $\frac{V_N^*}{C}$ can similarly be related to $\frac{dA_N(V_N^*)}{dV_N^*}$, i.e. the change in neck area, A_N, parameterized solely in terms of V_N^*. We hence obtain $\frac{dA_N(V_N^*)}{dV_N^*} \sim \frac{V_N^*}{C}$, with the corresponding interfacial free energy, $\mathcal{W}$, being equal to $\mathcal{W} = \gamma A_N(V_N^*) = \frac{1}{2}\frac{(V_N^*)^2}{C}$. The capacitance C can hence be interpreted as the coefficient that describes how the surface area of the neck, A_N, and the interfacial free energy stored in it due to its deformation by the CP, depends on the volume of the CP collected behind the neck. Now, we proceed with the main analysis by substituting the relation $K_F - K_B = \frac{1}{W}\frac{v_N^*}{c}$ in the pressure balance (Eq. (2)) together with $Q_B = Q_C - Q_N = Q_C - dV_N^*/dt$, to obtain: $\frac{\gamma v_N^*}{W^3 Hc} = R_G(t) \cdot (Q_C - dV_N^*/dt)/4$. This equation resembles the well-known equation for electric RC systems ($\frac{Q}{C} = -R \cdot dQ/dt$, with Q the electric charge), although with a time-dependent resistance $R_G(t)$. The solution gives the flow rate to the neck: $Q_N = \frac{qCa}{qCa + \beta}Q_C$, with constant $\beta = \frac{4}{\alpha_G}\frac{A_G^2}{W^3 H}\frac{1}{c}$. Note that the full expression for Q_N includes an additional time-dependent term that decays fast and can be neglected (see Supplementary Note 2). Strikingly, this model predicts that Q_N does not depend on time, implying that, after a short initial transient, the flow through the gutters is constant in time. Consequently, the front of a forming droplet should propagate at a fixed speed during droplet formation[22]. Our experiments confirm this surprising prediction (see Supplementary Note 3 and Supplementary Fig. 2). Finally, we arrive at the following expression for the relative leaking strength: $\bar{\eta} = \eta = \frac{Q_B}{Q_N} = \frac{Q_C - Q_N}{Q_N} = \frac{\beta}{qCa}$. Incorporating this functional dependence in Eq. (1), we obtain:

$$l_D = l_0 + qv_{N0}\left(1 + \frac{\beta}{qCa}\right) \qquad (3)$$

This generalized equation implies that all data from Fig. 1b should collapse onto a single master curve when using this functional form for the dependence of droplet size on the ratio of flow rates and the capillary number. Indeed, fitting a single set of parameters β, v_{N0}, and l_0 to all our data, we find a single master curve for $\bar{\eta} = \frac{\beta}{qCa} = \frac{l_D - l_0}{qv_{N0}} - 1$ as shown in Fig. 3. We confirm the universality of this behaviour for different fluid systems and channel sizes (see Supplementary Notes 4, 5 and Supplementary Figs. 3, 4). For rectangular channels with different aspect ratios, we confirm that the general behaviour is the same, with the details of the leaking mechanisms depending on the aspect ratio (Supplementary Note 6, Supplementary Fig. 5 and Supplementary Table 4). With the functional behaviour of the leaking strength well captured, the generalized Eq. (3) accurately describes the experimental data on droplet length (see also Supplementary
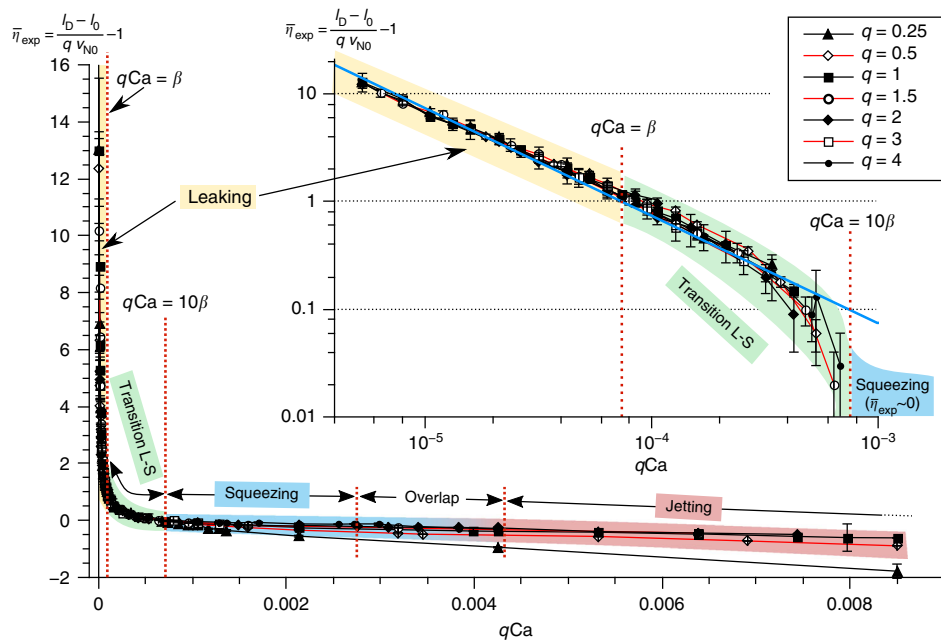
Fig. 3 Experimental verification of the leaking-regime-model. Master curve for $\bar{\eta}$ experimentally determined from all data in Fig. 1b using $\overline{\eta_{\exp}} = \frac{l_D - l_0}{q v_{N0}} - 1$ (Eq. 3) and $\overline{\eta_{\exp}} = \frac{\beta}{q\mathrm{Ca}}$ (definition) with fit parameters $l_0 = 1.46 \pm 0.14$, $v_{N0} = 2.04 \pm 0.11$, and $\beta = 7.4 \times 10^{-5} \pm 0.3 \times 10^{-5}$. In the leaking regime, the flow through the gutters is at least equal to the flow to the neck (i.e. $\overline{\eta_{\exp}} \geq 1$ for $q\mathrm{Ca} \leq \beta$). By contrast, in the squeezing regime, the flow though the gutters is negligibly small compared with the flow to the neck (i.e. $\overline{\eta_{\exp}} \ll 1$ for $q\mathrm{Ca} > 10\beta$). The intermediate regime ($\beta < q\mathrm{Ca} < 10\beta$) is identified as the transition between leaking and squeezing. Inset: log-log master curve for $q\mathrm{Ca} < 10\beta$. Blue solid line: theoretical scaling $\bar{\eta} = \frac{\beta}{q\mathrm{Ca}}$. All experimental data collapse on this single curve in the leaking regime, while deviations of $\overline{\eta_{\exp}}$ from the theoretical scaling for $\bar{\eta}$ at $\overline{\eta_{\exp}} < 0.1$ are attributed to a remaining dependency of v_{N0} (taken constant here) on q and Ca as explained later. The transition between squeezing and jetting does not occur at a single value of $q\mathrm{Ca}$ for curves with different q, which is highlighted in the graph in the 'overlap' region. In the next part, we will explain how to parameterize the system to capture the squeezing–jetting transition for all these curves based on a single parameter

Note 7 and Supplementary Fig. 6). This agreement demonstrates that the present analysis captures the mechanisms governing droplet formation in the leaking regime. Figure 3 also shows that the leaking regime transitions smoothly into the squeezing regime. Without a sharp boundary, the lower limit of the squeezing regime, in which droplet length does not significantly depend on Ca, may be defined as $q\mathrm{Ca} \gg \beta$, as evident from Eq. (3). In case a particular application requires the sensitivity of the final droplet length (with respect to Ca) to be less than a threshold value of say 10% ($\bar{\eta} < 0.1$), $q\mathrm{Ca} = 10\beta$ provides an application-tailored lower limit for the squeezing regime.

Scaling of the squeezing to jetting transition. To explain why $\overline{\eta_{\exp}} = \frac{l_D - l_0}{q v_{N0}} - 1$ deviates from the theoretical scaling $\bar{\eta} = \frac{\beta}{q\mathrm{Ca}}$ at the largest values of $q\mathrm{Ca}$, we take a closer look at the shapes of the rear of the droplet at end of the necking stage. For the capillary-dominated regime, we expect self-similar shapes of the interface—that is, shapes that solely depend on the instantaneous volume of the neck $V_N^*(t)$. Considering the shape of the interface at the moment of pinch-off, we observe that the shapes are indeed all similar at low $q\mathrm{Ca}$ (Fig. 4a). The volume filled by the CP during the necking stage, V_{N0}—being directly related to this shape—is the same for all these cases, and so is β. In contrast, the interface shape prior to pinch-off is no longer self-similar at higher $q\mathrm{Ca}$, i.e. no longer determined solely by V_N^*. Viscous deformation of the interface, so far left out of the description, hence introduces a dependence on q and on Ca in v_{N0}, explaining the deviation from Eq. (3) at high $q\mathrm{Ca}$, as observed in the inset of Fig. 3.

We hypothesize that, for the larger values of $q\mathrm{Ca}$, the instantaneous neck shape is not solely parameterized by V_N^*, as

in the case for low $q\mathrm{Ca}$, for which the final shape at pinch-off (for $V_N^*(t = \tau)$) has a universal value (though with different necking times τ for different conditions). To capture how viscous dissipation alters $V_N^*(t = \tau)$ beyond the leaking regime, we therefore introduce an additional parameter, which we call the 'shape number' S.

We derive an expression for S using Onsager's variational principle[53,54], which is an extension of Rayleigh's least energy dissipation principle[55]. Onsager's principle allows for taking into account the dynamic change in free energy of the interface as well as the energy dissipated by viscous flow. It has been successfully applied in the field of soft matter physics[56]. In isothermal systems, Onsager's principle minimizes the so-called Rayleighian $\mathcal{R}$, which takes the following general form[57]:

$$\mathcal{R} = \Phi(x, \dot{x}) + \dot{\mathcal{W}}(x, \dot{x}). \tag{4}$$

Here, $\mathcal{W}$ is the interfacial free energy of the system with $\dot{\mathcal{W}}$ being its rate of change. Φ is the dissipation function, which is equal to half the rate of energy dissipation. x represents the set of variables of the system and $\dot{x}$ their time derivatives. In our system, viscous dissipation is the only source of energy dissipation. The rate of viscous dissipation for laminar flow can generally be expressed in terms of the hydrodynamic resistance (R) and the flow rate (Q) as RQ^2 [58]. In our system, for the larger values of $q\mathrm{Ca}$, viscous dissipation mainly stems from the flow through the neck. For that $q\mathrm{Ca}$ range, gutter flows are negligibly small and the neck is squeezed by almost all of the incoming CP ($Q_N \approx Q_C$). The flow rate in the neck itself hence equals the sum $Q_C + Q_D$. The viscous resistance in the neck, R_N, depends on its instantaneous shape and hence is parameterized by V_N^* and S. The dissipation
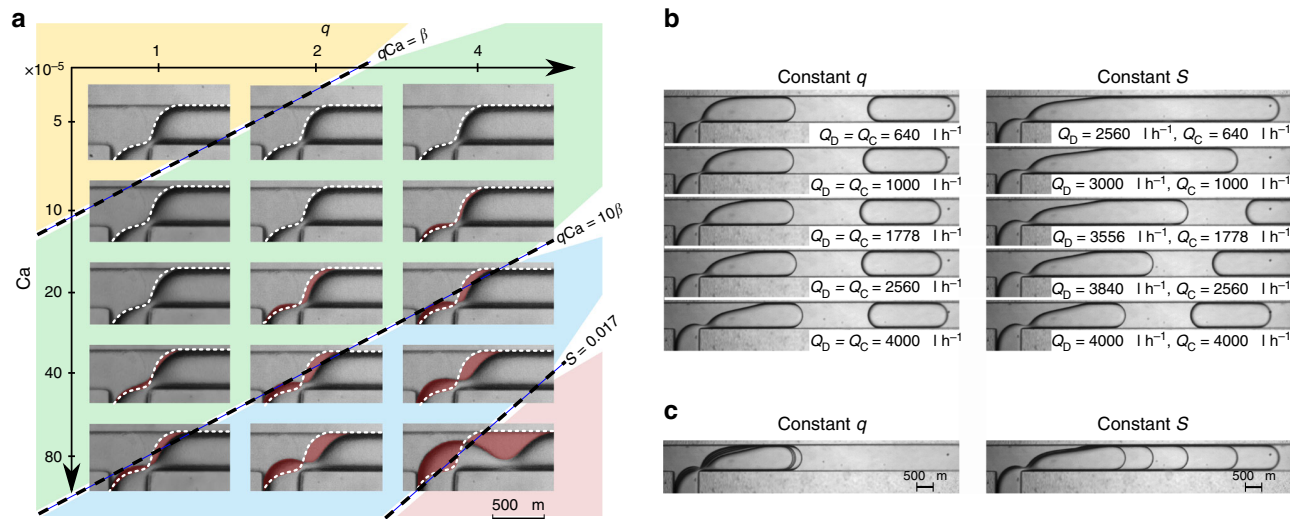
Fig. 4 Variations of the shape of the neck. **a** The neck just before breakup for different values of Ca and q in a T-junction with channels of a square cross section ($W = H = 360\ \mu$m). All shapes are compared with the shape in the top left corner (white dashed line) with the differences highlighted in colour. The diagonal lines separating the snapshots correspond to qCa $= \beta$ and qCa $= 10\beta$. For the leaking regime (qCa $< \beta$; yellow) and for the transition between leaking and squeezing (qCa $< 10\beta$; green), this clearly shows that the shape prior to pinch-off is the same irrespective of the values of q and Ca, confirming that the parameters depending on the shape such as v_{NO}, $K_B(V_{N0}^*)$ and $K_B(0)$ are constant in the leaking regime and in the transition regime between leaking and squeezing. For the squeezing regime (qCa $> 10\beta$; blue) and the jetting regime ($S > 0.017$; red), the remaining dependency of the shape on q and Ca is clearly visible. **b** Comparison of shapes of the neck for a variety of combinations of Q_C and Q_D. For better visualisation, a T-junction with flattened channels ($W = 2H = 800\ \mu$m) was used. The left column—constant $q(=1)$, the right one—constant $S(=0.017)$. Snapshots in the same row were taken for the same Q_C (i.e. the same Ca). **c** Composition of overlaid images from each column from **b**. It is visible that, although the length of a droplet is similar for constant q (a well-known feature of the squeezing regime), the shapes of the neck differ significantly. By contrast, these shapes are the same for constant S

function hence is estimated as $\Phi = \frac{1}{2} R_N(V_N^*, S) \cdot (Q_C + Q_D)^2$. The free energy of the system $\mathcal{W}$ is equal to the interfacial energy of the neck $\mathcal{W}(V_N^*, S) = \gamma A_N(V_N^*, S)$, where $A_N(V_N^*, S)$ is the instantaneous surface area of the neck. The rate of change of the free energy can be estimated as $\dot{\mathcal{W}}(V_N^*, S) = \gamma \frac{\partial A_N(V_N^*, S)}{\partial V_N^*} \frac{\partial V_N^*}{\partial t} = \gamma K(V_N^*, S) Q_N \approx \gamma K(V_N^*, S) Q_C$, with $K(V_N^*, S)$ the instantaneous curvature of the neck. We hence obtain the following Rayleighian

$$\mathcal{R} = \frac{1}{2} R_N(V_N^*, S)(Q_C + Q_D)^2 + \gamma K(V_N^*, S) Q_C \quad (5)$$

Solving the minimization equation for the Rayleighian with respect to S for fixed V_N^*, $\frac{d\mathcal{R}}{dS}\big|_{V_N^*} = 0$, we obtain:

$$2\frac{k_S(V_N^*)}{r_S(V_N^*)} = \frac{(Q_C + Q_D)^2}{Q_C} \propto \text{Ca}(1 + q)^2 \quad (6)$$

where $k_S(V_N^*) = \gamma \frac{dK(S, V_N^*)}{dS}\big|_{V_N^*}$ and $r_S(V_N^*) = -\frac{dR_N(S, V_N^*)}{dS}\big|_{V_N^*}$, with $k_S(V_N^*)$ and $r_S(V_N^*)$ both defined as positive functions based on the expectation that larger S implies larger deformation of the interface (and hence larger $K(S, V_N^*)$) and smaller viscous resistance (and hence smaller $R_N(S, V_N^*)$). With the left-hand side of Eq. (6) only depending on the shape of the neck, this analysis teaches that the neck shape is fully governed by V_N^* and the parameter Ca$(1 + q)^2$, which we call the 'shape number' defined as $S = \text{Ca}(1 + q)^2$. We hence expect the same neck shape prior to pinch-off ($V_N^*(t = \tau)$) for different conditions, as long as S is the same. Before we test the validity using experiments, we stress that the same analysis can be applied for low qCa with the neck shape solely parameterized in terms of V_N^*, with the Rayleighian being equal to $\mathcal{R} = \frac{1}{2} R_G \cdot \frac{Q_B^2}{4} + \frac{V_N^*}{C}(Q_C - Q_B)$. Minimizing $\mathcal{R}$ with respect to Q_B for fixed V_N^*, we obtain the same balance $\left(\frac{V_N^*}{C} = R_G \cdot \frac{Q_B}{4}\right)$ as the one

derived using the momentum balance as a starting point, confirming the validity of the approach.

The above analysis predicts that, for the larger range of qCa, all neck shapes prior to pinch-off are uniquely defined by the value of S. Remarkably, this is exactly what we find in experiments, with all interface shapes collapsing onto a master shape for fixed S, as evident from Fig. 4b, c. Having established the physical origin of this S-number, we finalize the description of droplet formation. We use the S-number to predict the upper boundary for squeezing regime, and to explain the mechanism behind the transition between squeezing and jetting.

At the limit of high rates of flow in the squeezing regime, we expect shear to wash the instability away from the junction, as observed in the convective regime in jetting. Since this mechanism is not captured in the S-number description, we expect that, in that limit, the shape of the neck just before breakup (for $V_N^*(t = \tau)$) will no longer be uniquely captured by S. To test this hypothesis experimentally, we determined the relation between $V_N^*(t = \tau)$ and S. We use the breakup distance D (see inset Fig. 5a) as a proxy for $V_N^*(t = \tau)$ as it is a well-defined direct observable. Data for different values of q collapse perfectly on the same curve for $d = D/W \lesssim 1$ and $S \lesssim 0.017$. For larger S, the breakup shape is indeed no longer uniquely defined by S as evident from the curves for different q. We therefore interpret this point ($S_{crit} \approx 0.017$) as the transition from squeezing to jetting, supported by the experimental observation that for larger S, a long thread of the DP penetrates the main channel, characteristic for the jetting regime. This threshold value of S accurately predicts the transition for all curves (Fig. 5b). We note that, to the best of our knowledge, the S-number criterion is the first attempt to provide a universal scaling of the squeezing–jetting transition.

In summary, we derived a complete model for the generation of droplets at low Ca under microscale geometrical confinement. The explicit inclusion of the magnitude of the leaking flow of the continuous phase past a growing droplet allowed us
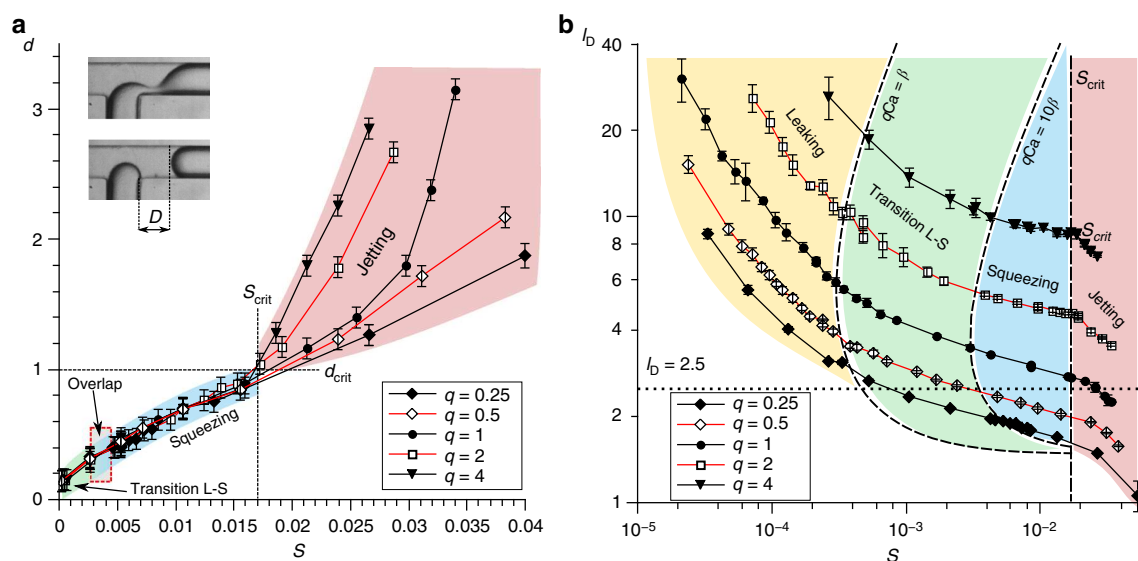
Fig. 5 Quantitative test of the S-number as the scaling factor of the formation of droplets in the squeezing regime. **a** Measurements of the dimensionless distance $d = D/W$—the distance between the internal corner of the junction and the rear interface of the droplet immediately after breakup—as a function of the S-number. Inset: shape of the neck prior to breakup (top) and immediately after breakup (bottom). The measured value of d corresponds to the deformation of the shape of the neck. The overlap between transition L–S and squeezing corresponds to the fact that the transition between these regimes is captured by a single value qCa for all curves, but not for a single value of the S-number. **b** Normalized length of droplets l_D versus the S-number showing that the transition from squeezing to jetting occurs at a single value for the S-number for all curves ($S_{crit} \sim 0.017$). For the series with $q < 1$ the length of the droplets (except for the leaking regime) is below or close to $l_D = 2.5$. In the case of such short droplets, a more accurate description should include shear during the filling stage as in models for the dripping regime

to uncover the leaking regime of drop formation and to reformulate the squeezing model for the size of the droplets, including the transitions between leaking and squeezing, and between squeezing and jetting. The insights from this work can be used to revisit droplet formation at low Ca in other common geometries, such as Y-junctions, cross-junctions, and flow-focusing devices, including many fine details such as the influence of channel aspect ratio and viscosity contrast that, to date, have escaped a unified model of droplet formation in microfluidic confinement.

From a practical point of view, the leaking regime is the least attractive mode of breakup, because it presents a very sharp dependence of droplet volume on the control parameters—such as rates of flow. One may either use the equations here described to find the squeezing regime for channels with a square cross section, or, easier, use a T-junction with circular channels that preclude leaking and present a very wide range of parameters that result in squeezing.

Methods

Device fabrication. We fabricated the chips via direct milling in polycarbonate (PC) sheets (Macroclear, Bayer, Germany) using a CNC milling machine (Ergwind, Poland). This machine has a reproducibility of positioning of 5 μm. The milled chips were bonded to a flat slab of polycarbonate using a hot press at 130 °C. No further channel modifications were applied. The height and width of the rectangular channels was 360 μm, except for the chips used to produce Fig. 4b, c, Supplementary Fig. 5 ($W = 2H = 800$ μm) and Supplementary Fig. 4 ($W = H = 200$ μm). These dimensions, which may be larger than those typically encountered, were chosen to enable reaching low Ca values, without being constrained by the lower limit of the flow rate of the syringe pumps.

Experiments. We used a stereoscope equipped with a high-speed camera (PCO HS1200) to record images of droplet formation. We analyzed the sequences of images with a custom written script in MATLAB (Mathworks), which automatically recognized droplets and measured their length. In order to obtain data with a good precision, long sequences of droplets (typically > 30) were observed, which for the low Ca values took up to 10 h.

In order to feed our system with liquids, we used Nemesis pumps (Cetoni GmbH, Germany) with 100 μl glass syringes, connected to the chip using PE-60 tubing (Beckton-Dickinson, USA). In addition, we performed some measurements with 1000 μl syringes to test whether the pumps generate fluctuations in flow rates that could disturb the measurements[59]. The measurements from both syringes were in good agreement (see Supplementary Note 8 and Supplementary Fig. 7), confirming that there are no significant fluctuations in our feeding system. Having confirmed that the syringe pumps produce steady flows for our range of operating conditions, we have chosen their use over, for example, pressure driven systems, as they allow direct control over the flow rate.

We used fluorinated oil FC-40 (3M, USA) as DP and hexadecane (Sigma Aldrich Co.) as CP for the measurements reported in the main article. We chose this set after multiple attempts with different fluid combinations. The chosen fluid system ensured the absence of wetting of the channel walls by the DP, without further channel treatment or addition of surfactants. Dynamic effects resulting from surfactant transport[17] are hence not at play. Additional fluid systems used to construct Supplementary Fig. 3 are further detailed in Supplementary Note 4 and Supplementary Table 1.

Viscosities of the used liquids were estimated by measuring the time required for a given volume to flow through a calibrated capillary for a known pressure drop over the capillary, which was controlled using a pressure regulator and a precise manometer. We repeated the measurements for different values of the pressure drop obtaining a linear relation between pressure drop and calculated flow rate. A linear fit provided the values of viscosities. This resulted in $\mu_C = 3.6$ mPa s and $\mu_D = 4.1$ mPa s for hexadecane and FC-40, respectively. Values for the other fluid systems are reported in Supplementary Table 2.

The interfacial tension between both liquid phases was estimated by the pendant droplet method using a custom set-up enabling observation of the interface of a pendant droplet of FC-40 immersed into hexadecane. We calculated the interfacial tension by the use of a custom Matlab script applying the Laplace-Young theorem to the droplet shape extracted from the acquired images. This resulted in $\gamma = 7.3$ mN m^{-1} for the hexadecane—FC-40 fluid system. Values for the other fluid systems are reported in Supplementary Table 3.

Data availability

The data that support the plots within this paper and other findings of this study are available from the corresponding authors upon reasonable request.

References

1. Garstecki, P., Fuerstman, M. J. & Whitesides, G. M. Oscillations with uniquely long periods in a microfluidic bubble generator. *Nat. Phys.* **1**, 168–171 (2005).
2. Beatus, T., Tlusty, T. & Bar-Ziv, R. Phonons in a one-dimensional microfluidic crystal. *Nat. Phys.* **2**, 743–748 (2006).
3. Fuerstman, M. J., Garstecki, P. & Whitesides, G. M. Coding/decoding and reversibility of droplet trains in microfluidic networks. *Science* **315**, 828–832 (2007).
4. Baroud, C. N., Gallaire, F. & Dangla, R. Dynamics of microfluidic droplets. *Lab. Chip.* **10**, 2032–2045 (2010).
5. Wong, H., Radke, C. J. & Morris, S. The motion of long bubbles in polygonal capillaries. Part 2. Drag, fluid pressure and fluid flow. *J. Fluid. Mech.* **292**, 95–110 (1995).
6. Jakiela, S., Makulska, S., Korczyk, P. M. & Garstecki, P. Speed of flow of individual droplets in microfluidic channels as a function of the capillary number, volume of droplets and contrast of viscosities. *Lab. Chip.* **11**, 3603–3608 (2011).
7. Jakiela, S., Korczyk, P. M., Makulska, S., Cybulski, O. & Garstecki, P. Discontinuous transition in a laminar fluid flow: a change of flow topology inside a droplet moving in a micron-size channel. *Phys. Rev. Lett.* **108**, 134501 (2012).
8. Rao, S. S. & Wong, H. The motion of long drops in rectangular microchannels at low capillary numbers. *J. Fluid. Mech.* **852**, 60–104 (2018).
9. Zhu, P. & Wang, L. Passive and active droplet generation with microfluidics: a review. *Lab. Chip.* **17**, 34–75 (2016).
10. Anna, S. L. Droplets and bubbles in microfluidic devices. *Annu. Rev. Fluid. Mech.* **48**, 285–309 (2016).
11. Thorsen, T., Roberts, R. W., Arnold, F. H. & Quake, S. R. Dynamic pattern formation in a vesicle-generating microfluidic device. *Phys. Rev. Lett.* **86**, 4163 (2001).
12. Garstecki, P., Fuerstman, M. J., Stone, H. A. & Whitesides, G. M. Formation of droplets and bubbles in a microfluidic T-junction-scaling and mechanism of break-up. *Lab. Chip.* **6**, 437–446 (2006).
13. De Menech, M., Garstecki, P., Jousse, F. & Stone, H. A. Transition from squeezing to dripping in a microfluidic T-shaped junction. *J. Fluid. Mech.* **595**, 141–161 (2008).
14. Christopher, G. F., Noharuddin, N. N., Taylor, J. A. & Anna, S. L. Experimental observations of the squeezing-to-dripping transition in T-shaped microfluidic junctions. *Phys. Rev. E* **78**, 036317 (2008).
15. Steijn, V., van, Kleijn, C. R. & Kreutzer, M. T. Predictive model for the size of bubbles and droplets created in microfluidic T-junctions. *Lab. Chip.* **10**, 2513–2518 (2010).
16. Glawdel, T., Elbuken, C. & Ren, C. L. Droplet formation in microfluidic T-junction generators operating in the transitional regime. II Modeling. *Phys. Rev. E* **85**, 016323 (2012).
17. Glawdel, T. & Ren, C. L. Droplet formation in microfluidic T-junction generators operating in the transitional regime. III. Dynamic surfactant effects. *Phys. Rev. E* **86**, 026308 (2012).
18. Nekouei, M. & Vanapalli, S. A. Volume-of-fluid simulations in microfluidic T-junction devices: influence of viscosity ratio on droplet size. *Phys. Fluids* **29**, 032007 (2017).
19. Chakraborty, I., Ricouvier, J., Yazghur, P., Tabeling, P. & Leshansky, A. M. Droplet generation at Hele-Shaw microfluidic T-junction. *Phys. Fluids* **31**, 022010 (2019).
20. Gañán-Calvo, A. M. & Gordillo, J. M. Perfectly monodisperse microbubbling by capillary flow focusing. *Phys. Rev. Lett.* **87**, 274501 (2001).
21. Anna, S. L., Bontoux, N. & Stone, H. A. Formation of dispersions using "flow focusing" in microchannels. *Appl. Phys. Lett.* **82**, 364–366 (2003).
22. Chen, X., Glawdel, T., Cui, N. & Ren, C. L. Model of droplet generation in flow focusing generators operating in the squeezing regime. *Microfluid. Nanofluidics* **18**, 1341–1353 (2014).
23. Umbanhowar, P. B., Prasad, V. & Weitz, D. A. Monodisperse emulsion generation via drop break off in a coflowing stream. *Langmuir* **16**, 347–351 (2000).
24. Kawakatsu, T., Kikuchi, Y. & Nakajima, M. Regular-sized cell creation in microchannel emulsification by visual microprocessing method. *J. Am. Oil. Chem. Soc.* **74**, 317–321 (1997).
25. Dangla, R., Fradet, E., Lopez, Y. & Baroud, C. N. The physical mechanisms of step emulsification. *J. Phys. Appl. Phys.* **46**, 114003 (2013).
26. Dangla, R., Kayi, S. C. & Baroud, C. N. Droplet microfluidics driven by gradients of confinement. *Proc. Natl Acad. Sci. USA* **110**, 853–858 (2013).
27. Li, Z., Leshansky, A. M., Pismen, L. M. & Tabeling, P. Step-emulsification in a microfluidic device. *Lab. Chip.* **15**, 1023–1031 (2015).
28. Chakraborty, I., Ricouvier, J., Yazghur, P., Tabeling, P. & Leshansky, A. M. Microfluidic step-emulsification in axisymmetric geometry. *Lab. Chip.* **17**, 3609–3620 (2017).
29. Eggersdorfer, M. L., Seybold, H., Ofner, A., Weitz, D. A. & Studart, A. R. Wetting controls of droplet formation in step emulsification. *Proc. Natl Acad. Sci. USA* **115**, 9479–9484 (2018).
30. Nisisako, T. & Torii, T. Microfluidic large-scale integration on a chip for mass production of monodisperse droplets and particles. *Lab. Chip.* **8**, 287–293 (2008).
31. Amstad, E. et al. Robust scalable high throughput production of monodisperse drops. *Lab. Chip.* **16**, 4163–4172 (2016).
32. Amstad, E. et al. Parallelization of microfluidic flow-focusing devices. *Phys. Rev. E* **95**, 043105 (2017).
33. Teh, S.-Y., Lin, R., Hung, L.-H. & Lee, A. P. Droplet microfluidics. *Lab. Chip.* **8**, 198–220 (2008).
34. Seemann, R., Brinkmann, M., Pfohl, T. & Herminghaus, S. Droplet based microfluidics. *Rep. Prog. Phys.* **75**, 016601 (2012).
35. Kaminski, T. S., Scheler, O. & Garstecki, P. Droplet microfluidics for microbiology: techniques, applications and challenges. *Lab. Chip.* **16**, 2168–2187 (2016).
36. Guo, M. T., Rotem, A., Heyman, J. A. & Weitz, D. A. Droplet microfluidics for high-throughput biological assays. *Lab. Chip.* **12**, 2146–2155 (2012).
37. Klein, A. M. et al. Droplet barcoding for single-cell transcriptomics applied to embryonic stem cells. *Cell* **161**, 1187–1201 (2015).
38. Jakiela, S., Kaminski, T. S., Cybulski, O., Weibel, D. B. & Garstecki, P. Bacterial growth and adaptation in microdroplet chemostats. *Angew. Chem. Int. Ed.* **52**, 8908–8911 (2013).
39. Zhao, C.-X. Multiphase flow microfluidics for the production of single or multiple emulsions for drug delivery. *Adv. Drug Deliv. Rev.* **65**, 1420–1446 (2013).
40. Vladisavljević, G. T. et al. Industrial lab-on-a-chip: design, applications and scale-up for drug discovery and delivery. *Adv. Drug Deliv. Rev.* **65**, 1626–1663 (2013).
41. Göke, K. et al. Novel strategies for the formulation and processing of poorly water-soluble drugs. *Eur. J. Pharm. Biopharm.* **126**, 40–56 (2018).
42. Carugo, D., Bottaro, E., Owen, J., Stride, E. & Nastruzzi, C. Liposome production by microfluidics: potential and limiting factors. *Sci. Rep.* **6**, 25876 (2016).
43. Muijlwijk, K., Berton-Carabin, C. & Schroën, K. Cross-flow microfluidic emulsification from a food perspective. *Trends Food Sci. Technol.* **49**, 51–63 (2016).
44. Liu, H. & Zhang, Y. Droplet formation in a T-shaped microfluidic junction. *J. Appl. Phys.* **106**, 034906 (2009).
45. Liu, H. & Zhang, Y. Droplet formation in microfluidic cross-junctions. *Phys. Fluids* **23**, 082101 (2011).
46. Tice, J. D., Lyon, A. D. & Ismagilov, R. F. Effects of viscosity on droplet formation and mixing in microfluidic channels. *Anal. Chim. Acta* **507**, 73–77 (2004).
47. Guillot, P., Colin, A., Utada, A. S. & Ajdari, A. Stability of a jet in confined pressure-driven biphasic flows at low reynolds numbers. *Phys. Rev. Lett.* **99**, 104502 (2007).
48. Garstecki, P., Stone, H. A. & Whitesides, G. M. Mechanism for flow-rate controlled breakup in confined geometries: a route to monodisperse emulsions. *Phys. Rev. Lett.* **94**, 164501 (2005).
49. Wong, H., Morris, S. & Radke, C. J. Three-dimensional menisci in polygonal capillaries. *J. Colloid Interface Sci.* **148**, 317–336 (1992).
50. Ajaev, V. S. & Homsy, Gm Modeling shapes and dynamics of confined bubbles. *Annu. Rev. Fluid. Mech.* **38**, 277–307 (2005).
51. Musterd, M., van Steijn, V., Kleijn, C. R. & Kreutzer, M. T. Calculating the volume of elongated bubbles and droplets in microchannels from a top view image. *RSC Adv.* **5**, 16042–16049 (2015).
52. Mortensen, N. A., Okkels, F. & Bruus, H. Reexamination of Hagen-Poiseuille flow: shape dependence of the hydraulic resistance in microchannels. *Phys. Rev. E* **71**, 057301 (2005).
53. Onsager, L. Reciprocal relations in irreversible processes. I. *Phys. Rev.* **37**, 405–426 (1931).
54. Onsager, L. Reciprocal relations in irreversible processes. II. *Phys. Rev.* **38**, 2265–2279 (1931).
55. Strutt, J. W. Some general theorems relating to vibrations. *Proc. Lond. Math. Soc.* **s1–4**, 357–368 (1871).
56. Doi, M. Onsager's variational principle in soft matter. *J. Phys. Condens. Matter* **23**, 284118 (2011).
57. Zhou, J. & Doi, M. Dynamics of viscoelastic filaments based on Onsager principle. *Phys. Rev. Fluids* **3**, 084004 (2018).
58. Oh, K. W., Lee, K., Ahn, B. & Furlani, E. P. Design of pressure-driven microfluidic networks using electric circuit analogy. *Lab. Chip.* **12**, 515–545 (2012).
59. Korczyk, P. M., Cybulski, O., Makulska, S. & Garstecki, P. Effects of unsteadiness of the rates of flow on the dynamics of formation of droplets in microfluidic systems. *Lab. Chip.* **11**, 173–175 (2011).

Acknowledgements

Author contributions

P.M.K., V.vS. and P.G. designed the study. P.M.K., S.B. and D.Z. planned experiments and performed measurements. P.M.K., V.vS. and P.G. provided mathematical models. P. M.K. and V.vS. share the first authorship. P.M.K., V.vS., S.B., D.Z., D.A.B. and P.G. contributed to the preparation of the manuscript.

Additional information

Supplementary Information accompanies this paper at https://doi.org/10.1038/s41467-019-10505-5.

Competing interests: The authors declare no competing interests.

Reprints and permission information is available online at http://npg.nature.com/reprintsandpermissions/

RESEARCH PAPER

Impact of inertia and channel angles on flow distribution in microfluidic junctions

S. Blonski[1] · D. Zaremba[1] · M. Jachimek[1] · S. Jakiela[2] · T. Wacławczyk[3] · P. M. Korczyk[1]

© The Author(s) 2020

Abstract

In the present paper, we provide evidence of the vital impact of inertia on the flow in microfluidic networks, which is disclosed by the appearance of nonlinear velocity–pressure coupling. The experiments and numerical analysis of microfluidic junctions within the range of moderate Reynolds number ($1 < \mathrm{Re} < 250$) revealed that inertial effects are of high relevance when $\mathrm{Re} > 10$. Thus, our results estimate the applicability limit of the linear relationship between the flow rate and pressure drop in channels, commonly described by the so-called hydraulic resistance. Herein, we show that neglecting the nonlinear in their nature inertial effects can make such linear resistance-based approximation mistaken for the network operating beyond $\mathrm{Re} < 10$. In the course of our research, we investigated the distribution of flows in connections of three channels in two flow modes. In the splitting mode, the flow from a common channel divides between two outputs, while in the merging mode, streams from two channels join together in a common duct. We tested a wide range of junction geometries characterized by parameters such as: (1) the angle between bifurcating channels (45°, 90°, 135° and 180°); (2) angle of the common channel relative to bifurcating channels (varied within the available range); (3) ratio of lengths of bifurcating channels (up to 8). The research revealed that the inertial effects strongly depend on angles between the channels. Additionally, we observed substantial differences between the distributions of flows in the splitting and merging modes in the same geometries, which reflects the non-reversibility of the motion of an inertial fluid. The promising aspect of our research is that for some combinations of both lengths and angles of the channels, the inertial contributions balance each other in such a way that the equations recover their linear character. In such an optimal configuration, the dependence on Reynolds number can be effectively mitigated.

1 Introduction

Classical microfluidics is seen as a domain of viscous-dominated flows, where simple Ohm-like circuit analysis (analogical to electric circuits) can be applied with sufficient precision (Oh et al. 2012). That approach completely neglects inertia. However, there are loads of examples utilizing the inertial effects in microfluidics (Carlo 2009; Nunes et al. 2014; Amini et al. 2014; Zhang et al. 2015), showing that the impact of inertia can be significant. Thus, this arises vital questions: how we can recognize if the inertia can be neglected in a particular microfluidic system; what are the consequences of the unjustified omit of this inertia; what are the limitations for the applicability of the electric-like-circuit analysis in microfluidics?

The ratio of inertial and viscous interactions is described by the Reynolds number. For the flow through a long channel, the Reynolds number is defined as $\mathrm{Re} = \rho U W / \mu$, where ρ and μ are density and dynamic viscosity of the liquid, respectively, U—mean velocity of the fluid, W—the width of the channel. In the case of a circular pipe, experimentally obtained critical Reynolds number $\mathrm{Re} \approx 2300$ gives the upper limit for which the inertial effects can be neglected. In this range, the flow through a pipe is thought to be laminar. According to Hagen–Poiseuille's law, stationary, viscous, laminar and incompressible flow satisfies the linear relation

✉ S. Blonski
  sblonski@ippt.pan.pl

✉ P. M. Korczyk
  piotr.korczyk@ippt.pan.pl

1 Institute of Fundamental Technological Research, Polish Academy of Sciences, Pawinskiego 5B, 02-106 Warsaw, Poland

2 Department of Physics and Biophysics, Institute of Biology, Warsaw University of Life Sciences, Nowoursynowska 159, Building 34, 02-776 Warsaw, Poland

3 Faculty of Power and Aeronautical Engineering, Institute of Aeronautics and Applied Mechanics, Warsaw University of Technology, Nowowiejska 24, 00-665 Warsaw, Poland

✷ Springer

between the pressure drop and volumetric flow rate. Therefore, Hagen–Poiseuille's law can be seen to be analogical to Ohm's law, where the pressure drop is equivalent to the voltage drop, the volumetric flow rate is equivalent to the electric current and the so-called hydraulic resistance is equivalent to the electric resistance (Mortensen et al. 2005). This analogy provides a simplified description of the flow through a microfluidic channel, where the channel is treated as a one-dimensional wire, characterized by the constant resistance. The fact that the hydraulic resistance is proportional to the length of a channel and inversely proportional to the square of its cross-sectional area (the diameter to the power of 4) allows to obtain the required resistance of the channels during the process of design and fabrication. Moreover, if the electric circuit analogy is satisfied, the analytical solutions describing fluid flow in microfluidic networks can be derived from equivalent electric circuit equations which typically reduce to a system of linear algebraic equations (Oh et al. 2012).

Due to its convenience, this methodology is very commonly applied in microfluidics (Oh et al. 2012), e.g.: in the design of concentration-dependent microfluidic networks (Dertinger et al. 2001; Yamada et al. 2006; Lee et al. 2009, 2010), prediction of flow distribution in hierarchical networks (Hulme et al. 2007) design of systems built with combinations of discrete 3D modules (Bhargava et al. 2015), investigation of systems for filtering particles (Stiles et al. 2005), analysis of hydrodynamic trapping of droplets (Bithi and Vanapalli 2010; Korczyk et al. 2013; Zaremba et al. 2018), prediction of flow of droplets in microfluidics networks (Engl et al. 2005; Fuerstman et al. 2007; Cybulski et al. 2015, 2019; Zaremba et al. 2019), description of formation of droplets in microfluidic systems (van Steijn et al. 2013; Korczyk et al. 2019) and the generation of concentration gradation in droplets (Wegrzyn et al. 2012).

Despite numerous examples of successful and impressive applications of linear approximation in modelling of flows in microfluidics, this approach has significant limitations. Its reliability requires elimination from the design process any nonlinearity. However, inertial effects, even if negligible in straight, regular channels can appear for Re ≪ 2300 in any non-regular element of the microfluidic network (Amini et al. 2014) where the flow is forced to submit to a sudden change of speed or direction (e.g. bends, branching point, contractions and expansions).

To minimize the impact of inertia, the microfluidic network can be built of only straight channels. However, the junctions linking the channels are unavoidable in the construction of non-trivial microfluidic networks. Commonly, the effect of branching points is assumed to be negligible in comparison with the resistance of channels. Although such a condition could be achieved by the use of appropriately long channels, it would cost the enlargements of the microfluidic

architecture's size. Moreover, such an increase in the size of the device is contrary to the idea of miniaturization—the vital advantage of microfluidics. Another way to damp inertial effects is to keep Reynolds number low (e.g. Re < 1), what can be obtained simply by decreasing the rate of flow but with the cost of limiting the maximum throughput of the device. Microfluidics is a very rapidly developing discipline with an increasing area of applications including those which require high throughput (van Berkel et al. 2011). In this context, the expansion of microfluidics towards moderate Reynolds numbers (or even higher ones) seems to be the unavoidable process. The challenge which microfluidics faces now is to develop more complex, but still tractable, mathematical model(es) containing nonlinear effects, as there is no remedy to eliminate inertia. The main aim of this paper is to propose, verify and validate a new modelling approach concerning aforementioned issues.

In this paper, we analyse a junction as a source of nonlinearity in microfluidic networks for moderate Reynolds numbers ($1 <$ Re < 250). A junction, which connects at least three channels, is a ubiquitous element in microfluidic devices. As shown in Fig. 1a, this junction allows for dividing one inlet flow (Q_{in}) into two output flows Q_1 and Q_2, where $Q_{in} = Q_1 + Q_2$. In the reverse arrangement, it can be used to combine two input flows into one output flow.

The series of consecutive operations of splitting and merging of streams containing a sample and a buffer allow for the precise manipulation on concentrations of compounds. This approach is used to generate the desired distribution of concentration of reagents and for the generation of precisely defined gradients (Dertinger et al. 2001; Yamada et al. 2006; Lee et al. 2009, 2010). The final result of the cascade of splitting and merging of flows relies on the ratio of output flows $\beta = Q_1/Q_2$ distributed in each splitting node. Hence, this distribution ratio needs to be determined at the design stage.

According to the linear approximation (as shown in the circuit diagram in Fig. 1b), the geometry of the junction is described by two parameters—the linear resistances of output arms R_1, R_2. Thus, the pressure drops in both output arms are: $\Delta p_1 = p_{in} - p_0 = Q_1 R_1$ and $\Delta p_2 = p_{in} - p_0 = Q_2 R_2$, respectively. If the channels have the same cross sections, the resistances depend only on the lengths of arms (L_1 and L_2). Because $\Delta p_1 = \Delta p_2$, the ratio of flows after splitting is given by the inverted ratio of lengths of outlet arms: $\beta = Q_1/Q_2 = R_2/R_1 = L_2/L_1$. Note that although the real geometry of the junction is also described by the angles between the channels: ϕ_1 and ϕ_2, these angles are not taken into account in the linear approximation. The consequence of such a reduced description is that the linear model predicts the output flows ratio β constant, regardless of the change of the magnitude of total incoming flow Q_{in}. In other words, it does not account for any dependence of
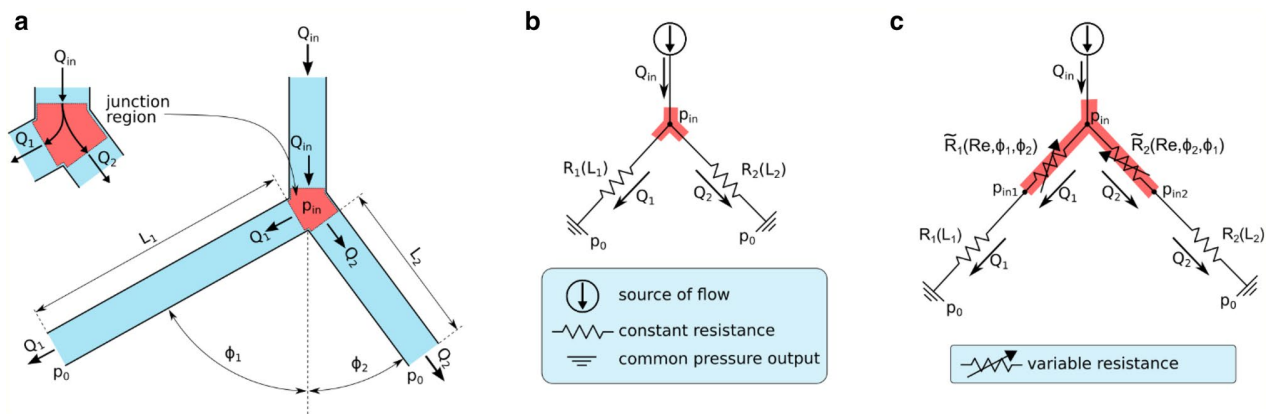
Fig. 1 The geometry of a junction and its electric representations. **a** The scheme of the microfluidic junction. **b** Electrical circuit diagram representing the junction in linear approximation—the flow depends only on linear resistances determined by the lengths of its arms. **c** The extended diagram, which includes dependence on the angle between arms of the junction. The influence of the angle between the arms on the local pressure loss is presented in the diagram as variable resistances $\tilde{R}_1$ and $\tilde{R}_2$ depended on Re. The highlighted red area in all graphs corresponds to the region of the junction or its representation in an equivalent circuit diagram

β on the Reynolds number. In the range of Re numbers in which this linear approximation is correct, the design of the microfluidic network enables the encoding of an arbitrary series of dilutions, where each dilution is hard-wired into the architecture by the ratio of lengths of channels behind each splitting point.

Although the linear approach has been commonly applied for a variety of microfluidic systems, there are examples in the literature, where the linear approximation for microfluidic junctions failed the proper prediction of the splitting ratio. Zeitoun et al. analysed the *T*-junction as an asymmetric splitter of incoming flow introduced through the inlet arm connecting with both outlet arms at a right angle (Zeitoun et al. 2013). The asymmetry was introduced by different lengths of outlet arms (different hydraulic resistances). They proved that the ratio of the output flows depends on the magnitude of the input flow. The higher the input flow Q_{in} (the higher Re), the higher the discrepancy from the prediction of β given by the linear resistance analysis. The authors have assumed that these nonlinearities are introduced by the start-up flow effect. This model, however, does not include any impact of the angle between the arms.

The experimental flow observations and CFD simulations in microfluidic junctions revealed that the first signs of secondary flows could appear for Re < 1 (S. Suteria et al. 2018). Other research disclosed formation of three-dimensional flow patterns with more complex morphology (even for Re < 200), such as standing recirculation zones with thin-layered spiral secondary flows (Karino et al. 1990; Vigolo et al. 2014; Ault et al. 2016; Oettinger et al. 2018) and even flow reversal zones (Karino et al. 1990). Due to the high dissipativity of such structures, they significantly contribute to the pressure drop driving the flow. The asymmetry of those structures in asymmetrical junctions can be problematic for the prediction of the splitting ratio of output flows.

Berkel et al. built a system for rapid blood cell analysis (van Berkel et al. 2011). They used this system containing a junction to divide the sample liquid into parts in required proportions, which then were being mixed with a buffer to finally obtain the required concentration of the sample. To circumvent the impact of the nonlinearity and make the device independent on the input flows, they investigated numerically different junction combinations. Finally, through a series of trials, they found the geometry which satisfied their requirements. This work has shown that inertial effects depend on the angles between the channels. However, the analysis of the impact of the angles has been limited only to the optimization of a single device.

Oh et al. in their review on electric circuit analogy in microfluidics noticed that nonlinearities in junctions can be problematic (Oh et al. 2012). They advised the use of slanted junctions instead of right-angle junctions to minimize these effects. This conclusion rightly suggests the impact of the angles on the inertial effects; however, it is rather an intuitive remark, which lacks deeper quantitative consideration.

The junctions in larger scales and for high Reynolds number have been investigated as a part of pipe systems (Matthew 1975; Hager 1984; Bassett et al. 2001) or as a part of vascular networks (Mynard and Valen-Sendstad 2015). In hydraulics, elements such as junctions or bends are considered to be a source of substantial pressure losses and described by the local pressure losses coefficients. These coefficients have been in general estimated experimentally for different geometries and are widely used in the practice of design of pipe systems (Idelchik 2005). While some concepts of hydraulics can be transferred into microfluidics,

that cannot be done directly without appropriate adaptation. The reason is that the scope of hydraulics is the range of high Reynolds numbers, while microfluidics operates within small or moderate Reynolds numbers, where both viscous and inertial interactions are essential.

Therefore, the challenge is to describe pipe-like systems within the transitional range starting from low to moderate Reynolds number—in the range of the majority of microfluidics applications. The knowledge of this transition is vital to judge the applicability of the linear, electric-like circuit, analysis of microfluidic systems. The other goal is to find the description, which takes into account nonlinearities and allows for the proper analysis of nonlinear microfluidic systems.

In this paper, we developed an experimental approach, which allows for precise and effective investigation of the splitting ratio β in microfluidic junctions for moderate Re. We show measurements of β as a function of Reynolds number in a simple microfluidic system of junctions. Significant variations of β clearly prove the discrepancy from the linear model. We show that the magnitude of these variations strongly depends on the angles between channels of the junction and more importantly, that for some combinations of angles these variations can be damped.

Additionally, we propose a mathematical model of a junction accounting for the inertial effects and its dependence on angles. The knowledge about the role of geometry allows us to design a microfluidic junction, in which the sum of all nonlinear elements in the equations vanishes and the solution recovers its linear character and independence from the Reynolds number. This work provides a practical guide for minimization of the nonlinear effects by the optimization of the junction geometry.

2 Materials and methods

2.1 Fabrication of microfluidic devices

The microfluidic devices were fabricated by direct milling of the structure of channels in transparent, 5-mm-thick polycarbonate plates (Makrolon® GP, Bayer, Germany) using a CNC milling machine (MFG4025P, Ergwind, Poland) and a 2-flute fishtail milling bit with a diameter of 385 μm (FR208, InGraph, Poland). Engraved channels (grooves) were cleaned out with a high-pressure water washer (Karcher, K7 Premium, Germany), to remove turnings and loosely bound bulk material, formed during the milling process. Further, the milled chips were washed by hand with 1% water solution of Alconox detergent (Alconox, Alconox Inc., USA), washed with isopropanol and deionized water and finally dried out by compressed air. Then, to obtain closed microfluidic channels, the engraved plate was bounded to another

flat slab of polycarbonate using a hot press (AW03, Argenta, Poland) at a temperature of 135 °C and with 0.1 bar/cm^2 pressure. The chip was kept in the press at this high temperature for 10 min and then allowed to cool down remaining under pressure. No further channel modifications were applied.

2.2 Measurements of the dye's concentration

In all presented experiments, we used as an indicator sodium pyruvate (Sigma-Aldrich, Germany) in aqueous solution with starting concentration $C_0 = 100$ mM. As the buffer liquid, we used distilled water.

We used a Multiskan Go Microplate Spectrophotometer (Thermo Scientific) to measure the absorbance of the mixture collected in PMMA UV cuvettes (BRAND, Germany) with a minimum filling volume of 1.5 mL.

All absorbance measurements were taken at the wavelength of 316 nm, which corresponds to the local maximum in the spectrum of absorbance we took in the wavelength range from 200 to 500 nm.

As the principle of concentration estimation based on the measurements of absorbance, it is important to operate in the linear regime. Before all measurements of flow ratios, the calibration curve was determined to investigate relation between absorbance and concentration. The series of measurements for concentrations of sodium pyruvate up to 600 mM allowed us to estimate the maximum level for the linear regime—about 100 mM. We used this maximum value of concentration as a base starting value of concentration in our experiments.

2.3 Flow control

The chip was connected with the syringes via polyethylene tubing (PE60 Intramedic Tubing, Becton–Dickinson, USA), and the liquids were dispensed by syringe pumps (NE-1000, New Era Systems Inc.). 100 mM aqueous solution of sodium pyruvate was inducted into one of the microchannels, while for the other input we used distilled water. Both pumps operate with equal flow rates between: 5 and 350 mL/h. After flushing the channels for 3–5 min and eliminating the bubbles to stabilize the flow, 1.5 mL of the solutions was collected in two cuvettes from each of two outlets. In order to reduce evaporation and changes in the concentration of the liquids, the cuvettes were closed at the end of every experiment. Afterwards, the measurements of concentration from each cuvette were performed.

2.4 Numerical simulations

For the numerical analysis of the water flow through the investigated channel's junctions, we used steady, isothermal,

laminar model of incompressible, viscous liquid flow, implemented in ANSYS Fluent software. Therein, discretization of the liquid flow model governing equations is obtained using the finite volume method. Full, three-dimensional models of the analysed channel's junctions were designed and created in Autodesk AutoCAD software and then transferred to ANSYS Meshing to generate the computational meshes representing the experimental devices. The boundary conditions (known from experiment) were set as velocity inlets at the inlets to the model, and as pressure outlets (pressure = 0) at the outlets. In the preliminary analysis, different meshes were tested until a mesh independent solution was obtained. As a compromise between accuracy and computational cost, we choose the mesh having 20×20 elements in the cross section of the channel. Further, mesh refining caused much higher consumption of the computer's operating memory and little to none changes of velocity magnitude in the centre of the channel (less than 0.1%). Performed computations delivered accurate details about the flow structure in the analysed devices, including the flow rates in individual segments of the channel's network.

3 Results and discussion

In the following, we show the experimental evidence of the angle's impact on the flow distribution in a microfluidic junction, on the example of a specially designed microfluidic rectangular device. Afterwards, we extend the classical circuit analysis to provide the mathematical model accounting for the angles of the junctions. Next, using the new model we analyse numerically the microfluidic junctions to investigate the possibilities for the mitigation of inertial effects by the adjusting of angles. Finally, on the example of the rectangular device, we show the minimization of the inertia's impact which can be achieved by using the optimization formula obtained in the course of this research.

3.1 Experimental and numerical evidence of the effect of inertia

3.1.1 Experiments

The experimental investigations of the single microfluidic junction (as shown in Fig. 1) may be problematic. They would require the use of direct measurements of the flow with the use of: flow-metres, pressure sensors (Kim et al. 2006); or indirect methods, e.g.: utilizing photobleaching (Cooksey et al. 2019), micro-PIV measurements (Santiago et al. 1998; Blonski et al. 2007) or weighting the output flows (Zeitoun et al. 2013).

Here, we propose the concept of a symmetric, rectangular device for the precise estimation of the flow distribution

via the measurement of the indicator's concentration. The microfluidic device consists of two identical junctions (see Fig. 2a), which outputs are so connected that they ensure rotational symmetry on the whole device. Thus, the arms of the junctions form an internal rectangle. Two inputs of two independent inflows are placed in the opposite vertices of the rectangle. Two other opposite corners serve as outputs.

If two input flows are equal, the channel's symmetry implies the symmetry of the flow in the device. Therefore, the flow rates on opposite sides of the rectangle are equal. Particularly, flow rates in both long sides (of the length L_1) are the same and equal Q_1 and similarly, flow rates in both short arms (L_2) are identical and equal Q_2 (see Fig. 2a).

Let us consider the addition of the optical indicator with a concentration C_0 in the liquid injected to one of the inlets (as shown in Fig. 2a) while the clear buffer is injected into the opposite inlet. As illustrated in Fig. 2a, in our device the flow of indicator Q_1 encounters the flow of a buffer Q_2 at the outlet I, while the flow of indicator Q_2 encounters the flow of buffer Q_1 at outlet II. In result, we obtain different mixing ratios at each outlet. Thus, the resultant concentrations of the indicator are $C_I = C_0 Q_1 / (Q_1 + Q_2)$ and $C_{II} = C_0 Q_2 / (Q_1 + Q_2)$ for outputs I and II, respectively (see Fig. 2a). What is important for our investigations, is that the ratio of these concentrations equals the ratio of flows: $C_I / C_{II} = Q_1 / Q_2 = \beta$.

As the concentration of the indicator is its quantity, which can be easily measured by the use of a spectrophotometer, the proposed design of the device provides a convenient method for the accurate and non-invasive measurement of the ratio of flows Q_1 / Q_2. In our experiments, the quantity we measured directly by the use of a spectrophotometer was the absorbance A, which according to the Beer–Lambert law is proportional to the concentration. Thus, the ratio of flows was estimated directly as the ratio of absorbances: $\beta = Q_1 / Q_2 = A_I / A_{II}$. This makes the estimation of β independent of possible fluctuations of starting concentration C_0. The above-proposed approach ensures the high precision of measurements and a high reproducibility of results. The spectrophotometer is a very common and rather standard equipment available in most laboratories. Hence, this method may be very simply implemented in the investigation of flow distributions within microfluidic networks.

In order to investigate the impact of angles between channels on the flow distribution in junctions, we conducted a series of experiments in rectangular devices with different angles ϕ_1 and ϕ_2 (Fig. 2b). To focus solely on the impact of angles, we kept other geometric parameters constant, i.e. both lengths $L_1 = 16.67$ mm and $L_2 = 10$ mm with the constant $\beta_0 = L_2 / L_1 = 0.6$ and a constant sum of both angles $\phi_1 + \phi_2 = 90°$, which sets the right angles between the output arms. All channels had a square cross section of the width $W = 0.385$ mm, and relative lengths of arms were: $l_1 = L_1 / W = 43.29$ and $l_2 = L_2 / W = 25.97$.
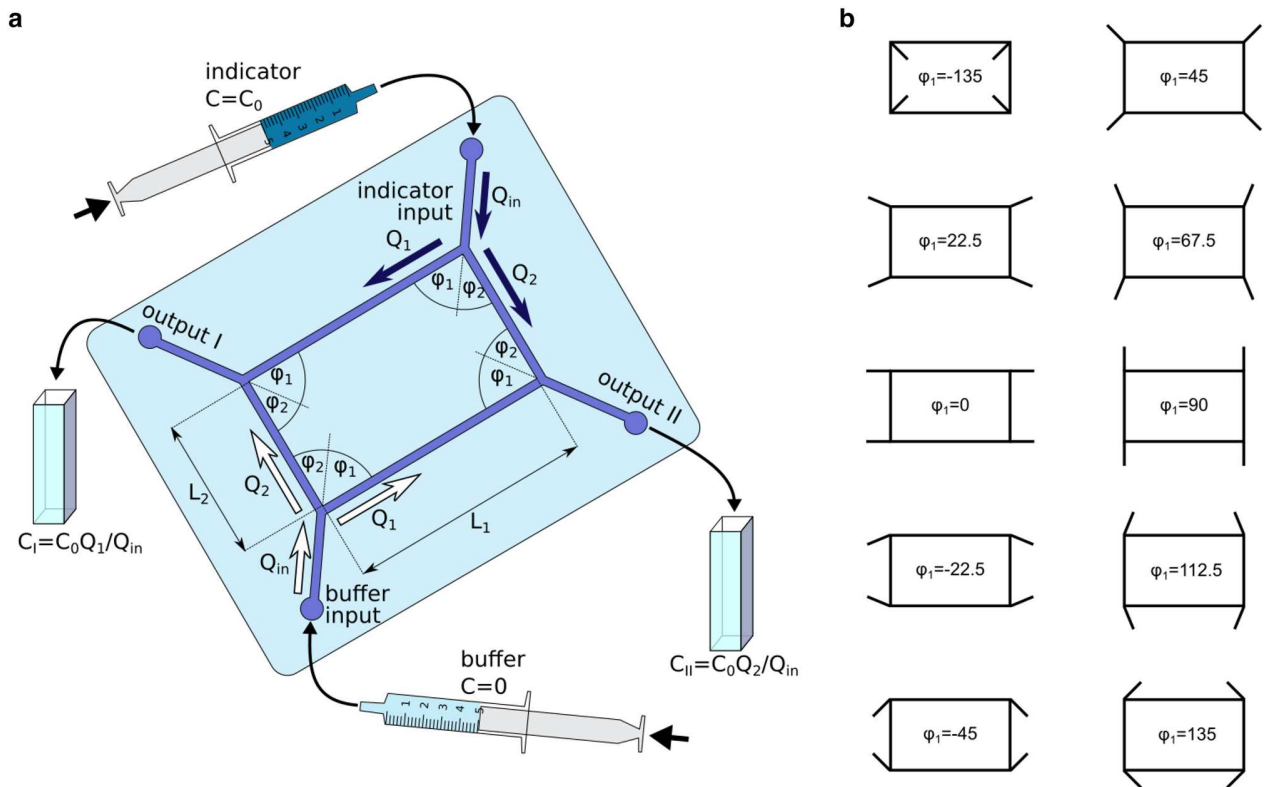
Fig. 2 Schematic view of the experimental setup. **a** The idea of the experiment, **b** Configurations of inlets and outlets in the investigated microfluidic devices for all considered angles

The internal rectangle formed by the sides L_1 and L_2 was an element repeated in the architecture of each device used in this research. The only elements with varying configurations were two inlet channels and two output channels, which are connected to vertices of the rectangle at different angles ϕ_1 and ϕ_2 as shown in Fig. 2b. To minimize the number of varying parameters, the inlet and output channels were connected at the same angle ensuring the symmetry of the whole device. We have produced and tested devices characterized by the set of angles ϕ_1 with a step of 22.5°; however, investigations herein are limited only to cases where both values of angles ϕ_1 and ϕ_2 were not larger than 135° and not smaller than −135°. The reason for that is, for the omitted values of angles, the input and output channels would partially overlap the channels of the internal rectangle, as, e.g. for angles 180° or −180° they would overlap completely. Taking this into account, we chose the following set of angles ϕ_1: − 135°, − 45°, − 22.5°, 0°, 22.5°, 45°, 67.5°, 90°, 112.5°, 135°.

In order to obtain identical flow symmetry of the flow, we ensured the same conditions at both inlets and the same conditions at both outlets (as shown in Fig. 2). The liquids flowing out from the outputs were directed into UV cuvettes via tubing of equal lengths. The collecting cuvettes were

placed at the same level, which ensured equal pressures at both outlets.

3.1.2 Experimental results and numerical simulations of rectangular devices

Parallelly to the experiments, we investigated the same set of microfluidic geometries by the use of 3D numerical simulations. In order to simulate the conditions of the experiments, we applied the same conditions to the device, i.e. equal volumetric flow rates to both input channels and equal pressure to both output channel. Unlike in the experiments, where we used the chemical indicator and optical methods for indirect measurement of the flow ratio, in the numerical simulations, the flow rates in both channels-sides-of-rectangle were measured directly.

Figure 3 depicts the results of measurements of β normalized by β_0 for different devices characterized by the specific angle ϕ_1 taken in a wide range of Re. Therein, we present the results of numerical simulations as well. Both numerical and experimental data are very similar to each other. The minimal quantitative differences between simulations and experiment could be explained as a discrepancy between the ideal in silico case and the real experiment, which may

Fig. 3 Results of the experimental measurements (solid lines) and numerical simulations (dashed lines) for the rectangular devices with $\beta_0 = 0.6$ and with different angles of inlets and outlets. **a** The range of angles from $-22.5°$ to $112.5°$. **b** The range of angles from $112.5°$ to $-22.5°$
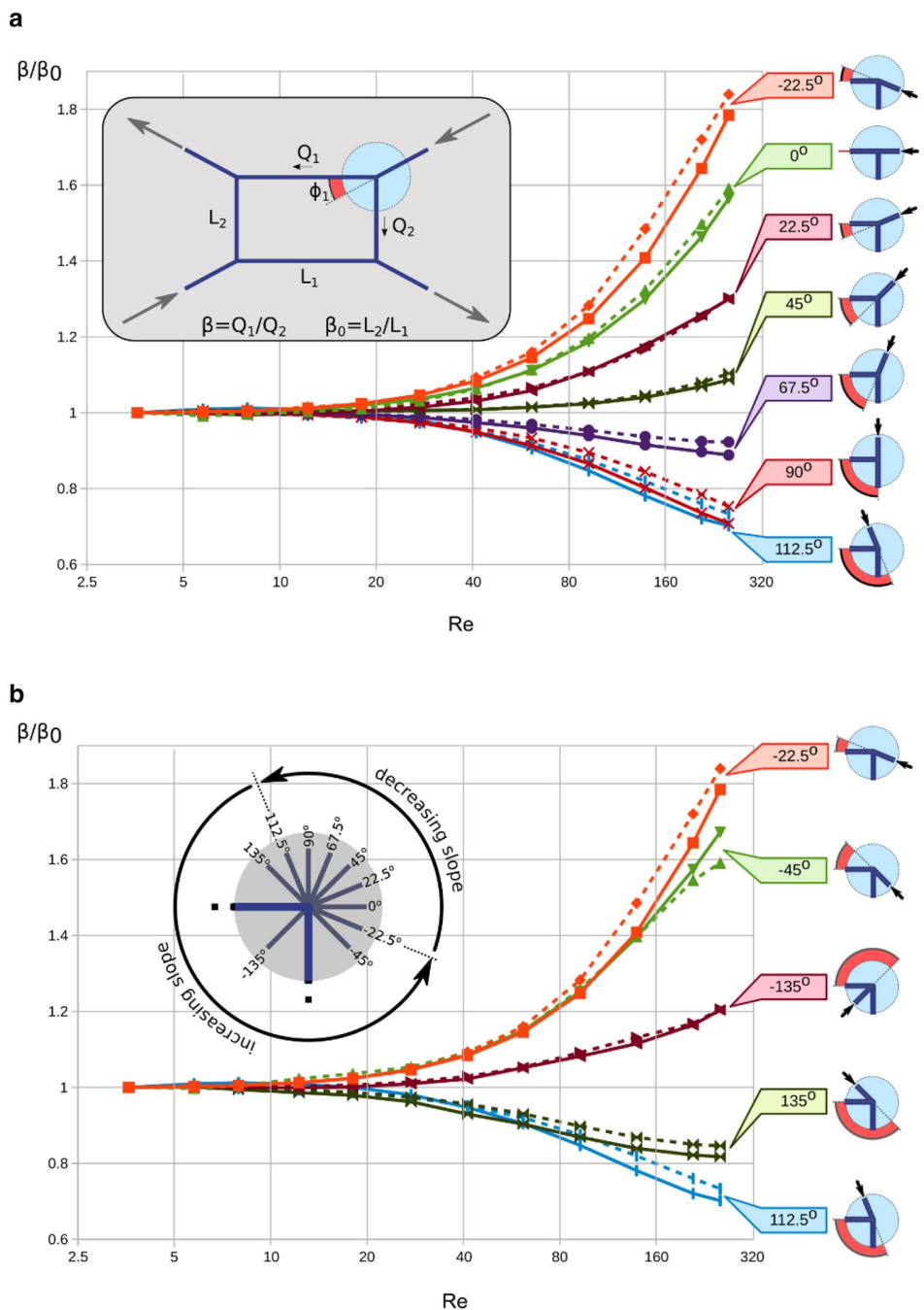
be influenced by a number of factors. In the particular case of our experiments, the main issue might be the fabrication precision of the microfluidic chip, which relies on a two-step process including micro-milling and bonding. However, despite some quantitative discrepancies, the qualitative similarity between both approaches is very good. Hence, we conclude, the numerical model can be used for the prediction of the flow distribution in microfluidic junctions.

Analysing data sets in Fig. 3, we can notice that for low Re all data for different angles converge to unity ($\beta/\beta_0 = 1$),

what proves for low Re the inertial effects vanish. So, in the regime of low Re there is no effect of the angle between the arms of the junction.

Observations of the data in Fig. 3 for higher values of Re implies that we can distinguish Re = 10—an arbitrary transition threshold between the range of Re where inertial effects can be neglected, and the range of Re where the inertia significantly impacts on the distribution of flows (Re > 10). In the latter regime, the larger the Re is the larger the deviation of β/β_0 from unity. The rate of growth of this deviation

depends on the angle ϕ_1 and—more importantly—for each geometry the slope of the curves in Fig. 3 depends on Re.

Extreme deviations of β/β_0 unity in the case of our data sets are observed for $\phi_1 = -22.5°$ and $\phi_1 = 112.5°$. Those observations directly prove that the angles between the arms of a junction can significantly influence the distribution of flow in junctions. Thus, the linear approximation may be completely inadequate for the mathematical description of flows in branching points for moderate Re.

The other interesting fact that we infer from the results in Fig. 3 is that the smallest deviations of β/β_0 can be expected between $\phi_1 = 45°$ and $\phi_1 = 67.5°$. Notice that β/β_0 rises with Re for $\phi_1 = 45°$ and decreases for $\phi_1 = 67.5°$. Thus, we can hypothesize that between these values of the angle ϕ_1, there exists an optimal value for which the dependence on Re vanishes.

3.2 Mathematical analysis

The classical circuit analysis commonly used in microfluidics does not account for any nonlinear effects and cannot explain the results of above-described experiments, where we observed the dependence of flows on both angle and Re. In this section, we propose a mathematical description which extends the linear circuit analogy. Here, we take into account the possible inertial effect that can occur in the junction. In this purpose, we adapt the hydraulic approach to the simplified description of a network of channels.

3.2.1 Description of the pressure losses in hydraulics

The pressure losses in the course of the motion of a fluid are due to the irreversible transformation of mechanical energy into heat. In classical hydraulics, two kinds of pressure losses are distinguished in principle: major losses (or frictional losses) Δp_F due to friction and minor losses (or local losses) Δp_L due to the change of velocity, e.g.: in bends, expansions, contractions, valves, etc. (Idelchik 2005).

The energy difference can be expressed in terms of the Bernoulli theorem, which results in the following equation commonly used in hydraulics:

$$\left(p_{start} + \frac{1}{2}\rho U_{start}^2\right) - \left(p_{end} + \frac{1}{2}\rho U_{end}^2\right) = \Delta p_F + \Delta p_L \quad (1)$$

Here, p_{start} and p_{end} are static pressures at the start point and the endpoint of the hydraulic conduit, respectively. $\frac{1}{2}\rho U_{start}^2$ and $\frac{1}{2}\rho U_{end}^2$ are dynamic pressures, which depend on the mean velocities U_{start} and U_{end} at selected points. The hydrostatic pressure is constant and is not relevant in this paper.

The major loss Δp_F is caused by a viscous friction during the flow of liquid in pipes and can be expressed by the use of the Darcy–Weisbach equation: $\Delta p_F = \frac{1}{2}\lambda\rho U^2 L/W$. Where ρ

is the density of the liquid, L—channel length, W—hydraulic diameter (here equal the width of the channel), $U = Q/S$ —the mean flow velocity calculated as the volumetric flow rate Q divided by the cross-sectional area of the channel S.

The friction factor λ depends on the Reynolds number and the characteristics of the channel such as the shape of its cross section and roughness of walls. The friction factor in laminar flows depends on the Re as: $\lambda \propto \mathrm{Re}^{-1}$. Thus, in the laminar regime, flow through the pipe can be expressed in terms of the modified Hagen–Poiseuille equation, which general form, applicable to any cross section of the channel is:

$$\Delta p_F = QR = Q\alpha L\mu S^{-2} \quad (2)$$

Here, R is the hydraulic resistance and α is a non-dimensional coefficient of resistance depending only on the shape of the cross-section, e.g. $\alpha = 28.6$ for square (Mortensen et al. 2005).

The minor losses (or local losses) appear at a disturbance of the flow in regions, where the flow encounters a sudden change of geometry. While viscous losses take place along the entire length of the microchannel (and depend on L), minor losses are taken into account only locally: $\Delta p_L = \frac{1}{2}\zeta\rho U^2$, where ζ is the local loss coefficient, specific for the geometry, in which the pressure loss takes place (Idelchik 2005).

In the case of the junction, we can expect that the local coefficients ζ can display the impact of angles between the channels connected in the junction (Matthew 1975; Hager 1984; Bassett et al. 2001; Mynard and Valen-Sendstad 2015). Indeed, the angles determine the change of flow direction, but usually, they are neglected in the electric-like-analysis of microfluidic systems, where branching points are reduced to point nodes.

Here, we consider a junction connecting three channels of the same, square cross sections characterized with the width W. At first, we consider only the case of a dividing junction which splits the incoming flow Q_{in} into two outcoming flows Q_1 and Q_2. We can expect that inertial effects can influence the splitting ratio $\beta = Q_1/Q_2 = U_1/U_2$.

Let us write the Bernoulli equations for both outflows in terms of local losses:

$$\left(p_{in} + \rho\frac{U_{in}^2}{2}\right) - \left(p_0 + \rho\frac{U_1^2}{2}\right) = \zeta_1\rho\frac{U_1^2}{2} + Q_1\frac{\mu}{W^4}\alpha L_1 \quad (3)$$

$$\left(p_{in} + \rho\frac{U_{in}^2}{2}\right) - \left(p_0 + \rho\frac{U_2^2}{2}\right) = \zeta_2\rho\frac{U_2^2}{2} + Q_2\frac{\mu}{W^4}\alpha L_2 \quad (4)$$

where ζ_1 and ζ_2 are coefficients of local pressure losses for both outputs. We assume that they can be expressed by the

common function $\zeta(\phi_i, \phi_j)$ of angles, $\zeta_1 = \zeta(\phi_1, \phi_2)$ and $\zeta_2 = \zeta(\phi_2, \phi_1)$, respectively.

The above set of equations can be expressed with the terms of pressure drop $\Delta p = p_{in} - p_0$, hydraulic resistances R_1 and R_2 and 'inertial' resistances $\tilde{R}_1$ and $\tilde{R}_2$ (see Fig. 1c):

$$\Delta p = R_1 Q_1 + \tilde{R}_1 Q_1 \tag{5}$$

$$\Delta p = R_2 Q_2 + \tilde{R}_2 Q_2 \tag{6}$$

where the hydraulic resistances are:

$$R_1 = \frac{\mu}{W^4} \alpha L_1 = \frac{\mu}{W^3} \alpha l_1 \tag{7}$$

$$R_2 = \frac{\mu}{W^4} \alpha L_2 = \frac{\mu}{W^3} \alpha l_2 \tag{8}$$

and the inertial resistances are:

$$\tilde{R}_1 = \mathrm{Re} \frac{\beta}{\beta + 1} \left(K_1 \alpha - \frac{1}{2} \frac{(1 + \beta)^2}{\beta^2} \right) \frac{\mu}{W^3} \tag{9}$$

$$\tilde{R}_2 = \mathrm{Re} \frac{1}{\beta + 1} \left(K_2 \alpha - \frac{1}{2} (1 + \beta)^2 \right) \frac{\mu}{W^3} \tag{10}$$

Here, the Reynolds number is taken for the inlet flow: $\mathrm{Re} = \rho U_{in} W / \mu$. For the simplicity of further calculations, we introduced $K_1 = K(\phi_1, \phi_2) = \frac{1}{2}(\zeta_1 + 1)/\alpha$ and $K_2 = K(\phi_2, \phi_1) = \frac{1}{2}(\zeta_2 + 1)/\alpha$, where $K(\phi_i, \phi_j)$ is a function of the angles ϕ_i and ϕ_j of the junction.

The set of Eqs. (5)–(6) leads to the following equation for β:

$$\beta = \frac{Q_1}{Q_2} = \beta_0 \frac{1 + \tilde{R}_2/R_2}{1 + \tilde{R}_1/R_1} \tag{11}$$

where β_0 is a constant coefficient set by the ratio of the lengths of the arms—$\beta_0 = R_2/R_1 = L_2/L_1 = \mathrm{const}$. In this equation, the inertial resistances introduce dependence on Re. Notice that if the numerator and the denominator in Eq. (11) are equal, it simplifies to the form:

$$\beta = \beta_0 = \beta_{opt} \tag{12}$$

where β_{opt} is the optimal value of β_0, ensuring the independence of β on Re. Finally, from Eqs. (7)–(12), we obtain the following relation:

$$\beta_{opt}(\phi_1, \phi_2) = \sqrt{K_2/K_1} = \sqrt{K(\phi_2, \phi_1)/K(\phi_1, \phi_2)} \tag{13}$$

Here, the coefficient $\beta_{opt}(\phi_1, \phi_2)$ is the optimal ratio of arms $\beta_0 = L_2/L_1$ for which $\beta(\mathrm{Re}) = \mathrm{const} = \beta_0$. The above implies that β_{opt} is solely a function of angles; hence, the condition $\beta(\mathrm{Re}) = \beta_0$ can be obtained by the proper adjustment

of the lengths of the arms L_1, L_2 and angles ϕ_1 and ϕ_2. In the optimal configuration, $\beta_0 = L_1/L_2 = \beta_{opt}(\phi_1, \phi_2)$ and β does not depend on Re.

Although we do not know the exact form of the equation, defining β_{opt} as a function of angles, we can state here the hypothesis that optimal adjustment of the geometry of the junction can exist. We explore this hypothesis later.

The set of Eqs. (7)–(11) yields the following equation for β:

$$\mathrm{Re} \frac{1}{l_1} \left(K_1 \beta^2 - K_2 \right) = (\beta_0 - \beta) \cdot (1 + \beta) \tag{14}$$

where $l_1 = L_1/W$.

Introducing $\beta_{opt}^2 = K_2/K_1$, Eq. (14) reads:

$$\mathrm{Re} \frac{K_1}{l_1} \left(\beta^2 - \beta_{opt}^2 \right) = (\beta_0 - \beta) \cdot (1 + \beta) \tag{15}$$

The only non-negative solution of quadratic Eq. (15) is given by:

$$\beta = \frac{(\beta_0 - 1) + \sqrt{4\left(\beta_0 + \beta_{opt}^2 \mathrm{Re}\frac{K_1}{l_1}\right)\left(1 + \mathrm{Re}\frac{K_1}{l_1}\right) + (\beta_0 - 1)^2}}{2 + 2\mathrm{Re}\frac{K_1}{l_1}} \tag{16}$$

Here, we still do not know the values of K_1, K_2 and so β_{opt}, but we can assume all of them to be positive.

Investigating the limits of β for both vanishing and high values of Re, we obtain the limits:

$$\lim_{\mathrm{Re} \to 0} \beta = \beta_0 \tag{17}$$

and

$$\lim_{\mathrm{Re} \to \infty} \beta = \beta_{opt} \tag{18}$$

Equation (17) is in line with our previous expectation and the data from the investigations of the rectangular device. This explains that β starts from $\beta(\mathrm{Re} = 0) = \beta_0$ so for low Re it works analogically to electric circuits. Equation (18) implies that for large values of Re, value of β tends to β_{opt}.

In other words, in the limit of low Re [see Eq. (17)] the distribution of flows is determined only by the lengths of the arms of the junction ($\beta_0 = L_2/L_1$), while for large Re [see Eq. (18)] this distribution is determined by the angles (as β_{opt} is the function of angles only). Thus, we can expect that $\beta(\mathrm{Re})$ is an increasing function if $\beta_0 < \beta_{opt}$ or a decreasing function if $\beta_0 > \beta_{opt}$. For $\beta_0 = \beta_{opt}$, the dependence on Re disappear. Thus, the above conclusions from the hydraulic description of the junction are in qualitative agreement with the previously obtained data.

In the following, we investigate separate junctions by the use of numerical simulations to show the difference between

the splitting junctions and the merging ones. Afterwards, we show that even with the lack of the explicit form of $K(\phi_1, \phi_2)$ we can provide the approximate description of β_{opt} as a function of angles.

3.3 Numerical investigations of separate junctions

Once the numerical model had been verified on the base of experimental data, we performed a series of numerical investigations of single junctions. The great advantage of numerical simulations is that the boundary conditions can be easily and precisely defined, and all parameters can be measured without any disturbance of the system.

Particularly in the case of our research, thanks to numerical simulations, we could investigate separately, single junctions. The rectangular device used in experiments consists of four junctions, two splitting junctions and two merging ones. Measurements from that device yielded the evidence of the impact of angles, but the results are the combinations of effects from both junctions of different types.

Although the general mathematical description can be applied to both kinds of junctions, due to the irreversibility of inertial flows, we can expect that local losses are different. To investigate these effects separately, we conducted a series of numerical experiments in single junctions of both types (see Fig. 4). In the case of simulating the single splitting junction, we set the same pressure on both outlets of the junction and a constant flow rate in the input channel. In the case of the simulation of the single merging junction, we set the same pressure on both inputs and the constant flow rate in the common output channel.

In order to avoid uncertainties in the comparison of results from different separate junctions, in all considered cases we kept $L_1 = 10$ mm constant, changing $\beta_0 = L_2/L_1$ by adjusting L_2.

3.3.1 Flow through a splitting junction

The example results of the simulations of the flow through the splitting junctions are presented in Fig. 5a where we

compare data for junctions characterized by two different values of parameter β_0 (0.5 and 4). We investigated different configurations of junctions changing angles ϕ_1 and ϕ_2, keeping the sum of these angles constant ($\phi_1 + \phi_2 = 90°$). Hence, two output arms form the right angle and only the angle of the input channel changes. The length of the first arm in both cases was the same and equal to $L_1 = 10$ mm, what for the width of the channel $W = 0.385$ mm results in a non-dimensional length $l_1 = L_1/W = 25.97$. For both values of β_0, we used a set of angles of the inlet channel characterized by the angle ϕ_1 within the range from $-45°$ to $135°$ with a step of $22.5°$. For each geometry of the junction in numerical simulations, we estimated the ratio of flows $\beta = Q_1/Q_2$ as a function of Reynolds number in the range from 3.85 to 269.5.

The results, depicted in Fig. 5a, reveal the significant differences between junctions with different angles. Value of $\beta = Q_1/Q_2$ is approximately equal β_0 for small Re, while for larger Re, β depends significantly on Re. Depending on the value of ϕ_1, β can be a decreasing or increasing function of Re. In any case, the deviation of β from the value of β_0 rises systematically with Re, with the rate of this deviation depending strongly on the angle ϕ_1. We can guess from the graph that the least deviation can be observed in the case for $\beta_0 = 0.5$ for the angle ϕ_1 between $45°$ and $67.5°$, while for $\beta_0 = 4$ the optimal angle is less than $22.5°$ but more than $0°$. These observations confirm our previous assumption that the optimal angles of the junctions are not universal, but they depend on β_0. In order to compare the deviation rate of different curves from the characteristic value of β_0, we quantified it by the use of a non-dimensional deviation coefficient Ψ defined as follows:

$$\Psi(\beta_0, \phi_1, \phi_2) = \sqrt{\frac{1}{\text{Re}_{\text{max}}} \int_0^{\text{Re}_{\text{max}}} \left(\frac{\beta(\text{Re})}{\beta_0} - 1\right)^2 d\text{Re}}$$

(19)

where Re_{max} is the top limit of the range of Reynolds number used in the simulations. Figure 5b plots the values of the

Fig. 4 Two arrangements of the flow in junctions: **a** the splitting junction, **b** the merging junction
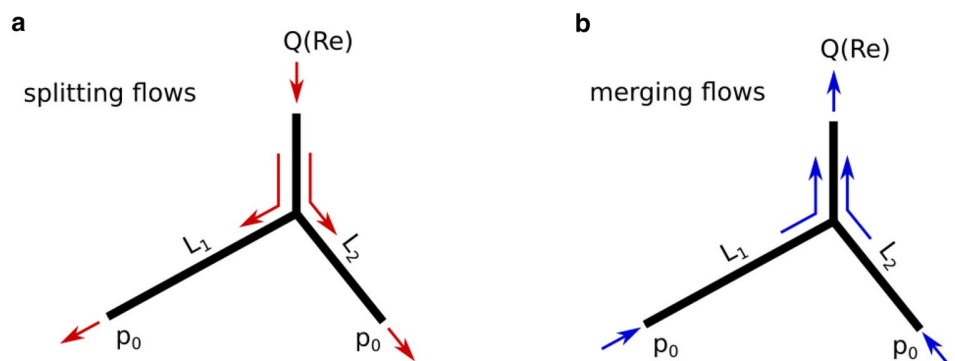
Fig. 5 Numerical analysis of the dividing junction. **a** $\beta = Q_1/Q_2$ as a function of Re for two examples of β_0 (=4,0.5) and for $\phi_1 + \phi_2 = 90°$. Each data series corresponds to different angles between channels characterized by the specific values of ϕ_1 (see the legend and schematic presentations of the geometry of junctions on the side panels). **b** Non-dimensional deviation coefficient Ψ [see Eq. (19)] as a function of angle ϕ_1 for the data series presented in **a**. The additional solid lines—the quadratic interpolation for three data points nearest the local minimum. The inset—optimal geometries of junctions, corresponding to estimations of ϕ_{opt}
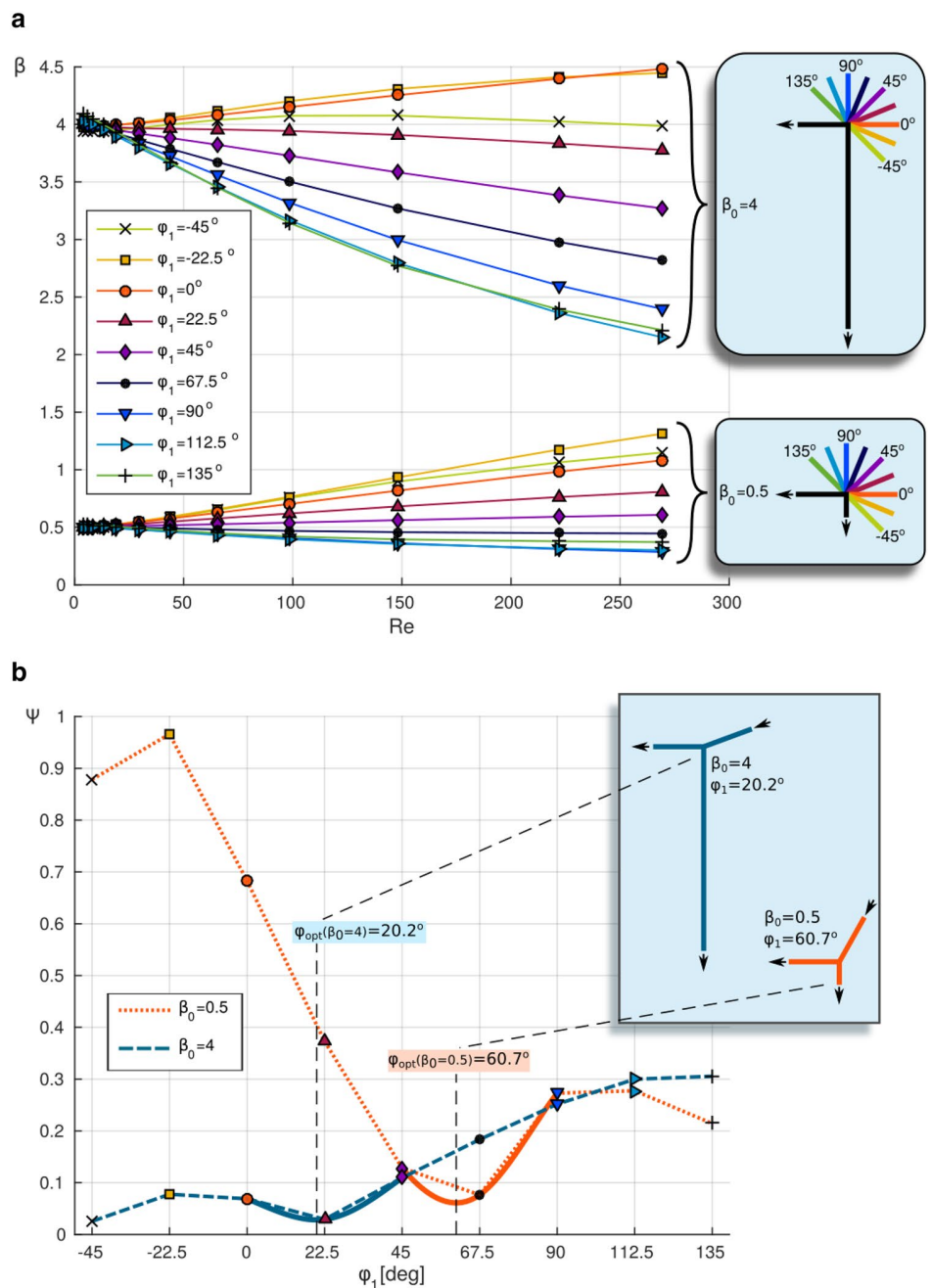
deviation coefficient Ψ as a function of angle ϕ_1 calculated for the data sets from Fig. 5a.

This clearly shows the high variation of the deviation rate for different angles for a given junction. Dependence of the coefficient Ψ on the angle can be used for the estimation of the optimal configuration by finding the minimum of Ψ. In this paper, for practical reasons, we limited ourselves only to the minimization of Ψ for positive values of angles ϕ_1 and ϕ_2, however, as we can see in Fig. 5b the optimal conditions may exist for negative angles as well

(see data for $\beta_0 = 4$, $\phi_1 = -45°$). For better resolution of the optimal value estimation of the angle ϕ_{opt}, we used quadratic interpolation for three data points nearest to the local minimum.

We repeated the above-mentioned optimization procedure for more junction configurations changing the value of β_0 within the range from 0.25 to 8 and for different sums of angles ϕ_1 and ϕ_2 (45°, 90°, 135°, 180°), keeping $l_1 = 25.97$ constant for all junctions. The optimal sets of angles for different values of β_0 are plotted in Fig. 6.
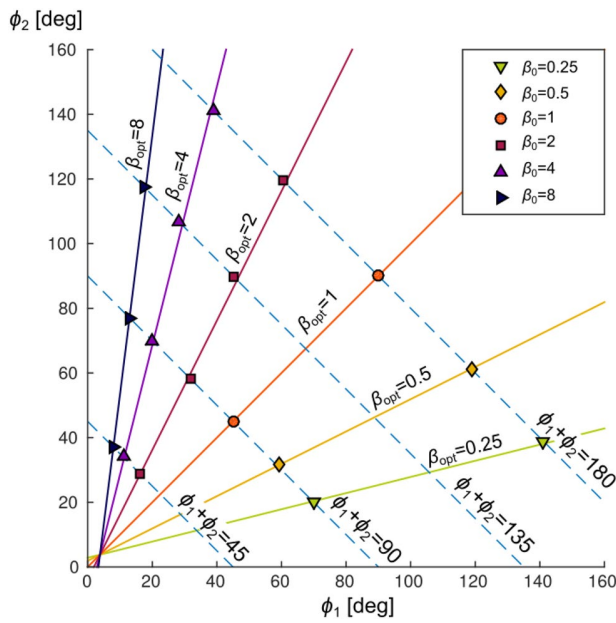
Fig. 6 Optimal values of angles ϕ_1 and ϕ_2 for different values of β_0 estimated from numerical simulations. Markers—the data obtained from numerical optimization (see legend). The solid lines—plots of the optimization formula [see Eq. (21)] for different values of β_{opt}, as indicated in the graph. The dashed lines—isolines of the constant sum of angles

Looking for an effective and simplified optimization formula, we fitted the following equation to the obtained data points:

$$\beta_0 = \frac{a \cdot \phi_2^2 + \phi_2 + b}{a \cdot \phi_1^2 + \phi_1 + b} \tag{20}$$

In result, we obtained the following values of fitting parameters: $a = 0.5 \cdot 10^{-4} \pm 2.0 \cdot 10^{-4}$ and $b = -3.8° \pm 0.2°$. Neglecting the vanishing parameter a, we rewrite the optimization formula in the following compact form:

$$\beta_0 = \frac{\phi_2 - 3.8°}{\phi_1 - 3.8°} \tag{21}$$

To test this optimization formula, we plotted in Fig. 6 additional lines for constant values of β_0, which very well agree with the data points obtained from numerical optimization.

3.3.2 Flow through a merging junction

We conducted numerical simulations for junctions, with reversed flow (see Fig. 4). In this case, two input flows

meet in the junction and merge forming one output flow. In order to describe the flow, by analogy, we can use an equation similar to Eq. (14):

$$\text{Re} \frac{1}{l_1} \left(\hat{K}_1 \beta^2 - \hat{K}_2 \right) = (\beta_0 - \beta) \cdot (1 + \beta) \tag{22}$$

where the additional coefficients $\hat{K}_1$ and $\hat{K}_2$ are introduced to distinguish them from the coefficients K_1 and K_2 for the splitting junction. Function $\hat{K}(\phi_i, \phi_j)$ describes the dependence of the local loss coefficients on angles: $\hat{K}_1 = \hat{K}(\phi_1, \phi_2)$ and $\hat{K}_2 = \hat{K}(\phi_2, \phi_1)$.

In this case, the numerical results reveal that unlike in the case of a splitting junction, in the merging junction β does not depend significantly on the angles (compare Figs. 5a and 7). This is not surprising as the local reverse flow regions are not created. That suggests that in the case of the merging junction the main reason for the pressure loss is the change of the total cross section of the flow.

Let us assume that $\hat{K}(\phi_i, \phi_j)$ can be expressed as a sum of a constant coefficient Λ and an angle-dependent part $\kappa(\phi_i, \phi_j)$: $\hat{K}(\phi_i, \phi_j) = \Lambda + \kappa(\phi_i, \phi_j)$. Because we observed that β weakly varies with the angle in the merging junction, we can assume that $\Lambda \gg \kappa(\phi_i, \phi_j)$. Applying the following substitution $\hat{K}_1 \approx \hat{K}_2 \approx \Lambda$ in Eq. (22) and dividing both sides of the equation by $(1 + \beta)$, we obtain:

$$\text{Re} \frac{\Lambda}{l_1} (\beta - 1) = (\beta_0 - \beta) \tag{23}$$

In the range of Re where β does not significantly differ from β_0, we can use the following approximation—$(\beta - 1) \approx (\beta_0 - 1)$, which applied to Eq. (23) leads to the following linear relation for $\beta(\text{Re})$:

$$\beta(\text{Re}) = \beta_0 + \text{Re} \frac{\Lambda}{l_1} (1 - \beta_0) \tag{24}$$

Via the fitting of Eq. (24) to the data sets obtained from numerical simulations, we estimated that parameter $\Lambda = 0.01$.

The optimizing formula given by Eq. (13) is formally the same in the case of both type of junctions, so in case of the merging junction we can state:

$$\hat{\beta}_{opt} = \sqrt{\hat{K}_2 / \hat{K}_1} \tag{25}$$

Here, we distinguish $\hat{\beta}_{opt}$ as an optimum for the merging junction. As we mentioned above in the case of the merging junction $\hat{K}_1 \approx \hat{K}_2$, thus $\hat{\beta}_{opt} \approx 1$. The conclusion is that unlike in the case of a splitting junction, the flows in merging junctions weakly depend on angles. So, practically this implies that the merging junction cannot be balanced for β_0 other than 1 while adjusting the angle.
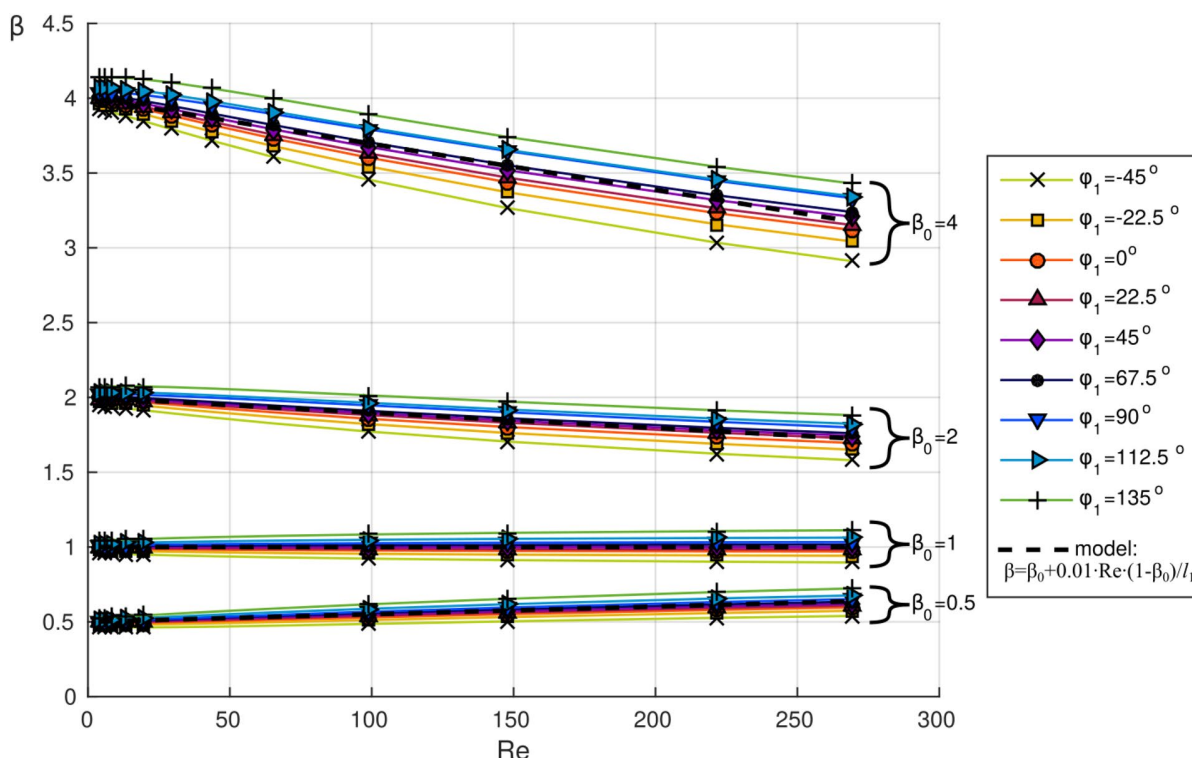
Fig. 7 Numerical analysis of the merging junctions. $\beta = Q_1/Q_2$ as a function of Re for four examples of β_0 (=4, 2, 1, 0.5) and for $\phi_1 + \phi_2 = 90°$. Each data series corresponds to different angles between channels characterized by the specific values of ϕ_1 (see the legend)

3.4 Optimization of the rectangular device

Above, we analysed the effect of inertia in both the splitting and the merging junctions, separately. Usually, microfluidic networks consist of both these types of junctions (e.g. our rectangular device). The effective minimization of inertial components in the mathematical models of such networks requires knowledge about the values of coefficients $K(\phi_i, \phi_j)$ and $\hat{K}(\phi_i, \phi_j)$. However, this preliminary study does not provide the explicit formulas of angle-dependence of these important coefficients.

Despite the lacks mentioned above, the important and useful result of this work is the optimization formula for the splitting junction given by Eq. (21). Hence, that raises the question, if this formula can be used for the first attempt of inertial effect mitigation in microfluidic systems comprising both kinds of junctions. Comparing the results from the rectangular device (Fig. 3) and both types of junctions (Figs. 5 and 7), we can observe the qualitative similarity of the rectangular device and the splitting junction, consisting in the high dependence on the angle in both cases. That suggests that in the system consisting of both the splitting and the merging junctions the inertial effects occurring in the splitting junctions dominate in regards to the performance of the whole device.

These conclusions imply that the first attempt of microfluidic network optimization can be made by neglecting the merging junctions and by only accounting for the splitting junctions. We applied this approach in the case of our rectangular device using the optimization formula [Eq. (21)] for $\beta_0 = 0.6$, $\phi_2 = 90° - \phi_1$ and obtained $\phi_1 = 55°$. It is worth to notice the yielded value of ϕ_1 is between $45°$ and $67.5°$ as we predicted from the experimental analysis of the rectangular device.

In order to test the efficiency of this optimization, we performed both numerical and experimental analysis of the rectangle device with $\phi_1 = 55°$, as presented in Fig. 8. The results show that thanks to the application of the simplified optimization procedure, the impact of inertia in the microfluidic network can be effectively reduced. In the case of the presented data, the deviation caused by the inertia is less than 5%. Even, if the inertial effects do not vanish completely, it is still much better to use the proposed optimization than choose the angle randomly (compare Figs. 3 and 8).

4 Conclusions

In this study, we show the experimental evidence of the impact of inertia on the distribution of flows in microfluidic networks in the range of moderate Re. To our knowledge,

Fig. 8 Optimization of the rectangle device. The plot shows the comparison of numerical (dashed lines) and experimental (solid lines) results for rectangular device for the optimized geometry with $\phi_1 = 55°$. The results for the two nearest angles $\phi_1 = 45°$ and $\phi_1 = 67.5°$ from Fig. 3 are presented for the reference
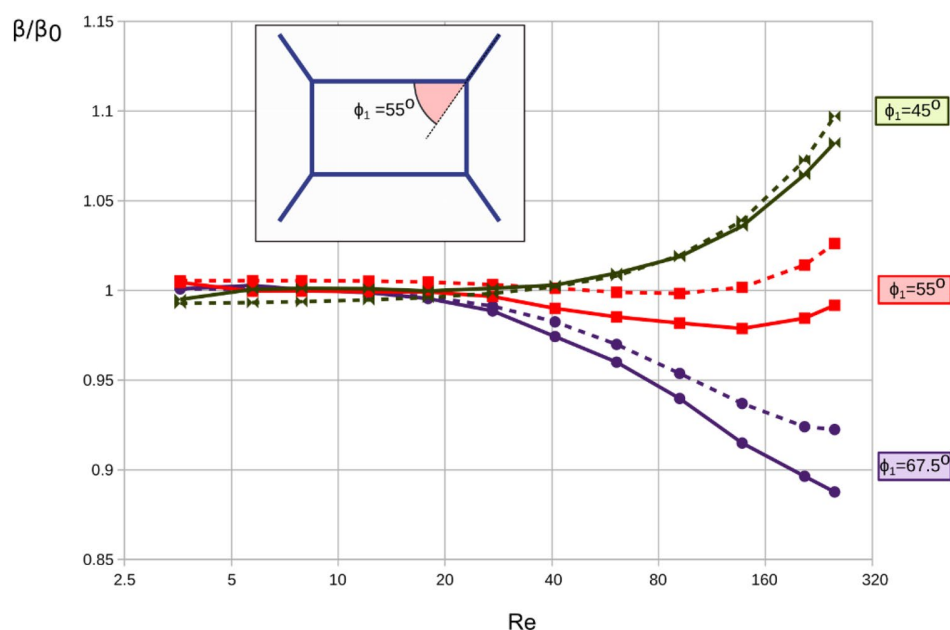
this is the first attempt to estimate the effect of angles between channels on the magnitude of inertial effects and assess the consequences of this effect for the flow distribution in microfluidic architectures. We show that the inertial effects, within the range of moderate Re, cannot be neglected; contrary, they may be critically affecting the flow.

The important outcome of this research is the optimization formula, which can be used for the effective mitigation of the nonlinear effects via the proper design of connections between channels. Thus, the output of this research is essential for the correct prediction of the operation of microfluidic networks and for its practical applications.

The presented study is a preliminary attempt to deal with nonlinearities in microfluidics. Some questions arose in the course of this work have been left without an answer and require further analysis. Although we provide guidelines, which can help in the finding of optimal angles for the mitigation of nonlinearities, we do not explain why a particular set of angles favours balancing the inertial effects in both arms of junctions. Our preliminary observations of flow patterns obtained from CFD revealed the spatial complexity of three-dimensional structures including secondary flows and flow reversal zones. The understanding of the role of these structures requires the analysis of their effect on the dissipation of energy and will be the focus of future works. This understanding of a variety of possible inertial phenomena that can occur in microfluidic systems is still the challenge and is a field for future exploration.

References

Amini H, Lee W, Carlo DD (2014) Inertial microfluidic physics. Lab Chip 14:2739–2761. https://doi.org/10.1039/C4LC00128A

Ault JT, Fani A, Chen KK et al (2016) Vortex-breakdown-induced particle capture in branching junctions. Phys Rev Lett 117:084501. https://doi.org/10.1103/PhysRevLett.117.084501

Bassett MD, Winterbone DE, Pearson RJ (2001) Calculation of steady flow pressure loss coefficients for pipe junctions. Proc Inst Mech Eng C J Mech Eng Sci 215:861–881. https://doi.org/10.1177/095440620121500801

Bhargava KC, Thompson B, Iqbal D, Malmstadt N (2015) Predicting the behavior of microfluidic circuits made from discrete elements. Sci Rep 5:15609. https://doi.org/10.1038/srep15609

Bithi SS, Vanapalli SA (2010) Behavior of a train of droplets in a fluidic network with hydrodynamic traps. Biomicrofluidics 4:44110. https://doi.org/10.1063/1.3523053

Blonski S, Korczyk P, Kowalewski T (2007) Analysis of turbulence in a micro-channel emulsifier. Int J Therm Sci 46:1126–1141. https://doi.org/10.1016/j.ijthermalsci.2007.01.028

Carlo DD (2009) Inertial microfluidics. Lab Chip 9:3038–3046. https://doi.org/10.1039/B912547G

Cooksey GA, Patrone PN, Hands JR et al (2019) Dynamic measurement of nanoflows: realization of an optofluidic flow meter to the nanoliter-per-minute scale. Anal Chem 91:10713–10722. https://doi.org/10.1021/acs.analchem.9b02056

Cybulski O, Jakiela S, Garstecki P (2015) Between giant oscillations and uniform distribution of droplets: the role of varying lumen of channels in microfluidic networks. Phys Rev E 92:063008. https://doi.org/10.1103/PhysRevE.92.063008

Cybulski O, Garstecki P, Grzybowski BA (2019) Oscillating droplet trains in microfluidic networks and their suppression in blood flow. Nat Phys 15:706–713. https://doi.org/10.1038/s41567-019-0486-8

Dertinger SKW, Chiu DT, Jeon NL, Whitesides GM (2001) Generation of gradients having complex shapes using microfluidic networks. Anal Chem 73:1240–1246. https://doi.org/10.1021/ac001132d

Engl W, Roche M, Colin A et al (2005) Droplet traffic at a simple junction at low capillary numbers. Phys Rev Lett 95:208304

Fuerstman MJ, Garstecki P, Whitesides GM (2007) Coding/decoding and reversibility of droplet trains in microfluidic networks. Science 315:828–832. https://doi.org/10.1126/science.1134514

Hager WH (1984) An approximate treatment of flow in branches and bends. Proc IMechE 198:63–69. https://doi.org/10.1243/PIME_PROC_1984_198_088_02

Hulme SE, Shevkoplyas SS, Apfeld J et al (2007) A microfabricated array of clamps for immobilizing and imaging *C. elegans*. Lab Chip 7:1515–1523. https://doi.org/10.1039/B707861G

Idelchik IE (2005) Handbook of hydraulic resistance. Jaico Publishing House, Mumbai

Karino T, Motomiya M, Goldsmith HL (1990) Flow patterns at the major T-junctions of the dog descending aorta. J Biomech 23:537–548. https://doi.org/10.1016/0021-9290(90)90047-7

Kim D, Chesler NC, Beebe DJ (2006) A method for dynamic system characterization using hydraulic series resistance. Lab Chip 6:639–644. https://doi.org/10.1039/B517054K

Korczyk PM, Derzsi L, Jakieła S, Garstecki P (2013) Microfluidic traps for hard-wired operations on droplets. Lab Chip 13:4096–4102. https://doi.org/10.1039/C3LC50347J

Korczyk PM, van Steijn V, Blonski S et al (2019) Accounting for corner flow unifies the understanding of droplet formation in microfluidic channels. Nat Commun 10:2528. https://doi.org/10.1038/s41467-019-10505-5

Lee K, Kim C, Ahn B et al (2009) Generalized serial dilution module for monotonic and arbitrary microfluidic gradient generators. Lab Chip 9:709–717. https://doi.org/10.1039/B813582G

Lee K, Kim C, Jung G et al (2010) Microfluidic network-based combinatorial dilution device for high throughput screening and optimization. Microfluid Nanofluid 8:677–685. https://doi.org/10.1007/s10404-009-0500-z

Matthew GD (1975) Simple approximate treatments of certain incompressible duct flow problems involving separation. J Mech Eng Sci 17:57–64. https://doi.org/10.1243/JMES_JOUR_1975_017_011_02

Mortensen NA, Okkels F, Bruus H (2005) Reexamination of Hagen–Poiseuille flow: shape dependence of the hydraulic resistance in microchannels. Phys Rev E 71:057301. https://doi.org/10.1103/PhysRevE.71.057301

Mynard JP, Valen-Sendstad K (2015) A unified method for estimating pressure losses at vascular junctions. Int J Numer Methods Biomed Eng 31:e02717. https://doi.org/10.1002/cnm.2717

Nunes JK, Wu C-Y, Amini H et al (2014) Fabricating shaped microfibers with inertial microfluidics. Adv Mater 26:3712–3717. https://doi.org/10.1002/adma.201400268

Oettinger D, Ault JT, Stone HA, Haller G (2018) Invisible anchors trap particles in branching junctions. Phys Rev Lett 121:054502. https://doi.org/10.1103/PhysRevLett.121.054502

Oh KW, Lee K, Ahn B, Furlani EP (2012) Design of pressure-driven microfluidic networks using electric circuit analogy. Lab Chip 12:515–545. https://doi.org/10.1039/C2LC20799K

Santiago JG, Wereley ST, Meinhart CD et al (1998) A particle image velocimetry system for microfluidics. Exp Fluids 25:316–319. https://doi.org/10.1007/s003480050235

Stiles T, Fallon R, Vestad T et al (2005) Hydrodynamic focusing for vacuum-pumped microfluidics. Microfluid Nanofluid 1:280–283. https://doi.org/10.1007/s10404-005-0033-z

Suteria NS, Nekouei M, Vanapalli SA (2018) Microfluidic bypass manometry: highly parallelized measurement of flow resistance of complex channel geometries and trapped droplets. Lab Chip 18:343–355. https://doi.org/10.1039/C7LC00889A

van Berkel C, Gwyer JD, Deane S et al (2011) Integrated systems for rapid point of care (PoC) blood cell analysis. Lab Chip 11:1249–1255. https://doi.org/10.1039/C0LC00587H

van Steijn V, Korczyk PM, Derzsi L et al (2013) Block-and-break generation of microdroplets with fixed volume. Biomicrofluidics 7:024108. https://doi.org/10.1063/1.4801637

Vigolo D, Radl S, Stone HA (2014) Unexpected trapping of particles at a T junction. PNAS 111:4770–4775. https://doi.org/10.1073/pnas.1321585111

Wegrzyn J, Samborski A, Reissig L et al (2012) Microfluidic architectures for efficient generation of chemistry gradations in droplets. Microfluid Nanofluid 14:235. https://doi.org/10.1007/s10404-012-1042-3

Yamada M, Hirano T, Yasuda M, Seki M (2006) A microfluidic flow distributor generating stepwise concentrations for high-throughput biochemical processing. Lab Chip 6:179–184. https://doi.org/10.1039/B514054D

Zaremba D, Blonski S, Jachimek M et al (2018) Investigations of modular microfluidic geometries for passive manipulations on droplets. Bull Pol Acad Sci Tech Sci 66:139–149. https://doi.org/10.24425/119068

Zaremba D, Blonski S, Marijnissen MJ, Korczyk PM (2019) Fixing the direction of droplets in a bifurcating microfluidic junction. Microfluid Nanofluid 23:55. https://doi.org/10.1007/s10404-019-2218-x

Zeitoun RI, Langelier SM, Gill RT (2013) Implications of variable fluid resistance caused by start-up flow in microfluidic networks. Microfluid Nanofluid 16:473–482. https://doi.org/10.1007/s10404-013-1241-6

Zhang J, Yan S, Yuan D et al (2015) Fundamentals and applications of inertial microfluidics: a review. Lab Chip 16:10–34. https://doi.org/10.1039/C5LC01159K